ISSN 1694-7398
journals.manas.edu.kg

JUNE 2024
Volume 12, Issue 1

MANAS JOURNAL OF ENGINEERING

MJEN

BISHKEK 2024

KYRGYZ TURKISH MANAS UNIVERSITY
MANAS JOURNAL OF ENGINEERING (MJEN)

ISSN: 1694- 7398
Year: 2024
Volume: 12
Special Issue: 1
http://journals.manas.edu.kg
journals@manas.edu.kg

PUBLICATION PERIOD

Manas Journal of Engineering (MJEN) is published twice year, MJEN is a peer reviewed journal.

CORRESPONDENCE ADDRESS
Kyrgyz Turkish Manas University
Chyngyz Aitmatov Avenue 56 Bishkek, KYRGYZSTAN
URL: http://journals.manas.edu.kg
e-mail: journals@manas.edu.kg
Tel : +996 312 492763- Fax: +996 312 541935

KYRGYZ TURKISH MANAS UNIVERSITY
MANAS JOURNAL OF ENGINEERING (MJEN)

CONTENT

Research article

Review Article

MANAS Journal of Engineering
ISSN 1694-7398 | e-ISSN 1694-7398

Volume 12, Issue 1, (2024) Pages 1-28
https://doi.org/10.51354/mjen.1197753

A Systematic Survey of Machine Learning and Deep Learning Models Used in Industrial Internet of Things Security

Ersin Enes Eryılmaz[1],*, Sedat Akleylek[2], Yankı Ertek[3], Erdal Kılıç[4]

[1] Department of Computational Science, Samsun, Türkiye, enes.eryilmaz@bil.omu.edu.tr, ORCID: 0000-0003-1163-970X

[2] Department of Computer Engineering, Samsun, Türkiye, sedat.akleylek@bil.omu.edu.tr, ORCID: 0000-0001-7005-6489

[3] Renaissance System and Technology Solutions, Ankara, Türkiye, yanki.ertek@ronesanssistem.com, ORCID: 0000-0001-7005-6489

[4] Department of Computer Engineering, Samsun, Türkiye, erdal.kilic@bil.omu.edu.tr, ORCID: 0000-0003-1585-0991

ABSTRACT

IIoT "Industrial Internet of Things" refers to a subset of Internet of Things technology designed for industrial processes and industrial environments. IIoT aims to make manufacturing facilities, energy systems, transportation networks, and other industrial systems smarter, more efficient and connected. IIoT aims to reduce costs, increase productivity, and support more sustainable operations by making industrial processes more efficient. In this context, the use of IIoT is increasing in production, energy, healthcare, transportation, and other sectors. IoT has become one of the fastest-growing and expanding areas in the history of information technology. Billions of devices communicate with the Internet of Things with almost no human intervention. IIoT consists of sophisticated analysis and processing structures that handle data generated by internet-connected machines. IIoT devices vary from sensors to complex industrial robots. Security measures such as patch management, access control, network monitoring, authentication, service isolation, encryption, unauthorized entry detection, and application security are implemented for IIoT networks and devices. However, these methods inherently contain security vulnerabilities. As deep learning (DL) and machine learning (ML) models have significantly advanced in recent years, they have also begun to be employed in advanced security methods for IoT systems. The primary objective of this systematic survey is to address research questions by discussing the advantages and disadvantages of DL and ML algorithms used in IoT security. The purpose and details of the models, dataset characteristics, performance measures, and approaches they are compared to are covered. In the final section, the shortcomings of the reviewed manuscripts are identified, and open issues in the literature are discussed.

ARTICLE INFO

Review article

Received: 01.11.2022
Accepted: 16.02.2024
Keywords:
industrial internet of things,
IIoT security,
deep learning,
machine learning,
Industry 4.0.

*Corresponding author

1. Introduction

The internet environment is changing at an incredible speed. The internet is not just about smartphones or laptops; it has gone beyond internet-connected devices. Physical devices communicate with each other or large systems through the Internet of Things (IoT). Users can complete their work in a short time with devices connected with IoT. As the future of IoT looks so promising, it will be an integral part of every device, from home appliances to security devices.

While the number of IoT devices worldwide was 15.14 billion in 2023, it will reach 29.42 billion devices in 2030 and will increase 2.3 times [1] because it is cheaper and more accessible. Almost 75% of devices connected to the IoT network use short-range technologies such as Bluetooth, Zigbee, and Wi-Fi. These technologies will naturally be used by default as long as these networks exist. IoT revenues will exceed $1,5 trillion by 2030. China, North America, and Europe have 73% of IoT global revenue [2]. With the expansion of the IoT ecosystem, security concerns are also increasing. Considering the IoT architecture brings together multiple pieces of sensing and communication. Integrating devices is not only a complex task but also demonstrates that IoT networks and devices are a system that requires constant attention [3], [4].

IoT can be divided into three main groups. Consumer IoT can be considered end-user applications, smartphones, smart watches, wearable devices, and internet-connected home devices. Large infrastructures for enterprises are referred to as

Commercial IoT, while controllers, actuators, sensors, industrial assets, remote telemetry, monitoring, and management systems are classified as Industrial IoT. In this survey, Industrial IoT (IIoT) will be discussed [4]. The IIoT is a new, fully connected, efficient vertical model for intelligent systems and is vulnerable to cyber threats. Malicious actors can exploit some vulnerabilities and risks due to the misapplication of security standards [6].

Automation and intelligent computing services such as industrial systems, critical infrastructure devices, embedded devices, and modern systems have come together with production engineering thanks to the internet. However, standardization with IIoT brings many new challenges, including legal and social aspects of security, and privacy. In particular, the increasing diversity of IoT network and IoT device presence requires highly scalable solutions for data communication, naming, information management, addressing and service delivery. Many IoT devices still have limited capabilities that require low-cost, low-power, fully networked architectures compatible with standard communication methods [7].

It is a well-known fact that IoT is an ecosystem where data is transmitted and requires some privileged features to manage large amounts of data. At this point, ML and DL models collect and analyze data with artificial intelligence (AI). The security of devices can be ensured by making predictions with DL and ML models from the data produced by IoT ecosystems. Using the AI concept in security ensures a regular data flow between IoT devices and proper management without human error. Thus, AI has become necessary in the growth of the IoT industry.

The communication protocol used in wearable technologies and industrial applications Bluetooth low energy: BLE has been seen in many attacks where it is vulnerable to attacks. Since the packets transmitted with BLE consist of plain text content, it has been seen to contain security vulnerabilities in user authentication and reconnection of two paired devices [4], [5].

The increasing benefits of internet-connected devices have also brought challenges related to security issues. With the widespread use of IoT devices, security problems have also increased, and anomalies have occurred in IoT networks. Anomalies in the IoT network and systems are detected by intrusion detection systems. Work on IDS has been ongoing since Anderson's network security monitoring work [8]. Since Anderson's technical report, manuscripts have continued for different intrusion detection systems based on various methods [9]-[15]. There are different approaches for detecting anomalies in IoT networks with DL and ML models [16]-[19]. The ML and DL algorithms used to detect anomalies in IIoT security recognize malicious network traffic by comparing it to benign network traffic. In the papers, support vector machine [20], Bayes networks [21], decision trees [22], k-nearest neighbors [23], random forest [24], and k-means [25], machine learning algorithms are preferred. As deep learning algorithms generally convolutional neural networks [26], recurrent neural networks [27], long short-term memory [28], gated recurrent unit [20], [29], autoencoder [30], generative adversarial network [31], restricted Boltzmann machines [32] and deep belief networks [33] are used.

1.1. Related Surveys

In this subsection, current manuscripts compiling recently published or highly cited ML and DL-based models for IIoT security are reviewed. Some of these survey manuscripts used the systematic literature survey method, and some consisted of summarizing the papers. A systematic literature survey is the distinction and examination of papers prepared to answer research questions according to predetermined selection and elimination criteria related to a selected topic. Table 1 summarizes the characteristics of the reviewed surveys.

IIoT security research activity is geographically dispersed, the most popular broadcast locations, and fog computing for IIoT security threats [34]. IIoT security requirements refer to the geographical distribution of scientific publications, popular publication areas, and distribution over the years. In addition, the future of fog computing in the industrial field is discussed and proposed four-layer IIoT security architecture [35]. Firstly, security analysis includes MAC, ucode, IP, and EPC. Analysis of the network layer is also available in capillary networks (HomePlug, BLE, Bluetooth, RFID, NFC, IrDA, INSTEON, EnOcean, ANT+, WirelessHART, UWB, ZigBee, Thread, and ISA 110.11a, etc.). Secondly, their coverage and functionality ranges are mainnet in the background (3G, LR-WAN, Ethernet, WiMax, WLAN) and backbone network (DASH7, LoRaWAN, NB-Fi, NB-IoT, SigFox, NWAVE, and RPMA). At the processing layer, security analysis resides in end-to-end data protection. Finally, application layers work on HTTP, MQTT, CoAP, SOAP, XMPP, REST, DDS, and AMQP protocols [36]. Protocol-based and data-based attacks show that traditional IoT attack prevention tools are no longer effective. Artificial intelligence methods, blockchain, and elliptic curve encryption seem to be new effective methods for securing IoT networks [37]. IoT security threats and countermeasures, common points, and differences between IoT and IIoT are defined. A literature review of different security approaches specific to IIoT [38]. Blockchain, AI algorithms, consensus mechanisms, storage and communication perspectives on smart supply chains, and Industry 4.0 are explained [39]. A comprehensive analysis of attacks against IIoT systems and solutions to these attacks, as suggested in the latest literature, is presented [40]. DL and ML methods and blockchain integration for the IoT perception, network, and application layers are discussed [41]. Reviews various DL techniques and their uses in different industries, including CNN, AE, and RNN. DL use cases for intelligent IoT technologies are summarized [42]. A systematic literature review specifically addressing DL and ML algorithms commonly used in IoT network security is proposed, but does not focus on IIoT [43]. A systematic survey of how deep learning approaches detect IoT network and system security and large-scale attacks is studied [44]. An anomaly-based

systematic survey with ML and DL together; however, the datasets are not exhaustive [45] and [46]. 40 manuscripts were summarized in databases such as Google Scholar, Academia, Science Direct, and IEEE with the keywords IoT, cyber security, cyber security frameworks, and cyber security approaches. No information is provided about ML and DL-based algorithms and the databases used [115]. ML and DL-based solutions for privacy threats in IoT systems were analyzed with dataset features without a systematic survey [116]. A detailed analysis of the IDS developed in the IoT environment was performed and a new smart IDS was proposed, which was tested on the NS3 simulator using fuzzy CNN by extracting features with information gain. This manuscript can be considered as a non-systematic detailed survey that includes experiments and analysis [117]. Many manuscripts have been summarized about ML or DL-based approaches to IoT security solutions [118]. Many manuscripts have been summarized about ML or DL-based approaches to IoT security solutions on between 2017 and 2022 [119].

One hundred five manuscripts were examined through different elimination and purification steps with the research questions' queries. The use of DL has been claimed to be a permanent and reasonable approach to IoT security. M. A. Al-Garadi et al. explained DL and ML methods with dataset details, but it is not a systematic survey [41]. R. Ahmad & I. Alsmadi gave a systematic review of manuscripts conducted in the years 2019-2020 specialized in IoT security, which explains the ML and DL methods with dataset detail and is not an IIoT-specific review. Our manuscript differs from other manuscripts in that it consists of systematically conducted manuscripts with detailed datasets where IIoT-specific ML and DL approaches were experimented on between 2019 and 2023 [43], [119].

Table 1. *Deep Learning and Machine Learning Based Survey Papers for IIOT Security*

Survey	Article Title	Journal Name	Year	Systematic survey?	ML and DL together?	Anomaly based?	Dataset detail?
[34]	Towards a systematic survey of industrial IoT security requirements: research method and quantitative analysis	ACM Digital Library Proceedings of the Workshop on Fog Computing and the IoT	2019	✓	X	✓	X
[35]	A Systematic Survey of Industrial Internet of Things Security: Requirements and Fog Computing Opportunities	IEEE Communications Surveys & Tutorials	2020	✓	X	X	X
[36]	Recent Technologies, Security Countermeasure and Ongoing Challenges of Industrial Internet of Things (IIoT): A Survey	MDPI Sensors	2021	X	X	X	X
[37]	Security trends in Internet of Things: A survey	SpringerLink SN Applied Sciences	2021	X	X	X	X
[38]	Challenges and Opportunities in Securing the Industrial Internet of Things	IEEE Transactions on Industrial Informatics	2021	X	X	X	X
[39]	Deep reinforcement learning for blockchain in industrial IoT: A survey	ScienceDirect /Elsevier Computer Networks	2021	X	✓	X	X
[40]	Cyber Threats to Industrial IoT: A Survey on Attacks and Countermeasures	MDPI IoT	2021	X	✓	X	X
[41]	A Survey of Machine and Deep Learning Methods for Internet of Things (IoT) Security	IEEE Communications Surveys & Tutorials	2020	X	✓	✓	✓
[42]	Deep Learning in the Industrial Internet of Things: Potentials, Challenges, and Emerging Applications	IEEE Internet of Things Journal	2021	X	X	✓	X
[43]	Machine learning approaches to IoT security: A systematic literature review	ScienceDirect /Elsevier Internet of Things	2021	✓	✓	✓	✓
[44]	A systematic review on Deep Learning approaches for IoT security	ScienceDirect/ Elsevier Computer Science Review	2021	✓	X	✓	✓

[45]	A Brief Review on Internet of Things, Industry 4.0 and Cybersecurity	MDPI Electronics	2022	✓	✓	✓	X
[46]	State-of-the-art survey of artificial intelligent techniques for IoT security	ScienceDirect/ Elsevier Computer Networks	2022	✓	✓	✓	X
[115]	Cybersecurity Risk Analysis in the IoT: A Systematic Review	MDPI Electronics	2023	✓	X	✓	X
[116]	A Survey of Machine and Deep Learning Methods for Privacy Protection in the Internet of Things	MDPI Sensors	2023	X	✓	X	✓
[117]	A Comprehensive Survey on Machine Learning-Based Intrusion Detection Systems for Secure Communication in Internet of Things	Hindawi Computational Intelligence and Neuroscience	2023	X	X	✓	✓
[118]	Internet of Things (IoT) Security Intelligence: A Comprehensive Overview, Machine Learning Solutions and Research Directions	SpringerLink Mobile Networks and Applications	2023	X	✓	X	X
[119]	Intelligent approaches toward intrusion detection systems for Industrial Internet of Things: A systematic comprehensive review	ScienceDirect/ Elsevier Journal of Network and Computer Applications	2023	✓	✓	✓	✓
Our paper	A Systematic Survey of Machine Learning and Deep Learning Models Used in Industrial Internet of Things Security	-	-	✓	✓	✓	✓

1.2. Motivation, Scope and Contribution of Manuscript

In this systematic literature survey, we focused on the schemes for anomaly-based attack detection in the IIoT network. This survey differs from the other survey manuscripts in Table 1 in that it is systematic, includes ML and DL models, is based on anomalies found in IIoT networks, includes details of the datasets used, and focuses on the framework of industrial internet of things. The general content and scope of this systematic review, which is prepared with the aim of providing detailed information to researchers working in the field of IIoT security, are as follows:

- The proposed schemes in the selected approaches are examined, and the information on these schemes is briefly summarized.
- Manuscripts that propose models developed to detect anomaly-based attacks in industrial IoT networks and reduce these attacks are systematically selected and eliminated according to specific criteria.
- It is stated which ML and DL models are used in the approaches.
- Manuscripts with performance metrics have been interpreted.
- Details of the datasets presented in the training and testing phases of the proposed models are given.
- The methods compared with the performance metrics reached by the setup of the models are shown.
- In the final section, the deficiencies of the examined manuscripts are outlined. Evaluation of what situations these deficiencies may lead to is presented.

The contributions of this survey are as follows:

- Research strategies with seven different academic databases were scanned.
- Article scans were made systematically.
- Survey articles and literature were searched.
- Frequently used abbreviations and metrics in the article and in the literature are explained in detail.
- Manuscripts with machine learning and deep learning models have been researched.
- The main idea, advantages, and disadvantages of the proposed models are explained.
- The benign and malignant numbers and features of the dataset used in the models were extracted.
- The usage purposes, tasks, and performance results of the models are given.
- The models against which the proposed schemes are compared, and open research problems are discussed.

1.3. Organization

In this systematic survey, to make the technical information outlined in the manuscript more understandable, IoT architecture, IIoT concept, vulnerabilities in IIoT devices, some attacks against IIoT devices, and ML and DL models are briefly explained in Section 2. Section 3 explains the research questions and objectives, search strategy, search process, and filtering criteria. The approaches taken in the selected manuscripts are summarized in Section 4. Section 5 answers

the research questions that a systematic review should answer, summaries of the models, advantages, and disadvantages, and details of the datasets used. In Section 6, DL and ML models, datasets, and their properties are evaluated, an overview of the models is presented, and the deficiencies encountered in the manuscripts examined are emphasized. Finally, our manuscript briefly addresses general and open issues, offering a comprehensive overview of the broader challenges. Table 2 shows the abbreviations and expansions frequently used in this survey.

Table 2. *Abbreviations and Expansions*

Abbreviation	Expansion	Abbreviation	Expansion
IDS	Intrusion Detection System	MLP	Multilayer Perceptron
DT	Decision Tree	AI	Artificial Intelligence
NB	Naive Bayes	RNN	Recurrent Neural Network
AE	Autoencoder	DAE	Denoising Autoencoder
RBM	Restricted Boltzmann Machines	SAE	Stacked Autoencoder
KNN	K-Nearest Neighbors	RF	Random Forest
FDI	False Data Injection	GAN	Generative Adversarial Networks
DoS	Denial of Service	LSTM	Long Short-Term Memory
UDP	User Datagram Protocol	CART	Classification and Regression Tree
DBN	Deep Belief Network	LR	Linear Regression
BN	Bayesian Network	RT	Random Tree
DDoS	Distributed Denial of Service	SDN	Software Defined Networking
SVM	Support Vector Machine	ICMP	Internet Control Message Protocol
NN	Neural Networks	ANN	Artificial Neural Networks
MitM	Man-in-the-middle	TCP	Transmission Control Protocol
CNN	Convolutional Neural Networks	ROC	Receiver Operating Characteristic Curve
ACC	Accuracy	DR	Detection Rate
TN	True Negative	AUC	Area Under the ROC Curve
PRE	Precision	TRT	Training Time
TP	True Positive	TET	Testing Time
REC	Recall	F1	F1-Score
FP	False Positive	LL	Log Loss
SPC	Specificity	G-mean	Geometric mean
FN	False Negative	RI	Rand Index
TPR	True Positive Rate	SR	Speedup Ratio
SNS	Sensivity	ER	Encryption Time
FPR	False Positive Rate	IMF	Intrinsic Mode Function
FAR	False Alarm Rate	GCM	Gradient Compression Mechanism
FNR	False Negative Rate	CCQ	Clustering Center Quality
PoR	Proof of Reliance	KBL	Kernel Based Learning
PoW	Proof of Work	RTU	Remote Terminal Unit
FL	Federated Learning	PSO	Particle Swarm Optimization
SSO	Swallow Swarm Optimization	CFS	Cloud Service System
RS	Random Subspace	SHOCFS	Secure High-Order Clustering with Fast Search
CEEMDAN	Complete Ensemble Empirical Mode Decomposition with Adaptive Noise	IABC	Improved Artificial Bee Colony
SCADA	Supervisory Control and Data Acquisition	SHODS3O-CFS	Safe High-Order Optimum Density Selection in a Hybrid Cloud Environment
AB	Adaboost	GXGBoost	Genetic-Based Extreme Gradient Boosting
VIF	Variance Isolation Forest	MQTT	Message Queuing Telemetry Transport

2. Preliminaries

In this section, basic definitions and background are given. At the same time, deep learning and machine learning models are briefly explained.

2.1. IoT, IIoT and Attack Types

With IoT, using other machines to talk to other machines on behalf of humans, the concepts of ubiquity apply. In the age of IoT, where people communicate with objects and objects communicate with each other, there are connectivity dimensions for everything and everyone, anytime, anywhere. Objects have identities and virtual personalities in the internet of the future [47]. IoT is a network where physical devices can communicate via the internet. IoT is to be connected to various devices that make use of different communication models from human to human, human to machine, or a machine to machine [48].

In recent years, IoT has been used in automotive, energy, health, manufacturing, water, finance, etc. It has entered a wide range of industry sectors, including IIoT. With machine learning, the IIoT will advance the fourth industrial revolution. While IIoT facilitates data collection in an industrial environment, the collected data are used for training algorithms with the help of ML and especially DL.

The industrial use of IoT technologies has emerged with the concept of Industry 4.0. IoT networks consist of structures that monitor, analyze and change data without human intervention. SCADA systems also consist of several smart devices that monitor and control machines in industries for years [49]. IIoT standardization has emerged as a technology developed on SCADA with scalability, resolution, and data analytics. Using AI methods, IIoT can create new security measures from data collected from the cloud. [50].

IIoT is considered to be a subset of IoT. IoT typically encompasses retail and lifestyle consumer devices. IoT usually consists of single device structures such as smart television, smart phone, wearable devices, home automation, and display systems. IIoT technologies, on the other hand, are potent systems formed by the combination of more and advanced IoT devices such as smart factories, smart city, smart grids, innovative vehicles, robotics. While the plans for IoT are between 2-5 years, 30-year frameworks are considered for IIoT systems. The IoT is sensitive to water, dust, and power fluctuations and is highly mobile. IIoT is also suitable for operation in extreme situations, and its mobility is low. While the IoT prioritizes critical operations, IIoT systems have to synchronize in milliseconds. Since IIoT is built on smart logistics, smart cities, and smart manufacturing processes, it has to rely on broader security measures than IoT. At the same time, security solutions that apply to the IoT also apply to the IIoT. The confidentiality, integrity, and availability (CIA) triad is an elementary information security and includes security requirements and objectives. Solutions for Industry 4.0 should be evaluated within this framework [35]. IoT consists of less scope, while IIoT consists of systems that receive data from sensors, analyze it, and transfer it to the cloud [38].

2.1.1. IoT and IIoT Layers

IoT is a 3-layer structure: application, network, and perception layer [38]. The perception layer provides the outside world communication of IoT devices. It houses the actuators and sensors that generate data. At the perception layer, attacks such as physical attacks, impersonation, and DoS are carried out. Some manuscripts explain the perception layer as the physical layer and the network layer as the communication layer [44].

IoT devices are connected to the internet environment through the network layer. The network layer forms a bridge between the perception and application layers. IoT networks reach the internet with wired and wireless communication technologies at the network layer. At the network layer, attacks such as DoS, MitM, and routing attacks are carried out.

On the other hand, the application layer consists of the perception and network layer communication data and IoT applications. Therefore, it can be difficult to ensure security due to the possibility of software changes creating different bugs. As a result, application layer attacks like malicious code injection, data leakage, and denial of service (DoS) are carried out.

In the early stages of IoT-related research, three layers were introduced. It has three layers: perception, network and application layers. Three-layer architecture defines the main idea of the Internet of Things, but it is not sufficient for IoT research. New research describes more multilayered architectures. IoT has five layers, the middleware, and the business layers, as well as the IoT detection, network, perception and application layers [87]. Middleware is a system and software that uses data collected by the perception layer and runs primarily on servers serving the upper layers. These software and services are part of training a new computationally demanding machine learning model. Application and business layers provide software for the end user [86], [87]. Middleware and network layers are vulnerable to attacks such as MitM and DoS. In addition, attacks such as SQL injection, session hijacking, and buffer overflow occur at the business and application layers. Some manuscripts have named the layers differently. These are called perception, application, business, transport and preprocessing layers [114].

2.1.2. IIoT Attacks and Countermeasures

Because IIoT is a natural evolution of IoT, there are similar security challenges and specific security concerns to protect critical industrial control systems.

There are always security vulnerabilities for devices connected to the Internet. If security vulnerabilities are not detected and fixed, devices turn into zombie and robot devices. Without security solutions, IoT devices turn into a

botnet. Large-scale attacks such as TCP timeouts and keeping HTTP connections open on web servers slowly consume the server's resources and ultimately cause it to stop responding to legitimate requests. Other large-scale volume-based attacks include SNMP, DDoS, TCP SYN packet, UDP flood, ICMP flood, slowdown, ping of death, zero-day attacks, known web server exploits, scrambling attack, OpenBSD, and amplification attack [51], [52]. The first purpose is to block IoT traffic and make it inaccessible to regular users.

There are two main attack techniques, anomaly, and signature-based. Signature-based attacks can be defined as exploitation or knowledge-based attacks, and anomaly-based attacks can be defined as behavior-based attacks [53]. Signature-based techniques rely on existing threats to identify attacks. Anomaly-based systems detect attacks based on traffic patterns [54]. Systems that detect signature-based attacks work well for attacks, but updating the signature database takes time. As datasets grow, it will become harder to compare input. This method cannot detect Zero-day attacks [55]. Anomaly detection systems block malicious traffic. Anomaly-based systems can detect unknown attack types and zero-day attacks. However, too many false positives are encountered with anomaly prevention systems [56].

Physical attacks such as RF interference or jamming, tampering, fake node injection, malicious code injection, permanent denial of service (PDoS), sleep denial attacks, and side channel attacks are made in the perception layer [57]-[59]. Against these attacks, there are techniques such as PUF-based Authentication, CUTE Mote, PAuthKey, support vector machine (SVM), masking technique, and NOS middleware [60]-[65]. At the network layer, there are RFID spoofing, traffic analysis attacks, routing information attacks, unauthorized access, sinkhole attack, selective routing, wormhole attack, MitM, Sybil attacks, DoS/DDoS attacks, replay attacks [57], [58], [66]. For attacks on the network layer, have privacy-protecting traffic obfuscation framework, SRAM-based PUF, hash chain authentication, cluster-based intrusion detection system, trust-aware protocol, secure MQTT: cross-device authentication, beacon encryption, EDoS Server: SDN-based IoT framework and machine learning models [67]-[77]. At the application layer, there are malware attacks such as viruses, worms, trojans, spyware, and adware [57], [66]. The most well-known of these are the Mirai botnet and Jeep hack attacks. Lightweight framework for attacks on the application layer; high-level synthesis (HLS), and malware image classification; there are prevention methods such as the lightweight neural network framework [78]-[81]. There are also data attacks such as unauthorized access, data inconsistency, and data breaches. Chaos-based schema against data attacks; blockchain architecture, blockchain-based ABE; privacy protection ABE, two-factor authentication; measures and methods such as DPP, ISDD, and machine learning [82]-[87]. As it can be seen, many prevention methods have been proposed for IoT attack types, and many of these proposed methods include machine learning methods. Table 3 presents IIoT attack types and suggested measures.

Table 3. *IIoT Attack Types and Recommended Measures*

Attack Type	IIoT Layer/Attack Target	Recommended Measures	Papers
Side channel attack, RF interference or jamming, fake node injection, tampering, permanent denial of service (PDoS), malicious code injection, sleep denial attack.	Perception Layer	PUF-based authentication, CUTE Mote, PAuthKey, machine learning methods, masking technique, NOS middleware.	[60]-[65]
RFID spoofing, traffic analysis attack, routing information attacks unauthorized access, Sinkhole-attack, selective routing, wormhole-attack, MitM, Sybil-attack, DoS/DDoS attacks, replay-attack.	Network Layer	Privacy-protecting traffic obfuscation framework, SRAM-based PUF, hash chain authentication, clustering-based intrusion detection system, trust-aware protocol secure MQTT; cross-device authentication, digital signature, and encryption (signcryption), EDoS Server; SDN-based IoT framework, machine learning methods.	[67]-[77]
Malware attacks like viruses, worms, trojans, spyware and adware, Mirai botnet, and jeep hack.	Application and Business Layer	Lightweight framework; high-level synthesis (HLS), lightweight NN, malware image classification.	[78]-[81]
Data inconsistency, unauthorized access, and data breach.	Middleware layer and Data Attack	The chaos-based scheme, blockchain architecture, blockchain-based ABE; privacy protection ABE, two-factor authentication; DPP, ISDD, and machine learning methods.	[82]-[87]

2.2. Machine Learning and Deep Learning Methods

ML is a branch of AI and computer science that imitates how humans learn, focusing on using data and algorithms and increasing their accuracy. For example, SVM, BN, DT, KNN, RF, and K-Means are machine learning, CNN, RNN, LSTM, GRU, GAN, RBM, DBN, and AE are deep learning algorithms [112]. In addition to these, there are ensemble

learning (EL) and transfer learning methods. At the same time, algorithms such as ABC, PSO, and SSO as machine learning methods based on biological intelligence are also used in IIoT attack detection and prevention.

3. Research Method

This section refers the method applied when selecting papers specific to ML and DL-based IIoT security and the numerical results found. At the same time, the research questions and objectives, query sentences and areas, criteria for selecting and screening from the remaining manuscripts, and the general flow of the research method are given in the tables.

3.1. Research Questions and Purposes

This systematic literature survey examines ML, and DL-based IDS approaches developed to prevent or detect attacks on IIoT devices and systems. To achieve this goal, the focus has been on which ML and DL models are used to distinguish between benign network traffic and malignant network traffic. In addition, the performance criteria used to evaluate the models and the preferred datasets for training and testing the models are reviewed. For this systematic review to reach its goal, the research questions (RQs) and the purposes of these questions are shown in Table 4.

Table 4. *Research Questions and Purposes*

Research Question Number	Research Questions	Purposes
RQ1	In IIoT security, what performance metrics or measures are evaluated in ML and DL models?	Evaluating the proposed machine learning and deep learning models in IIoT security with their performance metrics and defining the most used performance metrics.
RQ2	In terms of IIoT security, What are the malign and benign data types found in the datasets used in the ML and DL models, and what are the features of the datasets?	To reveal which datasets are preferred for training and testing of ML and DL models used in IIoT security and to learn the properties of these datasets.
RQ3	Which ML and DL approaches are used in IIoT security, and what are the application fields of the models?	To identify the tasks of the ML and DL models used in the proposed schemes to protect IIoT devices and systems from attacks and to measure the models' performances.

3.2. Research Strategy

In order to find articles that can be examined in this systematic literature survey, research is conducted in seven basic academic databases (Web of Science: WoS, Scopus, IEEE Xplore, ScienceDirect: Elsevier, Hindawi, Wiley Online Library, MDPI) accepted by the scientific community.

These academic databases are preferred because they have search engines that can be searched in detail to obtain the manuscripts to be examined. However, it has been observed that the other academic databases, SpringerLink and Google Scholar websites, have limited ability to perform detailed filtering, querying, and advanced search in search engines. These databases do not allow searching by query clauses, they only offer advanced search. Therefore, SpringerLink and Google Scholar databases were not used in this manuscript as they were not systematically searched.

The research questions shown in Table 4 were transformed into the necessary queries to conduct research in the seven databases described above, with Table 5. Table 5 indicates the query sentences used to search seven databases and in which areas they were made.

Table 5. *Query Sentences and Fields*

Database	Query Sentence	Query Area
Web of Science (WoS)	ALL=(("industrial internet of things security" or "iiot security" or "industrial iot security") and ("machine learning" or "deep learning"))	All metadata
Scopus	TITLE-ABS-KEY (("industrial internet of things security" OR "iiot security" OR "industrial iot security") AND ("machine learning" OR "deep learning"))	Title, abstract and keywords
IEEE Xplore	("All Metadata": industrial internet of things security or industrial iot security) AND ("All Metadata": deep learning or machine learning)	All metadata
ScienceDirect (Elsevier)	("industrial internet of things security" OR "IIot Security" OR "industrial iot security") AND ("Deep Learning" OR " Machine Learning ")	Title, abstract and keywords
Hindawi	("industrial internet of things" OR "IIot Security" OR "industrial iot security") AND ("Deep Learning" OR "Machine Learning")	All metadata

Wiley Online Library	("industrial internet of things security" OR "IIot Security" OR "industrial iot security") AND ("Deep Learning" OR " Machine Learning")	All metadata
MDPI	Keywords = ("industrial internet of things security" OR "IIot Security") AND ("Deep Learning" OR "Machine Learning")	Title and keywords

3.3. Search Process and Filtering Criteria

The criteria determined for selection and elimination among the manuscripts obtained as a result of the query sentences in Table 5 are given in Table 6.

This systematic review included manuscripts published in 2019-2023 (SC2). The reason for choosing this date range is that the manuscripts published before 2019 have been performed today. Then, among the journal manuscripts written in English (SC1) in this date range, articles published in Q1 or Q2 level journals (SC3) and manuscripts using ML and DL models in IIoT security (SC4) are listed. However, publications in the conference, editorial notes, books, and preprint stages were eliminated. Replicated manuscripts (EC1), which are literature searches or reviews and are also found in other academic databases, are eliminated. In the continuation of the review, manuscripts that do not deal with anomaly detection (EC2) in IIoT network security do not disclose the datasets used (EC3) and do not cover ML and DL models for IIoT security (EC4) are discarded. 252 papers were obtained from seven different databases with the help of query clauses in Table 5 and selection criteria in Table 6. The remaining papers were analyzed using the elimination criteria in Table 6, resulting in the examination of 25 different papers for this survey. During the analysis, it was preferred that the article was new and had been cited more. At the same time, the content of the remaining articles after the elimination criteria was read and the remaining articles were selected accordingly. When all selection and elimination processes are carried out, 25 articles containing the answers to the research questions in Table 4 along with their analysis processes are examined in detail within the scope of this systematic survey research. Figure 1 shows the general flow of the research method developed to select the articles to be reviewed.

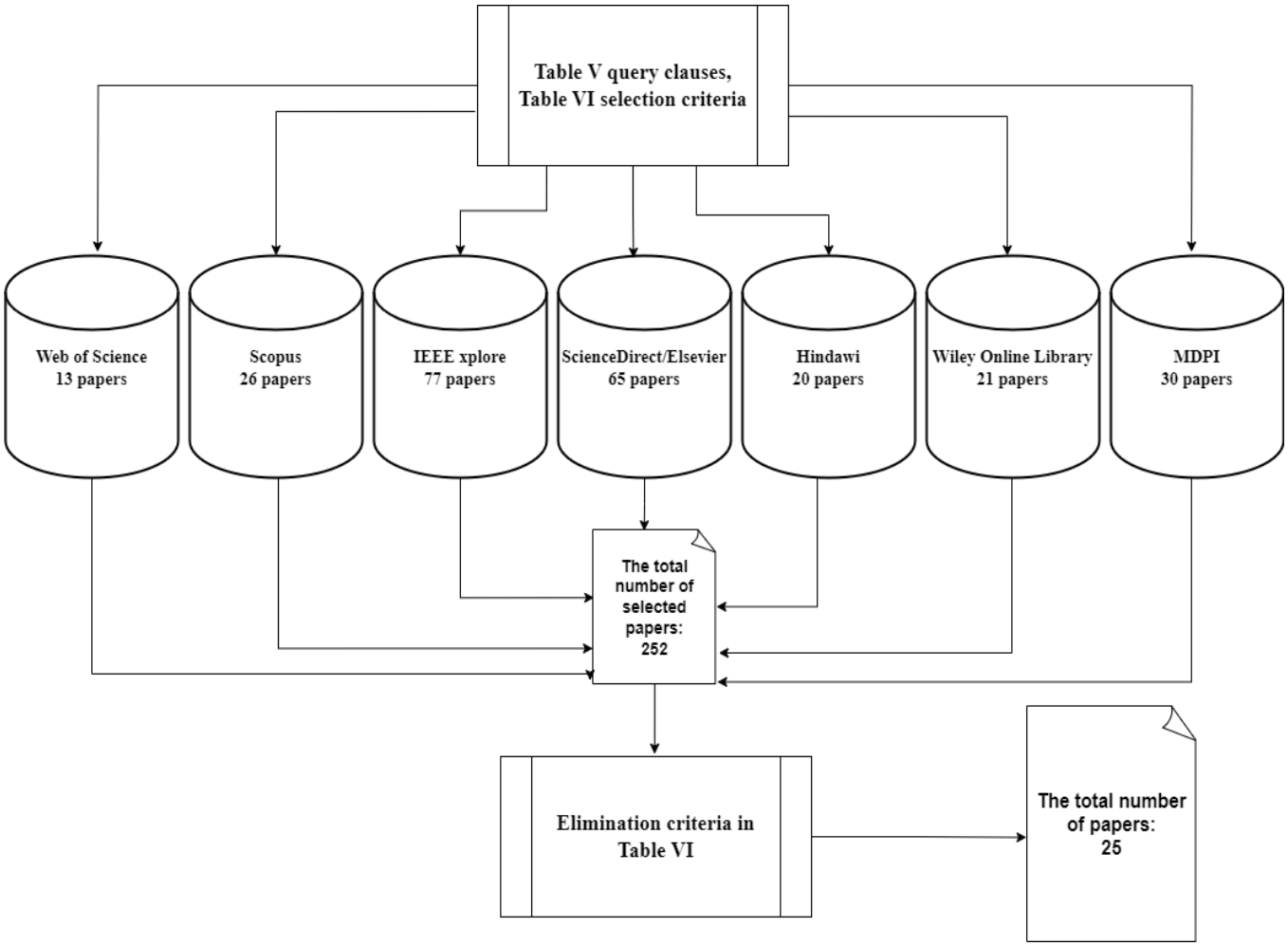

Figure 1. *General Flow of the Research Method*

Table 6. *Selection and Elimination Criteria*

Selection Criteria Number	Selection Criteria (SC)	Elimination Criteria Number	Elimination Criteria (EC)
SC1	Articles published in English in a journal.	EC1	Whether the article is a survey or a literature search.
SC2	Articles published in 2019-2023.	EC2	The focus of work on IIoT network anomaly detection.
SC3	Have an article-type manuscript published in a Q1 or Q2 level journal.	EC3	Articles lacks reference to the datasets employed in the research.
SC4	Articles using ML and DL models in IIoT security.	EC4	Articles do not include ML and DL models.

4. Descriptions of Manuscripts in the Literature

In this section, manuscripts on deep learning and machine learning used to ensure IIoT security in the literature are reviewed.

Researchers used a modified PoW algorithm PoR, which is computationally more challenging, to identify malicious IIoT devices based on blockchain-powered deep learning and verify the transactions of malicious nodes. The model has been tested with the Bot-IoT dataset [90].

The AE algorithm is used for false data injection (FDI) attack detection, and the DAE algorithm is used for noise removal of corrupted data. It also performed significantly

better than the SVM model. A distributed dataset of sensor readings was used for hydraulic system monitoring [91].

A new random hybrid deep network (HDRaNN) is tested on DS2OS and UNSW-NB15 datasets. HDRaNN has classified 16 types of cyber-attacks used for DS2OS and UNSW-NB15 with 98% and 99% higher accuracy, respectively. The model achieves its best performance for the optimum learning rate and a certain number of epochs. The results were evaluated with 10-fold cross-validation for the datasets. The HDRaNN model is run for 150 epochs. The simulation is run at five learning rates; 0,005 – 0,01 – 0,75 – 1,00 and 1,50 [92].

The KDL CUP99 used in GRU and SVDD log anomaly detection model is preprocessed by PCA to remove unnecessary features and increase productivity in the high-dimensional original dataset. Then, the advanced GRU-based algorithm with the SVDD algorithm for modeling the network log shows that it is better than traditional methods in detecting the anomaly according to the analysis of many experimental results on the dataset [93].

Different security attacks like spying, wrong setup, DoS, malicious control, malicious operation, probing, and scanning are remarked. ML algorithms are applied to the DS2OS dataset against attacks. To predict attacks, a RaNN-based random neural network model is suggested. Various evaluation criteria such as F1 measurement, accuracy, recall, and precision were used for the RaNN model. RaNN approach achieved 99,2% accuracy, 99,20% F1 score, 99,13% recall, 99,11% accuracy in 34,51 seconds. The detection accuracy is 5,65% better than other algorithms compared [94].

A deep random neural (DRaNN) based model for IDS in IIoT was estimated on the UNSW-NB15 dataset. The DRaNN model has successfully classified nine different attack types with low FPR and high accuracy of 99,54%. The results are compared with other DL-based IDS models. In addition, the proposed model achieved a high intrusion detection rate with 99,41% DR [95].

IIoT attack models are updated and validated with the collaborative data generator DNN. The approach using SCADA data is compared with DNN and SVM (sigmoid) models. In terms of performance in the proposed noisy environment, it gave better results than other models available. Classification performances are also reported for the dataset with different levels of noise added, ranging from 1% to 50% noise. It was classified with 95.42% accuracy without noise and 92.91% accuracy with semi-noise. It is classified as 17.85% Log Loss without noise (binary cross entropy) and 21.59% Log Loss with semi-noise [96].

An RS learning method and an RT combination were used to detect SCADA attacks using network traffic from the SCADA IIoT platform. All 15 different datasets in SCADA consist of thousands of different attacks. Datasets are randomly sampled at a rate of 1% to reduce the impact of a small sample size. With Binary Classification, 96,71% accuracy, 0,05% false positive rate (FPR), 0,22 ms total training time for 3738 samples, and 0,1 ms total test time for 1602 samples were measured. The proposed model is compared with the RSKNN model [97].

AMCNN-LSTM with gradient compression based on Top-k selection is used to detect anomalies accurately, while the model is used to train the FL scheme in anomaly detection. AMCNN with LSTM model accuracy is 96.85% for the power demand dataset [98].

Feature selection is made by training the original dataset in the first stage. Then the previously trained data is tested. It is then combined with the original sample set with a subset of other instances of the same classifier. Finally, Kernel-Based Learning (KBL) has been proposed, which clusters the controversial samples according to their distance from the center. The proposed method on 3000 malign and 5000 benign datasets yielded 86.08% accuracy and 0.8655 (KBL) G-mean, 80.69 accuracies, and 0.7843 (random) G-mean [99].

The features were normalized with the min-max technique in a single preprocessing step. PCA was used to reduce the size and extract the best features. Training, testing times, confusion matrix of the models, and computational complexity are given. The OCSVM model has been added to the proposed framework to detect unprecedented attacks. The OCSVM algorithm showed a detection accuracy of 86,14% in attacks that were not seen before in the natural gas pipeline dataset and 94,53% in attacks that were not seen before in the SWaT dataset. The total training time for the SWaT dataset is 1200 seconds, and the model testing time is 0,03 ms for each sample, with a total of 2,98 seconds. The total training time for the Gas Pipeline dataset is 1115 seconds, and a model test time of 0,02 ms for each sample, with a total of 1,1 seconds [100].

7 ML methods and 1 DL model were evaluated with the dataset TON_IoT containing telemetry data, operating system logs, and network traffic. The ML and DL frameworks used are LR, RF, LDA, CART, KNN, NB, SVM, and LSTM algorithms, and all models have been cross-validated by four times. The TON_IoT dataset consists of 7 different datasets: refrigerator sensor, GPS tracking, remote garage door, thermostat, smart light detection, weather, and Modbus datasets. These datasets feature nine types of cyber-attacks (Ransomware, scanning, backdoor, DoS, XSS, DDoS, password cracking attack, data injection and MitM). After the preprocessing and normalization steps, the datasets are trained with AI based model. LSTM model for refrigerator sensor 100% accuracy, accuracy, all models for garage door 100% accuracy, kNN algorithm for GPS tracking 88% accuracy, CART algorithm for Modbus 98% accuracy, LSTM for smart motion detection 59% accuracy, kNN for thermostat and except for the CART algorithms, all other models achieved 66% accuracy. For the weather dataset, the CART algorithm reached 87% accuracy. A new experiment result was made by combining the entire dataset, and the CART algorithm for

binary classification gave 88% accuracy, and again for the multi-classification model, the CART algorithm gave 77% accuracy [101].

The paper proposes a new anomaly detection approach based on centralized data collection and forwarding design that can successfully cooperate in using adaptable CEEMDAN feature with a single, smart optimization for IIoT small data. The swarm intelligence algorithm is used with the IABC OCSVM classifier to detect different anomalies. The recommended IABC-OCSVM model has high performance. The dataset was collected from sensors in an oil field in China. These sensors contain engine speed, electrical parameters, and flow and pressure information. WIA-PA transmits data to Remote Terminal Unit: RTU and RTU transmit data to a higher monitoring center via ModBus and TCP. There are 109672 IIoT data, 225 data strings, and 100 abnormal data strings. OCSVM is optimized using traditional ABC and PSO algorithms under five different attack powers. The training accuracy of the ABC-OCSVM model is 95,1%, and the test classification accuracy is 89%. The IABC-OCSVM model reaches average training accuracy of 94,5% and test accuracy of 89,8% [102].

IIoT cloud computing risks privacy disclosure by outsourcing users. There is the SHOCFS technique to solve this problem. With the SHOCFS method, the most suitable density peaks are determined, and the model's speed is tried to increase. Swallow swarm optimization (SSO) enables the selection of optimal density peaks of clustering models. A clustering algorithm is proposed to find optimal density points with the hybrid cloud SHODS3O-CFS model. In the SHODS3O-CFS model, the overlapping peaks of the cluster can be reduced. Clustering center quality (CCQ), Rand index (RI), speedup-ratio (SR), and encryption time performance metrics were used. It achieved a higher mean RI of 93.4%, compared to 29.68% and 17% of the proposed manuscript. The dataset is taken from the 5567 home energy consumption data warehouse participating in the UK Power Network meeting for the low carbon London project, and the dataset is available on the Kaggle website [103].

IoT-Flock developed as an open source, a benign and malignant health dataset is created for IoT devices. Six machine learning models were used to detect cyber-attacks and protect the health system from attacks. The RF algorithm showed the best performance with 99,7% accuracy, 99,79% sensitivity, 99,51% accuracy, and 99,65% F1 score [104].

Feature selection with Fisher score and genetic-based extreme gradient boosting model was used to detect IoT attacks. GXGBoost achieved 99.96% accuracy on the N-BaIoT dataset with 10-fold cross-validation. The dataset malicious Mirai and the Bashlite class are instantiated in the Benign class dimension [105].

Job Safety Analysis (JSA) was conducted to identify factors that cause worker accidents and injuries. With smart PPE, notifications from electronic devices are transmitted to operators, and ThingsBoard, an open-source IoT platform, provides communication between active sensors for data processing and IoT management. Device connectivity is provided via industry IoT protocols (HTTP, MQTT, CoAP), supporting cloud and on-premises deployments. CNN has been realized with the ThingsBoard platform. The cross-validation CNN has an accuracy of 92,05% [106].

The dataset for IoT and IIoT applications called the open-source Edge-IIoTset was proposed, and tests have been carried out on the dataset with ML and DL-based models [107].

EDIMA, an IoT botnet detection solution, is proposed. A new two-stage Machine Learning (ML) based detector developed for IoT bot detection uses supervised ML algorithms and an Autocorrelation function for bulk traffic classification. As a result, EDIMA has a high detection rate, low bot detection delays, and low RAM consumption in detecting IoT bots [108].

LSTM, CNN, and RNN deep learning methods based on a feature selection method based on LightGBM, and DDQN and DQN Deep Reinforcement Learning models were used [109].

IIoT threat detection was performed with the Cu-LSTMGRU + Cu-BLSTM hybrid model, and high accuracy was achieved with a low false positive rate. The proposed model was compared with the Cu-DNNLSTM and Cu-DNNGRU models [110].

Ensemble models RF-PCCIF and RF-IFPCC methods were used to improve IDS performances on Bot-IoT and NF-UNSW-NB15-v2 dataset [120].

23 features were selected with a feature selection based on correlation; SVM and Decision Tree classification models and NSL-KDD dataset are used to analyze network intrusion and attack detection performance [121].

Synchronous optimization of parameters and architectures by genetic algorithms with convolutional neural networks blocks (SOPA-GA-CNN) on five intrusion detection datasets in IIoT, including secure water treatment (SWaT), water distribution (WADI), Gas Pipeline, BoT-IoT and Power System Attack Dataset for the intrusion detection has been implemented [122].

The residual neural network (P-ResNet) model was implemented by combining seven IoT sensors (e.g., fridge_sensor, GPS_tracker_sensor, motion_light_sensor, garage_door_sensor, modbus_sensor, thermostat_sensor, and weather_sensors) TON_IoT datasets [123].

The main idea and focus of the examined approaches and the advantages and disadvantages of the models proposed in these approaches are given in Table 7.

Table 7. *An Overview of Suggested Approaches in Manuscripts*

Paper	Main Idea	Advantages	Disadvantages
[90]	A new modified PoW algorithm PoR, which is computationally more difficult, to identify malicious IIoT devices based on blockchain-powered deep learning	With the improved PoW algorithm, PoR, the operations of malignant nodes are made difficult.	Not applied in a real environment. Untested in different deep learning and machine learning models.
[91]	A new method of false data injection (FDI) attack detection using automatic encoders (AE) is introduced. Also, corrupted data is cleaned using denoising AEs (DAEs). DAE is very efficient in recovering clean data	Proposed framework can detect other types of attacks without any updates It is the first manuscript to recommend using DAEs to clean up corrupted (hacked) data.	The denoising autoencoder needs to be trained for all attack types. When the Autoencoder is supervised learning, it does not need to be constantly trained.
[92]	A new hybrid and random deep learning model (HDRaNN) DS2OS and UNSW-NB15 have been tested with two different datasets.	Various performance metrics HDRaNN is compared to key detection patterns.	Not applied in a real environment. Untested in machine learning models
[93]	Gated Recurrent Unit and Support Vector Domain Definition log anomaly detection model has been proposed. The model has been tested on the KDLLCUP99 dataset.	Compared with many deep learning models.	Not applied in a real environment. No known performance measures were used.
[94]	Attacks are classified with ML models. The best model is RaNN based random NN model.	Attacks are detected, and classified with high success rates such as 99,11% accuracy, 99,13% precision and 99,20% F1 score.	Not applied in a real environment. Untested in different machine learning models.
[95]	The DRaNN-based model was estimated on the UNSW-NB15 dataset.	The attacks were detected with 99,54% accuracy and 99,41% detection rate, with a high success rate of 0,76% false positives.	Not applied in a real environment. Untested in different ML and DL models.
[96]	A downsampling encoder-based collaborative data generator trained using an adaptive algorithm is proposed.	Real IIoT dataset. The data were classified by adding noisy data to the test dataset.	Accuracy and loss rates are given only as performance criteria, and other known criteria are not used.
[97]	RS learning method and RT combination were used to detect SCADA attacks using network traffic from the SCADA IIoT platform.	Creating a detection engine based on industrial protocols and a high DR of 96,71%	If a feature exists, the best feature is limited to random selection. Excessive execution time
[98]	A deep learning-based federated learning tool to detect communication-efficient, new anomalies to detect time series data in IIoT	It uses convolutional neural network units based on the attention mechanism, thus avoiding memory loss and gradient distribution problems.	The federated learning model is vulnerable for loss of malign anomaly attacks
[99]	ML-based KBL selection method is proposed for defense against hostile attacks in an IIoT environment.	Extracted from the malware dataset as static features with the Androguard tool.	Untested in different deep learning models. Feature selection method is used, which is not used very much in the literature.
[100]	A new two-stage community deep learning model and attack correlation scheme is proposed for unstable industrial control system data using the OCSVM model to detect unprecedented attacks.	Resistant to unstable datasets where the numbers of malignant and benign datasets are not close to each other. Capable of detecting never-before-seen attacks	Complex architecture
[101]	A new dataset (TON_IoT) is proposed, which includes Telemetry data of IoT and IIoT services, traffic of IoT network, and operating systems logs. It is designed based on integrating IoT/IIoT systems with three layers of Fog, Edge, and Cloud.	Variety of benign and malign events for different IoT or IIoT devices. Contains heterogeneous data sources.	Advanced parameter optimization is required to optimize hyper parameters and obtain better results.
[102]	CEEMDAN feature and swarm intelligence algorithm ABC-based IABC-OCSVM model.	The real-world dataset in China oil IIoT system. Attacks under five different attack power have been detected.	The dataset is not public and not detailed. No evaluation was made with different performance criteria. No comparison with deep learning models.
[103]	With IIoT cloud computing, the SHODS3O-CFS algorithm, which is a new SHOCFS technique, is recommended for users outsourcing privacy disclosure risk.	A safe optimized clustering method is proposed to obtain optimal density peaks.	No evaluation has been made with other ML and DL algorithms. Not tested in a real environment.
[104]	Developing a benign and malignant IoT use case with IoT-Flock, which creates open source IoT data, and traffic generation and evaluation of IoT health dataset with ML techniques.	An open source software has been created for IoT healthcare environments that capture data in the context-aware MQTT and COAP categories.	Deep learning models are not used.

[105]	IoT botnet network attacks are detected by feature selection with Fisher score and GXGBoost algorithm and identify the most relevant features.	A high detection rate (average accuracy results in 99,96%)	Hard to verify that parameters reach the global optimum, Sensitivity and randomness of the genetic algorithm used for the initial population
[106]	A smart helmet 5.0 CNN model that monitors environmental conditions and performs real-time risk assessment	The model was evaluated with ML and DL algorithms.	Except for the accuracy performance metric, no other performance metric is used.
[107]	The dataset for IoT and IIoT applications called the open-source Edge-IIoTset has been proposed, and tests have been carried out on the dataset with ML and DL-based models.	Data was collected from more than 10 IoT devices, and 61 new features were extracted from 1176 features. Performance was evaluated with ML and DL algorithms.	Realistic but not real environment
[108]	EDIMA, an IoT botnet detection solution, is proposed. A new two-stage Machine Learning (ML) based detector developed for IoT bot detection uses supervised ML algorithms and an Autocorrelation function for bulk traffic classification.	A high detection rate, Low bot detection delays, and low RAM consumption in detecting IoT bots.	Difficulty of retraining the model, Deep learning models are not used. Not tested in a real environment.
[109]	For IIoT, LSTM, CNN, and RNN, deep learning methods based on a feature selection method based on LightGBM, DDQN, and DQN Deep Reinforcement Learning models were used.	Both deep learning methods and deep reinforcement learning models were used.	Machine learning models are not used. Not tested in a real environment.
[110]	For the IIoT environment, a hybrid DL, SDN-enabled approach is proposed to detect threats and intrusions.	The model is programmable and expandable on iiot data devices. Open flow switches are used in SDN	Not tested in a real environment, Machine learning models are not used.
[120]	Ensemble models RF-PCCIF and RF-IFPCC methods	Pearson Correlation Coefficient (PCC) Isolation Forest (IF) to reduce computational cost and prediction time	Not used deep learning models, Not tested in a real environment.
[121]	Correlation based features selection SVM and DT methods	Correlation features selection	Not tested in a real environment, Deep learning models are not used.
[122]	Synchronous optimization of parameters and architectures by genetic algorithms with convolutional neural networks blocks (SOPA-GA-CNN)	On five intrusion detection datasets in iiot, including secure water treatment (swat), water distribution (WADI), Gas Pipeline, bot-iot and Power System Attack Dataset for the intrusion detection	Not tested in a real environment, Machine learning models are not used.
[123]	Residual neural network (P-ResNet) model with seven IoT sensors dataset	Combining seven iot sensors	Not tested in a real environment.

5. Results

In the results section, the determining research questions are answered.

5.1. RQ1: In IIoT security, what performance metrics or measures are evaluated in ML and DL models?

The performance of the ML and DL models used in the proposed schemes was evaluated by means of various criteria. These criteria are given in Table 8. Table 8 summarizes the definitions of performance criteria, their mathematical equations, if any, and in which manuscripts they are used. According to Table 8, it is seen that the criteria of F-1 score, precision, accuracy, recall, FPR, DR and FAR and are widely preferred for the evaluation of the models. Since these criteria were used, TP, FP, TN and FN values were measured in each manuscript. The total time taken for training (TRT) and testing (TET) models is also frequently used in manuscripts. Other criteria are used in the evaluation of the models in accordance with the purpose of the proposed models.

Table 8. *Performance Metrics Used in the Evaluation of Machine Learning and Deep Learning Algorithms*

Performance Metrics	Performance Description	Mathematical Equation	Articles Used
TP	A correctly predicted situation is correct	-	All
TN	An incorrectly predicted situation is correct	-	All
FP	False of a positively predicted situation	-	All
FN	False of a negatively predicted situation	-	All
ACC	Percentage of correctly classified sample data out of all classified sample data.	$\frac{TP+TN}{TP+TN+FP+FN} x100$	[90], [91], [92], [94], [95], [96], [97], [98], [99], [100], [101], [102], [104], [105], [106], [107], [108], [109], [110], [120],

			[121], [122] , [123]
PRE	Percentage of how accurately we guessed from all classes	$\frac{TP}{TP+FP}x100$	[90], [92], [94], [99], [100], [101], [104], [105]], [107], [108], [109], [110], [120] , [122], [123]
REC	Percentage of how accurately we guessed from all positive classes	$\frac{TP}{TP+FN}x100$	[90], [92], [94], [99], [100], [101], [104], [105]], [107], [108], [109], [110], [120], [123]
SPC (TNR)	Ratio of true negative samples.	$\frac{TN}{TN+FP}x100$	[99], [110]
F1	Harmonic mean of precision and recall measures. Low recall or high precision (or vice versa)	$\frac{2xPRExREC}{PRE+REC}x100$	[92], [94], [99], [100], [101], [104], [105]], [107], [108], [109], [120] , [122], [123]
SNS (TPR)	Rate of positive samples correctly classified as positive.	$\frac{TP}{TP+FN}x100$	[99], [110]
FPR/FAR	Rate of negative samples falsely classified as positive.	$\frac{FP}{FP+TN}x100$	[91], [93], [95], [97], [110]
G-Mean	Geometric mean of Specificity and Sensitivity	$\sqrt{SPCxSNS}$	[99]
MCC	Matthews correlation coefficient	$\frac{TP.TN-FP.FN}{\sqrt{(TP+FP)(TP+FN)(TN+FP)(TN+FN)}}$	[110]
FNR	Rate of positive samples falsely classified as negative.	$\frac{FN}{TP+FN}x100$	[110]
FDR	False Discovery Rate	$\frac{FP}{TP+FP}x100$	[110]
ROC	The curve obtained by plotting FPR versus TPR, as the threshold data values vary over a range.	-	[91], [92], [104], [110], [120], [123]
MSE	Mean square error	-	[91], [92], [104]
AUC	ROC area under the curve.	-	[91], [110], [120], [123]
RMSE	Root mean square error	$\left[\frac{1}{n}\sum_{i=1}^{m}\left(\lvert y_i-\hat{y}_p\rvert\right)^2\right]^{\frac{1}{2}}$	[98]
RI	The measure of the exact clustering results versus the actual clustering results of the clustering algorithm.	$\frac{TP+TN}{TP+TN+FP+FN}x100$	[102]
DR	Rate of correctly detected positive samples among total positive samples.	$\frac{TP}{TP+FN}x100$	[91], [93], [95], [108]
ER	The rate of how often the model misclassifies.	$\frac{FP+FN}{TP+TN+FP+FN}x100$	[103]
TRT	Total time spent training the model.	-	[93], [98], [99], [102], [103], [120], [121], [123]
TET	Total time spent testing the model.	-	[96], [99], [102], [103], [107], [110], [120], [122], [123]
ATR	Average time spent training the model.	-	[105]
ATE	Average time spent testing the model.	-	[105]
ET	The encryption time of the model.	-	[105]
Log Loss: LL	The log loss is found by subtracting the performance results of the model from the expected results. Lower log loss is better performance.	$-\sum_{c=1}^{M} yo,c\,log(po,c)$	[94]
CCQ	Distance between clustering centers produced	$\sqrt{\sum_{i=1}^{C}\lVert v_{ideal}^{i}-v^{i}\rVert^2}$	[103]
SR	Speedup ratio	-	[103]

5.2. RQ2: In Terms of IIoT Security, what are the Malign and Benign Data Types Found in the Datasets Used in the ML and DL Models, and the Features of What are the Datasets?

There are various types and numbers of datasets used for the manuscripts reviewed. With ML and DL algorithms, models are trained and tested on data sets. The datasets used in the models are selected by the purpose of the proposed schemes to ensure IIoT security. If the developed approaches are used to detect which attack types, datasets containing examples of those attack types are recommended for train and testing the models. Table 9 shows the datasets used to train and test the models or the datasets created by the authors for use in papers. The datasets encompass various types of malignant and benign samples, and pertinent information about the statistical properties of these samples, as well as the manuscripts in which they were utilized. The number of features, classes, and dimensions of the dataset is also given. However, detailed information about the datasets used in the manuscripts are not given in the articles in which they are used [91], [103], [104]. For this reason, the details of these datasets are not available in Table 9. Data types and attack types are not given for malign and benign [96]-[98], [102], [106].

The Bot-IoT [113] dataset contains 14 features. These are the numeric expression of feature status, the minimum duration of total records, the standard deviation of total records, number of inbound connections per destination IP, the average duration of total records, highest period of total records, total bytes per destination IP, the sequence number of the Argus agent, per unit time packets from source to destination, packets from destination to source, packets from source to destination, packets from destination to source per unit of time, total bytes per source IP, incoming connections per source IP [90]. The DS2OS dataset has eight classes and 13 features [92], [94], and the UNSW-NB15 dataset] has ten classes and 49 features [92], [95. The KDD CUP99 (NSL-KDD) dataset includes DOS, R2L, U2R, and Probe attack types with 42 features [93]. Datasets containing 15 different datasets in the SCADA network were sampled at a rate of 1%. Detailed information about the features was not given [96], [97]. There are time series datasets consisting of four real-world data (Engine, Power Demand, ECG, Space Shuttle) combined from various sensors. These datasets have normal subsequences and abnormal subsequences. No detailed information was given about the features [98]. In the manuscript found [99], the Android Malware dataset recommended and the number and types of features used were not given [111]. There are 17 features in the Pipeline dataset, 51 features, and 31 scenarios in the Swat dataset [110]. There are 52 features within the attack types (ransomware, scanning, backdoor, DoS, XSS, DDoS, password cracking attack, data injection, and MitM) [101]. The articles do not have dataset details and feature information [102]-[104]. The N-BaIoT dataset has 115 features derived from malignant and benign data [105], [110]. The number of features is not specified in the dataset created for Smart Kask 5.0 [106]. Edge-IIoTset dataset is generated from various IoT devices and proposes 61 new features [107]. IoT-NSS-BPR uses IoT-23 dataset, and UNSW IoT dataset. Dataset types are malware samples, malware traffic pcap files, and aggregate IoT traffic pcap files [108]. Real dataset of the natural gas pipeline transportation network publicly released by the U.S. Department of Energy's Oak Ridge National Laboratory [109].

Table 9. *Datasets Used in Models and Properties*

Dataset	Type and Number of Malign Data	Type and Number of Benign Data	Total Data Numbers	Number of Features/ Classes/ Dimensions	Articles Using
Bot-IoT: is a dataset containing detailed network information of benign and malignant data traffic and various network attacks.	- UDP DoS and DDoS: 39624597 - Service scanning: 1463364 - HTTP DoS and DDoS: 49477 - TCP DoS and DDoS: 31863600 - OS fingerprint: 358275 - Keylogging: 1469 - Data theft: 118	- UDP: 7225 - ICMP: 9 - TCP: 1750 - RARP: 1 - ARP: 468 - IGMP: 2 - IPV6-ICMP: 88	- Malign: 73360900 - Benign: 9543 - Total: 73370443	14 features	[91], [120], [122]
DS2OS: It includes 13 features and 7 malign and 1 benign data	-Spying: 532 -DoS: 5780 -Malicious Control: 889 -Wrong setup: 122 -Scan: 1547 -Malicious Operation: 805 -Data type probing: 342	Normal: 347935	-Malign total: 10017 -Benign total: 347935 -Total: 357952	13 features and 8 classes	[92], [94]
UNSW-NB15: 9 malign, 1	-Fuzzers: 24246	Normal: 93000	-Malign total:164673	49 features and 10	[92],

benign data produced by the Australian Cyber Security Center's Cyber Range Laboratory	-Backdoor: 2329 -Analysis: 2677 -Reconnaissance: 13987 -Exploits: 44525 -Generic: 58871 -DoS: 16353 -Shellcode: 1511 -Worms: 174		-Benign total: 93000 -Total: 257673	classes	[95], [120]
KDD CUP 99 NSL-KDD	-DOS:2000 -R2L:1000 -U2R:500 -PROBE:1500	Normal: 2000	-Malign total: 4000 -Benign total: 2000 -Total: 6000	42 features	[93], [121]
SCADA	28 attack scenarios	9 normal event scenarios	28 total scenarios	-	[96], [97]
Power Demand	Abnormal substring: 6	Normal substring: 45	Normal substring: 45 Abnormal substring: 6 Total substring: 51 Original sequence:1	1 Dimension	[98]
Space Shuttle	Abnormal substring: 8	Normal substring: 20	Normal substring: 20 Abnormal substring: 8 Total substring: 28 Original sequence:3	1 Dimension	[98]
ECG	Abnormal substring: 1	Normal substring: 215	Normal substring: 215 Abnormal substring: 1 Total substring: 216 Original sequence:1	1 Dimension	[98]
Engine	Abnormal substring: 152	Normal substring: 240	Normal substring: 240 Abnormal substring: 152 Total substring: 392 Original sequence:30	12 Dimension	[98]
Android Malware dataset suggested by the authors [111]	3000 malwares	5000 benign	Total 8000	-	[99]
Pipeline	60048 (21,86%) attack examples - Malicious state command injection (MSCI) -Naive malignant response injection (NMRI) -Reconnaissance (Recon) -Complex malignant response injection (CMRI) -DoS -Malign function code injection (MFCI) - Malignant parameter command injection (MPCI)	214580 (78,14%) normal samples	274628 total samples	17 features	[100] , [122]
Swat (safe water treatment)	12,1% attacks	87,9% normal	Total: 449920 samples	51 features 31 scenario	[100] , [122]
TON_IoT	Total: 162932 - XSS - scanning - data injection - DoS, - MitM - DDoS, - ransomware - backdoor - password cracking attack	Benign 35000 for all datasets Total benign: 245000	Malicious:162932 Benign: 245000 Total: 407932	- Refrigerator sensor:7 - GPS tracking:7 - Garage door:7 - Thermostat:7 - Intelligent light detection:7 - Weather:8 - Modbus:9 Total Features: 52	[101], [123]
Oil field dataset in China [102]	100 abnormal data strings	200 normal data strings	300 data strings	-	[102]
N-BaIoT	Mirai: 3668402 Bashlite: 1032056	Benign: 555932	Malignant: 4700458 Benign: 555932 Total: 5256390	115 features	[105], [110]
Dataset created by the authors [106] for Smart Helmet 5.0	-	-	11755 samples in total	12 scenarios	[106]
Edge-IoTset	Backdoor: 24862 DDoS_HTIP: 229022	Normal: 11223940	Normal: 11223940 Attack: 9728708	New 61 features with high	[107]

	DDoS_ICMP: 2914354 DDoS_TCP: 2020120 DDoS_UDP: 3201626 Fingerprinting: 1001 MITM: 1229 Password: 1053385 Port_Scanning: 22564 Ransomware: 10925 SQL_injectioion: 51203 Uploading: 37634 Vulnerability_scanner: 145869 XSS: 15915		Total: 20952648	correlations from 1176 found features	
IoT-NSS-BPR, IoT-23 dataset, UNSW IoT dataset	IoT-NSS-BPR: 23 live IoT malware samples, UNSW IoT dataset :28 different uninfected IoT devices collected at a gateway.	-	-	Best 8 features	[108]
U.S. Department of Energy's Oak Ridge National Laboratory natural gas pipeline transportation network	NMRI 2763 CMRI 15466 MSCI 78 MPCI 7637 MFCI 573 DoS 1837 Recon 6805	Normal: 161156	Normal: 161156 Attack: 32396 Total: 193552	26 features and one label	[109]

5.3. RQ3: which ML and Dl Approaches are Used in IIoT Security, and What are the Application Fields of the Models?

Table 10 summarizes the usage areas of the models, the datasets they are trained and tested with, the performances they show as a result of the experiments, and the information about which models they are compared with.

When Table 10 is examined, a feedforward multilayer multiclass neural network with Microsoft Azure Machine Learning Studio is used with the Bot-IoT dataset with various hyperparameters. An advanced intrusion detection method using a deep learning model together with blockchain is proposed for malignant IIoT devices. High-performance results have been achieved with this model [90].

It is aimed to detect false data injection attacks with an automatic encoder algorithm that is easy to train and learns hidden complex relationships. When SVM and AE were compared, AE gave more successful results. A DAE was used to get rid of the effects of the attack on the data [91].

HDRaNN, proposed for cyber-attack detection in IIoT uses implementations of HDRaNN and MLP. The HDRaNN includes input, hidden, and output layers. Performance measurements were made on two separate datasets such as UNSW-NB15 and DS2OS. With the HDRaNN model, attacks are classified with an accuracy of 98% and over 99% for the UNSW-NB15 and DS2OS datasets. HDRaNN model has been compared with RNN, DBN, DAE, and RBM deep learning models [90].

A log anomaly and malignancy detection model based on GRU and Support Vector Domain Definition algorithms framework is proposed. Numerous experiments and analyses of experimental results on the KDL CUP99 dataset have shown that the advanced GRU-based algorithm is better than traditional deep learning models in detecting an anomaly. The highest DR was measured at 99,6%, and the smallest FAR at 0,01%. Five types of anomalies (DoS, R2L, U2R, PROBE, and mixed) were detected with five algorithms (GRU-SVDD, BGRU-MLP, LSTM, LSTM-RNN, PCA-SVM) [93].

RaNN deep learning model evaluated accuracy, precision, precision, and F1 score performance metrics on the DS2OS dataset. The RaNN model is compared with SVM, DT, and ANN models. RaNN model accuracy is compared with the accuracy of previous intrusion detection models [94].

Intrusion detection was performed on a model UNSW-NB15 dataset based on a DRaNN model for intrusion detection in IIoT. Feature transformation and normalization were performed in the preprocessing step. With the DRaNN model intrusion detection system, the data is classified as normal or attack [95].

The down sampler-based data generator for SCADA attacks detection is alternatively updated and validated using a deepNN splitter during training. A GAN was developed to generate conflicting attack data, and this generated data was classified [96].

A reliable ensemble learning model with a combination of the SCADA network RS learning method and RT has been tested on 15 different datasets. The model, whose classification accuracy and model complexity was balanced, performed well compared to other cutting-edge approaches [97].

Firstly, the FL model is developed to collaboratively train anomaly detection on decentralized edge devices. Secondly, the attention mechanism CNN-LSTM model is proposed for the correct detection of anomalies. The AMCNN-LSTM scheme uses CNN units based on the attention mechanism to capture important detailed features, thus avoiding memory loss and gradient distribution problems. Thirdly, in order to increase communication efficiency, anomaly detection has been made in the industrial area with the model that compresses the gradients based on Top-k feature selection [98].

It has been tested with feature selection methods such as random, L1, Euclidean, and KBL. High performance was obtained with the KBL selection method SVM algorithm [99].

OCSVM was used to detect previously unseen attacks, creating a boundary around normal samples and reporting others as never-seen attacks. The proposed model is a complex deep neural network consisting of partially or fully connected layers that detect IoT attacks [100].

4-fold cross-validation of LR, RF, LDA, CART, KNN, NB, and SVM models were evaluated on the newly proposed TON_IoT dataset. 80% of the data and 20% of the data are allocated to the test dataset to train/validate ML methods. Classification results are given for the TON_IoT dataset refrigerator sensor, GPS tracking, garage door, thermostat, smart light detection, weather, and Modbus datasets with different models. As a result of the estimation made by combining the whole dataset, the CART algorithm for binary classification reached the most successful result with 88% accuracy, and again for the multi-classification model, the CART algorithm achieved the most successful result with 77% accuracy. Training and testing times for binary classification are high for LSTM, SVM, and KNN models and low for LR, LDA, RF, CART, and NB models. Training and testing times for multiclassification are high for LSTM, SVM, LR, and KNN models and low for LDA, RF, CART, and NB models [101].

A new IABC-OCSVM anomaly attacks classification scheme is proposed for the IIoT small dataset that can skillfully cooperate in CEEMDAN model feature use compatible with the smart optimizer OCSVM classifier. With CEEMDAN decomposition, energy entropies are measured with IMF components. Multi-scale analysis of the IIoT dataset is performed. The IABC-OCSVM model created with Gaussian mutation was found to have 94.5% training

accuracy, 89.8% test accuracy, and 0.0081 seconds test time [102].

SHODS3O-CFS clustering algorithm and the most appropriate density selection in the hybrid cloud are suggested. The SHODS3O-CFS algorithm gave clustering center accuracy (RI) of 87.7% for 50 data objects, while PPHOCFS achieved lower RI results of 62.7% and SHOCFS 76.6%. The SHODS3O-CFS algorithm achieved 95,2% RI for 250 data objects. The PPHOCFS and SHOCFS methods, on the other hand, yielded lower clustering accuracy of 66% and 81,2% RI, respectively [103].

Benign and malignant data in pcap format with IoT-Flock software were converted into CSV format with the python program. The categorical properties of the dataset, such as the protocol type (MQTT and COAP), have been replaced with numeric values using the Label Encoder to facilitate further processing. Missing data is filled with 0. The most important ten features consist of TCP and MQTT data by feature selection with the LR algorithm. The dataset was tested with NB, KNN, RF, AB, LR, and DT algorithms. Confusion matrix, ROC-AUC, F1 score, precision, accuracy, recall, and values of each algorithm are given. The RF model showed the best performance with 99,70% accuracy, 99,79% recall, 99,51% accuracy and 99,65% F1 score [104].

Improved GXGBoost algorithm to well classify IIoT network attacks. Several trials have been conducted on the public N-BaIoT dataset of IIoT devices. GXGBoost achieved 99.96% accuracy on the N-BaIoT dataset using only three features out of 115 features [105].

An intelligent helmet prototype is presented that monitors environmental conditions and works in near real-time risk assessment. The dataset consisting of 11755 examples and 12 different attack-type scenarios is evaluated by ML and DL. The cross-validation CNN model for business risk analysis yielded 92,05% accuracy. The CNN approach is evaluated by comparing it with NB, SVM, and NN [106].

Normal centralized DT, RF, KNN, SVM, DNN model PRE, REC, and F1 have 100% and federated 2-class IID and Non-IID ACC:100% performance. Edge-IIoTset, produced by ten different IoT devices, was evaluated together with two different ML-based IDS with the centralized and federated mode in 7 different layers [107].

The EDIMA model has been proposed. EDIMA consists of a traffic parser, feature extractor, ML-based bot detector, policy engine, ML model constructor, and a malware PCAP database. RF algorithms ACC, PRE, REC, and F1 have 100% performance [108].

LightGBM feature selection method, PPO2 interface, and CNN, RNN, LSTM, DDQN, and DQN model were used. Deep Reinforcement Learning model DDQN has a 97,74 F1-score [109].

The hybrid model (Cu-LSTGRU + Cu-BLSTM), Cu-DNN-LSTM, and Cu-DNN-GRU were evaluated, and (Cu-LSTMGRU + Cu-BLSTM) gave the highest performance result with an F1-score rate of 99.47%. Model GRU-RNN has been compared with Autoencoder (EDSA) and Multi-CNN [110].

RF-PCCIF and RF-IFPCC have 99.98% and 99.99% Acc and prediction time of 6.18 sec and 6.25 sec, respectively, on Bot-IoT. The two models also achieve 99.30% and 99.18% accuracy and prediction time scores of 6.71 sec and 6.87 sec on NF-UNSW-NB15-v2, respectively [120].

Quadratic SVM has 99.7% accuracy, prediction speed is 1100 s and training time is 465.28 s. Fine Tree has 99.4% accuracy, prediction speed is 570.000 sec and training time is 11.029 seconds [121].

(SOPA-GA-CNN) has 98.1 F1 Score with gas pipeline dataset [122].

P-ResNet has a performance of 87% accuracy, 88% precision, 86% recall, 86% F1 Score, 83% ROC AUC, TRT: 24401.586s, TET: 3.014s [123].

Table 10. *An Overview of the Models*

Papers	Models/Methods Used and Their Tasks	Datasets and Uses	Performance	Compared Models or Approaches
[90]	A feedforward multilayer multiclass neural network with various hyperparameters is used with Microsoft Azure Machine Learning Studio to simulate the deep learning model.	Bot-IoT: the dataset is split 6:4 into training and test data.	- Overall ACC: 95,9% - Average ACC: 98,36% - Micro average PRE: 95,9% - Micro-average REC: 95,9% - Macro averaged REC: 58,18%	-
[91]	The Auto-encoder algorithm is used to reveal false data injection attacks. Clean corrupted data (AE) performed better with the support vector machine (SVM) algorithm in terms of ROC. Pump, coolant, valve, and accumulator values are measured.	The dataset includes a total of 15 sensor data. (volumetric flow, pressure, engine, temperature, cooling, vibration, and power).	MSE training loss: 3.99e-7 MSE validation loss: 4.37e-7 AE ACC: 97,65% SVM ACC: 85,1% AE DR: 100% SVM DR: 88,55% AE FAR: 6,42% SVM FAR: 16,3% DAE MSE: 0,0064 AE MSE: 0,1 AE TRT:1 min SVM TRT:15 min	-SVM RBF Kernel -SVM Linear Kernel -SVM Gaussian Kernel

[92]	HDRaNN model has been used for cyber-attack detection in IIoT.	DS2OS is used for training and testing. Attack distributions are given in detail. A confusion matrix was created.	ACC: %98,56 PRE: %98,25 REC: %98,36 F1: %98,3 LL: %36,24 AUC-ROC: %91,28	RNN, DBN, DAE, RBM
		UNSW-NB15 is used for training and testing. Attack distributions are given in detail. A confusion matrix was created.	ACC: 99,19% PRE: 99,07% REC: 98,98% F1: 99,02% LL: 12,23% AUC-ROC: 98,82%	
[93]	A log anomaly detection model based on GRU and Support Vector Domain Definition algorithms framework	10% of the KDL CUP 99 dataset is trained.	DR: 99,6% FAR: 0,01%	BGRU-MLP, LSTM, PCA-SVM and LSTM-RNN
[94]	Detecting attacks in DS2OS dataset with a new lightweight random neural network model	Intrusion detection was performed by dividing the DS2OS dataset 8:2 train and test data	ACC: 99,2% PRE: 99,08% REC: 99,16% F1: 99,04% TET: 34,51 ms	SVM, DT, ANN
[95]	Intrusion detection was performed on the UNSW-NB15 dataset with DRaNN based model.	UNSW-NB15 is used for 75% training and 25% testing. Attack distributions are given in detail.	ACC: 99,54% DR: 99,41% FPR: 0,76%	BLSTM RNN, Adaboost, CNN and WDLSTM, DL, FFDNN, DNN, DBN
[96]	The down sampler-based data generator for SCADA attack detection is alternatively updated and validated using a deepNN splitter during training. Developing and classifying a GAN to generate conflicting attack data	SCADA: 36000 samples, half of which benign traffic and half of malign attack traffic	Noiseless ACC: 95,42% Semi-noisy ACC: 92,91% GAN ACC: 95,55% GAN LL: 47,55% TRT: 2,58h	DNN, SVM
[97]	An improved ensemble learning model is proposed to detect SCADA cyberattacks based on the combination of RS learning method and RT.	SCADA 15 datasets and thousands different attacks. Datasets are randomly sampled at a rate of 1%.	Binary Classification ACC: 96,71% FPR: 0,05% TRT: 0,22 TET: 0,1	RSKNN
[98]	AMCNN-LSTM model based on the attention mechanism is proposed.	Engine, Space Shuttle, ECG, Power Demand	For Power Demand, AMCNN-LSTM ACC: 96,85% RMSE: <5% AMCNN-LSTM time with GCM: 25min AMCNN-LSTM time without GCM: 90min	SVM, SAE, GRU, CNN with LSTM and LSTM
[99]	In the malware literature, the KBL selection method has a 6% performance improvement over random selection.	Android Malware dataset	ACC: 86,08% G-Mean: 86,55% AUC: 95,8% SVM ACC: 98,5%	DNN, SVM, RF, Bayes
[100]	The proposed IDS consist of two unsupervised SAEs, feature extraction using PCA and a Decision Tree classification and using OCSVM to detect previously unseen attacks	Pipeline dataset created by Mississippi State University	ACC: 96,2% PRE: 96,17% REC: 96,2% F1: 96,18% TRT: 1200s TET: 2,98s	DT, SVM, K-Means, NB, AIKNN, LSTM
		Swat (safe water treatment) dataset created by Singapore Technological University	PRE: 99,99% REC: 99,99% F1: 99,98% TRT: 1115s TET: 1,1s	DT, LADS-ADS, DNN, ID CNN, MADGAN, Tabor, LSTM, ST-ED
[101]	A new dataset (TON_IoT) is proposed for the next generation IoT and IIoT dataset for data-driven IDS. On the TON_IoT dataset, LR, RF, LDA, CART, KNN, NB, and SVM models were evaluated with 4-fold cross-validation. All algorithms classification results are given on seven different datasets, TON_IoT dataset, refrigerator sensor, GPS tracking, garage door, thermostat, smart light detection, weather, and Modbus datasets. In addition, for the combined_TON_IoT dataset, which is the combination of all	Refrigerator sensor	For LSTM; ACC, PRE, REC and F1: 100% TRT:190,493 TET:3,705	LR, RF, LDA, CART, KNN, NB, SVM, LSTM
		GPS tracking	For KNN; ACC: 88% PRE: 89% REC: 88% F1: 88% TRT: 0,08 TET: 1,508	
		Garage door	For all algorithms ACC, PRE, REC and F1: 100% NB TRT: 0,01sec	

	data sets, all algorithms are evaluated with binary and multi-classification models, and attack types are classified.		TET: 0,02sec	
		Thermostat	For NB; ACC: 66% PRE: 44% REC: 66% F1: 53% TRT: 0,009 TET: 0,002	
		Intelligent light detection	For LSTM; ACC: 59% PRE: 35% REC: 59% F1: 44% TRT: 63,132 TET: 3,73	
		Weather	For CART; ACC: 87% PRE: 88% REC: 87% F1: 87% TRT: 0,258 TET: 0,03	
		Modbus	For CART; ACC: 98% PRE: 99% REC: 98% F1: 99% TRT: 0,367 TET: 0,01	
[102]	An improved ABC algorithm IABC-OCSVM, based on an arrow-variable Gaussian mutation with CEEMDAN decomposition compatible with the intelligent optimizer OCSVM classifier	Pressure, engine speed, flow and some electrical parameters	Training ACC: 94,5% Test ACC: 89,8% TET: 0,0081s	EEMD and CEEMDAN ABC-OCSVM, PSO-OCSVM
[103]	SHOCFS was used for speed improvement and detection of optimum density peaks, SSO was used to select optimum density points of the clustering model, and the SHODS3O-CFS method was suggested in a hybrid cloud. The SHODS3O-CFS model reduces overlapping peaks in the cluster and increases security in the hybrid cloud.	Incorporating daily weather changes into energy use, clustering center quality collected from data in England, Wales and Scotland is evaluated on clustering center quality, encryption time, accuracy, speed-up rate performance measures.	RI: 95,2% ER: 778,80ms SR: 36,86 CCQ: 0,401	PPHOCFS and SHOCFS
[104]	Data in MQTT and COAX categories from environment monitoring sensors and patient monitoring sensors were created with IoT-Flock software. The created dataset was evaluated with NB, KNN, RF, AB, LR, and DT algorithms. The model that gave the best results was the RF algorithm.	From environmental monitoring sensors (air-humidity, air-temperature, co, fire, smoke, barometer, solar radiation sensors) and patient monitoring sensors (remote electrocardiogram (ECG) monitoring, galvanic skin response (GSR) sensor), infusion pump pulse oximetry (SPO2), nose/mouth air flow sensor, blood pressure monitor sensor, glucose meter, electromyography (EMG) sensor, body temperature sensor	ACC: %99,51% PRE: 99,7% REC: 99,79% F1: 99,65% AUC: 100%	NB, KNN, RF, AB, LR
[105]	GXGBoost performed several experiments on the public N-BaIoT dataset for efficient classification	The N-BaIoT dataset consists of the malignant Mirai, Bashlite and Benign datasets.	ACC: 99,96% PRE: 99,95% REC: 99,95% F1: 99,95% ATR: 545,040 sec ATE: 4,208 sec	DNN, DT, KNN, DAE, SVM, VIF
[106]	CNN model ThingsBoard tool. ThingsBoard. CNN algorithm works independently with an alarm system in	It consists of a dataset of 11,755 examples and 12 different scenarios.	ACC: 92,05%	NN, NB, SVM

	simulation.			
[107]	DT, RF, SVM, KNN, DNN centralized model and 2-class (binary classification), 6-class (multi-classification), and 15-class (multi-classification) federated DL approach.	Edge-IIoTset, produced by 10 different IoT devices, was evaluated together with 2 different ML-based IDS with centralized and federated mode in 7 different layers.	Normal centralized DT, RF, KNN, SVM, DNN model PRE, REC, F1: 100% federated 2-class IID and Non-IID ACC:100%, etc. [107]	DT, RF, SVM, KNN, DNN and Federated DL models
[108]	Supervised ML algorithms (NB, SVM, RF model) and Autocorrelation Function	Top 8 features selected to train ML classifiers	RF ACC, PRE, REC, F1:100%	NB, SVM, RF
[109]	GBM's feature selection algorithm, and PPO2 interface of the Stable baseline to implement model training has been used. DRL-IDS intrusion detection agent is tested on the training and validation sets.	26 features are removed and only 3 features are used without reducing performance.	For DDQN ACC: 99,05% PRE: 98,42% REC: 97,08% F1: 97,74%	CNN, RNN, LSTM, DDQN, DQN
[110]	Hybrid model (Cu-LSTMGRU + Cu-BLSTM) 10-fold cross-validation multiclass, GPU-Enabled, Compared with hybrid algorithms, Cuda-DNNLSTM and Cuda-DNNGRU	N-BaIoT hosts malware, namely Bashlite and Mirai. It consists of 8 attacks and 115 features. 49500 normal IIoT data.	Cu-LSTMGRU + Cu-BLSTM ACC: 99,45% PRE: 99,34% REC: 98,49% F1: 99,47% FNR, FDR: 0.002 FOR: 0,004 FPR: 0,003 TPR: 99,33% TNR: 99,13% MCC: 99,13% TET: 9,79ms	Cu-DNN–LSTM and Cu-DNN–GRU, GRU-RNN, Autoencoder (EDSA) Multi-CNN
[120]	RF-PCCIF and RF-IFPCC Ensemble model	Bot-IoT with 15 selected features and with NF-UNSW-NB15-v2 with 24 features	Bot-IoT ACC: RF-PCCIF: 99,98% RF-IFPCC: 99,99% UNSW-NB15-v2 ACC: RF-PCCIF: 99,3% RF-IFPCC: 99,18% TRT: 145.24s	Information gain and gain ratio, Chi-square, CNN, ET
[121]	Linear SVM, Quadratic SVM, Fine Tree, Medium Tree	NSL-KDD	Linear SVM ACC: 99.3% Quadratic SVM ACC: 99.7% Fine Tree ACC: 99.4% , TRT: 11.029s Medium Tree ACC: 95.9%	Linear SVM, Quadratic SVM, Fine Tree, Medium Tree
[122]	synchronous optimisation of parameters and architectures by genetic algorithms with convolutional neural networks blocks (SOPA-GA-CNN)	Secure water treatment (SWaT), water distribution (WADI), Gas Pipeline, BoT-IoT and Power System Attack Dataset	Gas pipeline: ACC: 99,04% PRE: 98,14% REC: 98,07% F1: 98,1%	SVM, RNN, LSTM, NB, BiLSTM, CNN, VCDL, Deep-IFS
[123]	Residual neural network (P-ResNet)	Seven IoT sensors (e.g., fridge_sensor, GPS_tracker_sensor, motion_light_sensor, garage_door_sensor, modbus_sensor, thermostat_sensor, and weather_sensors)	P-ResNet ACC: 87% PRE: 88% REC: 86% F1: 86% ROC AUC: 83% TRT: 24401.586s TET: 3.014s	LSTM, NN, CNN, RNN, FCN, LeNet, IncepNet, MCDCNN

6. Conclusion, Discussions and Open Research Problems

In this manuscript, a systematic literature survey used in Industrial Internet of Things security was done, and studies on ML and DL models used to detect anomaly-based attacks in IIoT networks were examined. The examined approaches are obtained from the Web of Science, Scopus, IEEE Xplore, ScienceDirect, Hindawi, Wiley Online Library, and MDPI academic databases using the query sentences in Table 5. Among the papers revealed as a result of the queries, 25 of them were selected and summarized according to the selection and elimination criteria given in Table 6, with the publication years between 2019 and 2023. A systematic literature survey used in Industrial Internet of Things security was done, and manuscripts on ML and DL models used to detect anomaly-based attacks in IIoT networks were examined. The examined approaches are obtained from the Web of Science, Scopus, IEEE Xplore, ScienceDirect, Hindawi, Wiley Online Library, and MDPI academic databases using the query sentences in Table 5. Among the papers revealed as a result of the queries, 25 of them were selected and summarized according to the selection and elimination criteria given in Table 6, with the publication years between 2019 and 2023.

When the reviewed manuscripts are evaluated, it is concluded that many manuscripts have different deficiencies. These deficiencies are summarized as follows:

- There are extra security measures in the blockchain to make it harder for malicious nodes to verify transactions and connect to other devices, but it has not been compared to other DL and ML algorithms [90].
- Except for a few manuscripts, their datasets have not been publicly shared [99], [103], [105]. Therefore, the performance results of the proposed approaches are controversial. Additionally, if the datasets are shared publicly, other researchers will be able to evaluate the usability of these datasets and improve the datasets.
- Some datasets do not include detailed counts of malignant and benign data types [91], [96]-[98], [103], [104]. The lack of these details prevents obtaining sufficient information about the datasets.
- Most of the models proposed in the manuscripts have not been tested in a real-life. Therefore, the performance values of these approaches in an environment where they are actually used cannot be estimated. Manuscripts should be tested in a real environment, and their performance should be measured.
- The vulnerabilities of the proposed approaches against various types of attacks were not addressed in the reviewed manuscripts. Apart from a manuscript [100], other systems proposed to be secure against certain types of attacks can be used as schemes, frameworks, models, or parts. The status of security levels against different or unknown attack types is unknown. That is, the usability of the proposed models in the real-world environment is questioned.
- A manuscript has not been tested in other machine learning and deep learning models, except for biologically inspired intelligence-based methods, and has been evaluated with performance measures that are not often used. The results obtained in different models with known performance metrics will become important for the evaluation of the manuscript [103].
- Some studies did not provide any conclusions regarding training or testing times, such as the ML and DL models used in other reviewed manuscripts. An analysis of the resource consumption of IIoT devices with insufficient resources cannot be made. Therefore, the efficiency of approaches that include models without resource consumption and training-test time analysis in a real IIoT environment is unknown [90]-[93], [95], [99].

The source codes of the ML and DL models used in the manuscripts examined were not shared in a public environment, except for the manuscript [103]. Therefore, these models are not known to be established, as shown in manuscripts. In addition, by sharing the source codes of the approaches, other researchers examining the codes will contribute more to the literature in their future manuscripts.

In this survey, firstly, short and concise explanations about the approaches proposed in the selected articles are given. Then, the main ideas, advantages and disadvantages found in these manuscripts are summarized in Table 7. Second, the criteria used to evaluate the performance of the ML and DL models used in the approaches are shown in Table 8. Third, various information about the datasets used in the testing and training processes of the models are presented in Table 9. Fourth, the ML and DL approach used in the proposed approaches to IIoT security are given in Table 10. Table 10 summarizes the usage areas of the models, the datasets they use, the training-test result performances, and the information about which models they are compared with. In the evaluation part, the shortcomings of the manuscripts examined are given. In the conclusion part, the manuscript is summarized, and open research problems are briefly explained.

IIoT leverages a variety of existing and emerging technologies such as communication networks, sensing technologies, and high-performance processing platforms to build its entire ecosystem. As a result, IIoT security and privacy concerns don't just focus on monolithic technology issues. There is an integrated heterogeneous environment from the physical security of connected devices to the communication security of networks, from data security to IIoT application security. It covers a wide variety of IIoT ecosystems, consisting of various security protocols, defense schemes, and many standards of IIoT structure. Most models have traditional methods of protecting and defending data communications. It is debatable whether these traditional mechanisms deployed are

still sufficient to protect the latest IIoT technologies; this section also discusses the overt security and privacy issues of IIoT.

- Classes with fewer datasets will give less successful results in the real environment or a new dataset, as they will cause data to be overfitting [98], [102]. The imbalance of datasets, that is, very different numbers of benign and malignant datasets will also create complexity and invalidate learning for different data and real environments [90], [92]-[95], [100].
- Except for some manuscripts, other datasets are old and outdated [93], [107]. Therefore, it is difficult to find a suitable benchmark dataset to apply ML and DL models in IIoT security. However, most of the datasets used are not publicly available or the datasets are too small, especially for deep learning models [102].
- While machine learning models are successful in some datasets, deep learning models give more successful results in others [101]. Some approaches do not make comparisons between ML and DL models. In addition, some articles do not apply preprocessing and feature selection steps for datasets [91]. Therefore, too many features are obtained. Feature selection and feature extraction are very important in terms of performance and complexity, especially for ML models. The performance of ML models can be increased by selecting the feature.
- Several authors working on the same dataset did not compare the results of the manuscripts [90], [99], [91]. Some articles do not include dataset details and feature information [96]-[99], [102]-[104], [106].
- Anomaly detection, which is mainly used, may not be applied in the same way in all areas. For example, while temperature change is very important in the field of industrial medicine, it may not be that important for a smart factory. Therefore, anomaly detection should not be applied to all areas in the same way [98], [100], [102], [106].
- Normal data may be close to the cluster containing the anomaly data, and anomaly data may be close to the cluster containing the normal data [46]. In such cases, anomaly detection becomes very difficult. Normal data may change according to time and space and appear as an anomaly. In these cases, it may be necessary to change the hyperparameters used in the ML and DL models.
- The DL and ML models used in IIoT security focus only on the accuracy performance metric in some articles [96], [102], [106]. Instead, manuscripts including precision, recall, and F1 score performance criteria should be conducted to better understand the manuscripts. In some cases, performance criteria such as log loss, speedup ratio, g-mean, rand-index, and specificity are used, which are not used much in the literature [92], [102].
- For an accurate assessment of the energy consumption and computational complexity of the proposed approaches, on which platforms the datasets are created and tested, training, testing, real-time response, and execution times are not explicitly given [90], [92], [93], [95], [99], [103], [104], [106].
- Zero-day attacks are a type of security vulnerability that is exploited the day a vulnerability is discovered or before an update is available by the developer. Dynamically changing zero-day attacks can cause unknown malicious behavior to be detected [46].
- False positives will cause economic worsening that will affect the relevant services and production areas. Whenever a false positive is found, especially medical, industrial units will have to stop production. False negatives are even more problematic. It is the appearance of a condition as negative as a result of a test when it actually is. As a result of misinterpretation of data due to unforeseen conditions, not only economic but also human losses will occur [98], [100], [102], [104], [106]. Such cases are still important problems to be solved.

As a result, in this systematic survey, detailed information about open research problems in the literature and models consisting of deep learning and machine learning algorithms to find anomalies in IIoT networks and reduce these anomalies are given.

REFERENCES

[1] L.S. Vailshery, Number of Internet of Things (IoT) connected devices worldwide from 2019 to 2023, with forecasts from 2022 to 2030, https://www.statista.com/statistics/1183457/iot-connected-devices-worldwide/ , Statista, Last accessed: October 31, 2021.

[2] M. Hatton, The IoT in 2030: Which applications account for the biggest chunk of the $1.5 trillion opportunity? TransformaInsights, https://www.kisa.link/PsHW, Last accessed: October 31, 2021..

[3] F. Meneghello, et al., *IoT: Internet of Threats? A Survey of Practical Security Vulnerabilities in Real IoT Devices*, IEEE Internet of Things Journal, vol. 6, no. 5, pp. 8182–8201, 2019.

[4] C. Xenofontos, et al. Consumer, commercial and industrial iot (in) security: attack taxonomy and case studies. IEEE Internet of Things Journal, 2021.

[5] D. Antonioli, et al., Blurtooth: Exploiting cross-transport key derivation in bluetooth classic and bluetooth low energy, arXiv preprint arXiv:2009.11776, 2020.

[6] L. L. Dhirani, E. Armstrong, and T. Newe, Industrial IoT, Cyber Threats, and Standards Landscape: Evaluation and Roadmap. Sensors, 21(11), 3901, 2021

[7] A. R. Sadeghi, C. Wachsmann, & M. Waidner, *Security and privacy challenges in industrial internet of things*. In 2015 52nd ACM/EDAC/IEEE Design Automation Conference (DAC) (pp. 1-6). IEEE, June 2015.

[8] J. P. Anderson, *Computer security threat monitoring and surveillance*, Technical Report, James P. Anderson Company, 1980

[9] B. B. Zarpelão, et al, *A survey of intrusion detection in Internet of Things*, Journal of Network and Computer Applications, Volume 84, Pages 25-37, ISSN 1084-8045, https://doi.org/10.1016/j.jnca.2017.02.009, 2017

[10] E. Hodo, et al, *Threat analysis of IoT networks using artificial neural network intrusion detection system.* In 2016 International Symposium

on Networks, Computers and Communications (ISNCC) (pp. 1-6). IEEE, May 2016.
[11] E. Anthi, et al, *A supervised intrusion detection system for smart home IoT devices*. IEEE Internet of Things Journal, 6(5), 9042-9053, 2019.
[12] S. Raza, L. Wallgren, & T. Voigt, *SVELTE: Real-time intrusion detection in the Internet of Things.* Ad hoc networks, 11(8), 2661-2674, 2013.
[13] V. Kumar, A. K. Das, & D. Sinha, *UIDS: A unified intrusion detection system for IoT environment.* Evolutionary Intelligence, 14(1), 47-59, 2021.
[14] M. Eskandari, et al, Passban IDS: An intelligent anomaly-based intrusion detection system for IoT edge devices. IEEE Internet of Things Journal, 7(8), 6882-6897, 2020.
[15] E. Aydogan, et al. *A central intrusion detection system for rpl-based industrial internet of things*. In 2019 15th IEEE International Workshop on Factory Communication Systems (WFCS) (pp. 1-5). IEEE, May 2019.
[16] M. Zolanvari, et al., Machine learning-based network vulnerability analysis of industrial Internet of Things. IEEE Internet of Things Journal, 6(4), 6822-6834, 2019.
[17] J. B. Awotunde, C. Chakraborty, & A. E. Adeniyi, Intrusion Detection in Industrial Internet of Things Network-Based on Deep Learning Model with Rule-Based Feature Selection. Wireless Communications and Mobile Computing, 2021.
[18] A. H. Muna, N. Moustafa & E. Sitnikova, *Identification of malicious activities in industrial internet of things based on deep learning models.* Journal of Information security and applications, 41, 1-11, 2018.
[19] G. E. I. Selim, et al. Anomaly events classification and detection system in critical industrial internet of things infrastructure using machine learning algorithms. Multimedia Tools and Applications, 80(8), 12619-12640, 2021.
[20] A. F. M. Agarap, A neural network architecture combining gated recurrent unit (GRU) and support vector machine (SVM) for intrusion detection in network traffic data. In Proceedings of the 2018 10th international conference on machine learning and computing (pp. 26-30). 2018, February.
[21] S. Aljawarneh, M. Aldwairi, & M. B. Yassein. Anomaly-based intrusion detection system through feature selection analysis and building hybrid efficient model. Journal of Computational Science, 25, 152-160. 2018.
[22] L. Breiman, et al, *Classification and regression trees.* Routledge. 2017.
[23] L. Li, H. Zhang, H. Peng, & Y. Yang, *Nearest neighbors based density peaks approach to intrusion detection.* Chaos, Solitons & Fractals, 110, 33-40. 2018.
[24] A. L. Buczak & E. Guven. A survey of data mining and machine learning methods for cyber security intrusion detection. IEEE Communications surveys & tutorials, 18(2), 1153-1176. 2015.
[25] A. P. Muniyandi, R. Rajeswari, & R. Rajaram, Network anomaly detection by cascading k-Means clustering and C4. 5 decision tree algorithm. Procedia Engineering, 30, 174-182. 2012.
[26] R. Vinayakumar, K. P. Soman, & P. Poornachandran, *Applying convolutional neural network for network intrusion detection*. In 2017 International Conference on Advances in Computing, Communications and Informatics (ICACCI) (pp. 1222-1228). IEEE. September, 2017.
[27] A. A. Diro, & N. Chilamkurti. Distributed attack detection scheme using deep learning approach for Internet of Things. Future Generation Computer Systems, 82, 761-768. 2018.
[28] J. Kim, et al. *Long short term memory recurrent neural network classifier for intrusion detection*. In 2016 International Conference on Platform Technology and Service (PlatCon) (pp. 1-5). IEEE. (2016, February).
[29] P. Liu, X. Qiu, & X. Huang, X. Recurrent neural network for text classification with multi-task learning. arXiv preprint arXiv:1605.05101. 2016.
[30] M. Yousefi-Azar, et al. *Autoencoder-based feature learning for cyber security applications*. In 2017 International joint conference on neural networks (IJCNN) (pp. 3854-3861). IEEE. (2017, May).
[31] T. Salimans, et al. *Improved techniques for training gans*. Advances in neural information processing systems, 29, 2234-2242. 2016.
[32] U. Fiore, et al. Network anomaly detection with the restricted Boltzmann machine. Neurocomputing, 122, 13-23. 2013.
[33] Y. Zhang, P. Li, & X. Wang, Intrusion detection for IoT based on improved genetic algorithm and deep belief network. IEEE Access, 7, 31711-31722. 2019.
[34] K. Tange, et al. Towards a systematic survey of industrial IoT security requirements: research method and quantitative analysis, Proceedings of the Workshop on Fog Computing and the IoT, 2019.
[35] K. Tange, et al, *A Systematic Survey of Industrial Internet of Things Security: Requirements and Fog Computing Opportunities,* in IEEE Communications Surveys & Tutorials, vol. 22, no. 4, pp. 2489-2520, Fourthquarter 2020.
[36] T. Soo Fun, & A. Samsudin, Recent Technologies, Security Countermeasure and Ongoing Challenges of Industrial Internet of Things (IIoT): A Survey. Sensors, 21(19), 6647. 2021.
[37] S. Bhatt, & P.R. Ragiri, *Security trends in Internet of Things: A survey*. SN Applied Sciences, 3(1), 1-14. 2021.
[38] M. Serror, et al, *Challenges and Opportunities in Securing the Industrial Internet of Things*, IEEE Transactions on Industrial Informatics, vol. 17, no. 5, pp. 2985-2996, doi: 10.1109/TII.2020.3023507, May 2021.
[39] Y. Wu, et al. Deep reinforcement learning for blockchain in industrial IoT: A survey. Computer Networks, 191, 108004. 2021.
[40] K. Tsiknas, et al, Cyber Threats to Industrial IoT: A Survey on Attacks and Countermeasures. IoT, 2(1), 163-188, 2021.
[41] M. A. Al-Garadi, et al, *A Survey of Machine and Deep Learning Methods for Internet of Things (IoT) Security*, IEEE Communications Surveys & Tutorials, vol. 22, no. 3, pp. 1646-1685, 2020.
[42] R. A. Khalil, et al. *Deep Learning in the Industrial Internet of Things: Potentials, Challenges, and Emerging Applications*, IEEE Internet of Things Journal, vol. 8, no. 14, pp. 11016-11040, 15 July15, 2021.
[43] R. Ahmad & I. Alsmadi, Machine learning approaches to IoT security: A systematic literature review. Internet of Things, 100365. 2021.
[44] L. Aversano, et al. A systematic review on Deep Learning approaches for IoT security. Computer Science Review, 40, 100389. 2021
[45] Rudenko, R., Pires, I. M., Oliveira, P., Barroso, J., & Reis, A. (2022). A Brief Review on Internet of Things, Industry 4.0 and Cybersecurity. Electronics, 11(11), 1742.
[46] Ahanger, T. A., Aljumah, A., & Atiquzzaman, M. (2022). State-of-the-art survey of artificial intelligent techniques for IoT security. Computer Networks, 108771.
[47] L. Tan and N. Wang, *Future internet: The Internet of Things*, 2010 3rd International Conference on Advanced Computer Theory and Engineering (ICACTE), pp. V5-376-V5-380, 2010
[48] F. A. Alaba, et al, *Internet of Things security: A survey*, J. Netw. Comput. Appl., 88, 10–28, 2017.
[49] H. Boyes, et al. The industrial internet of things (IIoT): An analysis framework. Computers in industry, 101, 1-12. 2018.
[50] J. Sengupta, S. Ruj & S. D. Bit, *A comprehensive survey on attacks, security issues and blockchain solutions for IoT and IIoT*. Journal of Network and Computer Applications, 149, 102481. 2020.
[51] U. Saxena, J. S Sodhi, & Y. Singh. *An Analysis of DDoS Attacks in a Smart Home Networks*. In 2020 10th International Conference on Cloud Computing, Data Science & Engineering (Confluence) (pp. 272-276). IEEE. January 2020.
[52] S. Alzahrani and L. Hong, Generation of DDoS attack dataset for effective IDS development and evaluation, J. Inf. Secur. 9 (4), 225–241, 2018.
[53] Y. Gu, et al, Semi-supervised K-means DDoS detection method using hybrid feature selection algorithm, IEEE Access 7, 64351–64365, 2019.
[54] Y.N. Soe, et al, *DDoS attack detection based on simple ANN with SMOTE for IoT environment*, in: 2019 Fourth International Conference on Informatics and Computing (ICIC), pp. 1–5, 2019.
[55] N. Chaabouni, et al, *Network intrusion detection for iot security based on learning techniques*, IEEE Commun. Surv. Tutor. 21 (3), 2671–2701, 2019.

[56] P. García-Teodoro, et al, Anomaly-based network intrusion detection: techniques, systems and challenges, Comput. Secur. 28 (1), 18–28, 2009.

[57] I. Andrea, C. Chrysostomou, G. Hadjichristofi *Internet of things: security vulnerabilities and challenges*, 2015 IEEE Symposium on Computers and Communication (ISCC),), pp. 180-187, 2015.

[58] M.M. Ahemd, M.A. Shah, A. Wahid, *Iot security: a layered approach for attacks and defenses*, 2017 International Conference on Communication Technologies (ComTech), pp. 104-110, 2017.

[59] M. R. Bartolacci, et al, Personal denial of service (PDOS) attacks: A discussion and exploration of a new category of cyber crime. Journal of Digital Forensics, Security and Law, 9(1), 2. 2014.

[60] M.N. Aman, et al, *A light-weight mutual authentication protocol for iot systems*, GLOBECOM 2017 - 2017 IEEE Global Communications Conference, pp. 1-6, 2017.

[61] T. Gomes, et al, Cute mote, a customizable and trustable end-device for the internet of things, IEEE Sens. J., 17 (20), pp. 6816-6824, 2017.

[62] P. Porambage, et al, Pauthkey: a pervasive authentication protocol and key establishment scheme for wireless sensor networks in distributed iot applications, Int. J. Distributed Sens. Netw., 10 (7), 2014.

[63] X. Hei, et al, *Defending resource depletion attacks on implantable medical devices*, 2010 IEEE Global Telecommunications Conference GLOBECOM 2010, pp. 1-5. 2010.

[64] J. Choi and Y. Kim, *An improved lea block encryption algorithm to prevent side-channel attack in the iot system* 2016 Asia-Pacific Signal and Information Processing Association Annual Summit and Conference (APSIPA), pp. 1-4, 2016.

[65] S. Sicari, et al, Reato: reacting to denial of service attacks in the internet of things, Comput. Network., 137, pp. 37-48, 2018.

[66] P. Varga, et al, *Security threats and issues in automation iot*, 2017 IEEE 13th International Workshop on Factory Communication Systems (WFCS), pp. 1-6, 2017.

[67] J. Liu, et al, Epic: a differential privacy framework to defend smart homes against internet traffic analysis, IEEE Internet Things J., 5 (2), 2018.

[68] U. Guin, et al, *A secure low-cost edge device authentication scheme for the internet of things*, 31st International Conference on VLSI Design and 17th International Conference on Embedded Systems (VLSID). 2018.

[69] G. Glissa, et al, *A secure routing protocol based on rpl for internet of things*, IEEE Global Communications Conference (GLOBECOM), 2016.

[70] C. Pu and S. Hajjar, *Mitigating forwarding misbehaviors in rpl-based low power and lossy networks*, 2018 15th IEEE Annual Consumer Communications Networking Conference (CCNC), 2018.

[71] C. Cervantes, et al, *Detection of sinkhole attacks for supporting secure routing on 6lowpan for internet of things*, 2015 IFIP/IEEE International Symposium on Integrated Network Management (IM), 2015.

[72] P. Shukla, Ml-ids: A machine learning approach to detect wormhole attacks in internet of things, Intelligent Systems Conference (IntelliSys), 2017.

[73] D. Airehrour, J.A. Gutierrez & S.K. Ray, Sectrust-rpl: a secure trust-aware rpl routing protocol for internet of things, Future Gener. Comput. Syst., 2019.

[74] M. Singh, et al, *Secure mqtt for internet of things (iot)*, 5th International Conference on Communication Systems and Network Technologies, 2015.

[75] Y. Ashibani, Q.H. Mahmoud, *An efficient and secure scheme for smart home communication using identity-based signcryption*, 2017 IEEE 36th International Performance Computing and Communications Conference (IPCCC), 2017.

[76] V. Adat, B.B. Gupta, *A ddos attack mitigation framework for internet of things*, 2017 International Conference on Communication and Signal Processing (ICCSP), 2017.

[77] D. Yin, et al, A ddos attack detection and mitigation with software-defined internet of things framework, IEEE Access, 6, 2018.

[78] C. Liu, P. Cronin, C. Yang, *A mutual auditing framework to protect iot against hardware trojans*, 2016 21st Asia and South Pacific Design Automation Conference (ASP-DAC), 2016.

[79] S.T.C. Konigsmark, D. Chen, M.D.F. Wong, *Information dispersion for trojan defense through high-level synthesis*, 2016 53nd ACM/EDAC/IEEE Design Automation Conference (DAC), 2016.

[80] H. Naeem, et al, *A light-weight malware static visual analysis for iot infrastructure*, International Conference on Artificial Intelligence and Big Data (ICAIBD), 2018.

[81] J. Su, et al, *Lightweight classification of iot malware based on image recognition*, IEEE 42nd Annual Computer Software and Applications Conference (COMPSAC), vol. 02, 2018.

[82] T. Song, et al, A privacy preserving communication protocol for iot applications in smart homes, IEEE Internet Things J., 4 (6), 2017.

[83] C. Machado, A.A.M. Frhlich, *Iot data integrity verification for cyber-physical systems using blockchain*, 2018 IEEE 21st International Symposium on Real-Time Distributed Computing (ISORC), 2018.

[84] Y. Rahulamathavan, et al, *Privacy-preserving blockchain based iot ecosystem using attribute-based encryption*, IEEE International Conference on Advanced Networks and Telecommunications Systems (ANTS), 2017.

[85] D. Zheng, et al, Efficient and privacy-preserving medical data sharing in internet of things with limited computing power, IEEE Access, 6, 2018.

[86] P. Gope, B. Sikdar, Lightweight and privacy-preserving two-factor authentication scheme for iot devices, IEEE Internet Things J., 2018.

[87] J. Sengupta, et al, *End to end secure anonymous communication for secure directed diffusion in iot*, Proceedings of the 20th International Conference on Distributed Computing and Networking, ICDCN '19, 2019.

[88] F. Li, et al, *System statistics learning-based IoT security: Feasibility and suitability*, IEEE Internet Things J., vol. 6, no. 4, pp. 6396-6403, Aug. 2019.

[89] Magaia, Naercio, et al. Industrial Internet-of-Things Security Enhanced with Deep Learning Approaches for Smart Cities. IEEE Internet of Things Journal 8.8, 2020

[90] Sharma, M., Pant, S., Kumar Sharma, D., Datta Gupta, K., Vashishth, V., & Chhabra, A. *Enabling security for the Industrial Internet of Things using deep learning, blockchain, and coalitions.* Transactions on Emerging Telecommunications Technologies, 32(7), e4137. 2021.

[91] M. M. N. Aboelwafa, et al, *A Machine-Learning-Based Technique for False Data Injection Attacks Detection in Industrial IoT*, in IEEE Internet of Things Journal, vol. 7, no. 9, pp. 8462-8471, Sept. 2020.

[92] Z. E. Huma et al., A Hybrid Deep Random Neural Network for Cyberattack Detection in the Industrial Internet of Things, in IEEE Access, vol. 9, pp. 55595-55605, 2021.

[93] S. Liu, et al, *Network Log Anomaly Detection Based on GRU and SVDD*, 2019 IEEE Intl Conf on Parallel & Distributed Processing with Applications, Big Data & Cloud Computing, Sustainable Computing & Communications, Social Computing & Networking (ISPA/BDCloud/SocialCom/SustainCom), pp. 1244-1249, 2019.

[94] S. Latif, et al, A Novel Attack Detection Scheme for the Industrial Internet of Things Using a Lightweight Random Neural Network," in IEEE Access, vol. 8, pp. 89337-89350, 2020.

[95] S. Latif, et al, *DRaNN: A Deep Random Neural Network Model for Intrusion Detection in Industrial IoT*, 2020 International Conference on UK-China Emerging Technologies (UCET), pp. 1-4, 2020.

[96] M. M. Hassan, M. R. Hassan, S. Huda and V. H. C. de Albuquerque, *A Robust Deep-Learning-Enabled Trust-Boundary Protection for Adversarial Industrial IoT Environment*, in IEEE Internet of Things Journal, vol. 8, no. 12, pp. 9611-9621, 15 June15, 2021.

[97] M. M. Hassan, A. Gumaei, S. Huda and A. Almogren, *Increasing the Trustworthiness in the Industrial IoT Networks Through a Reliable Cyberattack Detection Model*, in IEEE Transactions on Industrial Informatics, vol. 16, no. 9, pp. 6154-6162, Sept. 2020.

[98] Y. Liu et al., Deep Anomaly Detection for Time-Series Data in Industrial IoT: A Communication-Efficient On-Device Federated Learning Approach, in IEEE Internet of Things Journal, vol. 8, no. 8, pp. 6348-6358, 15 April15, 2021.

[99] M. Khoda, T. Imam, J. Kamruzzaman, I. Gondal and A. Rahman, *Robust Malware Defense in Industrial IoT Applications Using Machine Learning With Selective Adversarial Samples*, in IEEE

Transactions on Industry Applications, vol. 56, no. 4, pp. 4415-4424, July-Aug. 2020.
[100] A. N. Jahromi, H. Karimipour, A. Dehghantanha and K. -K. R. Choo, *Toward Detection and Attribution of Cyber-Attacks in IoT-Enabled Cyber–Physical Systems*, in IEEE Internet of Things Journal, vol. 8, no. 17, pp. 13712-13722, 1 Sept.1, 2021.
[101] A. Alsaedi, N. Moustafa, Z. Tari, A. Mahmood and A. Anwar, TON_IoT Telemetry Dataset: A New Generation Dataset of IoT and IIoT for Data-Driven Intrusion Detection Systems, in IEEE Access, vol. 8, pp. 165130-165150, 2020.
[102] J. Zhao, et al, Anomaly Detection Collaborating Adaptive CEEMDAN Feature Exploitation with Intelligent Optimizing Classification for IIoT Sparse Data. Wireless Communications and Mobile Computing, 2021.
[103] T. Primya & G. Subashini, Swarm intelligence-based secure high-order optimal density selection for industrial internet-of-things (IIoT) data on cloud environment. International Journal of Communication Systems, 34(17), e4976, 2021.
[104] F. Hussain et al, A Framework for Malicious Traffic Detection in IoT Healthcare Environment. Sensors, 21(9), 3025. 2021.
[105] M. Alqahtani et al, IoT botnet attack detection based on optimized extreme gradient boosting and feature selection. Sensors, 20(21), 6336, 2020.
[106] I. Campero-Jurado et al. Smart Helmet 5.0 for industrial internet of things using artificial intelligence. Sensors, 20(21), 6241. 2020
[107] M. A. Ferrag, O. Friha, D. Hamouda, L. Maglaras and H. Janicke, "Edge-IIoTset: A New Comprehensive Realistic Cyber Security Dataset of IoT and IIoT Applications for Centralized and Federated Learning," in IEEE Access, vol. 10, pp. 40281-40306, 2022, doi: 10.1109/ACCESS.2022.3165809.
[108] Kumar, A., Shridhar, M., Swaminathan, S., & Lim, T. J. Machine learning-based early detection of IoT botnets using network-edge traffic. Computers & Security, 117, 102693. 2022
[109] Tharewal, S., Ashfaque, M. W., Banu, S. S., Uma, P., Hassen, S. M., & Shabaz, M. Intrusion detection system for industrial Internet of Things based on deep reinforcement learning. Wireless Communications and Mobile Computing, 2022.
[110] Javeed, D., Gao, T., Khan, M. T., & Shoukat, D. A hybrid intelligent framework to combat sophisticated threats in secure industries. Sensors, 22(4), 1582. 2022.
[111] D. Arp, et al. Drebin: Effective and explainable detection of android malware in your pocket. In Ndss (Vol. 14, pp. 23-26), February 2014.
[112] H. Satilmiş & S. Akleylek, A review of machine learning and deep learning models used for IoT security. Bilişim Teknolojileri Dergisi, 14(4), 457-481. 2021.
[113] N. Koroniotis, et al. Towards the development of realistic botnet dataset in the internet of things for network forensic analytics: Bot-iot dataset. Future Generation Computer Systems, 100, 779-796. 2019.
[114] Sethi, P., & Sarangi, S. R. (2017). Internet of things: architectures, protocols, and applications. Journal of electrical and computer engineering, 2017.
[115] AlSalem, T. S., Almaiah, M. A., & Lutfi, A. (2023). Cybersecurity Risk Analysis in the IoT: A Systematic Review. Electronics, 12(18), 3958.
[116] Rodríguez, E., Otero, B., & Canal, R. (2023). A survey of machine and deep learning methods for privacy protection in the Internet of Things. Sensors, 23(3), 1252.
[117] Santhosh Kumar, S. V. N., Selvi, M., & Kannan, A. (2023). A comprehensive survey on machine learning-based intrusion detection systems for secure communication in internet of things. Computational Intelligence and Neuroscience, 2023.
[118] Sarker, I. H., Khan, A. I., Abushark, Y. B., & Alsolami, F. (2023). Internet of things (iot) security intelligence: a comprehensive overview, machine learning solutions and research directions. Mobile Networks and Applications, 28(1), 296-312.
[119] Nuaimi, M., Fourati, L. C., & Hamed, B. B. (2023). Intelligent approaches toward intrusion detection systems for Industrial Internet of Things: A systematic comprehensive review. Journal of Network and Computer Applications, 103637.
[120] Mohy-Eddine, M., Guezzaz, A., Benkirane, S., Azrour, M., & Farhaoui, Y. (2023). An Ensemble Learning Based Intrusion Detection Model for Industrial IoT Security. Big Data Mining and Analytics, 6(3), 273-287.
[121] Alshahrani, H., Khan, A., Rizwan, M., Reshan, M. S. A., Sulaiman, A., & Shaikh, A. (2023). Intrusion Detection Framework for Industrial Internet of Things Using Software Defined Network. Sustainability, 15(11), 9001.
[122] Huang, J. C., Zeng, G. Q., Geng, G. G., Weng, J., & Lu, K. D. (2023). SOPA-GA-CNN: Synchronous optimisation of parameters and architectures by genetic algorithms with convolutional neural network blocks for securing Industrial Internet-of-Things. IET Cyber-Systems and Robotics, 5(1), e12085.
[123] Mehedi, S. T., Anwar, A., Rahman, Z., Ahmed, K., & Islam, R. (2022). Dependable intrusion detection system for IoT: A deep transfer learning based approach. IEEE Transactions on Industrial Informatics, 19(1), 1006-1017.

MANAS Journal of Engineering
ISSN 1694-7398 | e-ISSN 1694-7398

Volume 12, Issue 1, (202124) Pages 29-33
https://doi.org/10.51354/mjen.1220152

Use of BIM with Modular Construction in Future Construction Techniques

İlayda OMURTAY[1], Assoc. Prof. Asena SOYLUK[2] and Prof. Ali İhsan ÜNAY[3]

[1]Gazi University, Ankara/Turkey, ilayda.omurtay@gazi.edu.tr ORCID: 0000-0002-0922-9624
[2]Gazi University, Ankara/Turkey, asenad@gazi.edu.tr ORCID: 0000-0002-6905-4774
[3]Gazi University, Ankara/Turkey, unay@gazi.edu.tr ORCID: 0000-0002-9510-0375

ABSTRACT

Modular construction technology and applications are rapidly evolving. Modular construction is a process in which entire rooms or sections of rooms are built in a factory setting along with electrical, mechanical, and plumbing work and then transported to a final site for assembly. With modular construction, a building is built off-site, under controlled facility conditions, with the same materials and to the same codes and standards as conventionally built facilities, but in half the time. The modular construction method is used to build various types of buildings (whether they are apartment houses, office buildings, or hotels). This construction method is used for both permanent and relocatable projects. These projects can be built with two types of modules. These are 2D panels or 3D modules. These can be combined to form a third type, hybrid modular construction. Each has its advantages. 2D panels offer easy logistics and flexibility in building design and are mounted on site. Factory productivity is increased by using 3D volumetric solutions. They only need to be installed once they are delivered. The hybrid modular structure has the advantages of the previous two.

With the recent development of Building Information Modeling (BIM), the use of modular construction methods in conjunction with BIM becomes more common. As with any method, this one has advantages as well as disadvantages. Disadvantages of this method, such as a higher number of complex decisions, front-loaded design, etc., can be solved with BIM. Furthermore, the BIM platform can resolve the disadvantages of traditional construction methods, such as the difficulty of pre-project planning and coordination among members of interdisciplinary professions. With BIM and the modular construction method, physical conflicts between the structural system and its mechanical, electrical, and plumbing systems can be easily identified early in the design process, and resolution can be expedited. This article includes general information about the modular construction method, future application scenarios, use, and advantages of BIM. The document analysis method, one of the qualitative methods, was used, and in the light of the data obtained, comments and scenarios were tried to be created about the future of BIM and modular construction techniques. What distinguishes this study is that the concept of quality is examined in detail by using these two methods together.

ARTICLE INFO

Research article

Received: 16.12.2022
Accepted: 05.02.2024

Keywords:

Modular Construction, Prefabrication, Automation, Construction Techniques, Building Information Modeling (BIM), Quality in Project Management

*Corresponding author

1. Introduction

The Industrial Revolution occurred between the 1750s and 1850s saw major and significant changes in art, design, and architecture. Design requirements have changed as a result of industrialization. Due to the uniqueness of the construction industry, it presents several challenges for the direct adaptation of technologies used in many other industries. However, the motivation to industrialize the construction process comes from reducing construction costs and time, improving building quality, and producing more energy-efficient buildings. Modular construction systems that provide these benefits have advanced as the industrial revolution ushered in the modern era. Therefore, the modular construction method creates a methodology for design, drawing, and production automation.

2. Background

2.1 Modular Construction Manufacturing (MCM)

Modular systems, also known as cells, are the most industrialized prefabricated construction systems, with all or most of the building's components produced in the factory and only assembled on the construction site. Modular building units have been used since the nineteenth century. A carpenter in London wanted to build a prefabricated structure to aid his final migration to Australia. He built the first prefabricated house in 1837 [7]. Despite the fact that the modular construction concept has been around for over 100 years, the opportunities for modular construction were largely untapped until the revival of modular solutions like modular apartment buildings, modular hotels, modular classrooms, and modular office buildings. Since then, modular construction has advanced significantly, and much more sustainable, long-lasting methods are now used. Modular construction manufacturing (MCM) is a process in which building units are manufactured in a factory and shipped to the construction site for assembly. This systematic methodology covers the entire construction process of a project, from the initial design stage to final delivery. Modular construction involves the use of prefabricated units known as modules, which are then transported to the construction site. The modular construction method complies with the same building codes, raw materials, and standards as traditional construction projects. Modular construction materials that are commonly used include concrete, fsteel, and wood. The modular construction process consists of specific steps (Figure 1). First, modules are built off-site under factory conditions. Typically, modules for construction projects are fully equipped with all electrical, plumbing, heating, and interior trims. The modules are then delivered to the site by a truck. Modules are placed on the site. They can be attached side-by-side or end-to-end, and they can be linked together to form multiple floors to create buildings of any scale or layout. Because modular structures are used in modular construction work, they can be used for almost any temporary or permanent, large or small application, from site huts to cutting-edge operating theaters.

There are different types of modular buildings. Permanent Modular Construction (PMC) prefabricates single or multi-story buildings in deliverable modules off-site. Unlike projects that only use site-built construction, integrating PMC modules improves quality control and reduces waste. Permanent modular structures are also ideal for mixed-use applications. A relocatable building (RB) is constructed using a modular construction process and is partially or completely assembled for reuse and transportation to different construction sites. Furthermore, the versatility of an RB makes it an excellent choice for emergency and natural disaster relief services.

Relocatable modular buildings are ideal for on-site offices, medical clinics, sales centers, restroom facilities, schools, and other similar applications.

Aside from the types mentioned, a thorough examination of modular construction identifies additional categories based on the modular construction method. Closed modular construction (3D Modules) entails off-site design, development, and construction of entire rooms, including electrical wiring, plumbing, and HVAC. This prefabrication process, before delivering the completed module to the job site, installs and "closes up" all components in the manufacturing facility. Because building components can be expanded, downsized, relocated, and visually inspected on the job site while maintaining quality and engineering integrity, open modular construction (two-dimensional modules) adds versatility and simplifies the inspection process.

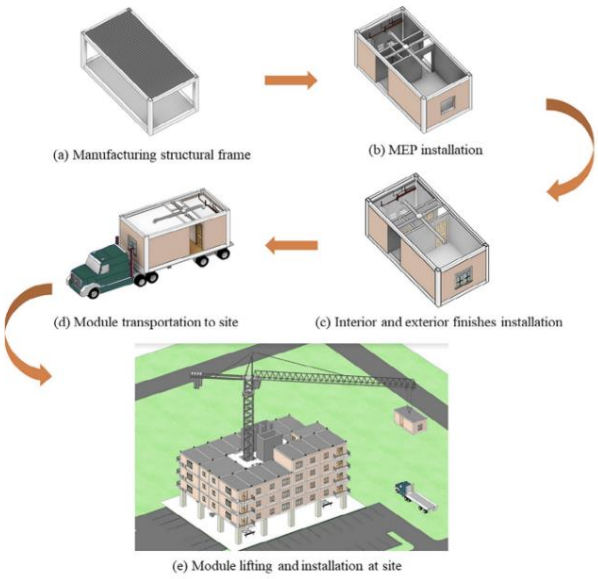

Figure 1: Modular construction – from manufacturing to site installation [7]

3. Materials and methods

3.1 Automation with BIM in Modular Construction

The first pillar of the industrialization or modularization of the building construction process is the automation of the design and drawing process. Managing the design and drawing process is an important issue in the architect/engineer/contractor (AEC) industry [5]. Automating the design and drawing process reduces unnecessary design activities, provides an infinite number of solutions, eliminates assumptions and design errors, and shortens the time required for any change.

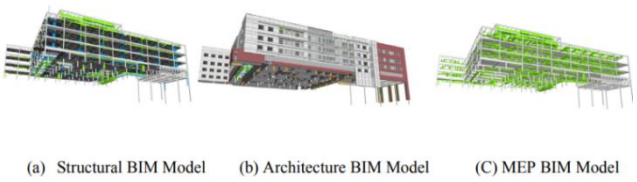

Figure 2: BIM Models in Healthcare Expansion Project [8]

Automation through modularization will have significant benefits for the construction industry, with benefits such as reducing overall project schedules, improving product quality, increasing on-site safety performance, reducing the need for skilled workers on-site, and decreasing in the negative environmental impact of construction operations [8]. One of the most difficult tasks faced in the modular construction delivery process has always been the coordination and manufacture of mechanical, electrical, and plumbing (MEP) systems. Three main factors contribute to the challenges of modular MEP fabrication. To begin with, the process is pretty split between design and construction firms. Second, the level of technology used in the various coordination scenarios varies widely between engineers and building contractors. Third, the process is to provide a model for private contractors' prefabrication plans [6]. The use of Building Information Modeling (BIM) for coordinating, documenting, fabricating, designing, and drawing MEP systems in modular structures seems to be a viable solution to these problems.

3.2 Building Information Modeling (BIM) Application in Construction

BIM is commonly defined as the process of developing an intelligent and computable three-dimensional (3D) data set and sharing it with the various types of professionals on the design and construction team. BIM technology creates an accurate virtual model of a building with precise geometry and relevant data to support procurement, fabrication, and on-site installation activities. To support automated production operations in factory settings, industrialization of the building construction process requires special methods of manufacturing and specific design criteria. Therefore, integration of the Building Information Model (BIM) with modular construction is required to support the manufacturer's needs for design and drafting in construction. The multidisciplinary nature of modular construction manufacturing makes BIM the right technology for the construction industry. BIM provides a core model loaded with project data that facilitates the data transfer process between different project stakeholders. The implementation of BIM systems in modular structures includes visualization of the designed structure; modeling; code reviews; manufacturing/factory drawings; communication; cost estimation; construction sequences; 4D model (3D models + timing information); conflict, interference, and collision detection processes; 5D BIM (cost estimation) [7]. Through this single information platform, BIM fosters collaboration between the design team, consultant, builders, and customers. It is aimed to achieve optimum efficiency and quality in the construction industry by using the technology of BIM to integrate architectural and structural design and modularity concepts into a model.

Despite the fact that modular building technologies offer significant benefits to the construction industry, the current construction delivery model does not support them due to the extensive project planning and MEP coordination required (Figure 2). With more BIM integration in construction projects, incorporating modular building technologies into projects becomes more effective and desirable because the entire planning, design, shop drawing development, manufacturing, and construction process can be streamlined. Physical conflicts between the structure and mechanical, electrical, and plumbing systems can be easily identified early in the design process and resolved.
It is predicted that optimum efficiency and quality will be achieved in the construction industry when the concepts of architecture, structural design, and modularity are integrated into a model using BIM technology.

4. Results and discussion

4.1 The Quality Provided by The Combination of BIM and Modular Construction

Construction product quality can be defined as the extent to which the needs expressed or implied during the construction process are guaranteed. Examples such as schedule performance, construction costs, and project completion on time are also included in the definition of quality. Technological advances are critical to improving the quality of a product in terms of its function. Modular construction is a method that architects and clients can use to improve the quality of their buildings, especially when used in conjunction with BIM. The PDCA circle in Figure 3 shows how the modular construction technique and BIM can improve quality when used effectively.

With modular construction method, the quality of the buildings will be much higher because the elements of the modules will be built to the desired size and shape, which will aid in meeting the quality standards. Moreover, the controlled environment of a manufacturing plant will lend itself to more thorough quality testing and traceability of components that enable the team to correct problems before the unit or system arrives at the work site. Also, BIM improves the quality and interoperability of design information. The use of BIM modeling services in modular construction increases the use of prefabricated modules while also resolving all potential issues during the design stage, saving time and money and improving project quality. By using BIM, thinking ahead of how the prefabricated product to be produced will look, how it will behave, or what kind of construction process it will go through will affect the quality of the construction. It can be integrated into the modular construction system of BIM at certain stages. For each phase of manufacturing, studies on the performance of the BIM library, system development for supporting BIM design, and the applicability of BIM for quantity take-off can be conducted using BIM. Creating virtual and simulation environments that support the design and assembly of prefabricated components and allow construction to be simulated can become standard practice. Production management for off-site production, process simulation for process management, and studies to reduce production errors can all be done using BIM. In the production process of modular elements, clash detection and

resolution in 3D models can be achieved with BIM. Finally, for the on-site construction phase, BIM can be used for lifting and on-site construction planning by visualizing lifting equipment. In addition, at all stages, studies to define the BIM implementation process and tasks can be conducted for improve product quality.

Through the use of BIM, controlled off-site production and 5D BIM cost estimation (modelling scheduling information to model construction sequences and adding financial cost) reduce costs. The modular structure integrated with 4D BIM (modelling scheduling information to model construction sequences) improves program performance. Detailed model-based shop drawings improve fabrication and construction quality. Resolving conflicts in the pre-construction phase saves rework, cost, and time. It improves site safety with modular building elements, 3D BIM visualization, and accurate drawing sets. Integrating BIM into the process makes modular construction workflows more beneficial and successful, with higher margins and higher product quality. Construction efficiency is increased by standardizing prefabricated modules with an integrated BIM repository and 3D visualization of relevant information.

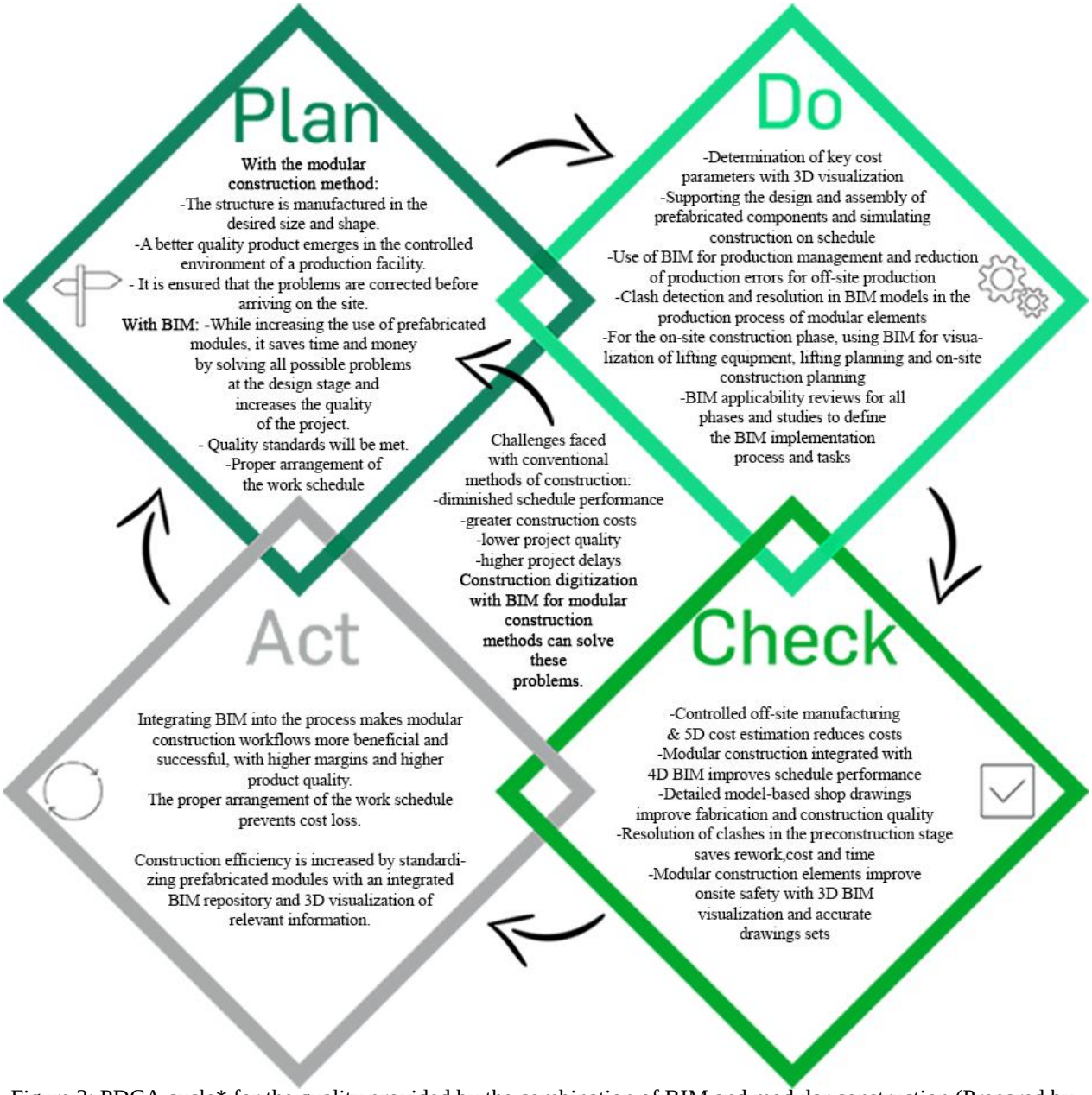

Figure 3: PDCA cycle* for the quality provided by the combination of BIM and modular construction (Prepared by Authors) *PDCA cycle is a management methodology that aims to continuously improve processes. The stages of this cycle are as follows: plan, do, check, and act.

4.2 Distinctions from Previous Studies

This study distinguishes itself from previous research in two key ways. Firstly, it goes beyond simply exploring the impact of the combined use of modular construction and BIM on quality. Instead, it implements the PDCA method as a comprehensive framework to systematically plan, execute, evaluate, and continuously improve the entire construction process. This iterative approach ensures that quality is not only measured but actively enhanced through ongoing refinement and adaptation.

Secondly, while existing literature may offer isolated studies on individual aspects of modular construction, BIM, or their combined impact on quality, this study bridges the gap by incorporating the PDCA method into the evaluation. This structured approach provides a rigorous and transparent framework for assessing and improving quality throughout the project lifecycle, setting it apart from less systematic investigations.

4.3 Recent Research and Research Gaps

While the literature lacks comprehensive comparative analyses, this study incorporates the PDCA method into the evaluation, providing a structured approach to assess and improve quality. Limited studies delve deeply into the impact of the combined use of modular construction and BIM on quality. The use of BIM has the potential to significantly improve the quality of construction projects.

6. Conclusion

Building information modeling (BIM) and modular construction are acknowledged as important technologies for resolving the current crisis in the construction sector. BIM and modular technology have a close relationship and can be used in conjunction to increase construction quality. BIM and modular building have been recommended as essential components of technology to advance the construction sector. Considering the quality-enhancing effect in the construction industry, the modular construction system and the use of BIM in modular construction are suggested as a future construction method. Consequently, it is advised that BIM and a modular approach be combined to raise the standard of the construction industry.

References

[1]. Alwisy, A., M. Al-Hussein, and S. H. Al-Jibouri. "BIM approach for automated drafting and design for modular construction manufacturing." Computing in civil engineering (2012). 2012. 221-228.

[2]. Bertram, Nick, et al. "Modular construction: From projects to products." McKinsey & Company: Capital Projects & Infrastructure (2019): 1-34.

[3]. Chen, LiJuan, and Hanbin Luo. "A BIM-based construction quality management model and its applications." Automation in construction 46 (2014): 64-73.

[4]. Chua, D. K. H., et al. "Process-parameter-interface model for design management." Journal of construction engineering and management 129.6 (2003): 653-663.

[5]. Korman, Thomas Michael. “Integrating multiple products over their life-cycles: An investigation of mechanical, electrical, and plumbing coordination.” Ph.D. Thesis, Department of Civil and Environmental Engineering, Stanford University, Stanford, CA, United States 2001.

[6]. Lawson, Mark, Ray Ogden, and Chris Ian Goodier. "Design in modular construction." Vol. 476. Boca Raton, FL: CRC Press, 2014.

[7]. Liew, J. Y. R., Y. S. Chua, and Z. Dai. "Steel concrete composite systems for modular construction of high-rise buildings." Structures. Vol. 21. Elsevier, 2019.

[8]. Lu, Na, and Thomas Korman. "Implementation of building information modeling (BIM) in modular construction: Benefits and challenges." Construction Research Congress 2010: Innovation for reshaping construction practice, Alberta, Canada, May 8-10, 2010. J.Ruwanpura, Y. Mohamed, S.Hyun Lee,2010, pp. 1136-1145.

[9]. Modular Building Institute [online]. Available from https://www.modular.org/ [Accessed September 17, 2022]

[10]. Moghadam, Mansooreh, Aladdin Alwisy, and Mohamed Al-Hussein. "Integrated BIM/Lean base production line schedule model for modular construction manufacturing." Construction Research Congress 2012: Construction Challenges in a Flat World. 2012, West Lafayette, Indiana, USA, May 21,2012, H. Cai, A. Kandil, M. Hastak, P. S. Dunston, pp.1271-1280.

[11]. Neelamkavil, Joseph. "Automation in the prefab and modular construction industry." Proceedings of the 26th International Symposium on Automation and Robotics in Construction, ISARC 2009, Austin, USA, June 24-27, 2009. Pp. 299-306

[12]. Le, Allen. "The Benefits and Challenges of Automation in the Modular Construction Industry." Student research, California Polytechnic State University, (2021).

[13]. Lee, Myungdo, et al. "Practical analysis of BIM tasks for modular construction projects in South Korea." Sustainability 12.17 (2020): 6900.

[14]. Shin, Jiwong, and Byungjoo Choi. "Design and Implementation of Quality Information Management System for Modular Construction Factory." Buildings 12.5 (2022): 654.

[15]. Smith, Ryan E. "Prefab architecture: A guide to modular design and construction." John Wiley & Sons, Hoboken, New Jersey, USA, 201.

MANAS Journal of Engineering
ISSN 1694-7398 | e-ISSN 1694-7398

Volume 12, Issue 1, (2024) Pages 34-38
https://doi.org/10.51354/mjen.1220416

Computational Hemodynamic Analysis of a Patient Specific Abdominal Aortic Aneurysm

Aykut Can Arslan[1], Huseyin Enes Salman[2,*]

[1] TOBB University of Economics and Technology, Ankara, Türkiye, arslanaykutcan@gmail.com, ORCID: 0000-0002-5097-8678

[2] TOBB University of Economics and Technology, Ankara, Türkiye, hsalman@etu.edu.tr, ORCID: 0000-0001-7572-9902

ABSTRACT

Abdominal aortic aneurysm (AAA) is a cardiovascular disease caused by the enlargement of the aorta in the abdomen over time. Unless treated, the growth of AAA continues, resulting in 80% death in the case of rupture. Today, the width of the aneurysm diameter is taken into account in clinical practice to examine the status of AAA. Although there are aneurysms that do not rupture despite reaching a diameter of 9 cm, it is reported that aneurysms with a diameter of 3 cm are ruptured in several cases. Therefore, analyzing only the AAA diameter is not a reliable method, and a deeper investigation is necessary for the rupture risk assessment. In this study, a patient's situation is analyzed using computational fluid dynamics (CFD) simulations, which allows to elucidate the flow dependent parameters such as velocity, vorticity, pressure, and wall shear stress (WSS). First, the patient-specific geometry was obtained and boundary conditions were defined at the inlet and the outlet of the flow domain. The effects of intraluminal thrombus (ILT) formation and patient's effort conditions were also included in the analysis. According to the results, WSS and vorticity increase with the increasing blood flow velocity. In terms of the rupture risk, it has been found that the effect of patient's effort level is more critical than the amount of ILT in the AAA.

ARTICLE INFO

Research article

Received: 17.12.2022
Accepted: 23.05.2024

Keywords:
abdominal aortic aneurysm, cardiovascular biomechanics, computational fluid dynamics, hemodynamic analysis

**Corresponding author*

1. Introduction

Abdominal Aortic Aneurysm (AAA) is a cardiovascular disease caused by the abnormal enlargement of the abdominal aorta over time [1]. Unless treated, growth continues and may result in rupture. In the case of rupture, a sudden death can occur at a rate of 80% [2]. The incidence of AAA is reported between 4% and 8% in men over the age of 50, while it is stated between 0.5% and 1% in women [3]. For the ages over 65 years, this probability is between 5% and 9%, but smoking increases this probability by 4 times [3]. Considering the incidence of AAA, the consequences of the rupture highlight the importance of diagnosis and treatment at an early stage.

The diameter of the healthy abdominal aorta ranges from 2 cm to 2.5 cm [4]. If the vessel diameter becomes 50% larger than the healthy value, this condition can be defined as a clinical case and diagnosed as aneurysm. AAA diameters may be larger than 5.5 cm depending on the patient's condition, and these patients are considered as critical in terms of rupture, and a surgical operation should be planned. Today, the width of the aneurysm diameter is taken into account in clinical practice to examine the status of AAA, but this examination criterion does not work well for all cases. Although there are aneurysms that do not rupture despite reaching a diameter of 9 cm, aneurysms with a width of 3 cm can rupture. In addition to the AAA vessel diameter, in order to determine the physical risk of the patient, it is necessary to consider the past history affecting the internal vascular structure, such as age, gender, smoking, enzymatic status of proteins in the microscale, and the patient's disease history. On the other hand, considering the engineering approaches, computational investigations can be conducted on the vascular structure, the state of the clot in the vessel, and the fluid properties [5, 6, 7].

In order to prevent the rupture, the rate of increase in vessel width may be important in addition to the aneurysm diameter in patients diagnosed with AAA. According to European Society for Vascular Surgery (ESVS) and American Heart Association (AHA), vessel diameters that grow more than 1 cm/year or exceed 5.5 cm may require medical intervention [8]. However, open surgery of aneurysm has high risks, so it is preferred only in cases that are considered to be the most risky. It should be noted that the open surgery is not the only treatment method, and in some cases, it can be planned to progress through the vein with endovascular methods and

return the diameter of the flow in the vein to normal levels with an endovascular stent [5].

In many previous studies, using numerical methods, blood flow in the aneurysm and strains in the vessel wall were obtained and the condition of the AAA was examined [9, 10]. It has been observed that the enlarged vessel with an aneurysm causes the flow volume to expand [10, 11]. As a result, the shear stress on the inner surface of the vessel decreases due to the drop in the blood flow velocity [4]. Due to the reduction of the shear stress on the inner surface of the vessel, the vessel cells trigger the abnormal development of blood vessel in response. In the light of this information, it is of great importance to examine the patient's condition by taking into account the vascular deformations and internal forces [12]. Intravascular pressure is the main source of rupture for transient and static conditions in vessel rupture, and most academic research has focused on resolving these forces using wall shear stress and pressure [13]. It has been observed that if the wall stress is greater than 65 N/cm² (650 kPa), the AAA structure cannot withstand the mechanical rupture [5]. In addition to these, the formation of clots in the vessel also changes the physical properties of the artery, as well as chemically causes the inner part of the artery to be insufficiently nourished and weakened biologically [12]. When past autopsy reports were reviewed, clots were found in 80% of the ruptured aneurysms. In this study, the wall shear stress, blood pressure, velocity and vorticity in the blood vessel were determined using a patient specific aneurysm model considering the level of clot in the vessel, and activity status of the patient.

2. Methodology

2.1 Geometry

The simulations for AAA analysis can be split into two groups. These are realistic models and idealized models. Idealized models have the ability to examine the effects of the parameters of interest independently while keeping the other parameters constant, but realistic models give results closer to reality [4]. For this reason, it is possible to obtain more realistic flow rates and pressure distributions by using realistic models instead of the idealized ones. Realistic models are obtained by rendering the vessel geometry of patients in 3D using the medical imaging methods.

In a realistic AAA model, there may be a clot deposit as it can be found in most of AAA patients [6, 7, 9]. Three different models were created for this situation. The vessel structures and geometries used in this study are provided in Figure 1 and Figure 2 [6]. When Figure 1 is examined, there is a fixed vessel wall on the outside, while there is a blood clot that restricts the blood flow. As the importance of blood clots, namely intraluminal thrombus (ILT), is stated in the introduction, it is quite possible to encounter a blood clot deposit in AAA patients, since blood clots are seen in many AAA autopsies [14]. However, different clot levels were also analyzed to examine the effect of ILT on flow variables. These analyses were conducted on the models with no clots (No ILT), light ILT, and dense ILT. The blood flow volumes for the vessels are given in Figure 2 in order to provide a comparison for better understanding the difference between the models [6]. From these figures, it can be clearly seen that the flow volume will decrease proportional to the increase in the amount of ILT.

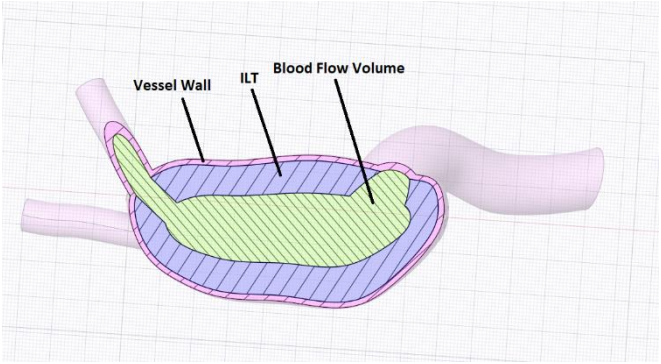

Figure 1. *Abdominal aortic aneurysm (AAA) layers.*

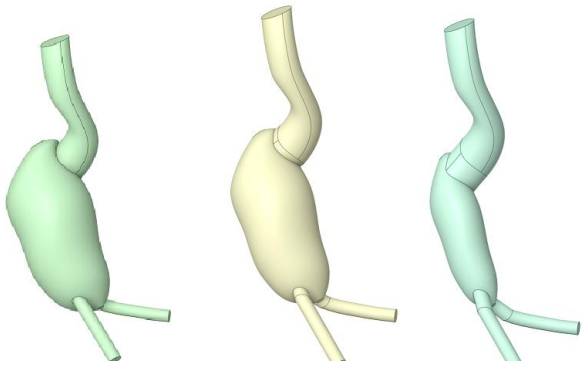

Figure 2. *Blood flow volumes for the no ILT (left), light ILT (middle), and dense ILT (right).*

2.2 Blood model

Blood is a non-Newtonian fluid; that is, its viscosity changes according to the shear stress on the fluid [4, 15]. However, in many studies in the literature, blood has been modeled as a Newtonian fluid due to its simplicity [4, 15]. In this study, the blood was modeled as a non-Newtonian fluid by employing the Carreau model [6, 9]. The coefficients of this model are obtained from previously published academic studies and tabulated in Table 1 [6]. In Figure 3, the viscosity changes are shown as a function of strain rate. Laminar flow analyses are performed using the Carreau model in ANSYS Workbench 2019 R2 platform by using the Fluent solver with laminar viscous flow model.

Table 1. *Carreau model parameters for the blood.*

Mass density [kg/m^3]	1050
Time constant, lambda [s]	10.976
Power-law index, n	-0.3216
Zero shear viscosity [kg/(ms)]	0.056
Infinite shear viscosity [kg/(ms)]	0.0033

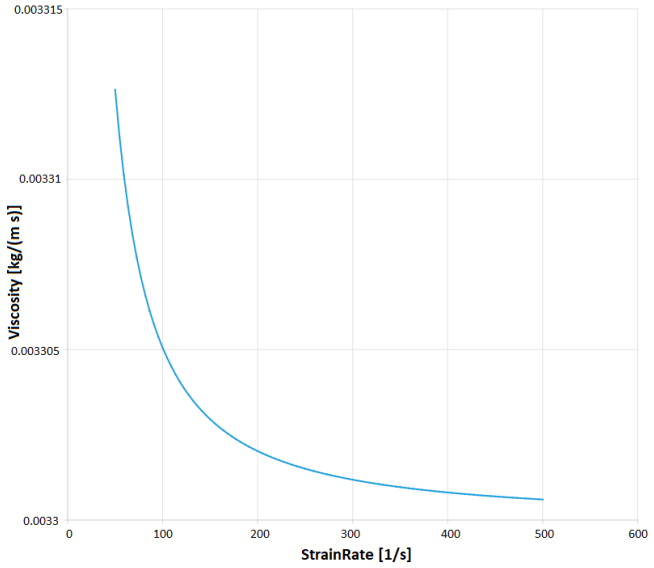

Figure 3. *The change in blood viscosity as a function of strain rate.*

2.3 Boundary conditions

In order to have realistic results, the boundary conditions should be chosen close to the physiologic flow conditions in AAA [4, 6]. For this purpose, an inlet flow profile and an outlet pressure profile are used as provided in Figure 4 and Figure 5, respectively [6, 9]. Figure 4 and Figure 5 show the time-dependent velocities and pressures used in the analysis [6, 9]. In addition, the inlet flow velocities during the effort, normal state, and resting conditions are provided in Figure 4.

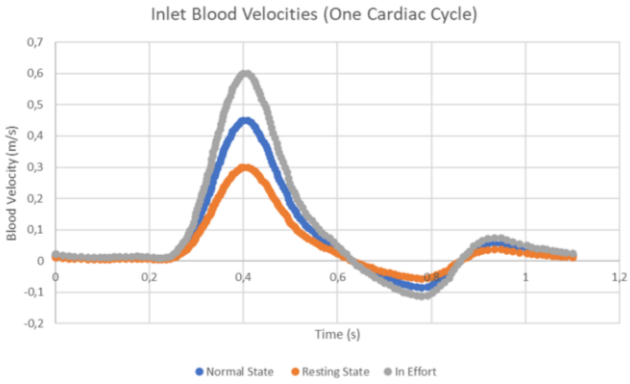

Figure 4. *Inlet blood velocity conditions during one cardiac cycle.*

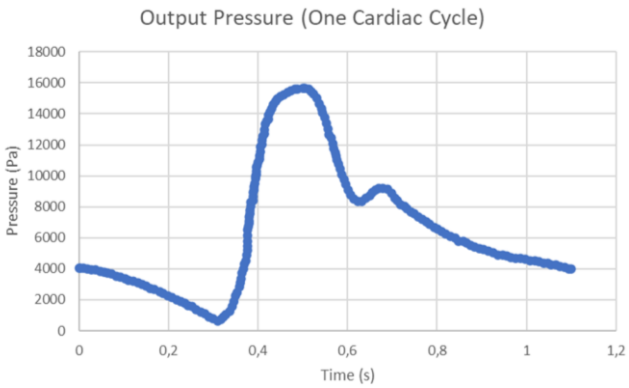

Figure 5. *Outlet pressure conditions during one cardiac cycle.*

3. Results

In this section, the results obtained are presented. A mesh independence study is performed and it is seen that a mesh composed of 450000 tetrahedral elements provide satisfactorily accurate results. Three cardiac cycles are simulated using a total of 600 time steps with 0.0055 s increments. The effects of ILT level and effort conditions are analyzed.

3.1 The effect of the blood velocity

It is important to examine AAA in different conditions since the heart does not constantly pump blood at a constant flow rate, and analysis results for slow (at rest), normal, and fast (in effort) conditions are provided in this section. In Figure 6, 7, and 8, the volume averaged vorticities, maximum wall shear stresses (WSS) on the AAA wall, and maximum blood pressure in the flow domain are investigated by considering different effort conditions, respectively.

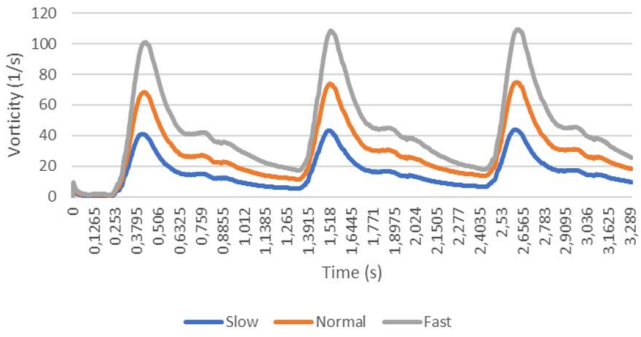

Figure 6. *Volume averaged vorticities for 3 consecutive cardiac cycles considering different effort conditions.*

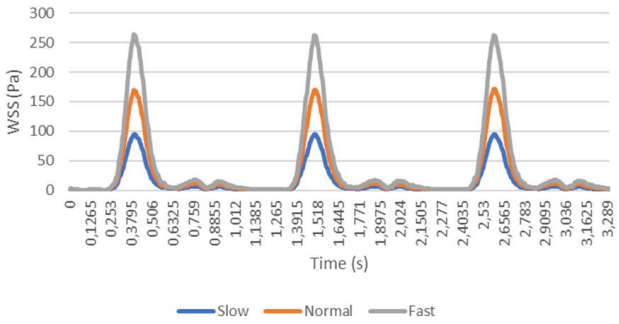

Figure 7. *Maximum WSS for 3 consecutive cardiac cycles considering different effort conditions.*

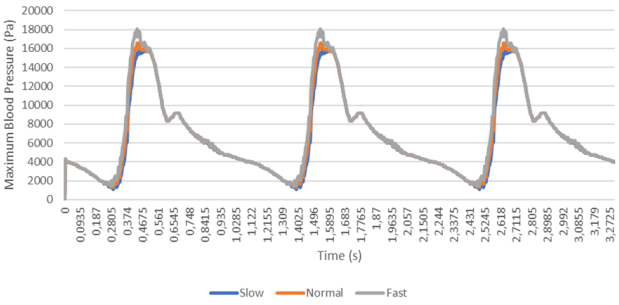

Figure 8. *Maximum blood pressures for 3 consecutive cardiac cycles considering different effort conditions.*

While the resting state is optimal in terms of loads on the vessel and flow parameters, a large increase has occurred in these values even in the normal state. The increase due to the effort conditions is high for the vorticity and WSS, on the other hand, blood pressure only varied by 3% depending on the effort conditions of the patient.

Vorticity is a metric that is defining the rotational behavior in the flow domain. With the increasing flow velocities depending on the patient activity, higher vorticity levels are observed in the aneurysm. This is due to the enlarged AAA section in the flow domain which is generating higher vorticity levels with increased flow velocities.

3.2 The effect of the ILT

The amount of ILT in the AAA limits the flow volume and changes the vascular structure. The effect of ILT on the WSS and vorticity is investigated in this section. In Figure 9, 10, and 11, the volume averaged vorticity, maximum WSS, and maximum blood pressure are investigated by considering different amount of ILT in the AAA, respectively.

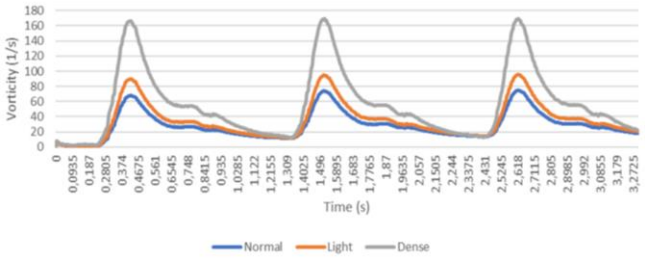

Figure 9. *Volume averaged vorticities for 3 consecutive cardiac cycles considering different ILT amounts.*

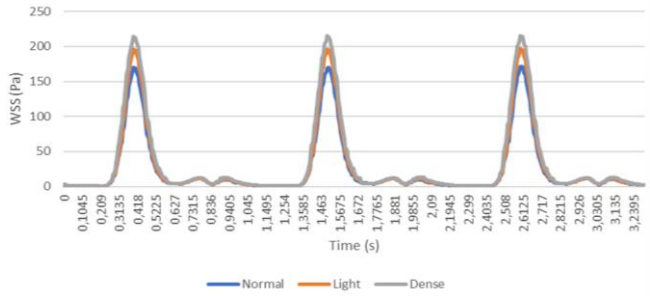

Figure 10. *Maximum wall shear stresses (WSS) for 3 consecutive cardiac cycles considering different ILT amounts.*

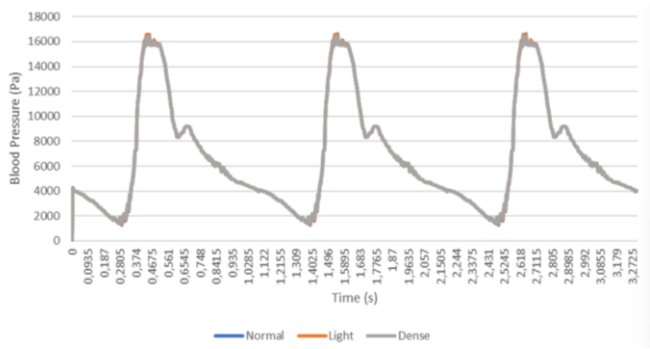

Figure 11. *Maximum blood pressures for 3 consecutive cardiac cycles considering different ILT amounts.*

4. Conclusion

In this study, the effects of effort conditions and ILT amounts are examined using computational fluid dynamics (CFD) analysis. As a general behavior, the increase in flow velocity caused an increase in vorticity and WSS levels.

There was no significant change in pressure in the investigated cases. This condition may be due to the applied outlet pressure boundary conditions in the analysis. Due to the lack of data in the literature, a common pressure boundary condition was used for three different activity conditions. In further studies, it is aimed to improve the models by implementing patient-specific boundary conditions in the CFD simulations.

In the numerical analysis, the most important parameter was considered to be the wall shear stress (WSS). It was observed

that WSS levels were heavily affected by the flow rate. While the increase in the amount of ILT increased the amount of WSS by approximately 10%, there was a WSS increase of 47% and 28% due to the 50% and 33% increase in flow rate, respectively. This shows that the effort conditions lead to different flow rates which significantly affect the WSS environment in the AAA.

WSS can be determined by dividing the fluid-driven friction force to the local wall area and do not have a direct effect on the rupture. However, the abnormal levels of WSS reduces the functional behavior of the endothelial cells on the AAA wall, and this condition leads to degenerated AAA wall with lowered mechanical strength. Therefore, the abnormal WSS levels play a role in the rupture of AAA in the long-term exposure. For the investigated cases, it is seen that the WSS values did not exceed 300 Pa in the modeled cases. It should be noted that even if the rupture does not occur at these levels, some risk factors may overlap and trigger the rupture mechanism.

In the light of the results obtained, it can be concluded that the effect of effort conditions is found to be more prominent than the amount of ILT burden in the AAA. If the AAA is exposed to high effort conditions with the high ILT burden at the same time, the rupture risk significantly increases as can be seen from the excessively increased vorticity and WSS levels around the aneurysmal enlargement.

Acknowledgement

This study is funded by TÜBİTAK (The Scientific and Technological Research Council of Türkiye) 3501-Career Development Program (Project number: 221M001).

References

[1]. Mutlu O, Salman H.E., Al-Thani H., El-Menyar A., Qidwai U.A., Yalcin H.C., "How does hemodynamics affect rupture tissue mechanics in abdominal aortic aneurysm: Focus on wall shear stress derived parameters, time-averaged wall shear stress, oscillatory shear index, endothelial cell activation potential, and relative residence time", Computers in Biology and Medicine, 154, (2023), 106609.

[2]. Bengtsson H., Bergqvist D., "Ruptured abdominal aortic aneurysm: a population-based study", Journal of Vascular Surgery, 18, (1993), 74-80.

[3]. Kontopodis N., Metaxa E., Papaharilaou Y., Tavlas E., Tsetis D., Ioannou C., "Advancements in identifying biomechanical determinants for abdominal aortic aneurysm rupture" Vascular, 23, (2014), 65-77.

[4]. Salman H.E., Ramazanli B., Yavuz M.M., Yalcin H.C., "Biomechanical investigation of disturbed hemodynamics-induced tissue degeneration in abdominal aortic aneurysms using computational and experimental techniques", Frontiers in bioengineering and biotechnology, 7, (2009), 111.

[5]. Hafez H., Druce P.S., Ashton H.A., "Abdominal aortic aneurysm development in men following a "normal" aortic ultrasound scan", European Journal of Vascular and Endovascular Surgery, 36, (2008), 553-558.

[6]. Arslan A.C., Salman H.E., "Effect of intraluminal thrombus burden on the risk of abdominal aortic aneurysm rupture", Journal of Cardiovascular Development and Disease, 10, (2023), 233.

[7]. Salman H.E., "Pıhtı birikiminin abdominal aort anevrizması yırtılma riskine etkisinin mühendislik yöntemleriyle incelenmesi", Fırat Üniversitesi Mühendislik Bilimleri Dergisi, 35, (2023), 597-614.

[8]. Chaikof E.L., Brewster D.C., Dalman R.L., Makaroun M.S., Illig K.A., Sicard G.A., Timaran C.H., Upchurch Jr G.R., Veith F.J., "The care of patients with an abdominal aortic aneurysm: the Society for Vascular Surgery practice guidelines" Journal of Vascular Surgery, 50, (2009), 2-49.

[9]. Kalipcilar A., Salman H.E., "Hemodynamic effects of intraluminal thrombus burden in an idealized abdominal aortic aneurysm", Journal of the Brazilian Society of Mechanical Sciences and Engineering, 45, (2023), 508.

[10]. Les A.S., Shadden S.C., Figueroa C.A., Park J.M., Tedesco M.M., Herfkens R.J., Dalman R.L., Taylor C.A., "Quantification of Hemodynamics in Abdominal Aortic Aneurysms During Rest and Exercise Using Magnetic Resonance Imaging and Computational Fluid Dynamics", Annals of Biomedical Engineering, 38, (2010), 1288-1313.

[11]. Salman H.E., "Numerical modeling of the sound generated on an intracranial aneurysm using computational fluid dynamics", Düzce University Journal of Science & Technology, 11, (2023), 908-921.

[12]. Scotti C.M., Finol E.A., "Compliant biomechanics of abdominal aortic aneurysms: a fluid–structure interaction study", Computers & Structures, 85, (2007), 1097-1113.

[13]. Salman H.E., Yalcin H.C., "Computational investigation of the effect of wall thickness on rupture risk in abdominal aortic aneurysms", Journal of Applied Fluid Mechanics, 14, (2021), 499-513.

[14]. Geest J.P.V., Sacks M.S., Vorp D.A., "A planar biaxial constitutive relation for the luminal layer of intraluminal thrombus in abdominal aortic aneurysms", Journal of Biomechanics, 39, (2006), 2347-2354.

[15]. Mutlu O., Salman H.E., Yalcin H.C., Olcay A.B., "Fluid flow characteristics of healthy and calcified aortic valves using three-dimensional lagrangian coherent structures Analysis", Fluids, 6, (2021), 203.

MANAS Journal of Engineering
ISSN 1694-7398 | e-ISSN 1694-7398

Volume 12, Issue 1, (2024) Pages 39-45
https://doi.org/10.51354/mjen.1222550

Investigation and Optimization of The Effect of Anhydrous Borax Mineral on The Vickers Hardness and Indentation Modulus Values of Iron Material

Şenol ŞAHİN[1], Ayşegül BODUR YILMAZ[2*], Talha Tunahan KESEMENLİ[3]

[1] Kocaeli University, Department of Mechanical Engineering, Kocaeli, Türkiye
sensah@kocaeli.edu.tr, ORCID: 0000-0002-7823-2245

[2] Kocaeli University, Institute of Sciences, Department of Mechanical Engineering, Kocaeli, Türkiye
206109009@kocaeli.edu.tr, ORCID: 0000-0003-1456-1282

[3] Kocaeli University, Institute of Sciences, Department of Mechanical Engineering, Kocaeli, Türkiye
talha.kesemenli@gmail.com, ORCID: 0000-0003-2305-8937

ABSTRACT

In this study, 5% and 10% by weight of anhydrous borax (AHB) was added to the iron (Fe) matrix material by powder metallurgy method and the effects of the additive ratio on the Vickers hardness (HV), Brinell hardness (HB) and Indentation modulus (E_{IT}) values of the composites (Fe/AHB) were investigated. In the productions carried out using Taguchi experimental design method, AHB additive ratio, and sintering temperature parameters were selected as control parameters that were thought to affect the physical and/or mechanical properties of the Fe/AHB composite materials. The productions were carried out according to the Taguchi L4 orthogonal array, which was created depending on the control parameters and levels. Vickers hardness and indentation modulus measurements of pure iron and Fe/AHB composite materials were performed in accordance with BS EN ISO 14577-1 standard and Brinell hardness measurement was performed in accordance with TS EN ISO 6506-1 standard. According to the signal-to-noise ratio (S/N) analysis performed with the experimental data, it was determined that the 10% AHB additive ratio and 950ºC sintering temperature optimized all the investigated properties of the Fe/AHB composite material. It was determined that the values for Vickers hardness, Brinell hardness and indentation modulus increased by 142.03%, 69.32% and 144.11%, respectively, in the levels where the properties of the composite material were optimized compared to pure Fe material. As a result of the qualitative examination of all samples after storage in a comfortable environment without daylight, it was also observed that the anhydrous borax additive delayed the corrosion time of pure iron material.

ARTICLE INFO

Research article

Received:
Accepted:

Keywords:
Anhydrous borax,
composites,
hardness,
iron,
powder metallurgy

**Corresponding author*

1. Introduction

Composites are a group of advanced technological materials formed by the combination of at least two different materials, where the components called matrix and reinforcement come together by creating an interface and behave as a single material. As technology has evolved, the properties expected from materials have changed and the increasing demand for lightweight materials with high chemical and mechanical strength in many sectors has increased the interest in composites [1,2].

Metal matrix composites (MMCs) with continuous fibers and whiskers as reinforcement were developed in the 1970s and proposed for applications requiring high performance. [3]. These materials have attracted great interest from the industry due to their unique mechanical and structural properties [3,4].

The improved mechanical strength, wear resistance, hardness, stiffness, damping capacity, thermal stability, ductility of metal matrix composites have attracted attention for a wide range of applications [3,5]. MMCs are ideally suited for use in ground transportation and aviation in the reduction of structural weight and related fuel consumption [5]. When the reinforcement materials preferred in the production of metal

matrix composites, which can be produced by different techniques [7] such as powder metallurgy, spray deposition technique, and stir casting, are examined; silicon carbide (SiC) with high hardness, wear resistance, toughness, fatigue resistance properties and boron carbide (B_4C) with high melting point, low density, great resistance to chemical substances are frequently preferred materials [5]. Boron carbide (B_4C), an important reinforcement material, is the hardest known material after diamond and cubic boron nitride (cBN) [6]. Since borides have higher hardness and thermal stability compared to carbides, borides have the potential to be a wear-resistant phase [8]. It is also known that B increases the hardenability of the iron matrix [9].

When the materials used in the production sector do not perform as expected, situations such as production inefficiencies, quality problems and consequently customer dissatisfaction inevitably arise. In this context, there are different methods developed to improve both expected material properties and product quality. The Taguchi method is one of the methods developed to obtain the most information with the least amount of time, cost, and energy by designing experimental studies. It has proven to be an effective tool to create optimal production conditions in a wide range of production environments, especially in achieving more efficient results with reduced trials [10,14].

In this study, a metal matrix composite was produced with iron (Fe) as the matrix material and anhydrous borax (AHB), a type of boron mineral, as an additive.

By evaluating the effects of anhydrous borax and/or anhydrous borax additive ratio and sintering temperature factors on the mechanical properties of the final product (composite material), it is aimed to determine the most effective additive ratio and sintering temperature to increase Brinell hardness, Vickers hardness and indentation modulus values and to develop Fe/AHB composite material. The experimental study was carried out by Taguchi experimental design method and Fe/AHB composites were produced by powder metallurgy method according to the obtained Taguchi orthogonal array.

2. Material And Methods

2.1. Iron (Fe)

Pure iron with a density of 7.87 g/cm^3, a melting temperature of 1535^{o}C and a grain size of 3 µm was used as matrix material for the production of composite materials

2.2. Anhydrous borax

Anhydrous borax mineral with the trade name Etibor-68 purchased from Eti Maden Operations, with a density of 2.37 g/cm^3 and a melting temperature of 742.5^{o}C, was ground and used under a sieve size of 20 µm as an additive material for the production of composite materials.

2.3. Implementation of Taguchi Method

Taguchi experimental design method was used to optimize the Brinell hardness, Vickers hardness and Indentation modulus values of the composites produced and to determine the optimum levels of the factors. In addition to the control factor of sintering temperature, which is thought to affect the quality and mechanical properties of the composite products by powder metallurgy method, the AHB additive ratio was also specified as a control factor in order to investigate the effect of different weight percentages of AHB additive. (see Table 1).

Table 1. *Control factors and their levels*

Factors	Level 1	Level 2
AHB additive ratio (wt. %)	5	10
Sintering temperature (^{o}C)	850	950

Depending on the factors and their levels, Taguchi L4 orthogonal array was selected (see Table 2) and the productions were carried out in accordance with the orthogonal array. At least 3 specimens were produced for each test set-up and Brinell hardness, Vickers hardness and indentation modulus values were determined by taking 5 different measurements on the specimens.

Table 2. *Experimental conditions for L4 orthogonal array*

Trials	AHB additive ratio (wt. %)	Sintering temperature (^{o}C)
1	5	850
2	5	950
3	10	850
4	10	950

Using the experimental data obtained after the measurements of Brinell hardness, Vickers hardness and indentation modulus values, signal-to-noise ratios (*S/N*) were examined by using the Minitab program, in accordance with the "larger is better" method (see Equation 1) to determine the parameters that optimize these values.

$$S/N = -10 \cdot \log\left(\frac{1}{n}\sum_{i=1}^{n}\frac{1}{y_i^2}\right) \quad (1)$$

2.4. Composite material production

In the preliminary preparation stage before production, AHB was first subjected to grinding in a RETSCH brand SK100 model device to reduce the grain size and then to sieving in a RETSCH brand AS200 model device to separate the particles according to grain size. In order to obtain a homogeneous mixture, Fe/AHB composites with different weight

percentages were prepared in a glass jar with a nickel ball inside using a MSE-TEC brand ball mill machine at a grinding speed of 200 rpm and a grinding time of 30 minutes. Then, Fe/AHB composite materials were obtained (see Figure 1) in a DIEX model induction furnace, in a graphite mold with an inner diameter of 20 mm, at a constant heating rate of 45ºC/min to the sintering temperature, under a constant 15 min holding time at sintering temperature, and at different sintering temperatures (850ºC – 950ºC). Since the sintering temperature was higher than the melting temperature of AHB used as an additive, AHB liquefied in the mold and caused fractures in the mold when pressure was applied. For this reason, the productions were carried out under a constant pressure of 2 MPa to prevent damage to the mold.

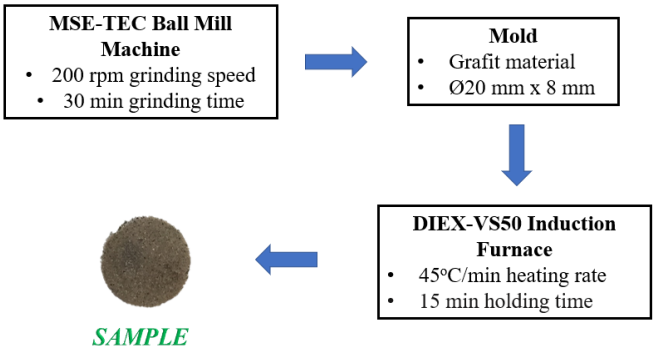

Figure 1. *Sample production steps*

2.5. Brinell hardness, Vickers hardness and Indentation modulus measurement

Vickers hardness and indentation modulus measurements were carried out under 1 kg load according to BS EN ISO 14577-1 standard on a Zwick BZ2.5/TS1S instrumented hardness tester at Tübitak National Metrology Institute. Brinell hardness measurement was carried out under 31.25 kg load according to TS EN ISO 6506-1 standard in a WOLPERT brand hardness tester in Kocaeli University Mechanical Engineering Department.

3. Results and Discussion

It has been determined in previous studies that the strength and stiffness of composite materials can be enhanced by the presence of intermetallic phases and compounds [15]. Due to the structure of MMCs, the interface between the matrix and the additive is important for increasing the mechanical properties. Because in the composite material exposed to load, it is desired to form a structure in such a way that the relevant load is transferred from the matrix to the additive through the interface [11].

3.1. Brinell hardness value

The Brinell hardness values of the materials are comparatively graphed in Figure 2, which was prepared using the experimental data obtained. When Figure 2 is examined, it is determined that the hardness value of the composite material produced at 850ºC sintering temperature with 5 wt% AHB additive increased by 25.40% compared to the reference pure Fe material produced at 850ºC sintering temperature. It was also found that the hardness value of the composite material produced at 950ºC sintering temperature with 10% AHB additive increased by 69.32% compared to the reference pure Fe material.

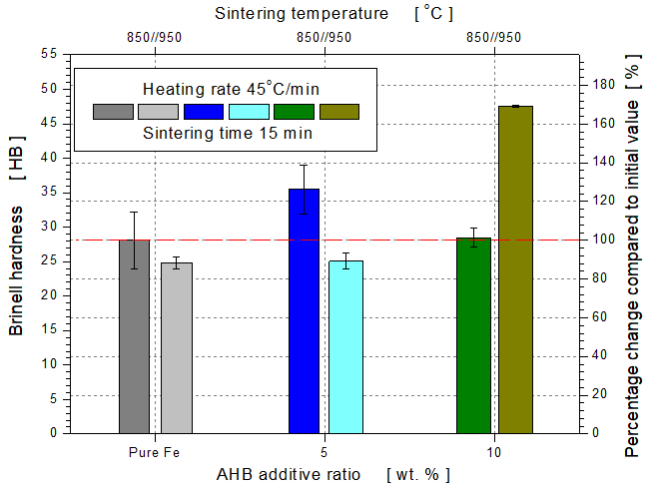

Figure 2. *Graph of the change in Brinell hardness values*

When the *S/N* ratio table (see Table 3) and graph (see Figure 3) are examined, it was determined that the most effective factor on Brinell hardness is the AHB additive ratio, which is the factor with the largest delta value. It was determined that the factor levels that optimized (maximized) the Brinell hardness value were 10% AHB additive ratio and 950ºC sintering temperature.

Table 3. *S/N ratio response table of Brinell hardness values of composites*

Level	AHB additive ratio	Sintering temperature
1	29.27	29.74
2	**31.08**	**30.61**
Delta	1.82	0.88
Rank	1	2

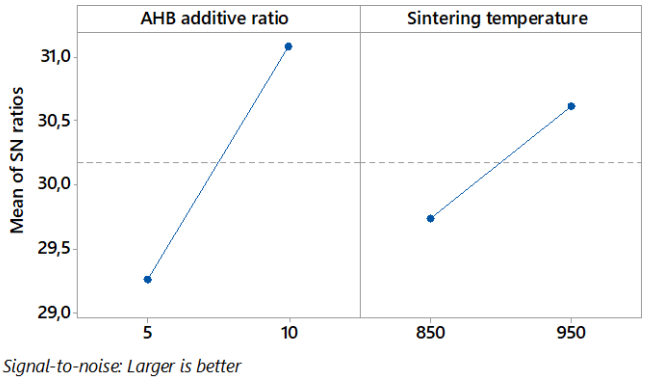

Figure 3. *Main effects plot of S/N ratios of Brinell hardness values of composites*

3.2. Vickers hardness value

The Vickers hardness values of the materials are comparatively graphed in Figure 4, which was prepared using the experimental data obtained. When Figure 4 is examined, it is determined that the hardness value of the composite material produced at 850ºC sintering temperature with 5 wt% AHB additive increased by 36% compared to the reference pure Fe material produced at 850ºC sintering temperature. It was also found that the hardness value of the composite material produced at 950ºC sintering temperature with 10% AHB additive increased by 142.03% compared to the reference pure Fe material.

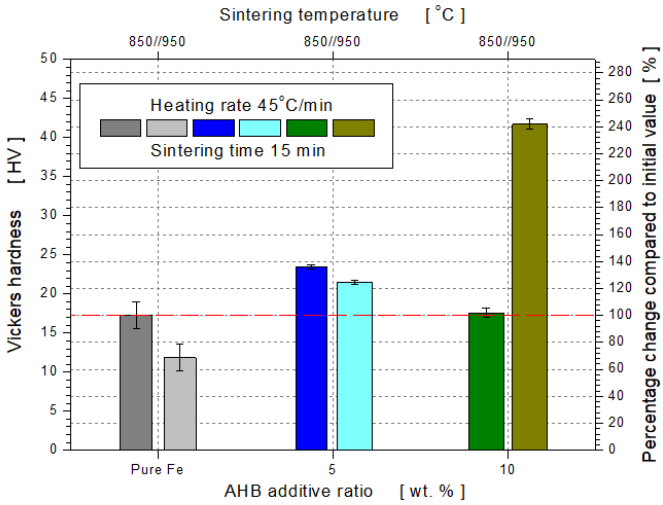

Figure 4. *Graph of the change in Vickers hardness values*

When the *S/N* ratio table (see Table 4) and graph (see Figure 3) are examined, it was determined that the most effective factor on Vickers hardness is the sintering temperature, which is the factor with the largest delta value. It was determined that the factor levels that optimized (maximized) the Vickers hardness value were 10% AHB additive ratio and 950ºC sintering temperature.

Table 4. *S/N ratio response table of Vickers hardness values of composites*

Level	AHB additive ratio	Sintering temperature
1	27.10	26.35
2	**29.07**	**29.81**
Delta	1.97	3.46
Rank	2	1

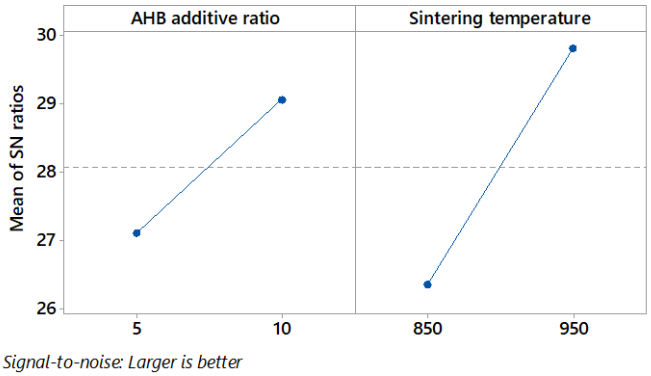

Figure 5. *Main effects plot of S/N ratios of Vickers hardness values of composites*

Because of the boron's low solubility in the iron lattice (approximately 500 parts per million), only minimal quantities are necessary to generate significant volumes of hard phases [12,13]. Additionally, boron enhances the hardenability of the iron matrix [16]. A review of past studies also shows that Fehmi and Mustafa's study [11] has similar results that boride phases formed in the inner structure considerably increase the hardness of iron-based composites.

3.3. Indentation modulus value

The Indentation modulus values of the materials are comparatively graphed in Figure 6, which was prepared using the experimental data obtained. When Figure 6 is examined, it is determined that the indentation modulus value of the composite material produced at 850ºC sintering temperature with 5 wt% AHB additive increased by 43.84% compared to the reference pure Fe material produced at 850ºC sintering temperature. It was also found that the modulus value of the composite material produced at 950ºC sintering temperature with 10% AHB additive increased by 144.11% compared to the reference pure Fe material.

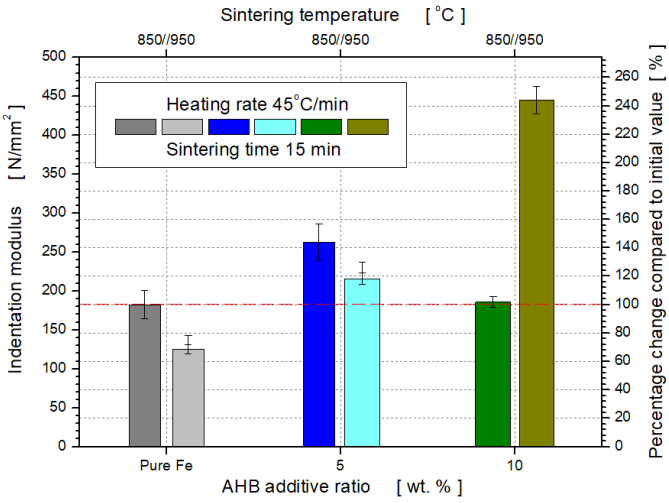

Figure 6. *Graph of the change in Indentation modulus values*

When the *S/N* ratio table (see Table 5) and graph (see Figure 7) are examined, it was determined that the most effective factor on Indentation modulus is the sintering temperature, which is the factor with the largest delta value. It was determined that the factor levels that optimized (maximized) the Indentation modulus value were 10% AHB additive ratio and 950ºC sintering temperature.

Table 5. *S/N ratio response table of Indentation modulus values of composites*

Level	AHB additive ratio	Sintering temperature
1	47.47	46.94
2	**49.53**	**50.05**
Delta	2.06	3.11
Rank	2	1

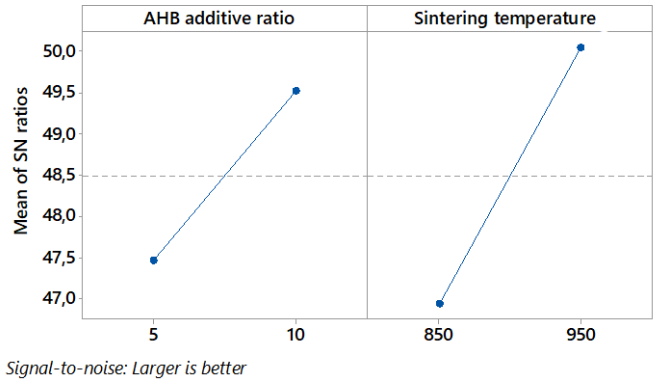

Figure 7. *Main effects plot of S/N ratios of Indentation modulus values of composites*

Calculations indicates that as the boron content increases, there is a heightened hybridization between B 2p and Fe 3d. Consequently, this strengthens the Fe-B bond, elevating both the elastic modulus and thermodynamic stability [12,17]. The rise in covalent bonding corresponds to a concurrent increase in hardness [12]. In their study also Lentz et al [12] also determined that; because of the strengthening of covalent bonding, the indentation hardness and indentation modulus of the Fe_3C phase can be improved significantly by increasing the B content in the $Fe_3(C,B)$ phase.

3.4. Qualitative examination

High wear and corrosion resistance is important to prevent a reduction in the mechanical resistance of equipment and economic loss of mechanical parts. As a result of the qualitative examination of all samples after storage during 12 months in a comfortable environment without daylight, it was observed that the anhydrous borax additive delayed the corrosion time of pure iron material (see Figure 8 and 9) Boron diffusion in the matrix controls the oxidation of Fe_2B boride [13]. Zheng Lva et al [13] also obtained a similar result that increasing boron concentration increases the oxidation resistance of pure iron.

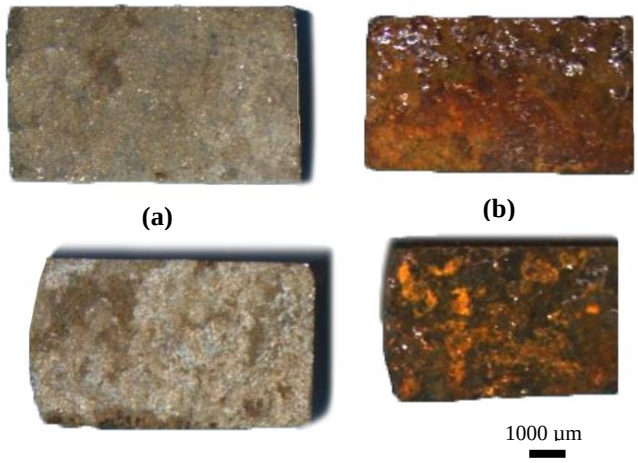

Figure 8. *Macro image of produced at 850ºC sintering temperature (a) Fe/AHB composite with 5% AHB additive and (b) pure Fe materials*

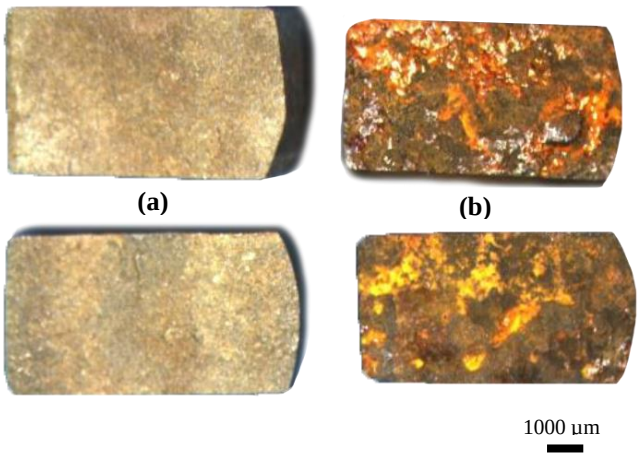

Figure 9. *Macro image of produced at 950ºC sintering temperature (a) Fe/AHB composite with 10% AHB additive and (b) pure Fe materials*

4. Conclusion

As a result of selected and/or preferred 2 control factors and their 2 levels as well as constant heating rate and constant sintering time parameters; Brinell hardness, Vickers hardness and indentation modulus were strongly affected by the AHB additive.

Comparing the pure Fe reference sample (850ºC) with 10% AHB added Fe composite sample prepared at 950ºC sintering temperature, the Fe/AHB composite sample with 10 wt.% additive showed the best results with 69.32%, 142.03% and 144.11% increase in Brinell hardness, Vickers hardness and indentation modulus, respectively.

The factors that optimize the Brinell hardness, Vickers hardness and indentation modulus together are the ratio of 10% SB additive and the sintering temperature of 950ºC.

As a result of the qualitative examination of all samples after storage during 12 months in a comfortable environment without daylight, it was observed that the anhydrous borax additive delayed the corrosion time of pure iron material.

In the future studies on the related subject, it is recommended to examine the effect of different levels of control factors and different constant heating rate, and constant sintering time parameters in addition to decreasing/increasing the particle size and/or additive ratios of anhydrous borax.

Acknowledgment

This study was prepared within the scope of the master's thesis titled "*Production of anhydrous borax added iron material by powder metallurgy and optimization of tribological and mechanical properties by experimental design method*" with the thesis number 651237 of the Council of Higher Education.

References

[1] Petersson, H., "Carbon Fiber Composite Materials in Modern Day Automotive Production Lines: A Case Study", Proceedings of the ASME 2013 International Mechanical Engineering Congress & Exposition IMECE2013, San Diego, California, USA, 2013.

[2] Reddy V. V., Mandava R. K., Rao V. R., Mandava S., "Optimization of dry sliding wear parameters of Al 7075 MMC's using Taguchi method", Materials Today: Proceedings, Vol 62, pp. 6684–6688, 2022

[3] Rana V., Kumar H., Kumar A., "Fabrication of hybrid metal matrix composites (HMMCs) –A review of comprehensive research studies", Materials Today: Proceedings, Vol 56 pp. 3102–3107, 2022

[4] Mangalgiri P.D., "Composite materials for aerospace applications", J. Bull. Mater. Sci. 22 (3) 657–664, 1999

[5] Seetharaman S., Subramanian J., Singh R. A., Wong W. L. E., Nai M. L. S., Gupta M., "Mechanical Properties of Sustainable Metal Matrix Composites:A Review on the Role of Green Reinforcements and Processing Methods", Technologies, https://doi.org/10.3390/technologies10010032, 2022

[6] Karacay E., "Production of boron carbide and its characterization", Gazi University, Institute of Science and Technology, Master Thesis, Ankara, Türkiye, 2008.

[7] Surappa M.K., "Microstructure evolution during solidification of DRMMCs (Discontinuously reinforced metal matrix composites): State of art", Journal of. Material Process Technology, vol 63 (1-3) pp. 325–333, 1997

[8] C. Xiang⁎, L. Yanxiang, "Effect of heat treatment on microstructure and mechanical properties of high boron white cast iron", Materials Science and Engineering A, A 528 pp. 770–775, 2010

[9] K.A. Taylor, S.S. Hansen, "The boron hardenability effect in thermomechanically processed, direct-quenched 0.2 Pct C steels, Metall". Trans. A. 21, pp. 1697–1708, 1990

[10] Inal M., Sahin S., ve Sahin Y., "Optimization of the Young's Modulus of Low Flow Polypropylene Talc/Colemanite Hybrid Composite Materials with Artificial Neural Networks", IFAC-PapersOnLine Volume 51, Issue 30, Pages 277-281, 2018

[11] F. Nair, and M. Hamamci, "Effect of In-Situ Synthesized Boride Phases on the Impact Behavior of Iron-Based Composites Reinforced by B4C Particles", Metals 2020, 10, 554; doi:10.3390/met10050554

[12] J. Lentz , A. Röttger, W. Theisen, "Hardness and modulus of Fe2B, Fe3(C,B), and Fe23(C,B)6 borides and carboborides in the Fe-C-B system", Materials Characterization 135, pp.192–202, 2018

[13] Z. Lva, H. Fub, J. Xinga, Z. Huanga, S. Maa, Y. Hua, "Influence of boron contents on oxidation behavior and the diffusion mechanism of Fe–B based alloys at 1073K

in air", Corrosion Science, Corros. Sci. 2016, http://dx.doi.org/10.1016/j.corsci.2016.03.002

[14] Bodur A., Sahin S., ve Sahin Y., Inal M., "Modelling of the Flexural Strength of Low Flow Polypropylene Talc/Colemanite Hybrid Composite Materials with Taguchi and ANFIS Methods", IFAC-PapersOnLine Volume 51, Issue 30, Pages 271-276, 2018

[15] Montealegre-Melendez I., Arévalo C., Ariza E., Pérez-Soriano E. M., Rubio-Escudero C., Kitzmantel M. and Neubauer E., "Analysis of the Microstructure and Mechanical Properties of Titanium-Based Composites Reinforced by Secondary Phases and B_4C Particles Produced via Direct Hot Pressing", Materials 2017, 10, 1240

[16] K.A. Taylor, S.S. Hansen, "The boron hardenability effect in thermomechanically processed, direct-quenched 0.2 Pct C steels", Metall. Trans. A. 21, 1697–1708, 1990

[17] O. Yu Gutina, N.I. Medvedeva, I.R. Shein, A.L. Ivanovskii, J.E. Medvedeva, "Electronic structure and magnetic properties of Fe_3C with 2p and 3p impurities", Phys. Status Solidi Basic Res. 246, 2167–2171, 2009

MANAS Journal of Engineering
ISSN 1694-7398 | e-ISSN 1694-7398

Volume 12, Issue 1, (2024) Pages 46-76
https://doi.org/10.51354/mjen.1264203

A review on effects of diethyl ether on cyclic variations in diesel engines

Ismet Sezer*,[1]

[1]Department of Mechanical Engineering, Gümüşhane University, Gümüşhane, Turkey, isezer@gumushane.edu.tr, ORCID: 0000-0001-7342-9172

ABSTRACT

Diethyl ether (DEE) can be used in diesel engines as a fuel or fuel additive. The review study was compiled from the findings of several studies in this area. The diverse techniques are employed to mitigate the detrimental pollutants emitted by diesel engines. The first approach to reducing emissions involves altering the fuel system and engine design to improve combustion, but this is an expensive and time–consuming process. The utilization of various exhaust gas devices, such as a particle filter and catalytic converter, is necessary for the second way. However, the engine performance could be negatively impacted by these tools. Additionally, these exhaust devices increases the vehicle and maintain costs. The use of different alternative fuels or fuel additives is the third way that reduces emissions while improving engine performance. The particulate matter (PM), smoke, and nitrogen oxides (NOx) are the main environmental pollutants released by diesel engines into the atmosphere. The decreasing PM and NOx emissions at the same time is practically very difficult. The majority of researches indicate that using alternative fuels, such as natural gas, biogas, and biodiesel, or blending additives with conventional or alternative fuels, is the best way to reduce emissions. However, the characteristics of the fuel have a significant influence on cycle variations, which have a significant impact on engine performance, fuel economy, and emissions. Therefore, it is very important that the results of studies on the impact of DEE on cyclic variation are evaluated together to practice applications and to guide future studies. As a result, the primary focus of this study is on the usage of DEE as a fuel or fuel additive with different diesel engine fuels. The aim of this review is to investigate, using the available knowledge in literature, how DEE affects cyclic variations.

ARTICLE INFO

Review article

Received: 13.03.2023

Accepted: 29.04.2024

Keywords:

Diesel engine, Fuel additives, Diethyl ether, Cyclic variations

**Corresponding author*

1. Introduction

Both automobiles and heavy–duty trucks frequently employ diesel engines [1]. These internal combustion engines exhibit dependability, durability, and great efficiency [2]. Unfortunately, the high emissions of diesel engines cause the problems since they release smoke, sulfur oxides (SOx), nitrogen oxides (NOx), particulate matter (PM), and total gaseous hydrocarbons (THC) [3, 4]. It is thought that switching from commercial fuels to alternative fuels derived from renewable resources will be the most effective strategy to minimize these emissions [5]. However, there are operational and technological constraints when employing renewable alternative fuels, and doing so will require extensive engine structural adjustments in order to replace fossil fuels [6]. The adjustments of engine construction are not necessary to lower emissions because fuel–side modification techniques like blending, emulsification, and oxygenation offer a simple solution. Enhancing fuel volatility, lowering fuel density, cutting fuel sulphur, reducing aromatic content, raising cetane number, and lowering fuel density can all be used to modify diesel fuel to lower exhaust emissions while maintaining engine performance. Diesel fuel containing oxygenates is one example of this [7]. The oxygenated fuels are thought to be the best option among alternative fuels. The emissions of diesel engines can be effectively reduced by using diethylene glycol dimethyl ether (DGM), dimethoxy methane (DMM), dimethyl ether (DME), methyl tertiary butyl ether (MTBE), dibutyl ether (DBE), dimethyl carbonate (DMC), methanol, ethanol, and diethyl ether (DEE) [8–9]. These oxygenated fuels can be utilized in their pure form, mixed with regular diesel fuel, or blended with other alternative fuels like biodiesel [10]. The reducing PM and other hazardous emissions from diesel engines is largely dependent on the oxygen content of the fuel's molecular structure. However, NOx emissions can change based on the engine's operating parameters; they can go up or down in

certain situations [11, 12]. Because DEE is both an oxygenated fuel and a cetane improver, it is especially well suited for diesel engines [13]. The purpose of this study is to investigate the use of DEE as a fuel or fuel additive in various diesel engine fuels. The engine's cyclic variations can be greatly altered by the fuel used, and this has a substantial impact on the engine's performance, fuel consumption, and exhaust pollutants. Thus, based on the literature, this review study examines how the addition of DEE affects the cyclic variations.

2. Properties of Diethyl Ether

As seen in Figure 1, diethyl ether (DEE) is the simplest ether expressed by its chemical formula $CH_3CH_2–O–CH_2CH_3$ ($C_4H_{10}O$), consisting of two ethyl groups bonded to a central oxygen atom. DEE is seen as a potential alternative fuel or oxygen additive for diesel engines due to its high oxygen content and cetane number. DEE is a liquid at ambient conditions, making it desirable fuel for storage and handling. As seen in Figure 2, DEE is thought to be a renewable fuel because it is made from ethanol through a dehydration process. DEE is also more advantageous than ethanol due to its higher heating value and noncorrosive nature [14].

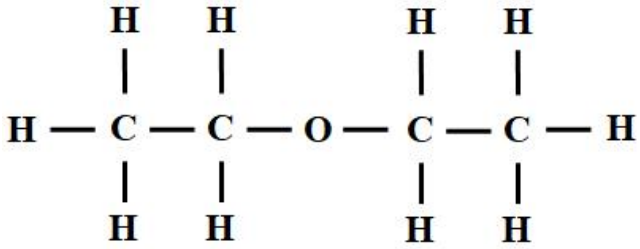

Figure 1. *Chemical composition of diethyl ether [3]*

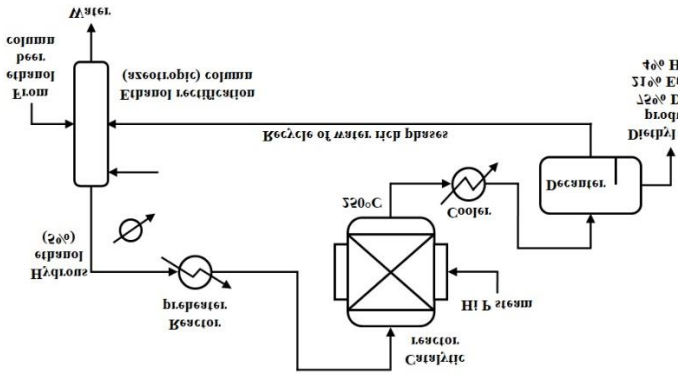

Figure 2. *Production of diethyl ether from ethanol [14]*

Excellent cetane number, appropriate energy density, high oxygen content, low auto ignition temperature, and high volatility are only a few advantageous of DEE, as seen in Table 1. Hence, whether applied as a pure or additive in diesel engines, it can help to increase engine performance and lower emissions and the problem of cold starting [14, 15].

Table 1. *Fuel properties of diesel fuel and DEE [15]*

Property	Diesel	DEE
Chemical formula	C_xH_y	$C_4H_{10}O$
Molecular weight	190–220	74
Density of liquid (kg/L)	~0.84	0.71
Viscosity at NTP* (cP)	2.6	0.23
Oxygen content (wt %)	–	21
Sulfur content (ppm)	~250	–
Boiling temperature (°C)	180–360	34.6
Autoignition temperature in air (°C)	315	160
Flammability limit in air (vol %)	0.6–6.5	1.9–9.5
Stoichiometric air–fuel ratio (AFR_s)	14.6	11.1
Heat of vaporization at NTP* (kJ/kg)	250	356
Lower heating value (MJ/kg)	42.5	33.9
Cetane number (CN)	40–55	125

3. Advantages and Drawbacks of Diethyl Ether

Table 1 lists the fuel properties for DEE along with its advantages and disadvantages. As DEE can be produced from ethanol by using acid catalysts to speed up the dehydration process, it meets the criteria for both biofuel and renewable fuel status. It is claimed that the dehydration of ethanol produces DEE in an inexpensive, consistent, and profitable manner. Furthermore, generating DEE is far less expensive than generating dimethyl ether (DME) [16, 17]. Since DEE is a liquid fuel at room temperature, it can be used as a fuel additive for diesel engines without requiring major modifications. DEE works well as a fuel additive without the need for a solvent because of its high miscibility with most diesel engine fuels. DEE can be utilized with petroleum fuels in internal combustion engines because of its high volatility and low flash point. DEE enhances atomization properties and makes it possible to deliver a consistent fuel–air mixture into the combustion chamber because of its low density and viscosity. Because of the high amount of oxygen in its chemical structure, DEE helps improve combustion, emissions, and engine performance. DEE has a high latent vaporization, which allows it to reduce intake air temperature and boost engine volumetric efficiency. Due in part to its low auto ignition temperature and improved low temperature characteristics, such as a higher cold filter plugging point (CFPP), DEE is an effective ignition enhancer. This facilitates smoother engine operation, particularly in colder climates. DEE increases combustion, engine efficiency, and most engine emissions because of its high cetane number and quick flame speed. However, because of its high volatility and propensity to oxidize and generate peroxides during storage, there are some worries about the influence of DEE on air pollution. To address these issues, antioxidant additives are needed. The high volatility of DEE also makes it difficult to maintain in storage. Another issue with DEE is its higher reactivity in air circumstances and its broader flammability limitations [14]. Because of its decreased calorific value, DEE can increase fuel consumption, particularly at high blending

ratios. The low density of DEE can also cause phase separation when it is added to other fuels. DEE's exceptionally low viscosity and lubricity can accelerate injection system wear, making it impossible to use DEE as the only sustainable fuel in diesel engines without changes. The combustion process may be delayed by DEE's lower viscosity, density, and bulk modules and its higher latent heat of vaporization may lessen the peak cylinder pressure and the heat release rate. In the fuel system, the high volatility of DEE might result in vapor lock. In particular, the inadequate fuel volatility and the insufficient fuel distribution among cylinders can result in auto–ignition, detonation, corrosion, and poor engine performance when DEE is utilized at high blending ratios.

4. Findings from Studies on Diethyl Ether

The number of studies was performed on the using DEE in diesel engines and a single cylinder direct injection experimental diesel engines generally were employed at the most of these studies. The parameters such as brake power, torque, engine efficiency, fuel consumption and the emissions of CO, HC, NOx, PM, smoke and CO_2 were monitored and analyzed to assess the impact of DEE on engine performance and emissions in the studies performed. It will be easier to correctly evaluate the results if these researches are categorized based on the fuel types. Accordingly, the studies on DEE can be listed as diesel– DEE blends [18–46], diesel–water–DEE blends [47], diesel–ethanol–DEE blends [48–58], diesel–ferric chloride ($FeCl_3$)–DEE blends [59], diesel–kerosene–DEE blends [60], diesel–acetylene gas–DEE blends [61–62], diesel–biogas–DEE blends [63], diesel–hydrogen–DEE blends [64], diesel–natural gas–DEE blends [65], diesel–toluene–DEE blends [66], biogas–DEE blends [67–68], liquefied petroleum gas (LPG)–DEE blends [69–70], ethanol–DEE blends [71–73], biodiesel–DEE blends [74–109], biodiesel–ethanol–DEE blends [110–111], biodiesel–water–DEE blends [112–113], biodiesel–biogas–DEE blends [114–115], diesel–biodiesel–DEE blends [70, 116–182], diesel–biodiesel–methanol/ethanol–DEE blends [183–187] and diesel–biodiesel–water–DEE blends [188–189]. Here is the summary of the main findings drawn from these studies. Sonawane et al. (2023) found that because DEE has the lower surface tension and dynamic viscosity than diesel, it created smaller droplets when added to the diesel fuel. The addition of DEE to diesel fuel also decreased the spray tip penetration because of the decreased density, surface tension, and viscosity. The addition of DEE aided to diesel the fuel vaporization by the reducing liquid penetration length. Compared to the 40% DEE (DEE40) addition, the 20% DEE (DEE20) addition to diesel demonstrated the higher number of droplets with smaller diameters. While DEE40 addition suggested better evaporation and atomization properties, DEE20 demonstrated greater atomization features. DEE20 caused a lot of smaller droplets to move more slowly, which reduced the axial droplet velocity. The significant changes in the droplet diameter caused by the superior evaporation characteristics of DEE40 produced the more fluctuations than DEE20 [18]. Patil and Thipse (2014) found that the adding DEE to diesel raised the cetane number, volatility, oxygen content, and boiling point while the reducing density, viscosity, and calorific value [19]. Rakopoulos et al. (2012) found that while the brake specific fuel consumption (BSFC) reduced with the DEE–diesel blends, the exhaust gas temperature (EGT) and the brake thermal efficiency (BTE) raised. Additionally, it was shown that while DEE–diesel blends reduced the emissions of smoke, NOx, and CO, they raised the HC emission [20]. Rakopoulos et al. (2013) found that the adding DEE to diesel resulted in a leaner fuel–air mixture, which reduced the maximum cylinder pressure and temperature, delayed the ignition timing, delayed the injection pressure, and reduced the heat losses [21]. Patil and Thipse (2016) found that the adding DEE to diesel raised BTE by 7.96% and NOx emissions by 3.66%, but reduced the emissions of smoke and HC by 12.5% and 15.38%, respectively [22]. Rathod and Darunde (2015) stated that DEE could be used in common rail direct injection (CDI) diesel engines without causing any problems because DEE–diesel blends showed the good performance close to pure diesel [23]. Karthik and Kumar (2016) found that the adding DEE to diesel raised BTE, with the exception of 20% DEE blending ratio. However, because DEE has a lower calorific value than diesel, DEE blends gave the higher fuel consumption than diesel. However, EGT and CO emission was reduced with the rising DEE ratio by the rising exhaust gas recirculation (EGR) while CO_2 emissions were raised [24]. According to Banapurmath et al. (2015), the rising DEE ratio gave a reduction in auto ignition temperature, an increase in latent heat of vaporization, and a greater cetane number. However, it also raised the peak cylinder pressure. The emissions of CO, HC, and smoke were reduced by raising the DEE ratio while BTE and NOx emissions were raised [25]. Lee and Kim (2017) found that although diesel–DEE blends had greater BSFC, the fuel conversion efficiency was equivalent and stable engine operation was achieved. Also, diesel–DEE blends reduced the emissions of HC, CO, and PM, but they raised NOx emissions [26]. Saravanan et al. (2012) found that diesel–DEE blends reduced the ignition delay (ID), combustion duration (CD), and BSFC while rising BTE. Diesel–DEE blends gave the lower NOx and PM emissions but higher CO and HC emissions [27]. Ibrahim (2016) found that the addition of DEE to diesel raised the maximum cylinder pressure and heat release rate (HRR) while decreasing CD. Despite the engine's acceptable stability, the coefficient of variation (COV) raised up to 15% DEE (DEE15) ratio. For DEE15 blend, BTE was raised by 7.2% while BSFC was reduced by 6.7% [28]. Likhitha et al. (2014) found that diesel–DEE blends raised BTE and reduced BSFC. When DEE ratio exceeded 15%, high knocking noises were noticed [29]. Kumar and Nagaprasad (2014) found that when EGR was raised and DEE additive delivered additional oxygen, BTE was raised and BSFC reduced. Also, addition of DEE and diesel particulate filter (DPF) reduced emissions of

CO, HC, NOx, and PM [30]. Balamurugan and Nalini (2016) found that addition of DEE to diesel raised BTE while lowering BSFC and smoke emissions by enhancing combustion [31]. Madhu et al. (2017) found that with 5% DEE (DEE5) blend, BTE and BSFC were raised by 19% and 11%, respectively. The addition of DEE raised CO and HC emissions while decreasing NOx and PM emissions [32]. Cinar et al. (2010) found that cycle–to–cycle changes were extremely small at 10% DEE (DEE10) premixed ratio. 40% premixed DEE (DEE40) ratio gave the audible knocking. EGT, NOx, and soot emissions were lowered up to 23.8%, 19.4%, and 76.1%, respectively. However, premixed DEE raised CO and HC emissions [33]. Yadav et al. (2018) found that when the compression ratio grew, BTE was raised and BSFC was reduced. However, when DEE ratio increased, BTE decreased and BSFC increased [34]. Uslu and Celik (2018) found that when DEE increased, BTE and BSFC decreased while EGT and the emissions of CO, HC, NOx, and smoke reduced. At 7.5% DEE ratio, the maximum increase in BTE was 8%, and at 10% DEE ratio, the maximum increase in BSFC was 10%. The emissions of CO and NOx were reduced to a maximum of 45% and 56% with 10% DEE. Smoke and HC emissions were down 31% and 28% with 7.5% DEE, respectively [35]. Sethi et al. (2020) found that addition of DEE raised the maximum cylinder pressure and temperature. For 15% DEE ratio, BTE increased by 27.1% and BSFC decreased by 15.8%. The inclusion of DEE resulted in an increase in CO_2 and NO emissions but a decrease in EGT, CO, and HC emissions [36]. Iranmanesh et al. (2008) found that adding of DEE decreased the calorific value of the blends and increased their volatility, which enhanced their cold starting ability. By adding DEE to diesel, brake power and BTE increased by 2% and 6.3%, respectively, and CO_2 emissions increased as well. ID, the peak cylinder pressure, BSFC, CO, HC, NOx, and smoke emissions all decreased [38]. Ayhan and Tunca (2018) found that when DEE was added to diesel, BTE increased but BSFC, torque, and brake power dropped. Additionally, there was a drop in emissions of CO, HC, and EGT. The use of DEE resulted in a 12% reduction in smoke and NO emissions [39]. Badajena et al. (2018) found that inclusion of DEE boosted energy conversion efficiency and BTE while decreasing BSFC by 15.8% and raising combustion temperature by 6.8% [40]. Agarwal et al. (2022) found that addition of DEE to diesel led to a minor rise in uncontrolled emissions, including formaldehyde, formic acid, sulfur dioxide, n–pentane, n–octane, and isobutene. Even so, these emissions were still quite low, and with a few little adjustments to equipment or fuel injection technique, they could be made even lower. With DEE blends, a reduced NOx emissions was obtained along with a slightly higher PM emission [42]. Jena et al. (2023) found that compared to conventional diesel combustion (CDC), partially premixed combustion (PPC) demonstrated higher BTE. In comparison to CDC mode, PPC mode had a higher peak cylinder pressure. In comparison to CDC mode, PPC mode had a larger heat release. In PPC mode, DEE–diesel blends showed higher BTE than diesel. At lower loads, 40% DEE addition produced a higher BTE than 20% DEE addition. At lower loads, PPC mode with diesel and DEE blends produced a lower BSFC than CDC mode. Emissions of CO and HC were greater in PPC mode than in CDC mode. In comparison to CDC mode, NOx emissions were 1.5–2 times greater in PPC mode. In PPC mode, DEE blends displayed somewhat more HC emissions than diesel at lower loads [43]. Sun et al. (2023) found that diesel engine running on 0.5% DEE premixed could start up rapidly at −10°C, but that as the ambient temperature dropped, the cold start performance of the engine gradually declined. Diesel was aided in igniting by DEE because the growing DEE ratio allowed the premixed DEE to burn at low intake temperatures. When 2% DEE was premixed, the engine started rapidly and steadily at a very low temperature of about −40°C. When DEE was premixed, lowering the starting fuel injection could cause detonations and speed variations. However, because of the advanced combustion phase, a reduction in the initial fuel supply led to extended speed–up duration during cold start. By delaying the primary injection timing to 2°CA ATDC (after top dead center) for 0.5% DEE premixing and 60% of the basic starting fuel injection quantity, the fastest start was accomplished [44]. According to Swamy et al. (2023), adding DEE increased peak pressure by 2.5% and 1.2% and BTE by 2.5% and 1% in comparison to adding ethanol and butanol. In comparison to ethanol and butanol addition, DEE reduced CO emission by 20% and 11%, HC emission by 17% and 12.2%, and smoke emission by 12.5% and 10.6%. However, DEE increased NOx emissions by 3.6% and 2.4%. Moreover, reductions of 26% and 24.4% in ID and 35.5% and 2.4% in CD were attained [45]. Fayyaz et al. (2023) found that addition of DEE alone increased BSFC by 29.9% compared to addition of manganese (Mn) to diesel. At lower loads, addition of 10% DEE increased torque by 5.4%, 15.4%, and 11.9%; at higher loads, the addition of 250, 375, and 500 mg Mn increased torque by 18.4%, 28.3%, and 23.9%. At lower load, DEE10 addition increased BTE by 4.2, 8.7, and 6.9%; at higher load, 250, 375, and 500 mg Mn increased BTE by 24.2, 28.2, and 26.9%. When 10% DEE was added at a lower load, BSFC decreased by 3.3, 6.8, and 5.7%; however, when 250, 375, and 500 mg of Mn were added at a greater load, BSFC increased by 10.6, 10, and 12.7%. When 10% DEE was added at lower load, CO_2 emissions increased by 11.6, 30.5, and 20.3%; when 250, 375, and 500 mg of Mn were added at higher load, CO_2 emissions increased by 18.4, 28.3, and 23.9%. It was declared that the optimal amounts of DEE and Mn were 10% and 375 mg, respectively [46]. Subramanian and Ramesh (2002) found that adding 10% DEE to water–diesel emulsion increased BTE by 1.9% and decreased CO, HC, NOx, and smoke emissions by 42.8%, 46.7%, and 14.8%, respectively. With addition of DEE, the ID, peak cylinder pressure, and maximum pressure rise rate decreased. The engine's performance was enhanced by the addition of DEE to the water–diesel emulsion, while having no negative impact on smoke or NOx emissions. But under high loads, the

emissions of CO and HC were more than those of diesel. Additionally, it was declared that DEE may be used to diesel engines as an additive to address the issues with water–diesel emulsions [47]. Iranmanesh (2013) found that addition of DEE enhanced the properties of diesel–ethanol blend, including distillation, boiling point, oxygen concentration, and ignition quality. DEE proved to be a potent co–solvent in the diesel–ethanol combination. Additionally, the diesel–ethanol blend's volatility increased, which enhanced its cold start capability. With addition of DEE, diesel–ethanol blend's density, viscosity, and heating value all decreased. The addition of DEE to diesel–ethanol blend also enhanced emissions and combustion, resulting in a simultaneous 36.6% reduction in smoke and NOx emissions. 8% DEE addition diesel–ethanol blend was the optimum for performance and emissions with the exception of smoke opacity in which 15% DEE gave the lowest smoke level. For 8% DEE, the minimum HRR, the lowest NOx emissions and the maximum BTE with the rising of a 5.6% were obtained at full load. Also, lowest CO and HC emissions were obtained at 8% DEE ratio [48]. Sudhakar and Sivaprakasam (2014) found that EGT, cylinder pressure, and HRR increased as DEE fumigation ratio with the diesel–ethanol blend increased. At 30% DEE fumigation ratio, there was a 13% increase in HRR. When compared to diesel at 30% DEE fumigation ratio, ID was shortened and cylinder pressure was increased by 3 bars [49]. Sudhakar and Sivaprakasam (2014) found that for 10, 20, and 30% DEE fumigation ratio with diesel–ethanol blend, BTE was increased by 29, 40, and 43% while smoke emission was decreased by 17, 31, and 32%. At high loads, CO and NOx emissions increased by 90% and 48%, respectively. At lower loads, there was 28% increase in HC emission; however, at greater loads, as the DEE fumigation ratio increased, minor fluctuations were recoded. At full load, heavy knocks were observed above the 30% DEE fumigation ratio [50]. Sudhakar and Sivaprakasam (2014) found that adding DEE to a diesel–15% ethanol blend boosted BTE by 15%. Applying EGR also modestly raised BTE. A higher DEE ratio resulted in a drop in ID. The fumigation ratios of 20 and 30% DEE reduced ID by roughly 3°CA. Applying EGR raised ID by roughly 2°CA once more, hence the ideal DEE fumigation ratio was 20% with up to 15% EGR. HRR and the maximum cylinder pressure were lowered by 4% when using 20% DEE fumigation ratio with EGR. The increasing DEE fumigation ratio raised NOx emissions by 49% and EGR reduced NOx emission by 51%. But, HC emission was increased by 33% at initial load and CO emission was increased by 65% at full load. Audible knocking occurred above 30% DEE fumigation ratio at full load [51]. Paul et al. (2015, 2017) found that 5% DEE ratio increased BTE, whereas 10% DEE ratio decreased it. The addition of ethanol to diesel DEE blends resulted in 15.9% increase in BTE and 14.3% decrease in brake specific energy consumption (BSEC). CO, HC, and PM emissions were lowered by 53.1%, 82.9%, and 91%, respectively, when diesel was mixed with 10% DEE and 10% ethanol [52, 53]. Lukhman et al. (2016) found that adding DEE to diesel–ethanol blends enhanced combustion, which increased BTE and decreased total fuel consumption (TFC) as well as CO, HC, NOx, and smoke emissions. The largest drop in TFC was 14%, and the maximum increase in BTE was 20%. CO, NOx, smoke, and CO_2 emissions decreased by 75%, 30%, 10%, and 20%, respectively [54]. Ashok and Saravanan (2007) found that adding DEE to ethanol–diesel blend decreased the ID, EGT, BSFC, maximum pressure rise rate, peak cylinder pressure, and PM emission. It caused 5.5% rise in BTE and 48.9% and 63.2% decrease in smoke and NOx emissions, respectively [55]. Temizer et al. (2022) found that adding ethanol or DEE to diesel decreased the maximum cylinder pressure by around 0.5–3.5%, HRR by approximately 2.3–6.2%, and NO emission by approximately 2–21%. Conversely, adding ethanol to diesel raised the turbulence kinetic energy (TKE) by 0.05%, but adding DEE to the ethanol–diesel blend decreased TKE by 2.7% [56]. Mohebbi et al. (2018) found that diesel–ethanol blends with 40% DEE addition increased the indicated mean effective pressure (IMEP) by 14% and decreased the maximum pressure rise rate by 33%. The higher DEE ratios caused more ID, which led in incomplete combustion and increased CO emission, but the high reactivity of DEE improved fuel oxidation and decreased HC emission. DEE's increased volatility and improved fuel–air mixing qualities enhanced combustion and decreased PM emissions [57]. It was determined by Kumar and Reddy (2015) that DEE addition to ethanol–diesel blends raised BTE and HC emission, while it reduced CO and CO_2 emissions [58]. Patnaik et al. (2017) found that adding $FeCl_3$ to diesel raised the peak pressure and temperature in the cylinder. $FeCl_3$ addition resulted in 8% rise in BTE as well as an increase in NO and CO_2 emissions. However, BSFC was decreased by 9%, and addition of $FeCl_3$ also decreased the emissions of smoke, HC, and CO. However, diesel–$FeCl_3$ blend with 15% DEE addition had the highest BTE, the lowest BSFC, and the lowest emissions of smoke, HC, CO, and CO_2 [59]. Patil and Thipse (2015) found that DEE was completely miscible in kerosene and diesel fuel. when the DEE ratio raised in diesel and kerosene blends, the oxygen content and cetane number raised while the density, kinematic viscosity, and calorific value decreased. Blends of DEE, kerosene, and diesel demonstrated superior performance in terms of BTE, BSFC, smoke emission at full load, and half load emissions. Additionally, they reported generally lower NO, nearly same CO, higher HC at full load, and lower HC at part load emissions [60]. Mahla et al. (2012) found that while diesel–acetylene gas dual fuel operation improved BTE and brake power without compromising BSFC up to a 20% DEE ratio, performance declined and engine knocking began afterwards. The addition of acetylene to diesel–DEE blends increased BTE and brake power while lowering EGT, BSFC and smoke emission. With 20% DEE, diesel–acetylene gas operation produced the highest BTE and lowest BSFC [61]. Raman and Kumar (2022) found that BTE increased by 1.7% at 80% load with diesel and acetylene gas dual fuel operation with 10% DEE. With 10% DEE and diesel–acetylene gas at

80% load, the emissions of HC, CO, NOx, and smoke were decreased by 27%, 45%, 22%, and 43%, respectively. For 10% DEE blend in dual fuel mode, the cylinder pressure, peak heat release rate, and ID were increased [62]. Mishra et al. (2024) found that in the diesel–biogas dual fuel mode with 5% DEE addition, HRR was delayed and the peak cylinder pressure was raised. In the case of a 0.8 kg/h biogas addition to diesel with 5% DEE at full load, BTE decreased by 12.7% and 5.2% while BSEC increased by 14.3% and 9%. When 5% DEE was added to diesel–biogas dual fuel low heat rejection engine, the emissions of CO and HC increased but smoke and NOx emissions decreased [63]. Barik et al. (2024) found that the best performance, combustion, and emissions were obtained with diesel, 20% DEE and H_2. For 20% DEE and H_2 with diesel at full load, CD and ID were reduced by 9% and 20.8%, respectively. In addition, at maximum load, 20% DEE and H_2 with diesel increased BTE by 0.6% and decreased BSFC by 3.7%. For 20% DEE and H_2 with diesel at full load, the emissions of HC and CO were lowered by 35% and 29.6%, whereas the emissions of NO and CO_2 were increased by 29.4% and 17.4% [64]. It was determined by Karabektas et al. (2014) that diesel–natural gas dual fuel operation had negative effect on the engine performance at low and medium loads while it improved the performance at high loads. The dual fuel operation gave lower NO emission at low and medium loads while it served the higher NO emission at high loads. The emissions of CO and HC were raised at low and medium loads while these emissions were reduced with dual fuel operation at high loads. However, the addition of DEE as pilot fuel in dual fuel mode reduced BSEC and raised BTE. Additionally, DEE addition reduced NO and CO emissions at all loads and the higher DEE addition also provided better performance and emissions compared to diesel–natural gas dual fuel operation [65]. It was determined by Ozer and Vural (2024) that the emissions were reduced with toluene and DEE addition to diesel and the reduction was continued with H_2, H_2+HHO and H_2+HHO+O_2 gas fuels addition to diesel–toluene–DEE blends. The addition of O_2 also increased the combustion efficiency and decreased the emissions. The addition of toluene improved BSEC by 1% while DEE addition increased BSEC by 0.75%. The increasing O_2 in the gas fuels with toluene or DEE reduced BSEC and the highest drop in BSEC was obtained with toluene mixtures. BTE was increased with adding gas fuels and highest increase in BTE was achieved with O_2 addition. The emissions of CO, HC and smoke were reduced with all tested blends and the highest reduction was obtained with highest O_2 addition. NOx emission was increased with all the fuel blends and the highest increase in NOx emission was gained with the highest amount of O_2. The use of H_2 reduced CO_2 emission, but the increase of O_2 raised CO_2 [66]. Sudheesh and Mallikarjuna (2010) found that using biogas in homogeneous charge compression ignition (HCCI) mode with DEE produced higher BTE at all loads. In comparison to biogas and diesel dual fuel operation and biogas spark ignition (SI) modes, BTE raised by 3.48 and 9.21% for biogas with DEE in HCCI mode, respectively. Additionally, for HCCI mode, there were very little emissions of NO and smoke, and less than 0.4% of CO. Comparing HCCI mode to biogas SI mode, HC emission was similarly reduced [67]. Mishra et al. (2023) found that port fuel injection method outperformed manifold injections in terms of BTE. Emissions of NOx and smoke were decreased by the manifold injections. By decreasing knock and somewhat lowering BTE, the rising biogas flow rate increased the maximum operational load limit [68]. Jothi et al. (2007) found that when compared to pure diesel, LPG–DEE blends decreased the cycle pressure, EGT, BTE, and NO emission by 23% and 65%, respectively, at full load. In comparison to diesel fuel, the highest reduction in smoke and PM emissions was 85% and 89%, respectively. Nonetheless, the LPG–DEE blends significantly increased the emissions of CO and HC [69]. Dora and Jothi (2019) found that as compared to diesel at 70% load, LPG–DEE operation decreased BTE by 26% and NOx emission by 30%. However, compared to diesel fuel, CO emissions from LPG–DEE blends were greater [70]. It was determined by Polat (2016) that HCCI combustion was achieved by even leaner mixtures with increasing DEE ratio, since DEE provided earlier combustion by acting as ignition improver. The peak cylinder pressure and BTE were increased with increasing inlet air temperature. The cylinder pressure, heat release rate and knocking tendency were increased with reducing fuel–air equivalence ratio (lambda) while BTE was decreased. 30% ethanol and 70% DEE blend gave the highest BTE. The increasing inlet air inlet temperature, lambda and DEE ratio reduced CO and HC emissions while almost zero NOx was obtained for all tested blends [71]. Prante et al. (2023) found that because DEE has a low boiling point and low viscosity, there can be some operational challenges when adding it. As a result, ethanol–DEE blends boosted BSFC while lowering brake power and BTE. But by modifying the fuel quantity and injection timing using a high pressure common rail injection system, DEE addition produced superior performance [72]. Mack et al. (2015) found that adding DTBP to ethanol–DEE blends affected the start of combustion more than adding DTBP to ethanol alone. For the earlier combustion timings, full combustion of ethanol was made possible by the addition of DTBP to ethanol–DEE blends; this was not possible for fuel blends of ethanol–DEE without DTBP [73]. It was determined by Subhash et al. (2023) that 5% DEE addition to biodiesel and biomix blend reduced the density about 0.3–0.6%, viscosity about 18.2–18.5%, flash point about 1.2–3.6%, acid value about 9.6–17.2%, iodine number about 11.9–12.2%, free fatty acid about 10.9–12.2% and heating value about 0.2–3.8%, while it raised the cetane number about 6.7–6.9% and oxidation stability about 19.1–35.2% [74]. According to Zapata–Mina et al. (2022), for the lambda between 2.1 and 2.2 the maximum BTE produced when 40% DEE and 60% fusel oil biodiesel blend were used; nevertheless, the performance of the HCCI engine was decreased as the DEE ratio increased. Using 80% DEE and 20% fusel oil biodiesel resulted in increased engine stability.

With an 80% DEE blend, there was an increase in exergy destruction between lambda 3.4 and 3.9. With 40% DEE and 80% DEE blends, the maximum and lowest exergy efficiency was achieved [75]. It was determined by Gurusamy et al. (2024) that addition of 8L/min hydrogen to intake manifold with Jatropha and Camphor oils increased BTE and the maximum BTE reached up to 33.7% at full load. Similarly, the maximum values of the cylinder peak pressure, heat release rate, exergy efficiency and sustainability index were 76.5 bar, 53.9 J/°CA, 43% and 1.73 with H_2 addition. The reductions in CO, HC, CO_2 and smoke emissions were noted with the rising NO emission. Further, 20% DEE addition to Jatropha and Camphor oils and 8L/min H_2 induction reduced BTE and a similar trend was noted in the emissions of CO, HC, NO and smoke. However, 10% DEE addition to Jatropha and Camphor oils with 8L/min H_2 resulted in increase in BTE and the maximum value of BTE was 34.2% [76]. Ergen (2024) found that adding DEE to biodiesel boosted BTE and engine output, but increased NO emissions as compared to diesel fuel. The optimal outcome was achieved with a 5% blend of DEE; this DEE ratio reduced NO emissions by 13% and boosted engine power by 5.7%. The combination of 10% EGR and 5% DEE–biodiesel blend produced the greatest results for engine performance and NO emission. In comparison to diesel, this combination decreased torque by 3% and NO emissions up to 70% [77]. It was determined by Raman and Roy (2023) that the maximum dissolution of expanded polystyrene (EPS) was 10 g/L in pure biodiesel and the biodiesel kinematic viscosity was raised by 23% for 10g/L EPS. The advances in EPS dissolution, performance and emissions were noted with DEE addition. The reduction in BSFC and increment in BTE was by 10% with only DEE addition while this was 7% for 10g/L EPS and DEE addition. 10% DEE and 10 g/L EPS addition reduced CO, HC and NOx with 22%, 38% and 1.25% and smoke also reduced while only EPS infusion significantly increased these emissions [78]. Kasiraman et al. (2011) found that at full load, 30% DEE blend produced a similar BTE and HRR to diesel fuel. Diesel had a BTE of 30.1% and 30% DEE blend of 29.7%. When 30% DEE was added to cashewnut shell oil biodiesel, the peak cylinder pressure and rate of maximum pressure rise raised, but ID and CD were lowered by 2°CA and smoke and NO emissions were reduced by 5% and 1.7%, respectively [79]. Pranesh et al. (2015) found that adding 25% DEE to cotton seed oil biodiesel boosted BTE by 6.6% and decreased CO, HC, and NOx emissions by 74%, 6.9%, and 45.7%, respectively [80]. Rakopoulos (2013) found that adding n–butanol and DEE to vegetable oil, or its biodiesel, enhanced engine performance and emissions without any solvent or stability issues during engine operation. The inclusion of DEE and n–butanol resulted in a decrease in BSFC and an increase in BTE. For every combination that was tested, the emissions of HC increased while the emissions of CO, NOx, and smoke decreased. Blends of DEE performed marginally better than blends of n–butanol [81]. Rakopoulos et al. (2016) found that although the cyclic variations were within acceptable limits, they were slightly larger for blends of n–butanol and DEE because of the higher ID. Because of the additional oxygen, the addition of n–butanol and DEE to cotton seed oil biodiesel decreased the emissions of smoke and NOx; nevertheless, the use of the n–butanol and DEE blends increased the emissions of HC while reducing CO emission [82]. Rakopoulos et al. (2014) found that adding ethanol, n–butanol, and DEE to cotton seed oil biodiesel resulted in delayed injection time, decreased ID and EGT, and increased cylinder pressure. The blends of ethanol, n–butanol, and DEE resulted in a decrease in CO, NOx, and smoke emissions but an increase in HC emissions. Additionally, adding ethanol, n–butanol, and DEE to cotton seed oil biodiesel enhanced BTE and BSFC [83]. It was determined by Krishna et al. (2014) that fuel consumption was reduced with rising DEE ratio from 5% to 25% from 56.09 g/min to 51 g/min compared to 55 g/min for karanja oil and 44 g/min for diesel. BTE was 26.73% for 25% DEE with karanja oil, 23.21% for karanja oil and 27.01% for diesel. CO emission was 0.045% for 25% DEE with karanja oil, 0.055% for karanja oil and 0.035% for diesel. NOx emission was 265 ppm for 25% DEE with karanja oil, 347 ppm for karanja oil and 488 ppm for diesel. HC emission was 27 ppm for 25% DEE with karanja oil, 44 ppm for karanja oil and 29 ppm for diesel [84]. It was determined by Singh and Sahni (2015) that DEE addition to biodiesel slightly reduced both BTE and BSFC at the same load condition [85]. Jawre and Lawankar (2014) found that as injection pressure increased, engine performance increased as well, and mixtures of biodiesel and DEE performed better than pure biodiesel. For 15% DEE blend, BTE was higher at 190 bars of injection pressure but decreased at 170 bars. Compared to 10% DEE blend, 5% DEE blend, and biodiesel, 15% DEE blend produced lower BSFC. At higher engine loads, smoke emission was reduced with all DEE blends [86]. Samraj et al. (2023) found that adding 15% DEE (DEE15) to light fraction waste cooking oil biodiesel produced the best outcomes in terms of emissions and performance. Compared to diesel at full load, the BSFC for DEE15 was higher by 28.9%, BTE was lower by 7.6%, and EGT was lower by 11.9%. When compared to diesel at full load, the emissions of HC, CO, and smoke were lower by 32.9%, 25%, and 29.4%, respectively, while NO emission were higher by 36% [87]. It was determined by Górski et al. (2020) that DEE addition to biodiesel reduced the viscosity, density and surface tension and improved low temperature properties of biodiesel. 10% and 30% DEE blends reduced viscosity by 53% and 82% and 30% DEE blend also reduced the density and surface tension up to 6% and 25%. The cold filter plugging point (CFPP) was improved by DEE addition and 30% DEE blend reduced CFPP up to −24°C. Hence, DEE blends seem valuable in coldest seasons. Linseed oil biodiesel showed the worse performance than diesel. However, these disadvantages could be reduced with DEE addition. The combustion of DEE blends was similar to diesel. 20% DEE blend reduced smoke emission to level of diesel fuel [88]. Rao and Reddi (2016) found that adding 15% DEE (DEE15) to mahua oil biodiesel

increased BTE and improved BSFC. At full load, the emissions were also significantly reduced by DEE15 [89]. According to Babu et al. (2012), adding 15% DEE (DEE15) to mahua oil biodiesel increased BTE and improved BSFC. At low and medium loads, the addition of DEE decreased NOx emissions; however, at high loads, DEE blends produced higher NOx emissions than diesel and lower NOx emissions than biodiesel. With the addition of DEE, there was a little decrease in smoke emissions and a reduction in NOx emissions of more than 10%. At full load, DEE15 decreased the smoke emission. At full load, DEE15 reduced CO emissions by 67%, however HC emissions grew steadily until 15% DEE ratio [90]. Sivalakshmi and Balusamy (2013) found that adding 5% DEE to neem oil biodiesel boosted HRR and peak cylinder pressure. Smoke and CO emissions decreased with all blends at all loads, however NOx and HC emissions increased when using DEE5 blend at maximum load. Additionally, BTE of 5% DEE blend was higher than biodiesel [91]. Senthil et al. (2015) found that adding ethanol, DME, and DEE to nerium oil biodiesel enhanced BTE at all loads. At all loads, the addition of DME, DEE, and ethanol resulted in reduced emissions of smoke and CO. When DME, DEE, and ethanol were added to nerium oil biodiesel at all loads, the levels of HC and NOx increased [92]. It was determined by Purushothaman and Nagarajan (2009) that the peak cylinder pressure and HRR were higher for orange oil–DEE blend than diesel–orange oil blend. BTE was higher by 3% and 1.2% for orange oil–DEE blend and orange oil–diesel blend than diesel. NOx emission was lower for orange oil–DEE blend and higher orange oil–diesel blend compared to diesel. CO emission was raised by 76% with orange oil–DEE blend and reduced by 7.6% for orange oil–diesel blend compared to diesel at full load. HC emission was higher for orange oil–DEE blend and lower for orange oil–diesel blend compared to diesel. Smoke emission was lower for orange oil–DEE blend and orange oil–diesel blends than diesel [93]. It was determined by Purushothaman and Nagarajan (2010) that 36 mg/s DEE addition gave the best combustion, performance and emission results. BTE was raised by 3% for 36 mg/s of DEE with orange oil compared to diesel at full load. The emissions of HC and CO were raised by 0.22 g/kWh and 8.8 g/kWh for 36 mg/s DEE with orange oil at low load and 0.01 g/kWh and 0.93 g/kWh at full load compared to diesel. The emissions of NOx and smoke were reduced by 8% and 4.7% at full load for 36 mg/s of DEE with orange oil compared to diesel. The peak cylinder pressure and heat release rate were higher by 7 bars and 15 J/°CA for 36 mg/s DEE with orange oil than diesel at full load [94]. Ali et al. (2009) found that as DEE ratio increased in palm oil biodiesel, the density and viscosity decreased. The inclusion of DEE enhanced the acid value and pour point as well, but the cloud point and energy content of the DEE–biodiesel blends did not significantly change. When compared to pure biodiesel at 8% DEE ratio, the reduction in heating value was 4.7% and the maximum pour point was 7°C [95]. Ali et al. (2014) found that besides a minor drop in energy content, adding ethanol, butanol, and DEE to palm oil biodiesel enhanced its acid value, density, viscosity, pour point, and cloud point. At a 5% DEE ratio, the pour point was reduced by a maximum of 5°C. The addition of 5% ethanol, butanol, and DEE resulted in a reduction of viscosity of 12%, 7%, and 16.5%. When compared to pure biodiesel, the addition of DEE, butanol, and ethanol to palm oil biodiesel also increased BSFC and brake power; the highest results were obtained with the addition of DEE [96]. It was determined by Kumar and Prasad (2014) that 30% DEE addition to palm oil biodiesel gave the best engine performance. However, 50% DEE blend was not tested, as the engine speed was fluctuated and temperature of engine reached to so high; hence engine cannot run by this blend [97]. Rajan et al. (2016) found that when DEE was added to pongamia oil biodiesel at full load, ID, maximum pressure rise rate, peak pressure, and HRR all decreased. At full load, BTE increased by 3.1% and 6.3% with 15% DEE blend and 3.7% less with diesel and 10% DEE blend and biodiesel, respectively. With 15% DEE blend, smoke and CO emissions were down 27% and 10%, respectively, although HC emissions were up when compared to diesel at full load. In addition, at full load, 15% DEE blend greatly decreased smoke and NO emissions by 32% as compared to biodiesel [98]. Górski et al. (2023) found that while the coefficient of variability of indicated mean effective pressure (COV of IMEP) for DEE blends did not surpass 4%, the increasing DEE ratio in rapeseed oil biodiesel led to excessive irregularity in engine operation when compared to diesel. Vapor locks, which resulted from DEE evaporating in the fuel line and stopping the fuel injector from operating, were the cause of the combustion degradation [99]. Lotko et al. (2018) found that the biodiesel–DEE blends characteristics were comparable to those of diesel. The viscosity, surface tension, and density of the rapeseed oil biodiesel were all decreased by the addition of DEE. Consequently, adding DEE to biodiesel could increase the fuel's quality and combustion. In comparison to pure biodiesel, the addition of DEE to the biodiesel decreased smoke output by 50% [100]. Smigins and Zakis (2020) found that adding DEE to rapeseed oil biodiesel decreased engine power by 6.2–17.3% and increased BSFC by 0.6–15.5% when compared to the biodiesel. All DEE blends showed the lower emissions of HC and NOx, but higher emissions of CO and CO_2 when compared to the biodiesel. With 20% and 30% DEE blends, NOx emissions were roughly 24% lower than that of the biodiesel [101]. Geo et al. (2010) found that BTE increased by 7.5% by using rubber seed oil biodiesel with 200g/h DEE injection into the intake air when instead of pure biodiesel, whereas it decreased by 4.7% when using diesel. When 200g/h DEE injection was used instead of biodiesel, smoke emission was decreased by 34.4%, although it was still 15% higher than that of diesel. The injection of DEE also decreased the emissions of CO and HC. When 200g/h DEE was injected instead of biodiesel, NOx emissions were decreased by 13.1%, although they were still greater 34.8% than that of diesel. In comparison to biodiesel, DEE injection increased the peak cylinder pressure

and pressure rise rate while lowering ID and CD [102]. Danesha and Manjunath (2016) found that while BTE was comparable to diesel, BSFC was decreased by adding DEE to simarouba glauca seed oil biodiesel. CO, HC, and NOx emissions decreased, while CO_2 emissions increased when DEE was added [103]. Górski et al. (2022) found that adding DEE to sunflower oil biodiesel improved atomization during injection into the combustion chamber and decreased the viscosity, density, and surface tension. The low temperature qualities were further enhanced by the inclusion of DEE, suggesting that the DEE blends might be used during the winter seasons. DEE inclusion lowered the flash points, ensuring the safety of transportation. When a sufficiently high concentration of DEE was added to the biodiesel, the combustion of DEE blends was comparable to that of diesel. Closer to diesel smoke levels were obtained with 30% DEE addition. DEE blends of HC and NOx emissions were comparable to those of diesel fuel [104]. Hariharan et al. (2013) found that the DEE blend of ID was longer 2.8°CA than that of diesel. By using 130 g/h DEE with tire pyrolysis oil biodiesel instead of diesel at full load, the peak cylinder pressure increased by 3 bars. BTE was decreased by 2.5 percent when DEE was added at full load instead of diesel. When utilizing of DEE blend instead of diesel, NOx emissions were decreased by 5%. In comparison to diesel, the DEE blend had 2%, 4.5%, and 38% more emissions of HC, CO, and smoke [105]. It was determined by Patil and Rao (2018) that engine performance of waste cooking oil biodiesel with 15% DEE and 10% EGR was comparable with diesel fuel. The rising EGR reduced BTE and NOx emission [106]. Devaraj et al. (2015) found that waste plastic pyrolysis oil (WPPO) has properties comparable to diesel and could therefore be used in diesel engines without modification. DEE addition to WPPO improved the fuel atomization and decreased viscosity, which improved BTE. 10% DEE produced a greater BTE than 5% DEE. At full load, BTE was greater than WPPO by 10% DEE. HRR and the peak cylinder pressure were lowered by the increasing DEE ratio. Diesel had less brake power than WPPO, and DEE blends had less brake power than WPPO. When DEE was added to WPPO biodiesel, the emissions of CO and NOx were reduced, but the emissions of HC were increased [107]. Kaimal and Vijayabalan (2016) found that when DEE ratio increased in waste plastic oil biodiesel, BTE decreased and BSEC increased. In comparison to diesel and biodiesel, DEE blends slowed down the combustion and decreased peak cylinder pressure and HRR. Additionally, adding DEE decreased smoke and NOx emissions by 25% and 29%, respectively at maximum load. CO emissions decreased with DEE blends but HC emissions increased. 15% DEE blend produced decreased emissions and improved combustion and performance [108]. Wiangkham et al. (2023) found that adding DEE to waste plastic oil biodiesel decreased the density, gravity, flash point, and viscosity while increasing their cetane index. At low loads, engine performance decreased with DEE blends at high loads by shortening ID. However, DEE addition produced earlier combustion; increased DEE ratio did not produce more advanced combustion. The amount of NOx emissions decreased at high loads with DEE addition, while the emissions of CO and HC remained relatively constant. It was declared that the best DEE ratio for the highest BTE and lowest NOx emission was between 10% and 14% [109]. Carvalho et al. (2020) found that BTE was consistent across all evaluated fuels and loads. In comparison to diesel, the biodiesel increased CO emissions by 20%, NOx emissions by 1%, and HC emissions by 1%. Because biodiesel with 20% ethanol has larger oxygen content and a lower cetane number, it also produces more NOx emissions. In comparison to biodesel and diesel, this combination also increased the emissions of CO and HC. The addition of DEE to the biodiesel–ethanol blend resulted in a 37% increase in HC emissions and 3–13% decrease in NOx and CO emissions, respectively. Additionally, BTE was increased at moderate and high loads using a biodiesel–ethanol blend with DEE addition [110]. Venu and Madhavan (2016) found that adding titanium oxide (TiO_2) or zirconium oxide (ZrO_2) improved combustion while producing the lower pollutants. In comparison to biodiesel–ethanol blend, the addition of TiO_2 increased NOx, HC, and smoke emissions while reducing BSFC and CO emission. In contrast, the addition of ZrO_2 increased BSFC and HC emissions while reducing CO, CO_2, and smoke emissions. Conversely, the addition of DEE increased HRR and the emissions of CO and HC while lowering BSFC and the emissions of NOx, and smoke. The simultaneous decrease in smoke and NOx showed how DEE affected low temperature combustion (LTC) [111]. Satyanarayanamurthy (2012) found that the water–DEE solution produced micro–explosions during combustion, which led to better diffused combustion and decrease in peak cylinder pressure. At full load, 15% water–DEE solution with biodiesel increased BTE by 2%. More than 20% water DEE infusion was required before the crank case oil dilution began. When water–DEE ratio increased from 5% to 15%, the amount of NO emissions was lowered by 500 ppm. HC emission produced by 15% water–DEE was nearly identical to that of pure diesel [112]. Sachuthananthan and Jeyachandran (2007) found that when compared to other blends and water–biodiesel emulsion, 15% DEE blend performed better and produced lower emissions. At full load, BTE was raised from 28.3% to 29% with 15% DEE blend. At full load, 15% DEE blend decreased CO emission from 0.175% to 0.1% and HC emissions from 75 ppm to 40 ppm. Diesel had smoke emission of 4.2 BSU (Bosch Smoke Units), biodiesel had 4.5 BSU, and water–biodiesel emulsion had 2.5 BSU. With 15% DEE blend; the emissions of smoke were decreased to 1.6 BSU. 10% DEE blend had NOx emission levels of 568 ppm, whereas 30% water–biodiesel emulsion had NOx emission levels of 651 ppm [113]. It was determined by Barik and Murugan (2016) that karanja oil biodiesel–biogas dual fuel operation with 4% DEE gave the better combustion, performance and emissions. 4% DEE injection raised BTE by 2.3% and reduced BSFC by 5.8%

compared to the dual fuel operation at full load. The emission of CO, HC and smoke were reduced by 12.2%, 10.6% and 5.7% with %4 DEE at full load. But, NO emission was higher 12.7% with %4 DEE compared to dual fuel operation; it was lower 10.9% than biodiesel at full load [114]. It was determined by Barik et al. (2017) that BTE was raised by 7.1% and BSFC was reduced 2.2% with karanja oil biodiesel–biogas dual fuel operation with DEE addition compared to biodiesel. The emissions of CO, HC and smoke were reduced by 42.2%, 39.5% and 42.8% at full load compared to diesel. But, NO emission was higher 7.6% than that of diesel, but it was 1.2% lower than that of biodiesel at full load [115]. Nanthagopal et al. (2019) found that all tested DEE blends had reduced the combustion characteristics. In comparison to pure diesel, the addition of DEE to the diesel–biodiesel blend increased BSFC by 12.5% and decreased BTE by 5.3%. The emissions of HC, CO, NOx, and CO_2 were reduced by 84%, 4.6%, 57%, and 5.2%, respectively with DEE blends at full load. With 12.5% DEE blend, smoke output increased to 80.1% [116]. Jeevanantham et al. (2019) found that adding 5% DEE to diesel–biodiesel blend increased BTE by 5.3% as compared to diesel. The addition of 5% DEE and 5% MTBE (Methyl tert–Butyl Ether) to the diesel–biodiesel blend decreased CO emissions by 8.1% and 14.8%, respectively. When added to a diesel–biodiesel blend, 10% MTBE and 10% DEE decreased NOx emissions by 8.8% and 32%, respectively, when compared to diesel at full load. With the addition of MTBE and DEE, the emissions of smoke and HC also decreased [117]. Dora and Jothi (2019) found that the addition of DEE to the diesel–biodiesel blend had no appreciable effect on engine performance. However, adding 2% DEE to blend of 80% diesel and 20% biodiesel resulted in an apparent drop in emissions. DEE blends shown a significant decrease in CO and NOx emissions [70]. It was determined by Prabakaran et al. (2022) that rising DEE ratio in diesel–biodiesel blends reduced calorific value, cetane number, viscosity and flash/fire point, but it increased density and cloud/pour point. Cetane values of DEE blends were higher than biodiesel, but cetane values were lower by 5.46%, 8.2% and 10.9% than diesel. HRR of 20, 30 and 40% biodiesel–diesel blends were lowered by 15.6%, 12.1% and 8.6% and this reduced the maximum cylinder pressure and temperature. Brake power of 40% biodiesel–diesel blends was similar to diesel, but it was lower 3.8% and 2.2% for 20% and 30% biodiesel–diesel blends. BTE of 40%, 30% and 20% biodiesel–diesel blends were lower 2%, 7.4%, and 11.3% than diesel. The emissions of CO and HC were reduced by 17–35% and 13–25% with DEE blends, while CO_2 emission was almost equal for all DEE blends. But, DEE blends emitted 11–19% more NOx emission than diesel [118]. Shinde and Yadav (2016) found that adding DEE to diesel–biodiesel blend increased the oxygen content and cetane number while decreasing the calorific value, density, and viscosity. DEE added to the diesel–biodiesel blend also enhanced BTE and BSFC with reduced emissions. DEE addition up to 15% ratio did not require any changes, but for improved performance and emissions, more than 15% DEE did [119]. It was determined by Pillai et al. (2023) that rising DEE addition to diesel–biodiesel blends improved BTE and BSFC with reduced the emissions of CO, HC, NOx and CO_2 [120]. Krishnamoorthi and Malayalamurthi (2017) found that when DEE was added to the diesel–biodiesel blend at full load for a CR of 17.5 and a number of nozzle holes of 5, BTE was higher by 4.3% and the NOx emission was decreased by 3.9%. The inclusion of DEE and increase in nozzle holes led to decrease in BSEC, HC, CO, and smoke emissions while increasing BTE and CO_2 emissions [121]. Kuberan and Alagumurthi (2017) found that adding DEE to diesel–biodiesel blend improved combustion, increasing BTE and lowering BSFC. When DEE was added, emissions of CO, HC, and NOx were also decreased [122]. It was determined by Chandirasekaran and Senthilkumar (2023) that smoke opacity was reduced by 14.3% and 3.6% for 5% DEE addition to diesel–biodiesel blend compared to pure diesel and biodiesel, besides improved engine performance [123]. According to research by Alruqi et al. (2023), at 220 bar injection pressure, 90% engine load, and 15% DEE addition to diesel–biodiesel blend, the maximum BTE and minimum BSFC were found to be 27.91% and 329g/kWh, respectively. Comparing 15% DEE blend to 20% biodiesel–80% diesel combination, BSFC was 13.54% lower. In comparison to 20% biodiesel–80% diesel blend, NOx emissions were likewise reduced with 5% DEE blend; however, they were higher with 15% DEE blend. In comparison to diesel, HC and CO emissions were likewise decreased by 29.65% and 6.89% using 15% DEE blend [124]. Ahmed et al. (2023) found that adding 20% DEE to diesel–animal fat biodiesel blend increased the cylinder pressure while lowering EGT. In comparison to blend of diesel and 20% biodiesel and diesel, 20% DEE addition produced BSFC that was 4.8% higher and 1.4% lower. In comparison to diesel, BSEC was greater for 20% DEE, 10% DEE, and 20% biodiesel–diesel blends by 1.93%, 8.5%, and 5.6%, respectively. In comparison to diesel, BTE was reduced by 7.1% and 9.3% with blends of 20% and 10% DEE, respectively. When comparing 20% DEE blend to diesel, the emissions of CO, HC, and NOx were decreased by 37.8%, 50.7%, and 4.18%, respectively. However, the emission of smoke increased by 20.8% [125]. It was determined by Gurusamy and Ponnusamy (2023) that DEE addition to diesel–campor fat biodiesel blend reduced the cylinder pressure and temperature, but hydrogen induction raised them. The rising hydrogen induction raised BTE, but rising DEE reduced BTE. The lowest CO emission was 0.111% for hydrogen induction without DEE, but it was reduced to 0.101% with 10% DEE addition then it raised by 20% DEE addition at full load. The lowest HC emission was 86 ppm for hydrogen induction without DEE, but it reduced by 10% DEE addition at all loads and it raised by 20% DEE addition. CO_2 emission was reduced with hydrogen induction, but it was higher by 10% DEE addition than 20% DEE addition. Smoke emission was lower with 10% DEE addition at full load than the other blends [126]. It was determined by

Kumar et al. (2015) that rising biodiesel ratio reduced performance. 90% diesel–10% cashew nut shell oil biodiesel blend gave closer performance to diesel, but 30% and higher biodiesel blends gave poor result. 20% biodiesel blend was the best and so it was blended with DEE at ratios of 5, 10 and 15%. 15% DEE blend gave the 26.5% of BTE which was close to that of diesel. 15% DEE blend emitted 1200 ppm of NOx while it was 1195 ppm for diesel, but 20% biodiesel blend emitted 1450 ppm of NOx. DEE addition reduced NOx up to 17% compared to 20% biodiesel blend. CO emission was also reduced by DEE addition. Smoke emission was 3.96, 3.38, 3.15 FSN (filter smoke number) for 20% biodiesel blend, 15% DEE blend and diesel [127]. It was determined by Kumar et al. (2017) that 80% diesel–20% cashew nut shell oil biodiesel blend reduced engine performance. BTE of 20% biodiesel blend was 27.52% while it was 29.73% for diesel. However, DEE addition to 20% biodiesel blend improved further BTE; it was 28.96% for 10% DEE blend which was very close to that of diesel. 20% biodiesel blend reduced smoke and CO_2 emissions, but it increased HC and NOx emissions. DEE addition to 20% biodiesel blend reduced HC, NOx and smoke emissions. HC emission was 30, 34, 29 and 23 ppm for diesel, 20% biodiesel, 10% DEE and 15% DEE. NOx emission was 1195, 1450, 1511, 1327, 1373 and 1200 ppm for diesel, 20% biodiesel, 30% biodiesel, 5% DEE, 10% DEE and 15% DEE. DEE addition to diesel–biodiesel blend also reduced NOx emission by 9.94% compared to 20% biodiesel blend. Smoke emission was 3.96, 3.38, 3.15 FSN for 20% biodiesel, 15% DEE and diesel [128]. Ganesha and Chethan (2016) found that the blend of 90% diesel and 10% cashew nut shell oil biodiesel had performance and combustion characteristics similar to that of diesel, with reduced emissions of CO and NOx. However, the addition of DEE increased the amount of HC emissions [129]. Pushparaj et al. (2014) found that cetane number, calorific value, sulphur level, and flash point of cashew nut shell oil biodiesel were superior to those of diesel. Density and viscosity of the diesel–biodiesel blend were enhanced by the addition of DEE. Compared to 20% biodiesel blend, 10% DEE blend decreased HC and NO emissions by 34.6% and 69.4% at full load. When using blend of 20% biodiesel and diesel, there was 17% reduction in smoke emission [130]. It was determined by Senthilkumar et al. (2023) that the higher total fuel consumption (TFC) was aroused with 90% diesel–10% cashew nut shell oil biodiesel blend than diesel for fuel injection pressure (FIP) of 190 bars. DEE addition to 10% biodiesel blend reduced TFC at FIP of 210 and 230 bars. DEE addition to 10% biodiesel blend also raised mechanical efficiency (ME) of 10% biodiesel blend by improving the combustion. The optimum results were obtained as TFC of 845 g/h and ME of 68.1% with 15% DEE (DEE15) blend at FIP 190 bar. 5% DEE (DEE5) blend also produced TFC of 915 g/h and ME of 71% at optimized FIP of 230 bars. The rising of FIP and DEE addition improved ME with a little increase in TFC for 10% biodiesel blend [131]. Senthilkumar and Murugesan (2023) found that combustion temperature and NOx emission were decreased by higher latent heat of vaporization and lower calorific value of DEE. At full load, 10% DEE addition to 90% diesel–10% cashew nut shell oil biodiesel blend resulted in a 71% reduction in NOx emissions. DEE burned more efficiently and produced less smoke because of its decreased density and viscosity. 8.2% less smoke was released under full load while using 10% DEE blend. At full load, 10% DEE blend enhanced BSEC and BTE and decreased CO and HC emissions [132]. Ahmad et al. (2023) found that, for all tested blends, BTE was less than that of diesel up to 3.3 kW. BTE greater with all blends except for 5% DBE (dibutyl ether) blend than diesel, which produced the best BTE above 30% at 4.24 kW. All tested blends exhibited reduction in NOx emission, with minimum value of 550 ppm. All blends exhibited reduction in HC emission, with a minimum value of 19.5 ppm. In comparison to diesel, 5% DEE blend increased BTE by 8.76% and decreased BSEC, BSFC, CO, and HC emissions by 8%, 2.6%, 15.7%, and 47.3% at 4.24 kW. Additionally, it resulted in notable drops in CO_2 and NOx emissions at all load [133]. According to Srihari et al. (2017), adding DEE to blend of 80% diesel–20% cotton seed oil biodiesel enhanced the density, cetane number, and auto ignition temperature. The maximum cylinder pressure was achieved with 3% DEE blend. Adding 3% DEE resulted in a significant decrease in emissions of HC, CO, and NOx. In comparison to the other blends, 3% DEE blend produced less smoke. DEE blends increased BTE and BSFC [134]. It was determined by Yesilyurt and Aydin (2020) that the rising DEE ratio in 20% diesel–80% cotton seed oil biodiesel blend increased ID and reduced the cylinder pressure and heat release rate. The rising DEE ratio also raised both BSFC and BSEC. 10% DEE blend reduced BTE by 17.39% while it raised BSFC by 29.15% compared to diesel. EGT of DEE blends was lower than diesel while it was higher than 20% biodiesel blend. DEE addition also reduced HC, smoke and NOx emissions up to 12.89, 4.12 and 8.84% compared to diesel. CO emission of 2.5% DEE and 5% DEE blends were lesser 31.86 and 32.29% than diesel while it was lower 21.79 and 22.47% than 20% biodiesel blend. CO_2 emission of diesel, 20% biodiesel, 2.5% DEE, 5% DEE, 7.5% DEE and 10% DEE blends were 400.97, 332.31, 282.44, 282.32, 336.84 and 380.63 g/kWh [135]. Karthick et al. (2014) found that BTE of all blends they tested increased as the load increased. The maximum BTE for blend containing 3% DEE at full load was 30.31%, which was 7.3% higher than diesel. When compression ratio (CR) was lowered, the emissions of smoke and NOx decreased. However, when diesel and jatropha oil biodiesel blends with DEE, the emissions of NOx increased and the emissions of smoke and NOx decreased. In terms of combustion, performance, and emissions, 3% DEE blend proved superior [136]. Satya et al. (2011) found that high injection pressure and a narrow nozzle hole enhanced engine performance and emissions. The addition of DEE to biodiesel blends containing 80% diesel and 20% jatropha oil biodiesel enhanced combustion and resulted in reduced emissions. 5% DEE blend reduced

emissions of BSFC and HC; while 15% DEE blend resulted in lower NOx emissions. The addition of DEE to the diesel–biodiesel blend resulted in reduced smoke opacity [137]. It was determined by Abraham and Thomas (2015) that all tested fuel blends gave best performance at CR of 18. The peak cylinder pressure of 80% diesel–20% jatropha oil biodiesel blend was lower due to the decreasing delay period. BTE of 20% biodiesel blend was higher than diesel due to the better combustion and its better lubricity. BSFC of the biodiesel was higher due to its lower calorific value. 20% biodiesel blend gave the higher mechanical efficiency due to the improved spray quality, high reaction activity and decreased heat loss due to the lower flame temperature. The emissions of CO and HC were reduced and CO_2 emission was raised with DEE addition to the diesel–biodiesel blend due to the complete combustion. NOx emission was raised with 20% biodiesel blend due to its high oxygen content and combustion temperature, while it was reduced with 5% DEE blend due to low cylinder temperature [138]. Firew et al. (2016) found that while engine power for 20% DEE blend was lower than that of diesel, it was higher than that of 80% diesel–20% jatropha oil biodiesel blend, and the other blends. At higher loads, BSFC of 10% DEE blend was lower than that of the other blends at lower loads, it was lowest for 20% DEE blend [139]. Prasad et al. (2012) found that using small nozzle hole and high injection pressure resulted in better engine performance and lower emissions. The blend of 80% diesel–20% jatropha oil with 5% DEE produced superior performance and reduced emissions. 10% DEE and 40% biodiesel blend resulted in reduced BSFC. Emissions of NOx and HC were reduced when 5% ethanol was blended with 40% biodiesel. The diesel–biodiesel blends with DEE addition had reduced NOx emissions and smoke opacity [140]. It was determined by Imtenan et al. (2015) that n–butanol and DEE addition to diesel–jatropha oil biodiesel reduced the density and viscosity of the biodiesel blends. 20% blend gave the higher cylinder pressure than diesel due to the higher cetane number, but n–butanol and DEE addition reduced the cylinder pressure due to the retarded combustion and the higher latent heat vaporization of n–butanol and DEE additives. 20% biodiesel blend gave 5.4% higher BSFC than diesel, while 10% n–butanol blend reduced 3.9% BSFC than 20% blend and 10% DEE addition to 20% blend reduced 6.8% BSFC than 20% biodiesel blend. 20% biodiesel blend gave 8.2% higher NO emission than diesel while 10% n–butanol and 10% DEE addition to 20% biodiesel blend gave 8.8% and 12% lower NO emission. 20% biodiesel blend reduced 27.5% CO emission than diesel. 5 and 10% n–butanol addition reduced CO emission by 23 and 30.7% than 20% biodiesel blend due to the higher oxygen content while 5 and 10% DEE addition to the biodiesel blend reduced 11 and 20.6% CO emission. 20% biodiesel blend reduced smoke opacity by 6.2% than diesel. 10% n–butanol and 10% DEE addition to the biodiesel blend reduced smoke emission by 27% and 38.5% than 20% biodiesel blend. 20% biodiesel blend reduced HC emission by 28% than diesel, but n–butanol and DEE blends increased HC emissions [141]. Rao and Chary (2018) found that adding DEE to blend of 80% diesel–20% jatropha oil biodiesel decreased the density, viscosity, and flash/fire point, but improved its energy content. EGT increased with load, and adding 3% DEE to the biodiesel blend produced the lowest EGT. As the load increased, BTE also increased. Diesel–biodiesel blend with 3% DEE was gave the highest BTE at full load. At full load, the BSFC was 3.32% lower with 6% blend of DEE [142]. It was determined by Varpe et al. (2020) that DEE was fully miscible in diesel and biodiesel. DEE addition to diesel–jatropha oil biodiesel raised the volatility, cetane number, and viscosity, while it reduced the density and calorific value of the blends. The higher CR and loads enhanced BTE and reduced BSFC for all tested blends. 20% biodiesel blend with 10% DEE addition improved the engine performance and emissions compared to the other blends. BTE was raised by 21.14% and BSFC reduced by 15.84% with 10% DEE addition to the diesel–biodiesel blend compared to diesel. Smoke emission was reduced by 54.62% and HC emission was raised by 42.12% with 10% DEE blend compared to diesel. NOx emission was also raised with all tested blends [143]. Biradar et al. (2011) found that adding DEE caused the injection timing to be delayed, whereas using blend of 80% diesel–20% karanja oil biodiesel caused it to advance. When DEE was added to the biodiesel blend, the injection time increased, ID decreased, and the peak HRR increased. With 10% DEE blend, BTE increased by 6%. The inclusion of DEE did not significantly alter CO and HC emissions. NOx emissions of 10% DEE blend were close to those of diesel, which were 717 ppm for 20% biodiesel blend and 662 ppm for diesel [144]. It was determined by Manickam et al. (2014) that the peak cylinder pressure and heat release rate were raised and ID was reduced with 10% DEE and 15% DEE blends compared to 80% diesel–20% karanja oil biodiesel blend at full load. 10% DEE blend reduced BSFC by 8.6% while 20% DEE blend raised BTE by 4.8%. 10% DEE and 15% DEE blends reduced CO emission by 27% and 14% compared to pure biodiesel. HC emission was raised by 24% and 8% for 10% DEE blend and 15% DEE blend compared to 20% biodiesel blend at full load. NO emission was reduced by 27% and 32% for 10% DEE and 15% DEE blends compared to diesel at full load, while smoke emission was raised by 14% and 10% for 10% DEE and 15% DEE blends compared to 20% biodiesel blend at full load [145]. Tudu et al. (2015) found that growing DEE ratio decreased ID and increased the peak cylinder pressure. At full load, the engine performance and emissions of 60% diesel–40% light fraction pyrolysis oil biodiesel blend were superior to those of the other blends when 4% DEE was added. With 4% DEE blend, BSFC was 6% lower than diesel at full load. When using 4% DEE blend instead of diesel at full load, NO emissions were 25% lower. The inclusion of DEE also decreased smoke emissions [146]. Nagdeote and Deshmukh (2012) found that adding ethanol to diesel–mahua oil biodiesel blends decreased the BSFC, but it was similar with

DEE addition. While the blends of ethanol and DEE had lower CO emissions than the biodiesel, they had greater HC emissions. When DEE was added to the biodiesel blend instead of ethanol, the emission of smoke was lowered further, but NOx emissions increased [147]. It was determined by Mallikarjun et al. (2013) that NOx emission was reduced by rising EGR, but engine performance was unsteady due to insufficient oxygen and thus CO and HC emissions were raised to high levels. Mahua oil biodiesel with 30% EGR gave the lowest NOx emission at full load, but HC and CO emissions were high at this EGR ratio. The biodiesel with 20% EGR gave low HC and CO emissions besides the rising BTE close to diesel. NOx emission was less than diesel at this EGR ratio. The emissions of CO, HC and PM with the biodiesel were raised with retarding injection timing. But, these emissions were still lower than that of diesel. Injection timing of 20.9°BTDC (before top dead center) gave the optimum results. DEE addition to 80% diesel–20% mahua oil biodiesel blend reduced NOx and the other emissions and also improved the engine performance [148]. Sudhakar and Sivaprakasam (2014) found that adding DEE to 80% diesel–20% mahua oil biodiesel blend decreased the viscosity while increasing the atomization of the fuel–air mixture. With addition of DEE to the biodiesel blend, ID and NOx emissions were also decreased. Blends containing DEE increased BTE and smoke output. At maximum load, DEE blends also had greater CO and HC emissions [149]. Vadivel et al. (2015) found that adding DEE to diesel–mustard oil biodiesel enhanced the BTE and BSFC. In comparison to diesel at full load, the emissions of CO, HC, NOx, and smoke were reduced by 30%, 20%, 28%, and 19% for 75% diesel–25% biodiesel blend with 5% DEE [150]. Akshatha et al. (2013) found that adding DEE to diesel–neem oil biodiesel blend enhanced the density, viscosity, and flash point. Blends of biodiesel did not significantly alter engine performance; however, adding DEE to the blends improved the emissions. When the injection pressure was increased to 290 bars, BTE of biodiesel blends increased by 3.5%, but it was still lower than that of diesel at 250 bars. With increasing injection pressure, all tested biodiesel and DEE blends showed significant reductions in CO and HC emissions [151]. It was determined by Kumar and Rao (2014) that DEE addition to 80% diesel–20% neem oil biodiesel blend raised BTE, while it reduced BSFC and emissions of CO, HC, NOx, CO_2 and smoke [152]. Shrivastava and Sungra (2018) found that adding DEE to diesel increased the emissions of HC but decreased the emissions of CO, NOx, and smoke. DEE addition to diesel, however, had a detrimental impact on performance; that is, it increased BSFC and decreased BTE. Conversely, when DEE was added to 85% diesel–15% neem oil biodiesel and 70% diesel–30% neem oil biodiesel, BSFC was decreased and BTE increased. When DEE was added to the biodiesel blends, the emissions of CO, NOx, and smoke were likewise decreased, but emissions of HC were increased [153]. Ibrahim (2018) found that, in comparison to diesel, diesel–neem oil biodiesel blend increased the minimum BSFC and decreased the maximum BTE by 8.1% and 6.8%, respectively. While adding 10% DEE to the biodiesel blend decreased BTE, adding 5% DEE to the biodiesel blend significantly increased engine performance at most loads. The start of combustion was unaffected significantly by any of tested fuels or blends; however, with higher loads, diesel had a longer CD and lower HRR than the other fuels and blends. The engine operating stability was largely unaffected by the addition of DEE to the biodiesel blend [154]. Ali et al. (2016) found that 80% diesel–20% nerium oil biodiesel decreased BTE. However, 80% diesel–20% nerium oil biodiesel blend with 15% DEE had closer BTE values to diesel. But, BSEC for 15% DEE blend was the same as diesel, but it was higher for 20% biodiesel blend. With the addition of DEE to the biodiesel blend, ID was shortened and HRR and peak cylinder pressure were decreased. With the addition of DEE to the biodiesel blend, emissions of NOx and smoke were reduced, while emissions of CO and HC increased [155]. It was determined by Annamalai et al. (2014) that the minimum pour point was –7°C for 6% DEE addition to diesel–palm oil biodiesel blend while it was 14°C for biodiesel. 6% DEE blend also reduced the viscosity, density, acid value, and heating value by 35%, 3.6%, 57% and 1% compared to biodiesel [156]. Ali et al. (2016) found that adding 8% DEE to 70% diesel–30% palm oil biodiesel blend decreased the viscosity, heating value, pour/cloud point, and temperature by 26.5%, 4%, 4°C, and 3°C in addition to lowering the density and acid value. The blend with 30% biodiesel had the lowest coefficient of variation (COV), and it increased as the DEE ratio increased [157]. Imtenan et al. (2014) found that adding DEE to diesel–palm oil biodiesel blends increased the brake power by 6.25%, reduced BSFC by 3.28%, and increased BTE by 4% when compared to 80% diesel–20% palm oil biodiesel blend. In addition to lowering NO and CO emissions, adding DEE to the biodiesel blend also increased HC emissions [158]. Imtenan et al. (2015) found that adding DEE to diesel–palm oil biodiesel blend decreased advanced combustion by increasing ID and decreased cylinder pressure and temperature because of the increased latent heat of evaporation. In comparison to 80% diesel–20% palm oil biodiesel blend with inclusion of DEE decreased CO and smoke emissions by 25% and 35.5%, respectively. When 10% DEE was added to the biodiesel blend, NO emission was similarly reduced by 20%; however, HC emission increased with DEE blends [159]. It was determined by Varaprasad and Rao (2017) that the lower DEE addition to diesel–palm oil biodiesel blends improved the more BTE. DEE addition to the biodiesel blends reduced the emissions as well. Hence, DEE could be used as a prospective additive in diesel engines [160]. Prasadarao et al. (2014) found that adding DEE to diesel–palm oil biodiesel blend increased BTE by 10.8% in addition to reducing BSFC, CO, NOx, and CO_2 emissions. The optimal blend for increasing performance and emissions was suggested to be 85% diesel, 15% biodiesel, and 5% DEE addition [161]. It was determined by Uslu (2020) that the best working parameters were determined as 5% DEE ratio, 6%

biodiesel ratio and 850 W loads. The best values of BTE, BSFC, NOx and smoke emissions were obtained as 30.73%, 824.59 g/kWh, 292.2 ppm and 68.91% for the optimum working parameters [162]. It was determined by Uslu and Aydın (2020) that the high biodiesel ratio in the diesel–palm oil biodiesel blend reduced CO and smoke emissions, but low biodiesel ratio raised BTE, reduced BSFC and the emissions of HC and NOx. Low DEE ratio in the diesel–palm oil biodiesel blend raised BTE, while it reduced BSFC and CO emission. High DEE ratio reduced NOx and smoke emissions. Middle DEE ratio gave the ideal EGT and HC emission. Early injection reduced the emissions of CO, HC and NOx, while the retarding injection improved EGT, BTE and smoke. The best BSFC was obtained at average injection timing. The best EGT and the emissions of HC and NOx were achieved at low load, while the best BTE, BSFC and CO emission was obtained at middle load. The high load gave the optimum values for only smoke emission [163]. It was determined by Hardiyanto and Prawoto (2023) that DEE addition to 65% diesel–35% palm oil biodiesel blend raised the engine power and BTE and reduced BSFC and the emissions compared to the 35% biodiesel blend. 4% DEE addition to the biodiesel blend raised BTE by 7.69% and reduced BSFC by 6.3% compared to BD35. DEE3 reduced CO by 1.82% compared to BD35 while it reduced by 8.25% compared to diesel. NOx emission for DEE4 was lower 53.48% than BD35 and it was less 48.88% than diesel. SO_2 for DEE4 was less 40.89% than BD35 and it was lower 71.17% than diesel [164]. Gurusamy and Subramanian (2023) found that benzyl alcohol and DEE premixing increased BTE by 4.5% and 8.75% in comparison to 50% diesel–50% pine oil biodiesel blend, but BSFC of biodiesel blend was lower. While NOx and smoke emissions were decreased, CO and HC emissions were increased when DEE and benzyl alcohol were premixed. When benzyl alcohol was premixed, the peak cylinder pressure and HRR increased; however, when DEE was premixed, they decreased [165]. Samuel et al. (2016) found that BTE was lower in all studied blends when compared to diesel, and that adding 15% DEE to the diesel–pongamia oil biodiesel blend resulted in BTE values that were closer to diesel. Diesel fuel produced the lowest BSFC values, and all tested blends raised BSFC at all loads. The biodiesel blend's addition of DEE decreased EGT as well as CO, NOx, and CO_2 emissions [166]. It was determined by Pugazhvadivu and Rajagopan (2009) that DEE addition to diesel–pongamia oil biodiesel blends reduced BTE and the emissions of NOx and smoke. 15% and 20% DEE blends was more beneficial for the reducing of NOx than 10% DEE blend [167]. Danesha and Manjunath (2016) found that at partial loads, 80% diesel–20% simarouba glauca seed oil biodiesel blend and 80% diesel–19% biodiesel with 1% DEE addition produced greater BTE than diesel. The addition of 0.5% and 1% DEE to the biodiesel blend produced nearly identical BSFC with diesel. At greater loads, the NOx emission for every tested blend was lower than that of diesel. All investigated blends had lower HC and CO emissions but higher CO_2 emissions [168]. Prabu et al. (2020) found that 90% diesel–10% soapnut oil biodiesel with 5% DEE had lower cylinder pressure and HRR than diesel, which resulted in smooth engine performance. 10% biodiesel and 5% DEE blend produced nearly identical BSFC with diesel. BTE was raised by 2.9% and NOx emission was reduced by 32.1% when DEE was added to biodiesel blend. However, adding DEE to the biodeiesel blend increased the emissions of CO and HC. It was determined that 10% biodiesel blend with 5% DEE was a good diesel replacement [169]. Muneeswaran and Thansekhar (2015) found that adding DEE to diesel–soybean oil biodiesel blends decreased ID, which in turn decreased the combustion temperature. When DEE was added to the biodiesel blends, the emissions of CO and NOx were decreased while the emissions of HC were increased. It was declared that reducing NOx emissions may be achieved by blending 70% diesel–30% biodiesel with DEE [170]. Navaneethakrishnan and Vasudevan (2015) found that adding DEE to 60% diesel–40% tamanu oil biodiesel increased BTE to 3.4 percent and BSFC to about the same as diesel. Adding DEE to the biodiesel blend decreased the cylinder pressure and all emissions, with the exception of NOx [171]. Raju et al. (2017) found that 80% diesel–20% tamarind seed oil biodiesel blend with 10% DEE increased BTE by 7.7% and decreased BSFC by 5.36% in comparison to diesel. The addition of DEE to the biodiesel blend increased NOx emissions while reducing CO, HC, and smoke emissions. At full load, the biodiesel blend with 10% DEE produced 43.85% less smoke than diesel. It was determined that blends containing 10% DEE and 20% biodiesel performed better and produced lower emissions than the other blends [172]. It was determined by Raju et al. (2020) that 12% addition to 80% diesel–20% tamarind seed oil biodiesel (BD20) blend raised the heat release rate and BTE by 8.88% and 4.22% compared to the 20% biodiesel. The emission of CO, HC, NOx and smoke for this blend were reduced by 10.68%, 33.33%, 10.33% and 27.72% compared to diesel at full load. It was declared that BD20 blend with 12% DEE was hopeful both experimentally and theoretically [173]. Tudu et al. (2016) and Murugan et al. (2017) found that increasing DEE ratio in 60% diesel–40% tyre derived pyrolysis oil biodiesel (BD40) decreased ID and increased cylinder pressure. When 4% DEE was added to the biodiesel blend, BSFC was 6% lower than that of diesel at full load. At maximum load, NO emission for this blend was 20% greater than that of BD40 and 25% lower than that of diesel. At full load, smoke emission of 3% and 4% DEE were 26% and 21% less than those of diesel and 39% and 34% less than those of BD40. Moreover, these DEE blends decreased CO emission [174–175]. It was determined by Padmanabhan et al. (2023) that BTE of 80% diesel–20% waste cooking oil biodiesel blend (BD20) with 20% DEE was higher 5.2% and BSFC was lower 15% than that of diesel. DEE blends also reduced the emissions of CO, HC and NOx emissions about 7–9%, 9% and 4.2–13.4%, respectively [176]. Krishnamoorthi and Natarajan (2015) found that when DEE mixes were used instead of diesel, BSFC and emissions

were reduced. The lowest emissions of HC, CO, NOx, and CO_2 were produced by 75% diesel–25% waste frying oil biodiesel (BD25) blend with 5% DEE [177]. It was determined by Dubey et al. (2023) that 65% diesel–35% waste soybean cooking oil biodiesel (BD35) blend with 10% DEE and 15% EGR was determined as an optimal. BSFC, BTE and the emissions of smoke, NOx, CO, and HC were obtained as 272 g/kWh, 31.47%, 18.94 HSU (Hartridge Smoke Unit), 91 ppm, 0.03% and 24 ppm at these optimal conditions [178]. Reddy et al. (2022) found that 80% diesel–20% waste plastic oil biodiesel (BD20) with 10% DEE increased BTE by 4.86% while improving cylinder pressure and HRR. Compared to diesel, BD20 blend with 10% DEE had emissions of CO, HC, and smoke that were reduced by 52%, 20.73%, and 15.49%, respectively [179]. Kotturi et al. (2023) found that adding DEE to 80% diesel–20% waste plastic oil biodiesel (BD20) decreased viscosity, which enhanced fuel mixture atomization and combustion efficiency. In comparison to BD20 and the other DEE blends, BD20 blend with 15% DEE produced better BTE. At high engine speeds, BSFC of DEE blends was more similar to diesel. The peak cylinder pressure and HRR were lowered by adding DEE to the BD20 blend. Additionally, it decreased CO and NOx emissions, but increased HC emissions [180]. More et al. (2020) found that 0.8% DEE addition to 80% diesel–20% used cooking oil biodiesel (BD20) blend increased BTE by 16.06% and decreased BSFC by 4.12%. In comparison to diesel, DEE blends decreased CO, HC, and NOx emissions by 20.41%, 34.69%, and 23.33%, respectively. Blends of DEE also decreased CO_2 emissions [181]. Senthil et al. (2015) found that adding 10% DEE to 80% eucalyptus oil–20% pongamia oil biodiesel (BD20) produced BTE values that were closer to those of diesel and significantly reduced BSEC, BSFC, and EGT at full load. Additionally, CO, HC, and smoke emissions of this blend were 30%, 10%, and 35.7% less than diesel at full load [182]. It was determined by Qi et al. (2011) that 5% DEE addition to 70% diesel–30% biodiesel (BD30) blend reduced BSFC compared to BD30 blend, while it was similar to that of BD30 blend for ethanol addition to BD30 blend. Ethanol or DEE addition to BD25 blend reduced smoke emission at higher loads. Ethanol blend raised the emissions of HC and NOx while DEE blend raised HC emission, but CO emission was lower for both ethanol and DEE blends. The peak cylinder pressure, pressure rise rate and heat release rate for DEE blend were similar to BD30 and higher than those of ethanol blend at low loads. The peak cylinder pressure, pressure rise rate and heat release rate for DEE blend were highest while they were lowest for BD30 blend at high loads. It was declared that DEE blend was better than those of ethanol and BD30 blends [183]. Roy et al. (2016) found that while CO and NOx emissions decreased, HC emissions increased following warm–up as opposed to cold start. Diesel–canola oil biodiesel blends increased NO emission relative to diesel, but they decreased CO and HC emissions. While the addition of DEE to diesel–biodiesel blend increased the emissions of HC, the addition of ethanol and DEE to the blends decreased the emissions of CO and NOx. There was no discernible increase in aldehyde emissions, and no blends produced any smoke after the warm–up period [184]. Carvalho et al. (2020) found that adding 10% ethanol to 80% diesel–20% biodiesel (BD20) blend decreased the maximum torque by 7.8% and 6.7% when compared to the diesel and BD20 blend. When ethanol was added to BD20 at low loads, CO and HC emissions increased in comparison to diesel and BD20 blend. The maximum engine torque was not significantly altered by adding 5% DEE to the diesel, biodiesel, and ethanol blend. At moderate and high loads, the addition of DEE reduced NOx and PM emissions by 71% when compared to diesel and BD20. Every tested blend of BTE was fairly close to each other, although the DEE blend produced the highest BTE at high loads [185]. It was determined by Venu and Madhavan (2017) that DEE addition to diesel–biodiesel–ethanol blend raised the peak heat release rate, BSFC and the emissions of HC, CO and CO_2 besides the reduction in peak pressure and the emissions of NOx and smoke. Alumina (Al_2O_3) addition to diesel–biodiesel–ethanol blend raised the emissions of NOx and smoke besides the reduction in the peak heat release rate, BSFC and the emissions of HC, CO and CO_2. Addition both Al_2O_3 and DEE resulted in higher particulate matter (PM) formation, but 5% DEE and 25 ppm Al_2O_3 addition reduced PM at higher loads. It was declared that 5% DEE and 25 ppm Al_2O_3 gave the better performance and emission characteristics [186]. It was determined by Venu and Madhavan (2017) that DEE addition to ethanol–biodiesel–diesel blend raised the combustion duration, cylinder pressure and BSFC with the reduced NOx, PM and smoke emissions. DEE addition to methanol–biodiesel–diesel blend raised PM, CO, CO_2 and smoke emissions with reduced combustion duration, cylinder pressure, heat release rate and BSFC. 5% DEE addition gave the higher cylinder pressure, heat release rate, EGT and NOx emission with reduced combustion duration and the emissions of HC, CO_2 and PM compared to 10% DEE addition. It was declared that 5% DEE addition to ethanol/methanol–biodiesel–diesel blends gave the better combustion, performance and emissions [187]. It was determined by Sathiyamoorthi et al. (2017) that DEE addition to nano emulsified 75% diesel–25% lemongrass oil biodiesel (BD25) blend with EGR reduced the emissions of NOx and smoke by 30.72% and 11.21% compared to BD25 blend. BTE and BSFC were raised by 2.4% and 10.8%, but the emissions of HC and CO were reduced by 18.18% and 33.31% for this fuel combination compared to BD25 blend. The cylinder pressure and heat release rate raised by 4.46% and 3.29% and ignition delay and combustion duration raised for this fuel combination compared to BD25 blend [188]. It was determined by Vellaiyan et al. (2023) that the optimum ratios for biodiesel, water and DEE were determined as 15.23%, 15% and 15%. BSFC, BTE, CO, HC, NOx and smoke values were obtained as 243.729g/kWh, 28.2358%, 31.0326ppm, 0.09248%, 717.542 ppm and 17.5861% at this optimum blending ratios [189]. The effects of DEE on the fuel

properties, injection, combustion, performance and emissions characteristics were also reviewed in details by Sezer (2018, 2019, 2020) [190–196].

5. Effects of Diethyl Ether on Cyclic Variations

The coefficient of variation (COV) of the indicated mean effective pressure (IMEP) is used to assess the stability of engine. The cycle to cycle variations are observed when cylinder pressure is measured over multiple thermodynamic cycles without interruption. The cycle to cycle pressure variation is mainly a result of variations in the combustion process from cycle to cycle [197]. The COV of IMEP is a significant indicator of the cyclic variability that may be computed from recorded cylinder pressure data. It is computed as follows [198, 199]:

$$\mathrm{COV} = \frac{\sigma_{\mathrm{IMEP}}}{\overline{\mathrm{IMEP}}} x100 \quad (1)$$

Where, $\overline{\mathrm{IMEP}}$ is the average indicated mean effective pressure calculated for a number of cycles N, while σ_{IMEP} is the standard deviation in IMEP. These parameters are calculated as follow [198, 198]:

$$\overline{\mathrm{IMEP}} = \sum_{i=1}^{i=N} \mathrm{IMEP(i)} / \mathrm{N} \quad (2)$$

$$\sigma_{\mathrm{IMEP}} = \sqrt{\frac{1}{\mathrm{N}-1} \sum_{i=1}^{i=N} \left(\mathrm{IMEP(i)} - \overline{\mathrm{IMEP}}\right)^2} \quad (3)$$

Heywood [197] declared that engine stability was negatively impacted when COV exceeded 10%. However, other studies declared that engine stability started to deteriorate when COV increased beyond 5% [199].

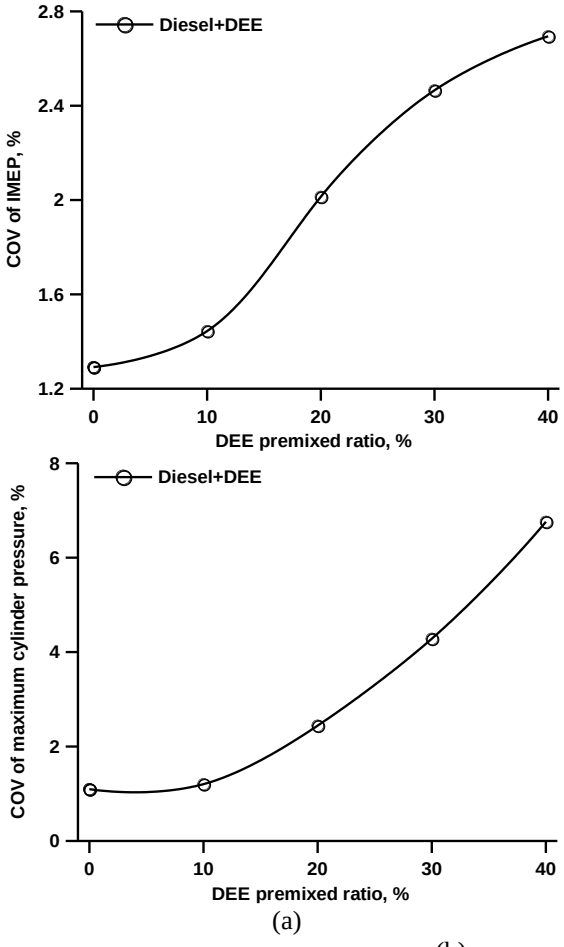

(a) (b)

Figure 3. *Variation of a) COV of IMEP and b) COV of maximum cylinder pressure (p_{max}) with DEE premixed ratio [31]*

The effects of the DEE premixed ratio on the cyclic variation of 50 consecutive cycles are displayed in Figures 3(a) and (b). The cyclic variation usually affected by knocking and combustion instability when considering the operating limits of engine. It is declared that DEE premixed ratio was limited to 40%, since audible knocking was observed during the tests. The cyclic variations for diesel fuel and 10% DEE premixed ratio were quite small as seen from Figures 3(a) and (b). The cyclic variations started to come into sight at 20% DEE premixed ratio. The difference in the maximum cylinder pressures of each cycle increased continuously as DEE premixed ratio was raised. The values of COV of IMEP shown in Figure 3(a) were determined as 1.29, 1.44 and 2.01 for diesel, 10% and 20% DEE premixed ratios, respectively. The COV of P_{max} shown in Figure 3(b) was also determined as 1.08, 1.2 and 2.44 for diesel, 10% and 20% DEE premixed ratios, respectively. During the high premixed DEE ratio, rapid combustion of the bulk premixed fuel occurred, leading to excessive heat release rate which caused unstable ignition timing. The knocking combustion is clearly observed from pressure oscillations especially during 30% and 40% DEE

premixed ratio. The cyclic variation was excessive with 40% DEE premixed ratio, with the fluctuation of the maximum cylinder pressure, ignition timing and crank angle related to the highest cylinder pressure. The COV of IMEP was 2.4 and 2.6 while the COV of p_{max} was 4.2 and 6.7 at 30% and 40% DEE premixed ratios. The higher premixed fuel ratio can lead to fuel film formation on the intake manifold walls and the head of the intake valve in external homogeneous charge formation with port type fuel injection. Hence, the trapped homogeneous charge in the cylinder at the intake valve closure can show variations from cycle to cycle. The rising intake charge temperature leads to the increased vaporization of premixed fuels and decreased formation of fuel films on the intake manifold wall. It can be concluded that controlling the intake charge temperature during the homogeneous charge formation can provide stable engine operation. It can reduce the ignition delay caused from intake charge cooling. The combustion temperature can be also increased by heating the intake charge. It can reduce the ignition delay caused from intake charge cooling and promotes the chemical reaction rate. In consequence, stable ignition and engine running can be achieved. The application of EGR can reduce cylinder pressure rise rate for higher premixed DEE ratio. Hence, it can be used for the engine knocking controlling [31].

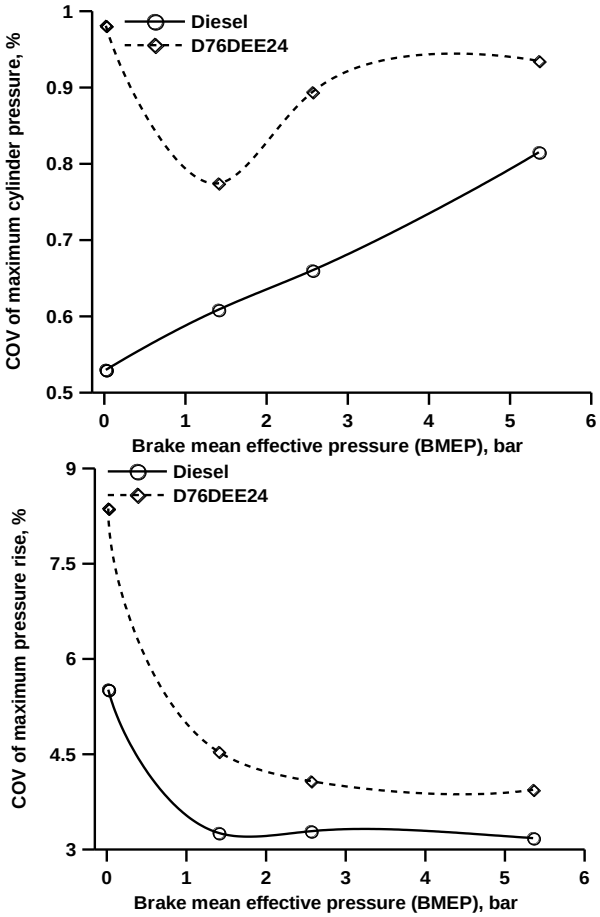

(a) (b)

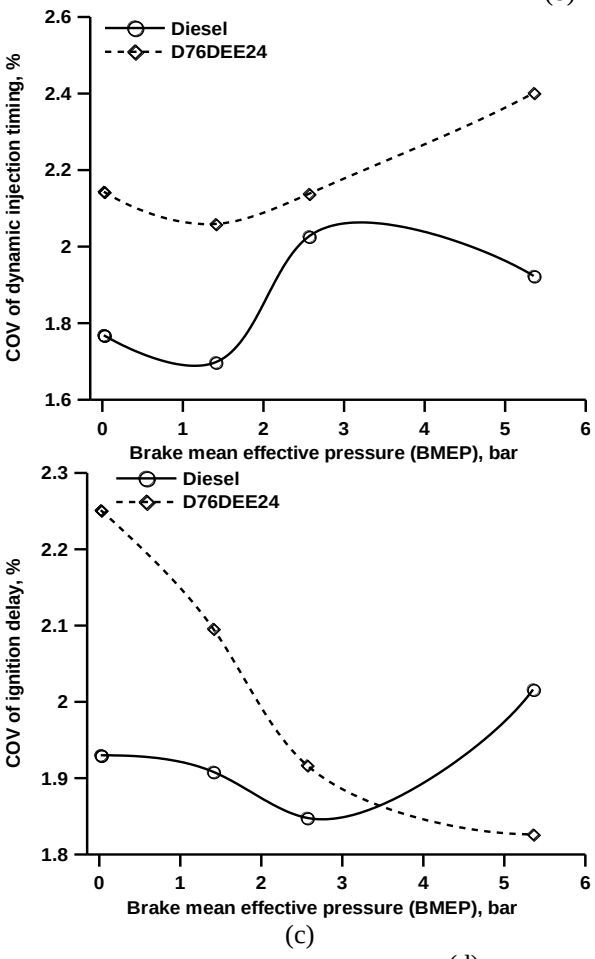

(c) (d)

Figure 4. *Variation the COV of a) maximum cylinder pressure, b) maximum pressure rise, c) dynamic injection timing and d) ignition delay with BMEP for diesel–DEE blend [74]*

Figure 4(a) and (b) demonstrate the COV of the maximum cylinder pressure and maximum pressure rise with brake mean effective pressure (BMEP) for pure diesel and the blend of 24% DEE with diesel fuel (D76DEE24), respectively. Figure 4(c) and (d) indicate the COV of dynamic injection timing and ignition delay, respectively. From Figure 4(a)–(d), it could be concluded that the addition of DEE up to 24% blending ratio did not significantly change cyclic variability when compared to diesel fuel, which was already small. It was declared that the analysis of the results from the figures show that neither the injection process nor the DEE ratio in diesel–DEE blend had any adverse effect on the observed cyclic variations. It was assessed from the results that the engine would not have an unstable operation for up to a 24% DEE addition [74].

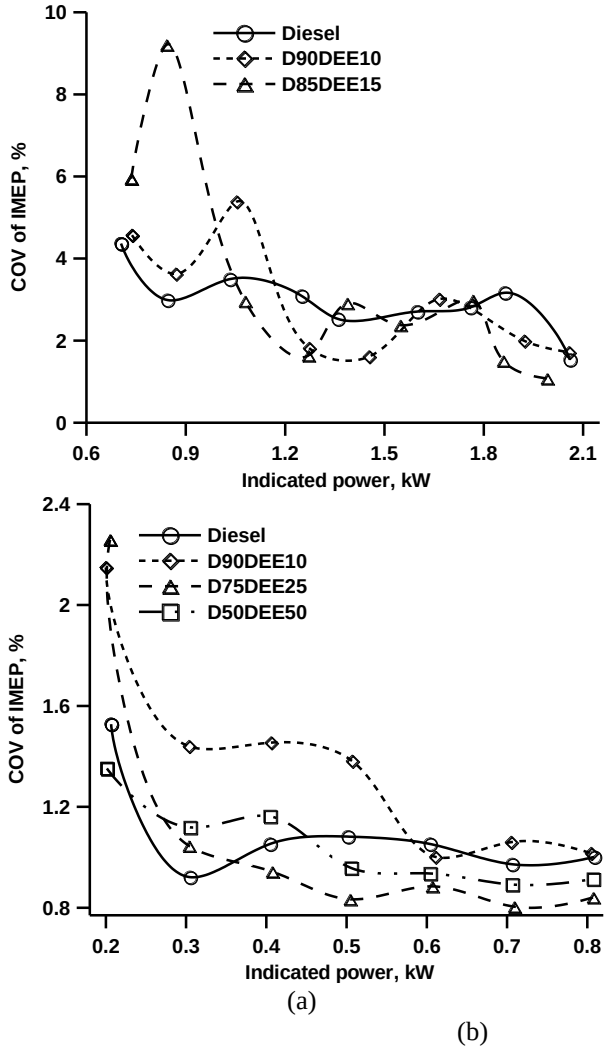

Figure. 5. *Variation the COV of IMEP for diesel fuel and various diesel–DEE blends with indicated power a) [26] and b) [24]*

Figure 5(a) shows COV of IMEP by the indicated power for tested fuels. It was stated that values of COV of IMEP were computed for five thermodynamic cycles. As seen from Figure 5(a), the values of COV are usually higher at the lower engine loads compared to higher loads especially for D85DEE15 blend. It was stated that this was because the engine was operated with the leaner fuel–air mixture during lower load operation and the operating of the engine with leaner fuel–air mixtures can raise the engine cyclic variations. It was determined that COV of IMEP values are below 5% for the most of engine loads especially at higher engine loads for all tested fuels. However, average COV of IMEP values raised slightly when DEE blends were used compared to diesel fuel. It was determined that average COV of IMEP for diesel, D90DEE10 and D85DEE15 was 2.85%, 2.98%, and 3.391%, respectively. It was stated that rising DEE ratio increased the amount of the fuel vapor bubbles due to high volatility of DEE causing vapor lock, which decreased engine stability and increased COV of IMEP [26]. Figure 5(b) indicates the COV of IMEP averaged over 200 engine cycles. Commonly, 5% COV of IMEP value is considered a cutoff that determines combustion stability. The COV of IMEP values were comparable and were less than 2.5% for all tested fuels under all engine loads, which pointed out very much stable combustion. As the engine load increased, the combustion stability also raised, showing the lower COV of IMEP values. This was because the quantity of injected fuel increased by rising engine load, which assisted the formation of the local fuel–rich region in the combustion chamber [24].

Figure 6 shows the COV of IMEP values for diesel, biodiesel (BD), and biodiesel–DEE blends including up to 40% DEE. The COV of IMEP values are about two/three times higher for DEE30 and DEE40 blends than that of diesel fuel. The results demonstrated that the combustion process of the biodiesel blend containing large amounts of DEE was more unstable. Such an engine operation presented the appropriate torque, but its uniformity of operation was also worse than that of diesel fuel. It was stated that the reason for higher variability of combustion process of biodiesel–DEE blends was sourced from disturbance of the fuel injection process. It was determined that the average value of IMEP was 0.648 bar for the cycle no of 70 while it is 0.731 bar for the cycle no of 71 when the engine was operated under 100 Nm and 1200 rpm operating conditions when engine fuelled with DEE40 blend. It was stated that lower IMEP was caused by a disorder in the fuel injection process. It was assumed that cause of failure in the fuel injector work was vapor lock formed in the fuel system caused by the evaporation of volatile DEE and it was also the reason for the difficult start–up of the engine fueled with biodiesel and large DEE ratio. The analysis of the results revealed that the variation in the combustion process depended on the variability of diesel fuel, biodiesel fuel, and biodiesel–DEE blends including up to 20% DEE ratio. In these cases, COV of IMEP did not exceed 4%. Moreover, it became obvious that COV of IMEP was raised with the higher DEE ratio in the biodiesel–DEE blends. Thus, the values of COV of IMEP for 30 and 40% of DEE with biodiesel were three times higher than those of diesel fuel. The results indicated that raised DEE into biodiesel is disadvantageous as it leaded to excessive roughness in engine operation compared to diesel fuel. The observed deterioration of the combustion process is caused by vapor locks, which were formed due to evaporation of volatile DEE in the fuel line, leading to the interrupted operation of fuel injector [97].

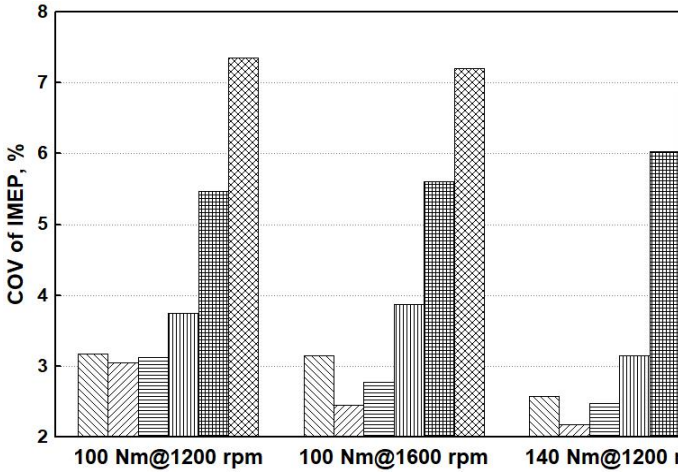

Figure 6. *Variation the COV of IMEP for diesel, biodiesel and biodiesel–DEE blends [97]*

Figure 7(a) shows the comparison of COV of IMEP determined from over a 200 consecutive cycles for all tested fuels. It is seen from Figure 7(a) that the variation in COV of IMEP was reduced by the rising number of cycles. This tendency indicated that the increase in the number of cycles was reduced the effects of cyclic variability in the averaged IMEP pressure data. Moreover, COV of IMEP tends to be constant with less than 1% error when the cycle number is more than 150 for all tested fuels. Therefore, 200 cycles was assumed sufficient to examine the engine cyclic variations. Figure 7(b) shows the effect of rising DEE ratio on COV of IMEP for BD30 blend. As seen from Figure 7(b) that COV of IMEP was lower for BD30 blend without DEE additive and increases with rising DEE ratio. This observation was due to effect of different chemical compositions, low flash point and high volatility of DEE on combustion process of the mixture which leaded to developed more engine cyclic variations [154]. Figure 7(c) indicates the variation of COV of IMEP with load for tall tested fuels. As seen from Figure 7(c) that COV of IMEP was lower than 5% for most of engine operating conditions. Therefore, it could be stated that adding DEE up to 10% into diesel–biodiesel blend did not negatively affect engine stability. Figure 7(c) also indicates that COV of IMEP generally reduced with the rising of load showing better engine stability. That could be explained as the engine consumed the richer air–fuel mixture at higher loads. The reducing the air–fuel ratio could decrease engine cyclic variations. The COV of IMEP for diesel fuel was determined about 3% for most of engine loads as seen in Figure 7(c). That could be considered slightly higher compared to other diesel engines because the air flow rate was measured using an orifice meter which was the flow restriction device which could induce relatively higher fluctuations in inlet pressure and air flow rate. However, COV of IMEP could change much from engine to engine according to engine specifications, operating conditions and fuel properties [152].

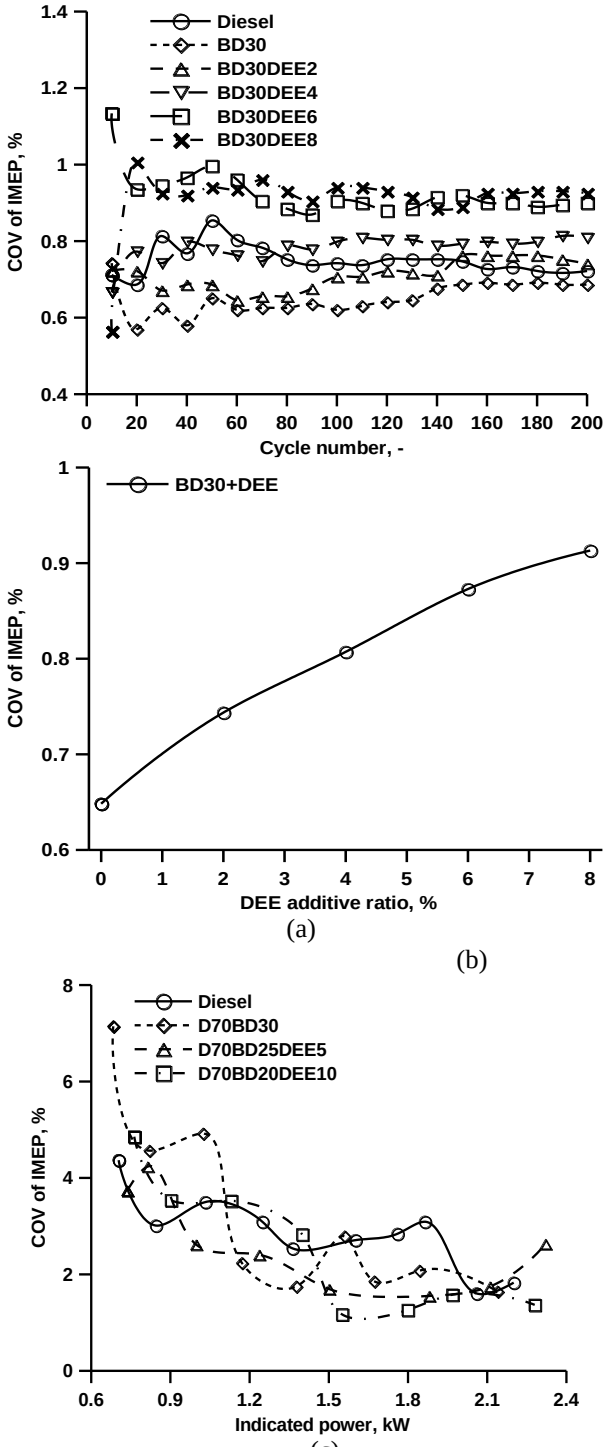

Figure 7. *Variation the COV of IMEP for diesel–biodiesel–DEE blends with a) cycle number, b) DEE ratio [154] and c) indicated power [152]*

Figure 8(a) shows the COV of maximum cylinder pressure rise with load (BMEP) for vegetable oil (VO), biodiesel (BD) and their blends with 20% diethyl ether. Firstly, it was observed that COV values of maximum cylinder pressure rise

with pure VO or its blend with biodiesel were lower than the values for DEE blends. All COV values were raised with load because the more fuel is injected and combusted. The lower COV values at high load were possibly due to the fuel mixture reaching then over–richness at the point where the maximum rate occurred. As regards the corresponding COV values, it could be observed that there were slight differences between the neat VO and its blend with biodiesel and little higher values with their blends with DEE, but inside acceptable limits for this parameter in diesel engines. The little higher values observed for DEE blends with either VO or its blend with biodiesel indicated that this might be due to their corresponding higher ignition delays, which may have the dominant factor for less repeatable first (premixed) part of combustion to occur as against a less delayed combustion. However, COV values among these blends did not seem to correlate with the ignition delays. To be noted that all COV values were reduced with load, given that in the case of lower loads, having also higher ignition delays, the smaller amount of fuel injected (less controllable) and the consequent combustion process were less repeatable. Figure 8(b) shows the COV of IMEP values with load for VO, BD, and their blends with 20% diethyl ether. The related COV values, it could be observed that there were slight differences between the neat VO and its blend with biodiesel, and little higher ones by their blends with DEE, but inside acceptable limits for diesel engines. The higher COV values observed with all blends against the neat bio–fuel cases indicate that this might be due to their corresponding higher ignition delays having the dominant factor. On the other hand, it was observed that there were no apparent differences at all DEE blends with either VO or its blend with biodiesel. This indicated that when all DEE blends were compared, the differences in their ignition delays were not evident, likely being compensated for by other factors that were integrated into the computation of the cylinder pressure diagram for IMEP. All COV of IMEP values were reduced with the rising engine load similar to Figure 8 (a) [80].

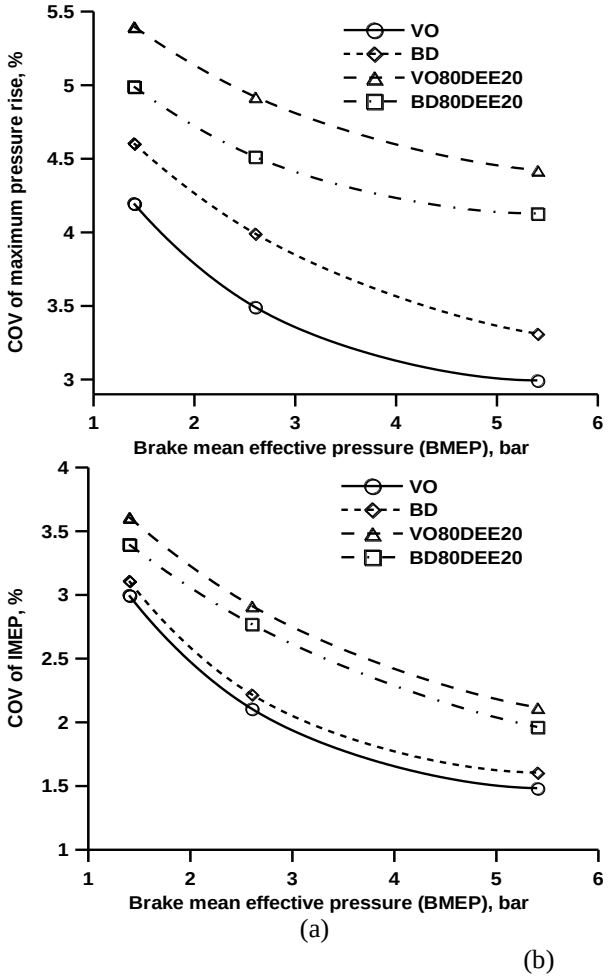

(a) (b)

Figure 8. *Variation of a) COV of IMEP and b) COV of maximum pressure rise for vegetable oil (VO), biodiesel (BD), VO–BD blend with DEE [80]*

Figure 9(a) shows the variation of COV of IMEP with engine speed for diesel, biodiesel, biodiesel–ethanol blends and ethanol–DEE blends. The engine stability was highly affected with B20E80, exceeding limits that would allow vehicle drivability. Hence, BD20E80 did not show in Figure 9(a). DEE80E20 presented the same cyclic variability like the other blends, but not following the same trend as presented in Figure 9(a). However, DEE60E40 showed much higher COV of IMEP values than other fuels and blends after engine speed of 1750 rpm and engine operation were interrupted at engine speed of 2250 rpm as in Figure 9(a). On the other hand, COV of IMEP values would be different as the fuel pump injection timing should be optimized for each blend. Nevertheless, the addition of ethanol into biodiesel appeared to benefit combustion stability due to lowers values of COV of IMEP. The more ethanol in biodiesel gave the more stable combustion. The increasing amount of DEE also improved combustion stability, but in a narrow range. Less than 60% DEE with ethanol did not allow engine operation while 80% DEE with ethanol (DEE80E20) gave good combustion

stability [70]. Figure 9(b) shows the starting fuel injection quantity (SFIQ) effect on the COV of engine speed during the initial 50 idle cycles at –10°C. Evidently, as the SFIQ decreased, COV of engine speed exhibited a corresponding reduction. It indicated that when 0.5% DEE was premixed, cutting down the fuel injection quantity enhanced the stability of engine speed during the cold start. This effect resulted primarily from the fact that a smaller fuel quantity led to a narrower gap between the maximum engine speed and the targeted idle speed, enabling the PID controller too quickly and precisely regulate fuel injection during the idle period. As seen in Figure 9(b), using a smaller SFIQ was beneficial for increasing the safety and stability of combustion during cold start of the diesel engine with 0.5% DEE premixed, but speed–up period was extended [42].

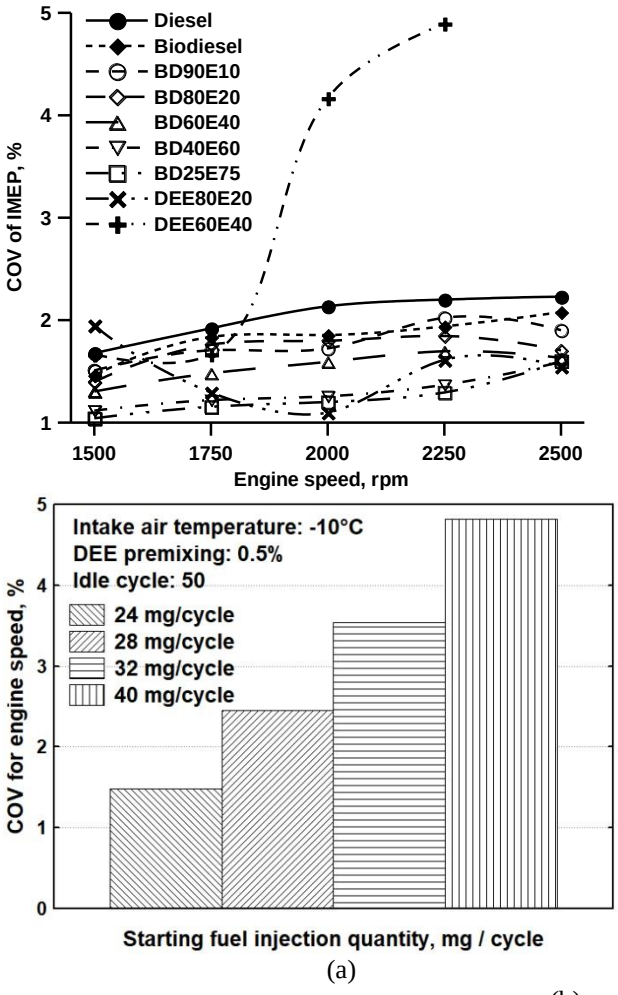

Figure 9. *Variation of a) COV of IMEP with engine speed for ethanol and DEE blends [70] and b) COV for engine speed with the starting fuel injection quantity (SFIQ) [42]*

6. Conclusions

The effect of diethyl ether (DEE) addition to various diesel engine fuels or fuel blends is investigated on the cyclic variations in this review study. The following conclusions can be summarized as results of the study.

- It was declared that coefficient of variation (COV) was usually higher for the low engine loads compared to the high loads due to engine was operated with the leaner fuel–air mixture. Operating of engine with leaner mixtures could increase cyclic variations by deteriorating combustion, while increasing quantity of injected fuel by rising engine load reduced cyclic variability due to enhancing combustion stability.
- It was determined that COV values raised a little with DEE addition to diesel fuel up to 24% DEE ratio, but it did not impact greatly the cyclic variability. COV values stayed under 2.5% for diesel–DEE blends up to 50% DEE ratio. COV values were determined as 2.85%, 2.98% and 3.391%, respectively for diesel, 10% DEE, and %15 DEE with diesel.
- It was declared that cyclic variations were often affected from knocking combustion which is also determined the engine operation limits. It was also declared that cyclic variations began to view at 20% DEE premixed ratio with diesel and knocking combustion could be noticed at 30% and 40% DEE premixed ratios. It was determined that COV of IMEP was 1.29%, 1.44%, 2.01%, 2.4% and 2.6% for diesel, 10%, 20%, 30% and 40% DEE premixed ratios, respectively. COV of maximum cylinder pressure (p_{max}) was also 1.08%, 1.2%, 2.44%, 4.2% and 6.7% for diesel, 10%, 20%, 30% and 40% DEE premixed ratios, respectively. It was concluded that DEE premixed ratio was limited to 40% because of the heavy audible knock.
- It was stated that COV of IMEP values was increased with biodiesel–DEE blends up to 40% DEE ratio. The COV of IMEP values for 30% and 40% DEE with biodiesel were two/three times higher than that of diesel fuel. It was declared that higher variability in COV of IMEP for biodiesel–DEE blends was sourced from deterioration of combustion which was sourced from vapor locks due to evaporation of volatile DEE in the fuel line.
- It was stated that the lower COV of IMEP was obtained with the diesel–biodiesel blend without DEE additive while DEE addition into diesel–biodiesel blend increased cyclic variations, but DEE addition up to 10% into diesel–biodiesel blend did not violently affect the engine stability. It was determined that COV of diesel fuel was around 3% for most engine loads and COV values were lower than 5% for the diesel–biodiesel–DEE blends.
- It was stated that small differences was observed in COV values of pure vegetable oil and vegetable oil–biodiesel blend. A little higher COV values were get by DEE addition to the vegetable oil, biodiesel and their blend, but the COV values obtained with all tested fuels were inside the acceptable limits.

- It was determined that rising ethanol addition to biodiesel fuel gave the more stable combustion and increase of DEE ratio in the ethanol–DEE blend improved combustion stability in a limited range. Higher than 80% ethanol with biodiesel and less than 60% DEE with ethanol did not allow engine operation while 80% DEE and 20% ethanol blend gave the better combustion stability.
- It was determined that reducing of injected main fuel for 0.5% DEE premixed ratio during engine start–up period was raised the stability of combustion (COV of engine speed) during cold start of the diesel engine, but speed–up period was expanded in that case.
- A single cylinder direct injection experimental diesel engine was employed in the most studies on using of DEE. Hence, it will be useful the using of the multi cylinder diesel engines mounted in the vehicle to generalize the findings about DEE for future researches.
- It was understood that DEE addition to different diesel engine fuels generally improves combustion, increases efficiency and reduces the most engine emissions with tolerable power reduction and reasonable increase in fuel consumption, but it is determined that DEE additive especially in high blending ratios increases frequently cyclic variations. Therefore, new methods have been explored the reduction of cyclic variations for future studies when DEE is used as a fuel or fuel additive in internal combustion engines.

References

[1]. Manikandan R., Sethuraman N., Experimental investigation of nano additive ceric oxide (CeO_2)–ethanol blend on single cylinder four stroke diesel engine, International Journal of Recent Development in Engineering and Technology, 3(2), (2014), 24–28.

[2]. Londhekar A.G., Kongre S.C., Effects of different additives on performance and emission of biodiesel fuelled compression ignition engine, International Journal of Science and Research, 6(2), (2017), 1947–1952.

[3]. Hagos F.Y., Ali O.M., Mamat R., Abdullah AA. Effect of emulsification and blending on the oxygenation and substitution of diesel fuel for compression ignition engine, Renewable and Sustainable Energy Reviews, 75, (2017), 1281–1294.

[4]. Patil R.N., Marlapalle B.G., Karanja (pongamia pinnata) biodiesel as an alternative fuel for DICI engine: A review, International Journal of Research in Aeronautical and Mechanical Engineering, 4(1), (2016), 96–101.

[5]. Geng P., Cao E., Tan Q., Wei L., Effects of alternative fuels on the combustion characteristics and emission products from diesel engines: A review, Renewable and Sustainable Energy Reviews, 71, (2017) 523–534.

[6]. Kumar B.R., Saravanan S., Use of higher alcohol biofuels in diesel engines: A review, Renewable and Sustainable Energy Reviews 60, (2016), 84–115.

[7]. Patil A.R., Taji S.G., Effect of oxygenated fuel additive on diesel engine performance and emission: a review, Journal of Mechanical and Civil Engineering, X, (2013), 30–35.

[8]. Senthilkumar R., Ramadoss K., Manimaran R., Prabu M., Emission, combustion, performance and characteristics of a CI engine using MTBE blended diesel fuel, International Conference on Advances in Engineering, Science and Management, ICAESM 2012, Nagapattinam, India, March 30–31, 2012, pp. 360–364.

[9]. Saravanakumar L., Bapu B.R.R., Prasad B.D., Performance and emission characteristics of a CI engine operating on methyl esters blended diesel with di–methyl carbonate additives, International Energy Journal, 14, (2014), 121–132.

[10]. Jawre S.S., Bhagat A., Moghe S.M., Pakhale V.A., Diethyl ether as additive and its effect on diesel engine performance–a review, Global Research and Development Journal for Engineering, 1(5), (2016), 27–31.

[11]. Chauhan B.S., Singh R.K., Cho H.M., Lim H.C., Practice of diesel fuel blends using alternative fuels: A review, Renewable and Sustainable Energy Reviews, 59, (2016), 1358–1368.

[12]. Valipour A., A review on effect of fuel additives on combustion, performance and emission characteristics of diesel and biodiesel fuelled engine, International Journal of Application or Innovation in Engineering & Management, 3(1), (2014), 366–273.

[13]. Krishnamoorthi M., Malayalamurthi R., A review on effect of diethyl ether additive on combustion, performance and emission characteristics of a diesel and biodiesel/vegetable oil fuelled engine, Advances in Natural and Applied Sciences, 10(7), (2016), 9–17.

[14]. Bailey B., Eberhardt J., Goguen S., Erwin J., Diethyl ether (DEE) as a renewable diesel fuel, SAE Technical Paper, (1997), Paper no: 972978.

[15]. Sezer I., Thermodynamic, performance and emission investigation of a diesel engine running on dimethyl ether and diethyl ether, International Journal of Thermal Sciences, 50, (2011), 1594–1603.

[16]. Onyekwere F.O., Ehirim E.O., Ukpaka C.P., Examination of conversion of ethanol into diethyl–ether product, International Journal of Thermodynamics and Chemical Kinetics, 5(1), (2019), 10–18.

[17]. Khan Z.A., Roy M.M., Performance and emission analysis of a modern small DI diesel engine using biodiesel–diesel blends and additives with EGR, Journal of Engineering Research and Application, 8(6), (2018), 34–46.

[18]. Sonawane U., Jena A., Agarwal A.K., Influence of fuel injection pressure on spray characteristics of diesel–diethyl ether blends for diesel engine applications: an experimental study, SAE Technical Papers, (2023), Paper no 2023–01–0309.
[19]. Patil K.R., Thipse S.S., Characterisation of the key fuel properties of oxygenated diethyl ether–diesel blends, Applied Mechanics and Materials, 612, (2014), 175–180.
[20]. Rakopoulos D.C., Rakopoulos C.D., Giakoumis E.G., Dimaratos A.M., Characteristics of performance and emissions in high–speed direct injection diesel engine fueled with diethyl ether/diesel fuel blends, Energy, 43, (2012), 214–224.
[21]. Rakopoulos D.C., Rakopoulos C.D., Giakoumis E.G., Dimaratos A.M., Studying combustion and cyclic irregularity of diethyl ether as supplement fuel in diesel engine, Fuel, 109, (2013), 325–335.
[22]. Patil K.R., Thipse S.S., The effect of injection timing on the performance and emission of direct injection CI engine running on diethyl ether–diesel blends, International Journal of Automotive and Mechanical Engineering, 13(3), (2016), 3773–3787.
[23]. Rathod P.H., Darunde D.S., Experimental investigation and performance analysis of diethyl ether (DEE) and tert–amyl ethyl ether (TAEE) blend with diesel in C.I.D.I. engine: a review, International Journal of Research in Science & Engineering, 2(1), (2015), 137–142.
[24]. Karthik A.V., Kumar S.P., Experimental study of 4–stroke diesel engine blending with alternate fuel diethyl ether (DEE) and exhaust gas recirculation (EGR) system, International Journal of Engineering Science and Computing, 6, (2016), 7054–7058.
[25]. Banapurmath N.R., Khandal S.V., Ranganatha S.L., Chandrashekar T.K., Alcohol (ethanol and diethyl ethyl ether)–diesel blended fuels for diesel engine applications–a feasible solution, Advances in Automobile Engineering, 4(1), (2015), 1–8.
[26]. Lee S., Kim T.Y., Performance and emission characteristics of a DI diesel engine operated with diesel/DEE blended fuel, Applied Thermal Engineering, 121, (2017), 454–461.
[27]. Saravanan D., Vijayakumar T., Thamaraikannan M., Experimental analysis of combustion and emissions characteristics of CI engine powered with diethyl ether blended diesel as fuel, Research Journal of Engineering Sciences, 1(4), (2012), 41–47.
[28]. Ibrahim A., Investigating the effect of using diethyl ether as a fuel additive on diesel engine performance and combustion, Applied Thermal Engineering, 107, (2016), 853–862.
[29]. Likhitha S.S.S., Prasad B.D., Kumar R.V., Investigation on the effect of diethyl ether additive on the performance of variable compression ratio diesel engine, International Journal of Engineering Research, 3(1), (2014), 11–15.
[30]. Kumar R.S., Nagaprasad K.S., Investigation on diesel engine performance by injecting di–ethyl ether as an additive with exhaust gas recirculation using diesel particulate filter, International Journal of Innovative Research in Science, Engineering and Technology, 3(8), (2014), 15192–15200.
[31]. Balamurugan T., Nalini R., Comparative study on performance and emission in four stroke diesel engine using different blended fuel, International Journal of Current Research and Development, 4(1), (2016), 58–64.
[32]. Madhu S., Chaitanya A.V.K., Bridjesh P., Effects of diethyl ether on performance and emission characteristics of a diesel engine using toroidal profile bowl piston by varying injection pressure, International Journal of Mechanical Engineering and Technology, 8(6), (2017), 96–106.
[33]. Cinar C., Can Ö., Sahin F., Yucesu HS., Effects of premixed diethyl ether (DEE) on combustion and exhaust emissions in a HCCI–DI diesel engine, Applied Thermal Engineering, 30, (2010), 360–365.
[34]. Yadav A., Singh S., Singh S., Bishnoi S., Goyal T., Pandey S., Performance characteristics of CI Engine fuelled Diethyl–Ether and its comparison with diesel fuelled CI engine, International Journal of Applied Engineering Research, 13(6), (2018), 358–362.
[35]. Uslu S., Celik M.B., Experimental investigation of the effects of diethyl ether diesel fuel blends on engine parameters in a low power diesel engine, International Journal of Engineering Sciences & Research Technology, 7(5), (2018), 125–138.
[36]. Sethi C., Patnaik P.P., Thatoi D.N., Acharya S.K., Performance, combustion & emission analysis on diesel engine utilizing diethyl ether as a fuel additives, Test Engineering and Management, 82, (2020), 2391–2408.
[37]. Sahoo A., Mishra A., Mishra S., Jena S.P., "Optimization of operating parameters of a diesel engine with diethyl ether as a fuel add–on. Journal of the Institution of Engineers (India): Series C, 102, (2021), 1521–1528.
[38]. Iranmanesh M., Subrahmanyam J.P., Babu M.K.G., Potential of diethyl ether as supplementary fuel to improve combustion and emission characteristics of diesel engines, SAE Technical Papers, (2008), Paper no 2008–28–0044, 305–311.
[39]. Ayhan V., Tunca S., The effect of diethyl ether–diesel blends a direct injection diesel engine on performance and emissions, Sakarya University Journal of Science, 22(2), (2018), 710–718.
[40]. Badajena A.K., Patnaik P.P., Thatoi D.N., Charya S.K.A., Mohanty U.K., Energy analysis of diesel engine using diethyl ether under different loading

condition, International Journal of Engineering & Technology, 7(4), (2018), 335–338.
[41]. Yeşilyurt M.K., Uslu S., Response surface methodology based optimization of a diesel engine fueled with diethyl ether/diesel fuel blends, International Congress of Academic Research, 3. International Congress of Academic Research, ICAR 2022, Osmaniye, Turkey, 13–16 May 2022, pp. 725–733.
[42]. Agarwal A.K., Prashumn, Valera H., Mustafi N.N., Diethyl ether–diesel blends fuelled off–road tractor engine: Part–II: Unregulated and particulate emission characteristics, Fuel, 308, (2022), Paper no 121973.
[43]. Jena A., Sonawane U., Agarwal A.K., Partially premixed combustion of diesel–diethyl ether blends in light–duty commercial engine, Fuel, 345, (2023), Paper no 128197.
[44]. Sun H., Zhang W., Wang Y., Experimental study on improving cold start performance of diesel engines at extremely low ambient temperatures with diethyl ether, Energy, 283, (2023), Paper no 129122.
[45]. Swamy L.R., Banapurmath N.R., Chandrashekar T.K., Soudagar M.E.M., Gul M., Nik–Ghazali N.–N., Mujtaba M.A., Shahapurkar K., Ağbulut Ü., Alshehri H.M., Sajjan A.M., Goodarzi M., Effect of injection timing and duration on the performance of diesel engine fueled with port injection of oxygenated fuels, Chemical Engineering Communications, 210(6), (2023), 1060–1072.
[46]. Fayyaz H.H., Mujtaba M.A., Jahangir S., Imran S., Malik M.A.I., Fayaz H., Saleel C.A., Hassan U., Quershi S., Farooq H., A comprehensive study on the performance and emission analysis in diesel engine via optimization of novel ternary fuel blends: Diesel, manganese, and diethyl ether, Heliyon, 9, (2023), Paper no 21133.
[47]. Subramanian K.A., Ramesh A., Use of diethyl ether along with water–diesel emulsion in a DI diesel engine, SAE Technical Papers, (2002), Paper no 2002–01–2720.
[48]. Iranmanesh M., Experimental investigations about the effect of new combination of biofuels on simultaneous reduction of NOx and smoke emissions in DI–diesel engine, International Journal of Automotive Engineering, 3(2), (2013), 379–392.
[49]. Sudhakar S., Sivaprakasam S., Experimental investigation on combustion characteristics in DI diesel engine using diethyl ether fumigation with ethanol blended diesel, International Journal of Renewable Energy Research, 4(4), (2014), 872–878.
[50]. Sudhakar S., Sivaprakasam S., Effects of diethyl ether fumigation in DI diesel engine using bio ethanol blended diesel, International Journal of Innovation and Scientific Research, 11(1), (2014), 65–71.
[51]. Sudhakar S., Sivaprakasam S., The effect of exhaust gas recirculation on diethyl ether fumigation in DI diesel engine with ethanol blended diesel, International Journal of Engineering Research & Technology, 3(10), (2014), 538–548.
[52]. Paul A., Bose P.K., Panua R.S., Debroy D., Study of performance and emission characteristics of a single cylinder CI engine using diethyl ether and ethanol blends, Journal of the Energy Institute, 88, (2015), 1–10.
[53]. Paul A., Panua R.S., Debroy D., Bose P.K., Effect of diethyl ether and ethanol on performance, combustion, and emission of single cylinder compression ignition engine, International Journal of Ambient Energy, 38(1), (2017), 2–13.
[54]. Lukhman M.M., Sadees P., Pradeep V., Murali M., Experimental investigation on diethyl ether as an ignition improver in diesel–ethanol emulsified fuel for C.I. engine, International Conference on Systems, Science, Control, Communication, Engineering and Technology, 2, (2016), 554–560.
[55]. Ashok M.P., Saravanan C.G., Effect of diethyl ether with emulsified fuel in a direct injection diesel engine, SAE Transactions, 116(4), (2007), 772–779.
[56]. Temizer I., Gucer F., Cihan O., A numerical approach in the investigation of the effects of diethyl ether and ethanol mixtures on combustion characteristics and NO emissions in a DI diesel engine, European Mechanical Science, 6(2), (2022), 110–118.
[57]. Mohebbi M., Reyhanian M., Hosseini V., Saida M.F.M., Aziz A.A., The effect of diethyl ether addition on performance and emission of a reactivity controlled compression ignition engine fueled with ethanol and diesel, Energy Conversion and Management, 174, (2018), 779–792.
[58]. Kumar M.M., Reddy S.S.K., Performance characteristics of single cylinder DI diesel engine by using di–ethyl ether as an additive with diesel ethanol blend, International Journal of Science, Engineering and Technology Research, 4(9), (2015), 3272–3275.
[59]. Patnaik P.P., Jena S.P., Acharya S.K., Das H.C., Effect of FeCl3 and diethyl ether as additives on compression ignition engine emissions, Sustainable Environment Research, 27, (2017), 154–161.
[60]. Patil K.R., Thipse S.S., Experimental investigation of CI engine combustion, performance and emissions in DEE–kerosene–diesel blends of high DEE concentration, Energy Conversion and Management, 89, (2015), 396–408.
[61]. Mahla S.K., Kumar S., Shergill H., Kumar A., Study the performance characteristics of acetylene gas in dual fuel engine with diethyl ether blends, International Journal on Emerging Technologies, 3(1), (2012), 80–83.
[62]. Raman R., Kumar N., Comparative assessment of di–ethyl ether/diesel blends on the performance, and emission characteristics in acetylene dual fuel engine,

International Journal of Engine Research, 24(6), (2022), 1–16.
[63]. Mishra S.K., Pradhan P., Jena S.P., Performance and combustion study of a low heat rejection engine running with biogas–diethyl ether–diesel, Waste Disposal & Sustainable Energy, 6, (2024), 151–162.
[64]. Barik D., Bora B.J., Sharma P., Mehdi B.J., Balasubramanian D., Krupakaran R.L., Ramegowda R., Kavalli K., Josephin J.S.F., Vikneswaran M., Varuvel E.G., Exploration of the dual fuel combustion mode on a direct injection diesel engine powered with hydrogen as gaseous fuel in port injection and diesel–diethyl ether blend as liquid fuel. International Journal of Hydrogen Energy, 52, (2024), 827–840.
[65]. Karabektas M., Ergen G., Hosoz M., The effects of using diethyl ether as additive on the performance and emissions of a diesel engine fuelled with CNG, Fuel, 115, (2014), 855–860.
[66]. Ozer S., Vural E., The effect of the addition of H_2, H_2+HHO and H_2+HHO+O_2 from the intake manifold on exhaust emissions in a diesel generator using diesel/toluene/diethyl ether as pilot fuel, International Journal of Hydrogen Energy, 52, (2024), 1247–1260.
[67]. Sudheesh K., Mallikarjuna J.M., Diethyl ether as an ignition improver for biogas homogeneous charge compression ignition (HCCI) operation–an experimental investigation, Energy, 35, (2010), 3614–3622.
[68]. Mishra N., Mitra S., Thapliyal A., Mahajan A., Khan T.M.Y., Manavalla S., Baig R.U., Janvekar A.A., Feroskhan M., Exploring the effects of DEE pilot injection on a biogas–fueled HCCI engine at different injection locations, Sustainability, 15, (2023), Paper no 10713.
[69]. Jothi N.K.M., Nagarajan G., Renganarayanan S., Experimental studies on homogeneous charge CI engine fueled with LPG using DEE as an ignition enhancer, Renewable Energy, 32, (2007), 1581–1593.
[70]. Dora N., Jothi T.J.S., Emission studies in CI engine using LPG and palm kernel methyl ester as fuels and di–ethyl ether as an additive, Journal of the Institution of Engineers (India): Series C, 100(4), (2019), 627–634.
[71]. Polat S., An experimental study on combustion, engine performance and exhaust emissions in a HCCI engine fuelled with diethyl ether–ethanol fuel blends, Fuel Processing Technology, 143, (2016), 140–150.
[72]. Prante G.A.F., Santos N.D.S.A., Martins M.E.S., Feasibility of replacing diesel with ethanol blended with biodiesel and diethyl–ether blends in a compression ignition engine. Journal of the Brazilian Society of Mechanical Sciences and Engineering, 45, (2023), Paper no 60.
[73]. Mack J.H., Buchholz B.A., Flowers D.L., Dibble R.W., The effect of the di–tertiary butyl peroxide (DTBP) additive on HCCI combustion of fuel blends of ethanol and diethyl ether, Society of Automotive Engineering, (2015), Paper no: 2005–01–2135.
[74]. Subhash G.V., Sivapirakasam S.P., Mohan S., Subramanian N., Phanindra K.H., Effect of diethyl ether additive on reformulated bio–mix blends from a mixture of different feed stock's, Waste and Biomass Valorization, 14, (2023), 261–276.
[75]. Zapata–Mina J., Ardebili S.M.S., Restrepo A., Solmaz H., Calam A., Can O., Exergy analysis in a HCCI engine operated with diethyl ether–fusel oil blends, Case Studies in Thermal Engineering, 32, (2022), Paper no 101899.
[76]. Gurusamy M., Subramaniyan M., Subramaniyan B., Assessment of hydrogen and diethyl ether enrichment on CI engine operating with binary blend of jatropha and camphor oil using response surface methodology, Energy, 289, (2024), Paper no 129919.
[77]. Ergen G., Comprehensive analysis of the effects of alternative fuels on diesel engine performance combustion and exhaust emissions: Role of biodiesel, diethyl ether, and EGR, Thermal Science and Engineering Progress, 47, (2024), Paper no 102307.
[78]. Raman S.M., Roy M.M., Microscopic study of EPS–infused biodiesel with DEE and its performance and emissions in a diesel engine, Biofuels, 14(7), (2023), 751–766.
[79]. Kasiraman G., Nagalingam B., Balakrishnan M., Effect of blending diethyl ether (DEE) with cashewnut shell oil (CNSO) on the performance, emission and combustion characteristics of a direct injection diesel engine, 2. International Conference on Advanced Energy Research, ICAER 2011, Mumbai, India, December 9–11 2011, (2011), pp. 1–9.
[80]. Pranesh G., Samuel P.M., Thankachan B., Manimaran M., Silambarasan R., Performance and emission characteristics of blending diethyl ether in cotton seed oil methyl ester using a direct injection diesel engine. International Journal on Applications in Mechanical and Production Engineering, 1(6), (2015), 14–16.
[81]. Rakopoulos D.C., Combustion and emissions of cottonseed oil and its bio–diesel in blends with either n–butanol or diethyl ether in HSDI diesel engine, Fuel, 105, (2013), 603–613.
[82]. Rakopoulos D.C., Rakopoulos C.D., Kyritsis D.C., Butanol or DEE blends with either straight vegetable oil or biodiesel excluding fossil fuel: Comparative effects on diesel engine combustion attributes, cyclic variability and regulated emissions trade–off, Energy, 115, (2016), 314–325.
[83]. Rakopoulos D.C., Rakopoulos C.D., Giakoumis E.G., Papagiannakis R.G., Kyritsis D.C.. Influence of properties of various common bio–fuels on the combustion and emission characteristics of high–speed DI (direct injection) diesel engine: Vegetable oil, bio–diesel, ethanol, n–butanol, diethyl ether, Energy, 73, (2014), 354–366.

[84]. Krishna R., Bandewar A.G., Dongare V.K., Experimental investigations of blending diethyl ether in karanja vegetable oil using a multi–cylinder diesel engine, International Journal of Research and Innovative Technology, 1(5), (2014), 70–73.
[85]. Singh I., Sahni V., Performance analysis of the compression ignition engine using karanja biodiesel with additive diethyl ether, Int'l Conference on Aeronautical, Automotive and Manufacturing Engineering, ICAAME'2015, Kuala Lumpur, Malaysia, August 25–26 2015, (2015), pp. 9–12.
[86]. Jawre S.S., Lawankar S.M., Performance analysis of Kusum methyl ester as alternative bio–fuel in diesel engine with diethyl ether as additive, International Journal of Innovative Research & Development, 3(5), (2014), 139–144.
[87]. Samraj A., Barik D., Bhatlu M.L.D., Rout S.K., Ayadi B., Aich W., Hussein A.K., Kolsi L., Effect of diethyl ether on the performance and emission characteristics of a diesel engine fueled with a light fraction of waste cooking oil, Processes, 11, (2023), Paper no 2613.
[88]. Górski K., Smigins R., Longwic R., Research on physico–chemical properties of diethyl ether/linseed oil blends for the use as fuel in diesel engines. Energies, 13, (2020), Paper no 6564.
[89]. Rao K.P., Reddi V.L., Performance evaluation of diesel engine with biodiesel along with additive for replacing diesel fuel, International Journal of Chemical Science, 14(4), (2016), 2379–2388.
[90]. Babu P.R., Rao K.P., Rao B.V.A., The role of oxygenated fuel additive (DEE) along with mahuva methyl ester to estimate performance and emission analysis of DI–diesel engine, International Journal of Thermal Technologies, 2(1), (2012), 119–123.
[91]. Sivalakshmi S., Balusamy T., Effect of biodiesel and its blends with diethyl ether on the combustion, performance and emissions from a diesel engine, Fuel, 106, (2013), 106–110.
[92]. Senthil R., Arunan K., Silambarasan R., Effect of oxygenated additives on exhaust emissions reduction in di diesel engine using biodiesel and its blends, Oxidation Communications, 38(2), (2015), 841–851.
[93]. Purushothaman K., Nagarajan G., Experimental investigation on a C.I. engine using orange oil and orange oil with DEE, Fuel, 88, (2009), 1732–1740.
[94]. Purushothaman K., Nagarajan G., Studies on the characteristics of orange oil–diethyl ether in a direct injection diesel engine, International Journal of Engine Research, 11, (2010), 219–228.
[95]. Ali O.M., Mamat R., Faizal C.K.M., Effects of diethyl ether additives on palm biodiesel fuel characteristics and low temperature flow properties, International Journal of Advanced Science and Technology, 52, (2013), 111–120.
[96]. Ali O.M., Yusaf T., Mamat R., Abdullah N.R., Abdullah A.A., Influence of chemical blends on palm oil methyl esters' cold flow properties and fuel characteristics, Energies, 7, (2014), 4364–4380.
[97]. Kumar J.S., Prasad S.V.M., Experimental study on performance characteristics of C.I. engine fueled with biodiesel and its blends diethyl ether, International Journal & Magazine of Engineering, Technology, Management and Research, 1(8), (2014), 36–40.
[98]. Rajan K., Prabhahar M., Senthilkumar K.R., Experimental studies on the performance, emission and combustion characteristics of a biodiesel–fuelled (pongamia methyl ester) diesel engine with diethyl ether as an oxygenated fuel additive, International Journal of Ambient Energy, 37(5), (2016), 439–445.
[99]. Górski K., Smigins R., Matijošius J., Tziourtzioumis D., Cycle–to–cycle variation of the combustion process in a diesel engine fueled with rapeseed oil–diethyl ether blends, Energies, 16, (2023), Paper no 720.
[100]. Lotko W., Hernik A., Stobiecki J., Kosmanis T., Górska M., Smoke emission of AD3.152 engine fuelled with rapeseed oil/diethyl ether blends, The Archives of Automotive Engineering, 80(2), (2018), 65–76.
[101]. Smigins R., Zakis A., Impact of diethyl ether/rapeseed oil blends on performance and emissions of a light–duty diesel vehicle, Energies, 13, (2020), Paper no 3788.
[102]. Geo V.E., Nagarajan G., Nagalingam B., Studies on improving the performance of rubber seed oil fuel for diesel engine with DEE port injection, Fuel, 89, (2010), 3559–3567.
[103]. Danesha D., Manjunath H., Production and characterization of biodiesel from simarouba glauca seed oil with diethyl ether as an additive and its performance and emission evaluation on single cylinder, four stroke C.I engine, International Journal of Research in Engineering and Technology, 5(13), (2016), 64–68.
[104]. Górski K., Smigins R., Matijošius J., Rimkus A., Longwic R., Physicochemical properties of diethyl ether–sunflower oil blends and their impact on diesel engine emissions, Energies, 15, (2022), Paper no 4133.
[105]. Hariharan S., Murugan S., Nagarajan G., Effect of diethyl ether on tyre pyrolysis oil fueled diesel engine, Fuel, 104, (2013), 109–115.
[106]. Patil S., Rao N.D., Performance analysis of C.I. engine fuelled with blend of biodiesel and diethyl ether with EGR technique, Iconic Research and Engineering Journals, 2(4), (2018), 150–108.
[107]. Devaraj J., Robinson Y., Ganapathi P., Experimental investigation of performance, emission and combustion characteristics of waste plastic pyrolysis oil blended with diethyl ether used as fuel for diesel engine, Energy, 85, (2015), 304–309.

[108]. Kaimal V.K., Vijayabalan P., An investigation on the effects of using DEE additive in a DI diesel engine fuelled with waste plastic oil, Fuel, 180, (2016), 90–96.
[109]. Wiangkham A., Klinkaew N., Aengchuan P., Liplap P., Ariyarit A., Sukjit E., Experimental and optimization study on the effects of diethyl ether addition to waste plastic oil on diesel engine characteristics, RSC Advances, 13, (2023), 25464–25482.
[110]. Carvalho M., Torres F., Ferreira V., Silva J., Martins J., Torres E., Effects of diethyl ether introduction in emissions and performance of a diesel engine fueled with biodiesel–ethanol blends, Energies, 13, (2020), 3787.
[111]. Venu H., Madhavan V., Effect of nano additives (titanium and zirconium oxides) and diethyl ether on biodiesel–ethanol fuelled CI engine, Journal of Mechanical Science and Technology, 30(5), (2016), 2361–2368.
[112]. Satyanarayanamurthy Y.V.V., Experimental investigations of real time secondary co–injection of water–diethyl ether solution in DI–diesel engine fuelled with palm kernel methyl ester, Journal of Engineering Science and Technology, 7(6), (2012), 711–721.
[113]. Sachuthananthan B., Jeyachandran K., Combustion, performance and emission characteristics of water–biodiesel emulsion as fuel with DEE as ignition improver in a DI diesel engine, Journal of Environmental Research and Development, 2(2), (2007), 164–172.
[114]. Barik D., Murugan S., Effects of diethyl ether (DEE) injection on combustion performance and emission characteristics of karanja methyl ester (KME)–biogas fueled dual fuel diesel engine, Fuel, 164, (2016), 286–296.
[115]. Barik D., Murugan S., Samal S., Sivaram N.M., Combined effect of compression ratio and diethyl ether (DEE) port injection on performance and emission characteristics of a DI diesel engine fueled with upgraded biogas (UBG)–biodiesel dual fuel, Fuel, 209, (2017), 339–349.
[116]. Nanthagopal K., Ashok B., Garnepudi R.S., Tarun K.R., Dhinesh B., Investigation on diethyl ether as an additive with calophyllum inophyllum biodiesel for CI engine application, Energy Conversion and Management, 179, (2019), 104–113.
[117]. Jeevanantham A.K., Nanthagopal K., Ashok B., Al–Muhtaseb A.H., Thiyagarajan S., Geo V.E., Ong H.C., Samuel K.J., Impact of addition of two ether additives with high speed diesel–Calophyllum Inophyllum biodiesel blends on NOx reduction in CI engine, Energy, 185, (2019), 39–54.
[118]. Prabakaran R., Manikandan G., Somasundaram P., Kumar P.G., Salman M., Jegadheesan C., Kim S.C., Feasibility of tea tree oil blended with diethyl ether and diesel as fuel for diesel engine, Case Studies in Thermal Engineering, 31, (2022), Paper no 101819.
[119]. Shinde S., Yadav S.D., Theoretical properties prediction of diesel–biodiesel–DEE blend as a fuel for C.I. engine with required modifications for optimum performance, International Journal of Current Engineering and Technology, 6(5), (2016), 1562–1567.
[120]. Pillai S.K., Rajamanickam U., Khurana S., Impact of diethyl ether on performance and emission characteristics of a VCR diesel engine fueled by dual biodiesel, Energies, 16, (2023), Paper no 4863.
[121]. Krishnamoorthi M., Malayalamurthi R., Experimental investigation on performance, emission behavior and exergy analysis of a variable compression ratio engine fueled with diesel–aegle marmelos oil–diethyl ether blends, Energy, 128, (2017), 312–328.
[122]. Kuberan J., Alagumurthi N., Experimental analysis of diesel engine using algae bio–fuel with diethyl ether as additives. Journal of Industrial Pollution Control, 33(2), (2017), 1801–1805.
[123]. Chandirasekaran J.D., Senthilkumar N., An analysis of the smoke output of a CI engine running on B10 novel algae biofuel with and without DEE additive and clean diesel as fuels, Journal of Survey in Fisheries Sciences, 10(1S), (2023), 2217–2225.
[124]. Alruqi M., Sharma P., Deepanraj B., Shaik F., Renewable energy approach towards powering the CI engine with ternary blends of algal biodiesel–diesel–diethyl ether: Bayesian optimized Gaussian process regression for modeling–optimization, Fuel, 334, (2023), Paper no 126827.
[125]. Ahmed S.A., Soudagar M.E.M., Rahamathullah I., Basha J.S., Khan T.M.Y., Javed S., Elfasakhany A., Kalam M.A., Investigation of ternary blends of animal fat biodiesel–diethyl ether–diesel fuel on CMFIS–CI engine characteristics, Fuel, 332, (2023), Paper no 126200.
[126]. Gurusamy M., Ponnusamy C., The influence of hydrogen induction on the characteristics of a CI engine fueled with blend of camphor oil and diesel with diethyl ether additive. International Journal of Hydrogen Energy, 48, (2023), 24054–24073.
[127]. Kumar A., Rajan K., Naraynan M.R., Kumar K.R.S., Performance and emission characteristics of a DI diesel engine fuelled with cashew nut shell oil (CNSO)–diesel blends with diethyl ether as additive, Applied Mechanics and Materials, 787, (2015), 746–750.
[128]. Kumar A., Rajan K., Kumar K.R.S., Maiyappan K., Rasheed U.T., Green fuel utilization for diesel engine, combustion and emission analysis fuelled with CNSO diesel blends with diethyl ether as additive, Materials Science and Engineering, 197, (2017), 1–10.
[129]. Ganesha T., Chethan K.S., An experimental investigation of the performance and emission of diesel

engine fueled with cashew shell oil methyl ester (CSOME) and it's blend with diethyl ether and conventional diesel. Imperial Journal of Interdisciplinary Research, 2(9), (2016), 922–929.
[130]. Pushparaj T., Alosius M.A., Ramabalan S., Experimental investigation on the effects of diethyl ether additive on cashew nut shell liquid biodiesel, Advanced Materials, 984–985, (2014), 924–931.
[131]. Senthilkumar N., Raj P., Ranjitha J., Muniappan A., A critical evaluation of additive blended cashew nut shell liquid blended biodiesel performance in compression ignition engine, Environment, Development and Sustainability, 25, (2023), 61–75.
[132]. Senthilkumar D., Murugesan S., Experimental investigation on impact of diethyl ether additives with cashew nut shell liquid biodiesel blends on performance characteristics of engine operating at optimum conditions. Emission Control Science and Technology, 9, (2023), 66–75.
[133]. Ahmad S., Jafry A.T., Haq M., Asif M., Ahmad K., Zafar F.U., Experimental study of castor biodiesel ternary blends with ethanol, butanol, diethyl ether and dibutyl ether in a diesel engine. Journal of Thermal Analysis and Calorimetry, 148, (2023), 927–941.
[134]. Srihari S., Thirumalini S., Prashanth K., An experimental study on the performance and emission characteristics of PCCI–DI engine fuelled with diethyl ether–biodiesel–diesel blends, Renewable Energy, 107, (2017), 440–447.
[135]. Yesilyurt M.K., Aydin M., Experimental investigation on the performance, combustion and exhaust emission characteristics of a compression–ignition engine fueled with cottonseed oil biodiesel/diethyl ether/diesel fuel blends. Energy Conversion and Management, 205, (2020), Paper no 112355.
[136]. Karthick D., Dwarakesh R., Premnath., Combustion and emission characteristics of jatropha blend as a biodiesel for compression ignition engine with variation of compression ratio, International Review of Applied Engineering Research, 4(1), (2014), 39–46.
[137]. Satya V.P.U., Murthy K.M., Rao G.A.P., Effective utilization of B20 blend with oxygenated additives, Thermal Science, 15(4), (2011), 1175–1184.
[138]. Abraham B.C., Thomas A.J., Performance evaluation of biodiesel with a combustion enhancer additive, International Journal of Mechanical Engineering and Technology, 6(8), (2015), 118–125.
[139]. Firew D., Babu N.R., Didwania M., The performance evaluation of diethyl–ether (DEE) additive with diesel blends using diesel engine test rig, International Journal of Scientific & Engineering Research, 7(6), (2016), 23–29.
[140]. Prasad U.S.V., Madhu Murthy K., Amba Prasad R.G., Effect of oxygenated additives on control of emissions in a DI diesel engine using biodiesel–diesel blends, International Conference on Mechanical, Automobile and Robotics Engineering, ICMAR'2012, Penang, Malaysia, December 14–15 2012, (2012), pp. 256–260.
[141]. Imtenan S., Masjuki H.H., Varman M., Rizwanul Fattah I.M., Sajjad H., Arbab M.I., Effect of n–butanol and diethyl ether as oxygenated additives on combustion–emission–performance characteristics of a multiple cylinder diesel engine fuelled with diesel–jatropha biodiesel blend. Energy Conversion and Management, 94, (2015), pp. 84–94.
[142]. Rao P.V., Chary D.P., Diethyl ether additive effect in the performance of single cylinder DI diesel engine with B20 biodiesel blend fuel, International Journal of Advanced Engineering Research and Science, 5(11), (2018), 171–176.
[143]. Varpe B.R., Kharde Y.R., Rahman K.F., Khidmatgar A., Effect of diethyl ether additive in Jatropha biodiesel-diesel fuel blends on the variable compression ratio diesel engine performance and emissions characteristics at different loads and compression ratios, Heat Transfer, 49(33), (2020), 1–21.
[144]. Biradar C.H., Subramanian K.A., Dastidar M.G., Performance improvement and emissions reduction of a DI diesel engine for use of karanja biodiesel–diesel blend (B20) using diethyl ether, SAE Technical Paper, (2011), Paper no: 2011–26–0004.
[145]. Manickam A.R., Rajan K., Manoharan N., Senthil Kumar K.R., Experimental analysis of a diesel engine fuelled with biodiesel blend using di–ethyl ether as fuel additives, International Journal of Engineering and Technology, 6(5), (2014), 2412–2420.
[146]. Tudu K., Murugan S., Patel S.K., Experimental study of diethyl ether addition on the performance and emissions of a diesel engine, International Journal of Ambient Energy, 38(4), (2015), 332–338.
[147]. Nagdeote D.D., Deshmukh M.M., Experimental study of diethyl ether and ethanol additives with biodiesel–diesel blended fuel engine, International Journal of Emerging Technology and Advanced Engineering, 2(3), (2012), 195–199.
[148]. Mallikarjun M.V., Mamilla V.R., Rao G.L.N., NOx emission control techniques when CI engine is fuelled with blends of mahua methyle esters and diesel, International Journal of Engineering Sciences & Emerging Technologies, 4(2), (2013), 96–104.
[149]. Sudhakar S., Sivaprakasam S., Potential of diethyl ether blends with biodiesel in di diesel engine–an experimental investigation, International Journal of Research in Engineering & Advanced Technology, 2(5), (2014), 1–6.
[150]. Vadivel N., Somasundaram P., Krishnamoorthi M., Performance and emission characteristics of a CI engine fueled with diesel–biodiesel (mahua/mustard) blend with diethyl ether additive, Journal of Chemical and Pharmaceutical Sciences, 7, (2015), 109–115.

[151]. Akshatha D.S., Manavendra G., Kumarappa S., Performance evaluation of Neem biodiesel on CI engine with diethyl ether as additive, International Journal of Innovative Research in Science, Engineering and Technology, 2(8), (2013), 3729–3736.

[152]. Kumar J.V., Rao C.J., Experimental investigation of performance and emission characteristics of diesel engine working on diesel and neem oil blend with diethyl ether as additive, International Journal of Technological Exploration and Learning, 3(5), (2014), 581–588.

[153]. Shrivastava N., Sungra T., A study to investigate the effect of diethyl ether as additive on the performance and emissions of engine using diesel and neem oil methyl ester as fuel, International Journal of Renewable Energy Research, 8(2), (2018), 888–894.

[154]. Ibrahim A., An experimental study on using diethyl ether in a diesel engine operated with diesel–biodiesel fuel blend. Engineering Science and Technology, an International Journal, 21, (2018), 1024–1033.

[155]. Ali O.M., Mamat R., Abdullah N.R., Abdullah A.A., Investigation of blended palm biodiesel–diesel fuel properties with oxygenated additive, Journal of Engineering and Applied Sciences, 11(8), (2016), 5289–5293.

[156]. Annamalai K., Kumar A.R.P., Premkartik K., Adelfa (NOME–Nerium Oil Methyl Ester) with DEE as the fuel additive for NOx reduction in DI Diesel engines–An experimental investigation, Journal of Scientific & Industrial Research, 73, (2014), 627–632.

[157]. Ali O.M., Mamat R., Masjuki H.H., Abdullah A.A., Analysis of blended fuel properties and cycle–to–cycle variation in a diesel engine with a diethyl ether additive, Energy Conversion and Management, 108, (2016), 511–519.

[158]. Imtenan S., Masjukia H.H., Varmana M., Arbaba M.I., Sajjada H., Rizwanul Fattaha I.M., Abedina M.J., Md. Hasib A.S., Emission and performance improvement analysis of biodiesel–diesel blends with additives. Procedia Engineering, 90, (2014), 472–477.

[159]. Imtenan S., Varman M., Masjuki H.H., Kalam M.A., Sajjad H., Arbab M.I., Effect of DEE as an oxygenated additive on palm biodiesel–diesel blend in the context of combustion and emission characteristics on a medium duty diesel engine, 4th International Conference on Environmental, Energy and Biotechnology, ICEEB 2015, Madrid, Spain, June 15–16 2015, Vol. 85, (2015), pp. 100–104.

[160]. Varaprasad K.S., Rao H.S.B., Experimental investigation on engine performance and exhaust emission analysis of diesel engine operating on palm oil biodiesel blends with diethyl ether as an additive, International Journal of Research and Innovation, (2017), 566–571.

[161]. Prasadarao B.V.V., HariBabu N., Ramana M.V. The role of oxygenated fuel additive (DEE) along with palm methyl ester and diesel to estimate performance and emission analysis of DI–diesel engine, International Journal of Engineering Research & Technology, 3(1), (2014), 1–9.

[162]. Uslu S., Multi–objective optimization of biodiesel and diethyl ether doped diesel engine by Taguchi method, International Journal of Automotive Science and Technology, 4(3), (2020), 171–179.

[163]. Uslu S., Aydın M., Effect of operating parameters on performance and emissions of a diesel engine fueled with ternary blends of palm oil biodiesel/diethyl ether/diesel by Taguchi method, Fuel, 275, (2020), Paper no 117978.

[164]. Hardiyanto C., Prawoto P., Effect of diethyl ether on performance and exhaust gas emissions of heavy–duty diesel engines fueled with biodiesel–diesel blend (B35), Automotive Experiences, 6(3), (2023), 687–701.

[165]. Gurusamy M., Subramanian B., Study of PCCI engine operating on pine oil diesel blend (P50) with benzyl alcohol and diethyl ether, Fuel, 335, (2023), Paper no 127121.

[166]. Samuel K.J., Raj R.T.K., Sreenivasulu N., Rajasekhar Y., Edison G., Saco S.A., An experimental study on performance and emissions of a direct ignition diesel engine with crude pongamia, pongamia methyl ester and diethyl ether blended with diesel, International Journal of Renewable Energy Research, 6(4), (2016), 1506–1515.

[167]. Pugazhvadivu M., Rajagopan S., Investigations on a diesel engine fuelled with biodiesel blends and diethyl ether as an additive, Indian Journal of Science and Technology, 2(5), (2009), 31–35.

[168]. Danesha D., Manjunath H., Production and characterization of biodiesel from Simarouba Glauca seed oil with diethyl ether as an additive and its performance and emission evaluation on single cylinder, four stroke C.I engine, International Journal of Research in Engineering and Technology, 5(13), (2016), 64–68.

[169]. Prabu S.S., Asokan M.A., Sukhadia D.S., Jain V., Sarwate S.M., Combustion, performance and emission behavior of soap–nut oil biodiesel/diesel blends in di diesel engine with diethyl–ether additive, Journal of Critical Reviews, 7(15), (2020), 4835–4843.

[170]. Muneeswaran R., Thansekhar M.R., Reduction of NOx emission in biodiesel (soybean) fuelled DI diesel engine by cetane improver, Journal of Engineering and Applied Sciences, 10(7), (2015), 2968–2973.

[171]. Navaneethakrishnan P., Vasudevan D., Experimental study on performance and exhaust emission characteristics of a C.I. engine fuelled with tri–compound oxygenated diesel fuel blends, Indian

Journal of Science and Technology, 8(4), (2015), 307–313.
[172]. Raju V.D., Kishore P.S., Subbarao R., Investigations on the effects of diethyl ether as fuel additive in diesel engine fueled with tamarind seed methyl ester, Springer Proceedings in Energy–Advances in Energy Research, 2(41), (2017), 447–456.
[173]. Raju V.D., Venu H., Subramani L., Kishore P.S., Prasanna P.L., Kumar D.V., An experimental assessment of prospective oxygenated additives on the diverse characteristics of diesel engine powered with waste tamarind biodiesel, Energy, 203, (2020), Paper no 117821.
[174]. Tudu K., Murugan S., Patel S.K., Effect of diethyl ether in a DI diesel engine run on a tyre derived fuel–diesel blend, Journal of the Energy Institute, 89, (2016), 525–535.
[175]. Murugan S., Tudu K., Patel S.K., Performance and emission studies of a naturally aspirated diesel engine. Journal of Clean Energy Technologies, 5(5), (2017), 359–365.
[176]. Padmanabhan S., Selvamuthukumar M., Mahalingam S., Giridharan K., Ganesan S., Influential study of oxygenated additives in waste cooking biodiesel blends on diesel engine performance, Multidisciplinary Science Journal, 5, (2023), Paper no 2023015.
[177]. Krishnamoorthi M., Natarajan A., Performance and emission characteristics of a CI engine fueled with diesel–waste fried oil blend with DEE as additive, International Journal for Research in Applied Science & Engineering Technology, 3(5), (2015), 65–72.
[178]. Dubey A., Prasad R.S., Singh J.K., Nayyar A., Response surface methodology (RSM) based experimental and model analysis of diethyl ether biodiesel–diesel blends with exhaust gas recirculation (EGR) on stationary diesel engine, Petroleum Science and Technology, 41(12), (2023), 1272–1291.
[179]. Reddy K.S., Rao Y.V.H., Raju V.D., Influence of diethyl ether on the diesel engine diverse characteristics fuelled with waste plastic biodiesel, Materials Today: Proceedings, 61, (2022), 1168–1175.
[180]. Kotturi R.K., Krishna M.V.S.M., Kumar B.S.P., Effect of diethyl ether on a CRDI diesel engine with waste plastic oil blend, Gradiva Review Journal, 9(7), (2023), 41–51.
[181]. More G.V., Koli S.R., Rao Y.V.H., Prasad P.I., Rao B.N., Effect of compression ratio on compression ignition engine with RUCO biodiesel/diethyl ether/diesel fuel blends, Energy Sources, Part A: Recovery, Utilization, and Environmental Effects, (2020).
[182]. Senthil R., Sivakumar E., Silambarasan R., Effect of diethyl ether on the performance and emission characteristics of a diesel engine using biodiesel–eucalyptus oil blends, RSC Advances, 5, (2015), 54019–54027.
[183]. Qi D.H., Chen H., Geng L.M., Bian Y.Z., Effect of diethyl ether and ethanol additives on the combustion and emission characteristics of biodiesel–diesel blended fuel engine, Renewable Energy, 36, (2011), 1252–1258.
[184]. Roy M.M., Calder J., Wang W., Mangad A., Diniz F.C.M., Cold start idle emissions from a modern Tier–4 turbo–charged diesel engine fueled with diesel–biodiesel, diesel–biodiesel–ethanol, and diesel–biodiesel–diethyl ether blends, Applied Energy, 180, (2016), 52–65.
[185]. Carvalho M.A.S., Achy A.R.A., Junior L.C.S.S., Ferreira V.P., Silva J.A.M., Pepe I.M., Torres E.A., Mechanical and emissions performance of a diesel engine fueled with biodiesel, ethanol and diethyl ether blends, Journal of the Brazilian Society of Mechanical Sciences and Engineering, 42, (2020), Paper no 182.
[186]. Venu H., Madhavan V., Effect of diethyl ether and Al_2O3 nano additives in diesel–biodiesel–ethanol blends: performance, combustion and emission characteristics, Journal of Mechanical Science and Technology, 31(1), (2017), 409–420.
[187]. Venu H., Madhavan V., Influence of diethyl ether (DEE) addition in ethanol–biodiesel–diesel (EBD) and methanol–biodiesel–diesel (MBD) blends in a diesel engine, Fuel, 189, (2017), 377–390.
[188]. Sathiyamoorthi R., Sankaranarayanan G., Pitchandi K., Combined effect of nano emulsion and EGR on combustion and emission characteristics of neat lemongrass oil (LGO)–DEE–diesel blend fuelled diesel engine. Applied Thermal Engineering, 112, (2017), 1421–1432.
[189]. Vellaiyan S., Kuppusamy S., Chandran D., Raviadaran R., Devarajan Y., Optimisation of fuel modification parameters for efficient and greener energy from diesel engine powered by water–emulsified biodiesel with cetane improver, Case Studies in Thermal Engineering, 48, (2023), Paper no 103129.
[190]. Sezer I., A review study on the using of diethyl ether in diesel engines: effects on fuel properties and engine performance, Energy Technology, 6(11), (2018), 2084–2114.
[191]. Sezer I., A review study on the using of diethyl ether in diesel engines: effects on fuel properties, injection and combustion characteristics, Energy and Environment, 31(2), (2020), 179–214.
[192]. Sezer I. A, Review Study on the using of diethyl ether in diesel engines: effects on CO emissions, International Journal of Automotive Science and Technology, 3(1), (2019), 6–20.
[193]. Sezer I., A review study on the using of diethyl ether in diesel engines: effects on HC emissions, European Journal of Science and Technology, 16, (2019), 109–124.

[194]. Sezer I., A review study on the using of diethyl ether in diesel engines: effects on NOx emissions, International Journal of Automotive Engineering and Technologies, 7(4), (2018), 164–183.
[195]. Sezer I., A review study on the using of diethyl ether in diesel engines: effects on smoke and PM emissions, MANAS Journal of Engineering, 7(2), (2019), 74–88.
[196]. Sezer I., A Review study on the using of diethyl ether in diesel engines: effects on CO_2 emissions, Journal of Chinese Society of Mechanical Engineers, 40(3), (2019), 263–272.
[197]. Heywood J.B., Internal Combustion Engine Fundamentals, McGraw–Hill Book Company, New York, 1988.
[198]. Ibrahim A., Bari S., Effect of varying compression ratio on a natural gas SI engine performance in the presence of EGR, Energy & Fuels, 23, (2009), 4949–4956.
[199]. Ibrahim A., Bari S., An experimental investigation on the use of EGR in a supercharged natural gas SI engine. Fuel, 89, (2010), 1721–1730.

MANAS Journal of Engineering
ISSN 1694-7398 — e-ISSN 1694-7398

Volume 12 (Issue 1) (2024) Pages 77-87
https://doi.org/10.51354/mjen.1274359

Polynomial Solutions of Electric Field Equations in Anisotropic Media

Meltem Altunkaynak
Department of Mathematics, Faculty of Sciences, Dokuz Eylül University, Buca, 35160 Izmir, Turkey,
meltem.topcuoglu@deu.edu.tr, ORCID: 0000-0002-6706-2957

ABSTRACT

The time-dependent system of partial differential equations of the second order describing the electric wave propagation in electrically and magnetically anisotropic homogeneous media is considered in the paper. A method for the computation of the polynomial solutions of the initial value problem for the considered system is proposed. Symbolic computations are used and these symbolic computations are implemented in Maple. It is proved also that these polynomial solutions are approximate solutions of the considered initial value problem with smooth initial data and the inhomogeneous term. The computational experiments confirm the robustness of the suggested method for the computation of electric fields in general electrically and magnetically anisotropic media.

ARTICLE INFO

Research article

Received: 02.04.2024
Accepted: 06.02.2024

Keywords: The time-dependent electric field equations, electromagnetic radiation, analytical method, symbolic computations, anisotropic media.

**Corresponding author*

1. Introduction

At the recent time the use and development of new anisotropic materials stimulates the growing interest for modeling electric and magnetic wave propagations inside these new materials. This topic is an important interdisciplinary area of research with many cutting-edge scientific and technological applications [6],[7],[11]. The physical properties of anisotropic media essentially depend on the orientation and position. For instance, in anisotropic homogeneous media the physical properties depend on the orientation and do not depend on the position [11]. The medium can be isotropic relative to some properties and anisotropic with respect to others. For example, anisotropic crystals and dielectrics are magnetically isotropic but electrically anisotropic. Some of materials are magnetically anisotropic but electrically isotropic and some of materials are electrically and magnetically anisotropic. One of the first and a very well known approach for modeling wave propagations is a 'plane wave approach', when a wave front is considered as an unbounded plane front in the space (see, for example [3],[6],[7],[11],[12]).

Besides that the electromagnetic waves are often raised by electric currents or charges located in some points, curves and surfaces [3],[6],[7]. For example, antenna radiation above the earth's surface is an important subject in radio wave communications. The boundary-value problem of radiation from a dipole antenna above a dielectric isotropic half space was first investigated by Sommerfeld and it thus became known as the Sommerfeld dipole problem. Electromagnetic wave radiations in a dielectric free space and half space from different types of currents(pulse polarized dipole, line currents, sheet currents, and shell currents) have been studied in [3],[6],[7],[11].

The observations of electric and magnetic fields in different anisotropic media generated by electric currents give an information about the dependence of electromagnetic field behavior and the structure of media. These observations allow engineers to study properties of known anisotropic materials and design new materials with the certain response to electric and magnetic fields for given source. Most of electromagnetic scattering problems,

initial value and initial boundary value problems have been solved by numerical methods, in particular, finite elements method, boundary elements methods, finite difference method, nodal method (see, for example, works [1],[9],[10],[13],[18],[20] and their references).

Nowadays computers can perform very complicated symbolic computations (in addition to numerical calculations) and this opens up new possibilities to solve initial value and initial boundary value problems. Symbolic computations can be considered as useful tools for analytical methods that can provide exact solutions of problems.

The main object studied in this paper is the following initial value problem (IVP) of radiation from the electric current in electrically and magnetically anisotropic media

$$\varepsilon\frac{\partial^2\mathbf{E}}{\partial t^2} + curl_x(\mu^{-1}curl_x\mathbf{E}) + \sigma\frac{\partial\mathbf{E}}{\partial t} = -\frac{\partial\mathbf{j}}{\partial t}, \quad (1)$$

$$\mathbf{E}\Big|_{t=0} = 0, \quad \frac{\partial\mathbf{E}}{\partial t}\Big|_{t=0} = 0. \quad (2)$$

In this paper, the IVP (1),(2) is solved using polynomial solution method. The method has been successfully applied to solve some IVPs before. In [14], [17], this method is applied to solve IVP for system of crystal optics for simulations of waves in homogeneous, anisotropic dielectrics and electrically anisotropic materials for the case when $\sigma = 0$, μ is identity matrix. In [15] PS method is applied to IVP for equations of electric and magnetic fields in general electrically and magnetically anisotropic media for the case when $\sigma = 0$, ε and μ are arbitrary matrices. In the paper [16], the method is applied to IVP for Maxwell's equations in bi-anisotropic materials. However, the IVP for Maxwell's equations in conducting media for the case when ε, μ are arbitrary positive definite matrices and σ is a symmetric matrix has not been studied yet.

In this paper, the IVP (1),(2) of radiation from electric current in electrically and magnetically anisotropic media is studied in the case when ε, μ and σ are arbitrary matrices. An analytical method for computing a polynomial solution of the Cauchy problem (1) with constant coefficients is studied. As an assumption the initial data and inhomogeneous term have polynomial presentations with respect to space variables. A solution of the initial value problem is found in polynomial form with undetermined coefficients depending on the time variable. For these undetermined coefficients, the recurrence relations which are used in the procedure of the coefficients recovery are found. To be able to implement this method the following studies are completed:

- Stability estimates (energy inequalities) for solutions of (1) in a finite domain of dependence (a finite domain containing characteristic cones) are described.
- Using these stability estimates, it is justified that the polynomial solutions are approximate solutions of the initial value problems with non-polynomial data.
- These theoretical results are confirmed by computational experiments which compare the exact solutions and polynomial solutions found by explained method.

This method can be applied for the isotropic, anisotropic or bi-anisotropic cases. If compared with the other methods, in the computation there are no grids and discretization which are not clear for complicated media such as anisotropic media. By the polynomial solution method, a solution of the initial value problem can be obtained easily if the initial data and inhomogeneous term have polynomial presentations with respect to space variables.

2. Maxwell system

Maxwell's equations are a set of partial differential equations that relate the electric field and magnetic field to the charge and current densities that specify the fields and give rise to electromagnetic radiation. The time dependent Maxwell equations in anisotropic homogeneous media can be written as follows [1], [11]

$$curl_x\mathbf{H} = \frac{\partial\mathbf{D}}{\partial t} + \mathbf{J}, \quad (3)$$

$$curl_x\mathbf{E} = -\frac{\partial\mathbf{B}}{\partial t}, \quad (4)$$

$$div_x(\mathbf{B}) = 0, \quad (5)$$

$$div_x(\mathbf{D}) = \rho, \quad (6)$$

where $x = (x_1, x_2, x_3)$ be a space variable from $\mathbb{R}^3$ and t be a time variable from $\mathbb{R}$. $\mathbf{E} = (E_1, E_2, E_3)$, $\mathbf{H} = (H_1, H_2, H_3)$ are electric and magnetic fields, with components $E_i = E_i(x,t)$, $H_i = H_i(x,t)$, $i = 1,2,3$; depending on x and t variables.

$\mathbf{D} = (D_1, D_2, D_3)$, $\mathbf{B} = (B_1, B_2, B_3)$ are electric and magnetic displacements with components $D_i = D_i(x,t)$, $B_i = B_i(x,t)$, $i = 1,2,3$; depending on x and t variables.

$\mathbf{J} = (J_1, J_2, J_3)$ is the density of the electric current where $J_i = J_i(x,t), i = 1,2,3$; ρ is the density of electric charges. The conservation law of charges is given by

$$\frac{\partial\rho}{\partial t} + div_x\mathbf{J} = 0.$$

In general, there are some relations that expresses $\mathbf{D}$, $\mathbf{B}$ and $\mathbf{J}$ in terms of $\mathbf{E}$ and $\mathbf{H}$ when the media is electrically and magnetically anisotropic homogeneous, these are

$$\mathbf{D} = \varepsilon\mathbf{E}, \ \mathbf{B} = \mu\mathbf{H}, \ \mathbf{J} = \sigma\mathbf{E} + \mathbf{j}. \quad (7)$$

Here ε is the dielectric permittivity characterizing the electrical properties, μ is magnetic permeability characterizing the magnetical properties, σ is the conductivity and $\mathbf{j}$ is the density of the currents arising from the action of the external electromagnetic forces.

In the paper, we suppose that for $t \le 0$

$$\mathbf{H}\,|_{t\le 0} = 0, \quad \mathbf{E}\,|_{t\le 0} = 0, \quad \mathbf{j}\,|_{t\le 0} = 0, \quad \rho\,|_{t\le 0} = 0. \quad (8)$$

Using equations (3)-(6),(7) and (8), two initial value problems can be obtained. One of the IVP is for the radiation from the electric current that is

$$\varepsilon\frac{\partial^2\mathbf{E}}{\partial t^2}+curl_x(\mu^{-1}curl_x\mathbf{E})+\sigma\frac{\partial\mathbf{E}}{\partial t}=-\frac{\partial\mathbf{j}}{\partial t}, \quad (9)$$

$$\mathbf{E}\Big|_{t=0}=0, \quad \frac{\partial\mathbf{E}}{\partial t}\Big|_{t=0}=0, \quad (10)$$

and other is IVP for magnetic field defined with equations

$$\frac{\partial\mathbf{H}}{\partial t}=-\mu^{-1}curl_x\mathbf{E}, \quad (11)$$

$$\mathbf{H}(x,t)|_{t=0}=0. \quad (12)$$

In this paper, using polynomial solution method (PS-method) the initial value problem (9),(10) is solved to obtain polynomial solution of electric field $\mathbf{E}(x,t)$. Using the solution of IVP (9),(10) IVP for magnetic field $\mathbf{H}(x,t)$ is solved symbolically.

As an assumption the matrices ε, μ that characterizes the electrical and magnetical properties are taken as symmetric positive definite matrices with constant elements and the conductivity σ is taken as a symmetric positive semi definite matrix with constant elements. Also, the components $j_i(x,t)$ of density of the current $\mathbf{j}(x,t)$ are considered in the following polynomial form

$$j_i(x,t)=\sum_{k=0}^{p}\sum_{m=0}^{p}\sum_{n=0}^{p}j_i^{k,m,n}(t)x_1^kx_2^mx_3^n, \quad (13)$$

where p is a fixed number. Using existence theorems it can be shown that the solution of the problem can be written in the form

$$E_i(x,t)=\sum_{k=0}^{\infty}\sum_{m=0}^{\infty}\sum_{n=0}^{\infty}E_i^{k,m,n}(t)x_1^kx_2^mx_3^n.$$

Applying the operator $D^\alpha=\dfrac{\partial^{|\alpha|}}{\partial x_1^\alpha\partial x_2^\alpha\partial x_3^\alpha}$ to (9),(10) for $\alpha>p$, following IVP can be obtained

$$\varepsilon\frac{\partial^2\mathbf{E}^\alpha}{\partial t^2}+curl_x(\mu^{-1}curl_x\mathbf{E}^\alpha)+\sigma\frac{\partial\mathbf{E}^\alpha}{\partial t}=0,$$

$$\mathbf{E}^\alpha\Big|_{t=0}=0, \quad \frac{\partial\mathbf{E}^\alpha}{\partial t}\Big|_{t=0}=0,$$

where $\mathbf{E}^\alpha=D^\alpha\mathbf{E}$.

The solutions of the IVP is $\mathbf{E}^\alpha=0$ inside the conoid of dependence, since $\mathbf{j}_i^\alpha=0$ for $\alpha>p$. Thus the components of the solution of the IVP (9),(10) is in the polynomial form

$$E_i(x,t)=\sum_{k=0}^{p}\sum_{m=0}^{p}\sum_{n=0}^{p}E_i^{k,m,n}(t)x_1^kx_2^mx_3^n$$

3. Initial value problems for electric and magnetic field

In this section, let us consider the IVP (9),(10) with inhomogeneous term that has polynomial presentation with respect to space variables. Note following theorem from [4] that is

Theorem. If ε is positive definite and σ is symmetric, positive semi-definite matrix then there exists a nonsingular matrix $\mathcal{S}=(S_{ij})$; $(i,j=1,2,3)$ such that

$$\mathcal{S}^T\varepsilon\mathcal{S}=I,$$

$$\mathcal{S}^T\sigma\mathcal{S}=\mathcal{D},$$

where $\mathcal{D}=(d_1,d_2,d_3)$, $d_j\geq 0$ $(j=1,2,3)$ is the diagonal matrix with eigenvalues of $\varepsilon^{-\frac{1}{2}}\sigma\varepsilon^{-\frac{1}{2}}$ on diagonal. Using this theorem and considering $\mathbf{E}=S\tilde{\mathbf{E}}$ in (9),(10) and multiplying with $\mathcal{S}^T$ from left hand side we obtain

$$\frac{\partial^2\tilde{\mathbf{E}}}{\partial t^2}+\mathcal{S}^Tcurl_x(\mathcal{M}^{-1}curl_x(\mathcal{S}\tilde{\mathbf{E}}))+\mathcal{D}\frac{\partial\tilde{\mathbf{E}}}{\partial t}=-\mathcal{S}^T\frac{\partial\mathbf{j}}{\partial t}, \quad (14)$$

$$\tilde{\mathbf{E}}(x,0)=0, \ \frac{\partial\tilde{\mathbf{E}}(x,t)}{\partial t}\Big|_{t=0}=0, x\in R^3. \quad (15)$$

$$(x\in R^3,\ t>0)$$

Let us consider the solution of (14),(15) in the following form

$$\tilde{\mathbf{E}}(x_1,x_2,x_3,t)=\sum_{k=0}^{p}\sum_{m=0}^{p}\sum_{n=0}^{p}\tilde{\mathbf{E}}^{k,m,n}(t)x_1^kx_2^mx_3^n, \quad (16)$$

where $\tilde{\mathbf{E}}^{k,m,n}(t)=\mathcal{S}^T\mathbf{E}^{k,m,n}(t)$, $\mathbf{E}^{k,m,n}(t)=(E_1^{k,m,n}(t),E_2^{k,m,n}(t),E_3^{k,m,n}(t))$. Substituting (13),(16) into (14) and (15) following IVP for ordinary differential equations are obtained

$$\frac{d^2\tilde{E}_i^{k,m,n}}{dt^2}+d_i\frac{d\tilde{E}_i^{k,m,n}}{dt}=\tilde{f}_i^{k,m,n}, \quad i=1,2,3, \quad (17)$$

$$\tilde{E}_i^{k,m,n}\Big|_{t=0}=0, \quad \frac{d\tilde{E}_i^{k,m,n}}{dt}\Big|_{t=0}=0, \quad (18)$$

here

$$\tilde{f}_i^{k,m,n}=\left(S^T\left(-\frac{\partial j}{\partial t}\right)\right)_i-S_{i1}^TB_1-S_{i2}^TB_2-S_{i3}^TB_3, \qquad i=1,2,3$$

where

$B_1=\mu_{31}^{-1}\Big((m+2)(m+1)\Big(S_{31}\tilde{E}_1^{k,m+2,n}+S_{32}\tilde{E}_2^{k,m+2,n}+S_{33}\tilde{E}_3^{k,m+2,n}\Big)\Big)-\mu_{31}^{-1}\Big((m+1)(n+1)\Big(S_{21}\tilde{E}_1^{k,m+1,n+1}+S_{22}\tilde{E}_2^{k,m+1,n+1}+S_{23}\tilde{E}_3^{k,m+1,n+1}\Big)\Big)+\mu_{32}^{-1}\Big((m+1)(n+1)\Big(S_{11}\tilde{E}_1^{k,m+1,n+1}+S_{12}\tilde{E}_2^{k,m+1,n+1}+S_{13}\tilde{E}_3^{k,m+1,n+1}\Big)\Big)-$

$$\mu_{32}^{-1}\Big((k+1)(m+1)\Big(S_{31}\tilde{E}_1^{k+1,m+1,n}+S_{32}\tilde{E}_2^{k+1,m+1,n}+S_{33}\tilde{E}_3^{k+1,m+1,n}\Big)\Big)+\mu_{33}^{-1}\Big((k+1)(m+1)\Big(S_{21}\tilde{E}_1^{k+1,m+1,n}+S_{22}\tilde{E}_2^{k+1,m+1,n}+S_{23}\tilde{E}_3^{k+1,m+1,n}\Big)\Big)-\mu_{33}^{-1}\Big((m+2)(m+1)\Big(S_{11}\tilde{E}_1^{k,m+2,n}+S_{12}\tilde{E}_2^{k,m+2,n}+S_{13}\tilde{E}_3^{k,m+2,n}\Big)\Big)+\mu_{21}^{-1}\Big((n+2)(n+1)\Big(S_{21}\tilde{E}_1^{k,m,n+2}+S_{22}\tilde{E}_2^{k,m,n+2}+S_{23}\tilde{E}_3^{k,m,n+2}\Big)\Big)-\mu_{21}^{-1}\Big((m+1)(n+1)\Big(S_{31}\tilde{E}_1^{k,m+1,n+1}+S_{32}\tilde{E}_2^{k,m+1,n+1}+S_{33}\tilde{E}_3^{k,m+1,n+1}\Big)\Big)+\mu_{22}^{-1}\Big((k+1)(n+1)\Big(S_{31}\tilde{E}_1^{k+1,m,n+1}+S_{32}\tilde{E}_2^{k+1,m,n+1}+S_{33}\tilde{E}_3^{k+1,m,n+1}\Big)\Big)-\mu_{22}^{-1}\Big((n+2)(n+1)\Big(S_{11}\tilde{E}_1^{k,m,n+2}+S_{12}\tilde{E}_2^{k,m,n+2}+S_{13}\tilde{E}_3^{k,m,n+2}\Big)\Big)+\mu_{23}^{-1}\Big((m+1)(n+1)\Big(S_{11}\tilde{E}_1^{k,m+1,n+1}+S_{12}\tilde{E}_2^{k,m+1,n+1}+S_{13}\tilde{E}_3^{k,m+1,n+1}\Big)\Big)-\mu_{23}^{-1}\Big((k+1)(n+1)\Big(S_{21}\tilde{E}_1^{k+1,m,n+1}+S_{22}\tilde{E}_2^{k+1,m,n+1}+S_{23}\tilde{E}_3^{k+1,m,n+1}\Big)\Big),$$

$$B_2=\mu_{11}^{-1}\Big((m+1)(n+1)\Big(S_{31}\tilde{E}_1^{k,m+1,n+1}+S_{32}\tilde{E}_2^{k,m+1,n+1}+S_{33}\tilde{E}_3^{k,m+1,n+1}\Big)\Big)-\mu_{11}^{-1}\Big((n+2)(n+1)\Big(S_{21}\tilde{E}_1^{k,m,n+2}+S_{22}\tilde{E}_2^{k,m,n+2}+S_{23}\tilde{E}_3^{k,m,n+2}\Big)\Big)+\mu_{12}^{-1}\Big((n+2)(n+1)\Big(S_{11}\tilde{E}_1^{k,m,n+2}+S_{12}\tilde{E}_2^{k,m,n+2}+S_{13}\tilde{E}_3^{k,m,n+2}\Big)\Big)-\mu_{12}^{-1}\Big((k+1)(n+1)\Big(S_{31}\tilde{E}_1^{k+1,m,n+1}+S_{32}\tilde{E}_2^{k+1,m,n+1}+S_{33}\tilde{E}_3^{k+1,m,n+1}\Big)\Big)+\mu_{13}^{-1}\Big((k+1)(n+1)\Big(S_{21}\tilde{E}_1^{k+1,m,n+1}+S_{22}\tilde{E}_2^{k+1,m,n+1}+S_{23}\tilde{E}_3^{k+1,m,n+1}\Big)\Big)-\mu_{13}^{-1}\Big((m+1)(n+1)\Big(S_{11}\tilde{E}_1^{k,m+1,n+1}+S_{12}\tilde{E}_2^{k,m+1,n+1}+S_{13}\tilde{E}_3^{k,m+1,n+1}\Big)\Big)+\mu_{31}^{-1}\Big((k+1)(n+1)\Big(S_{21}\tilde{E}_1^{k+1,m,n+1}+S_{22}\tilde{E}_2^{k+1,m,n+1}+S_{23}\tilde{E}_3^{k+1,m,n+1}\Big)\Big)-\mu_{31}^{-1}\Big((k+1)(m+1)\Big(S_{31}\tilde{E}_1^{k+1,m+1,n}+S_{32}\tilde{E}_2^{k+1,m+1,n}+S_{33}\tilde{E}_3^{k+1,m+1,n}\Big)\Big)+\mu_{32}^{-1}\Big((k+2)(k+1)\Big(S_{31}\tilde{E}_1^{k+2,m,n}+S_{32}\tilde{E}_2^{k+2,m,n}+S_{33}\tilde{E}_3^{k+2,m,n}\Big)\Big)-\mu_{32}^{-1}\Big((k+1)(n+1)\Big(S_{11}\tilde{E}_1^{k+1,m,n+1}+S_{12}\tilde{E}_2^{k+1,m,n+1}+S_{13}\tilde{E}_3^{k+1,m,n+1}\Big)\Big)+\mu_{33}^{-1}\Big((k+1)(m+1)(S_{11}\tilde{E}_1^{k+1,m+1,n}+S_{12}\tilde{E}_2^{k+1,m+1,n}+S_{13}\tilde{E}_3^{k+1,m+1,n}\Big)\Big)-\mu_{33}^{-1}\Big((k+2)(k+1)\Big(S_{21}\tilde{E}_1^{k+2,m,n}+S_{22}\tilde{E}_2^{k+2,m,n}+S_{23}\tilde{E}_3^{k+2,m,n}\Big)\Big),$$

$$B_3=\mu_{21}^{-1}\Big((k+1)(m+1)\Big(S_{31}\tilde{E}_1^{k+1,m+1,n}+S_{32}\tilde{E}_2^{k+1,m+1,n}+S_{33}\tilde{E}_3^{k+1,m+1,n}\Big)\Big)-\mu_{21}^{-1}\Big((k+1)(n+1)\Big(S_{21}\tilde{E}_1^{k+1,m,n+1}+S_{22}\tilde{E}_2^{k+1,m,n+1}+S_{23}\tilde{E}_3^{k+1,m,n+1}\Big)\Big)+\mu_{22}^{-1}\Big((k+1)(n+1)\Big(S_{11}\tilde{E}_1^{k+1,m,n+1}+S_{12}\tilde{E}_2^{k+1,m,n+1}+S_{13}\tilde{E}_3^{k+1,m,n+1}\Big)\Big)-\mu_{22}^{-1}\Big((k+2)(k+1)\Big(S_{31}\tilde{E}_1^{k+2,m,n}+S_{32}\tilde{E}_2^{k+2,m,n}+S_{33}\tilde{E}_3^{k+2,m,n}\Big)\Big)+\mu_{23}^{-1}\Big((k+2)(k+1)\Big(S_{21}\tilde{E}_1^{k+2,m,n}+S_{22}\tilde{E}_2^{k+2,m,n}+S_{23}\tilde{E}_3^{k+2,m,n}\Big)\Big)-\mu_{23}^{-1}\Big((k+1)(m+1)(S_{11}\tilde{E}_1^{k+1,m+1,n}+S_{12}\tilde{E}_2^{k+1,m+1,n}+S_{13}\tilde{E}_3^{k+1,m+1,n}\Big)\Big)+\mu_{11}^{-1}\Big((m+1)(n+1)\Big(S_{21}\tilde{E}_1^{k,m+1,n+1}+S_{22}\tilde{E}_2^{k,m+1,n+1}+S_{23}\tilde{E}_3^{k,m+1,n+1}\Big)\Big)-\mu_{11}^{-1}\Big((m+2)(m+1)\Big(S_{31}\tilde{E}_1^{k,m+2,n}+S_{32}\tilde{E}_2^{k,m+2,n}+S_{33}\tilde{E}_3^{k,m+2,n}\Big)\Big)+\mu_{12}^{-1}\Big((k+1)(m+1)\Big(S_{31}\tilde{E}_1^{k+1,m+1,n}+S_{32}\tilde{E}_2^{k+1,m+1,n}+S_{33}\tilde{E}_3^{k+1,m+1,n}\Big)\Big)-\mu_{12}^{-1}\Big((m+1)(n+1)\Big(S_{11}\tilde{E}_1^{k,m+1,n+1}+S_{12}\tilde{E}_2^{k,m+1,n+1}+S_{13}\tilde{E}_3^{k,m+1,n+1}\Big)\Big)+\mu_{13}^{-1}\Big((m+2)(m+1)\Big(S_{11}\tilde{E}_1^{k,m+2,n}+S_{12}\tilde{E}_2^{k,m+2,n}+S_{13}\tilde{E}_3^{k,m+2,n}\Big)\Big)-\mu_{13}^{-1}\Big((k+1)(m+1)\Big(S_{21}\tilde{E}_1^{k+1,m+1,n}+S_{22}\tilde{E}_2^{k+1,m+1,n}+S_{23}\tilde{E}_3^{k+1,m+1,n}\Big)\Big).$$

The solution of the IVP (17),(18) is

$$\tilde{E}_i^{k,m,n}=\frac{1}{d_i}\int_0^t(1-e^{d_i(\tau-t)})\tilde{f}_i^{k,m,n}(\tau)d\tau,\quad i=1,2,3. \tag{19}$$

Using (16) and (19), the solution $\tilde{\mathbf{E}}(x,t)$ of (14),(15) can be obtained. Since $\mathbf{E}=\mathcal{S}\tilde{\mathbf{E}}$ then a solution of the IVP (9),(10) can be obtained in polynomial form. Using the solution of IVP (9),(10), the IVP (11),(12) can be solved by symbolic calculation.

4. Existence of solutions for the IVPs

Equations (3)-(6),(8) can be rewritten as a first order hyperbolic system in the form

$$A_0\frac{\partial\mathbf{U}}{\partial t}+\sum_{j=1}^{3}A_j\frac{\partial\mathbf{U}}{\partial x_j}+B\mathbf{U}=\mathbf{F}, \tag{20}$$

$$\mathbf{U}(x,t)\Big|_{t=0}=0, \tag{21}$$

where $\mathbf{U}=\begin{pmatrix}\mathbf{E}\\ \mathbf{H}\end{pmatrix}$, $A_0=\begin{pmatrix}\varepsilon & 0\\ 0 & \mu\end{pmatrix}$, $B=\begin{pmatrix}\sigma & 0\\ 0 & 0\end{pmatrix}$ and $\mathbf{F}=-\begin{pmatrix}\mathbf{j}\\ \mathbf{0}\end{pmatrix}$, and the matrix A_j is defined as

$$A_j=\begin{pmatrix}0_{3\times3} & A_j^1\\ (A_j^1)^* & 0_{3\times3}\end{pmatrix}.$$

which has the components

$$A_1^1=\begin{pmatrix}0&0&0\\0&0&1\\0&-1&0\end{pmatrix},\quad A_2^1=\begin{pmatrix}0&0&-1\\0&0&0\\1&0&0\end{pmatrix},$$

$$A_3^1=\begin{pmatrix}0&1&0\\-1&0&0\\0&0&0\end{pmatrix}.$$

Consider the symmetric positive definite matrix A_0. There exists a symmetric positive definite matrix S such that $A_0^{-1} = S^2$, that is, $A_0^{-\frac{1}{2}} = S$. Let us denote the vector

$$\mathbf{U}(x) = S\mathbf{u}(x) \tag{22}$$

Substituting (22) into (20),(21) and multiplying the resulting formula with matrix S from the left hand side we obtain

$$\frac{\partial \mathbf{u}}{\partial t} + \sum_{j=1}^{n} \widetilde{A}_j \frac{\partial \mathbf{u}}{\partial x_j} + \widetilde{B}\mathbf{u} = \mathbf{f},\ x \in \mathbb{R}^n,\ t > 0, \tag{23}$$

$$\mathbf{u}(x,t)\Big|_{t=0} = 0,\ x \in \mathbb{R}^n, \tag{24}$$

where

$$I_6 = SA_0S, \widetilde{A}_j = SA_jS, \widetilde{B} = SBS, \mathbf{f} = S\mathbf{F}.$$

Since S and A_j, $j = 1,2,3$ are symmetric, the matrix $\widetilde{A}_j$ will also be symmetric, which implies that (23) is a symmetric hyperbolic system.

Theorem. Let $\widetilde{A}_j$ is a symmetric matrix with constant entries and let T be a fixed positive number then for an arbitrary $f_j(x,t) \in C([0,T];\mathcal{H}^1(\mathbb{R}^3))$ we have a unique solution of (23),(24) such that

$$u_j(x,t) \in C([0,T];\mathcal{H}^1(\mathbb{R}^3)) \cap C^1([0,T];\mathcal{L}^2(\mathbb{R}^3))$$

The theorem and the proof of the theorem can be found in [8].

5. Domain of dependence and uniqueness theorem inside conoid of dependence

In this section we describe the domain of dependence for first order symmetric hyperbolic systems and prove that the solution of the system is uniquely determined inside the conoid of dependence [2], [5], [19]. And we obtain the theorem for the uniqueness of the solution of considered IVPs.

Let us consider the symmetric hyperbolic system of the form (23),(24) where each $\widetilde{A}_j(x)$ is an $m \times m$ symmetric matrix. Let

$$\mathbf{A}(\xi) = \sum_{j=1}^{n} \widetilde{A}_j \xi_j$$

and $\lambda_j(\xi)$, $j = 1,\dots,m$ be the eigenvalues of $\mathbf{A}(\xi)$. We define the constant M as

$$M = \max_{\substack{i=1,\dots,m \\ |\xi|=1}} |\lambda_j(\xi)|. \tag{25}$$

Using the constant M we define the following domains for the arbitrary point P with coordinates $(x^0,t^0) \in \mathbb{R}^n \times (0,\infty)$

$$\Gamma(P) = \left\{(x,t) : 0 \le t \le t^0, |x - x^0| \le M(t^0 - t)\right\},$$
$$S(h) = \left\{x \in \mathbb{R}^n : |x - x^0| \le M|t^0 - h|\right\},\ 0 \le h \le t^0,$$
$$R(h) = \left\{(x,t) : 0 \le t \le h, |x - x^0| = M|t^0 - t|\right\}.$$

Here $\Gamma(P)$ is the conoid of dependence with vertex P. $S(h)$ is the surface constructed by the intersection of the plane $t = h$ and the conoid $\Gamma(P)$. For $t = 0$, $S(0)$ is the base of the conoid. $R(h)$ is the lateral surface of the conoid bounded by $S(0)$ and $S(h)$.

Theorem.(see, [2]) Let $(x^0,t^0) \in \mathbb{R}^n \times (0,\infty)$, and $S(h)$, $R(h)$, $\Gamma(P)$ be as defined above, and $\mathbf{u}(x,t) \in C([0,T];\mathcal{H}^1(\mathbb{R}^n;\mathbb{R}^m)) \cap C^1([0,T];\mathcal{L}^2(\mathbb{R}^n;\mathbb{R}^m))$ be a solution of (23). Then the following energy inequality is valid

$$\int_{S(h)} |\mathbf{u}(x,h)|^2 dx \le e^{Kh} \int_0^h \int_{S(t)} |\mathbf{f}(x,t)|^2 dxdt,$$

if

$$\max_j \max_{k,l} \max_{x \in S(0)} \left|\frac{\partial a_{kl}^j}{\partial x_j}\right| \le L, \quad \max_{k,l} \max_{x \in S(0)} \left|b_{kl}(x)\right| \le L.$$

Proof. Let Ω be the region bounded by $S(0)$, $S(h)$, $R(h)$ and $\partial\Omega = S(0) \cup S(h) \cup R(h)$. Multiplying (23) with $\mathbf{u}$ and integrating over Ω we have

$$\int_\Omega \left\{\mathbf{u}.\frac{\partial \mathbf{u}}{\partial t} + \mathbf{u}.\left(\sum_{j=1}^{n} \widetilde{A}_j \frac{\partial \mathbf{u}}{\partial x_j}\right)\right\} dxdt + \int_\Omega \mathbf{u}.\widetilde{B}(x)\mathbf{u}dxdt = \int_\Omega \mathbf{u}.\mathbf{f}dxdt. \tag{26}$$

Noting the relations

$$\mathbf{u}.\frac{\partial \mathbf{u}}{\partial t} = \frac{1}{2}\frac{\partial |\mathbf{u}|^2}{\partial t},$$
$$\mathbf{u}.\left(\sum_{j=1}^{n} \widetilde{A}_j \frac{\partial \mathbf{u}}{\partial x_j}\right) = \frac{1}{2}\sum_{j=1}^{n} \frac{\partial}{\partial x_j}\left(\mathbf{u}.\widetilde{A}_j\mathbf{u}\right) - \frac{1}{2}\sum_{j=1}^{n}\left(\mathbf{u}.\frac{\partial \widetilde{A}_j}{\partial x_j}\mathbf{u}\right)$$

Equation (26) can be rewritten as follows

$$\frac{1}{2}\int_\Omega \left\{\frac{\partial |\mathbf{u}|^2}{\partial t} + \sum_{j=1}^{n} \frac{\partial}{\partial x_j}\left(\mathbf{u}.\widetilde{A}_j\mathbf{u}\right) - \sum_{j=1}^{n}\left(\mathbf{u}.\frac{\partial \widetilde{A}_j}{\partial x_j}\mathbf{u}\right)\right\} dxdt + \int_\Omega \mathbf{u}.\widetilde{B}(x)\mathbf{u}dxdt = \int_\Omega \mathbf{u}.\mathbf{f}dxdt$$

and applying the divergence theorem one can get

$$\frac{1}{2}\int_{\partial\Omega}\left\{|\mathbf{u}|^2\nu_t+\sum_{j=1}^{n}\left(\mathbf{u}.\widetilde{A}_j\mathbf{u}\right)\nu_j\right\}dS - \frac{1}{2}\int_{\Omega}\sum_{j=1}^{n}\left(\mathbf{u}.\frac{\partial\widetilde{A}_j}{\partial x_j}\mathbf{u}\right)dxdt+\int_{\Omega}\mathbf{u}.\widetilde{B}(x)\mathbf{u}dxdt = \int_{\Omega}\mathbf{u}.\mathbf{f}dxdt, \tag{27}$$

where $\nu=(\nu_1,\ldots,\nu_n,\nu_t)$ is the outward unit normal on $\partial\Omega$. Since $\partial\Omega=S(0)\cup S(h)\cup R(h)$ and

$$\begin{aligned}\nu &= (0,\ldots,1) \quad \text{on} \quad S(h),\\ \nu &= (0,\ldots,-1) \quad \text{on} \quad S(0),\\ \nu &= \frac{(x_1-x_1^0,\ldots,x_n-x_n^0,M^2(t^0-t))}{(t^0-t)M\sqrt{1+M^2}} \quad \text{on} \quad R(h),\end{aligned}$$

formula (27) takes the form

$$\frac{1}{2}\int_{S(h)}|\mathbf{u}|^2dx-\frac{1}{2}\int_{S(0)}|\mathbf{u}|^2dx+\frac{1}{2}\int_{R(h)}|\mathbf{u}|^2\frac{M}{\sqrt{1+M^2}}dS + \frac{1}{2}\int_{R(h)}\sum_{j=1}^{n}\left(\mathbf{u}.\widetilde{A}_j\mathbf{u}\right)\frac{x_j-x_j^0}{(t^0-t)M\sqrt{1+M^2}}dS - \frac{1}{2}\int_{\Omega}\left\{\sum_{j=1}^{n}\mathbf{u}.\frac{\partial\widetilde{A}_j}{\partial x_j}\mathbf{u}-2\mathbf{u}.\widetilde{B}\mathbf{u}\right\}dxdt = \int_{\Omega}\mathbf{u}.\mathbf{f}dxdt. \tag{28}$$

Let us denote

$$\xi_j=\frac{(x_j-x_j^0)}{(t^0-t)M},\quad j=1,\ldots,n,$$

which satisfies $|\xi|=\sqrt{\xi_1^2+\ldots+\xi_n^2}=1$. Using this notation and

$$\mathbf{A}(\xi)=\sum_{j=1}^{n}\widetilde{A}_j\xi_j,$$

we write the following equality

$$\frac{1}{2}\int_{R(h)}\sum_{j=1}^{n}\left(\mathbf{u}.\widetilde{A}_j\mathbf{u}\right)\frac{x_j-x_j^0}{(t^0-t)M\sqrt{1+M^2}}dS = \frac{1}{2\sqrt{1+M^2}}\int_{R(h)}\sum_{j=1}^{n}\left(\mathbf{u}.\widetilde{A}_j\xi_j\mathbf{u}\right)dS = \frac{1}{2\sqrt{1+M^2}}\int_{R(h)}(\mathbf{u}.\mathbf{A}(\xi)\mathbf{u})\,dS. \tag{29}$$

Substituting (29) into (28) we get

$$\frac{1}{2}\int_{S(h)}|\mathbf{u}|^2dx-\frac{1}{2}\int_{S(0)}|\mathbf{u}|^2dx + \frac{1}{2\sqrt{1+M^2}}\int_{R(h)}\left[|\mathbf{u}|^2M+\mathbf{u}.\mathbf{A}(\xi)\mathbf{u}\right]dS - \frac{1}{2}\int_{\Omega}\left\{\sum_{j=1}^{n}\mathbf{u}.\frac{\partial\widetilde{A}_j}{\partial x_j}\mathbf{u}-2\mathbf{u}.\widetilde{B}\mathbf{u}\right\}dxdt = \int_{\Omega}\mathbf{u}.\mathbf{f}dxdt. \tag{30}$$

Consider the term $M\mathbf{I}+\mathbf{A}(\xi)$, where $\mathbf{I}$ is the identity matrix of order $m\times m$. Since $\mathbf{A}(\xi)$ is diagonalizable we can find a matrix $\mathbf{Z}$ which reduces $\mathbf{A}(\xi)$ to a diagonal matrix of its eigenvalues, denoted $\mathrm{diag}(\lambda_1,\lambda_2,\ldots,\lambda_m)$. Multiplying $M\mathbf{I}+\mathbf{A}(\xi)$ with matrix $\mathbf{Z}$ from right, and with its inverse $\mathbf{Z}^{-1}$, from left we have

$$\begin{aligned}\mathbf{Z}^{-1}\left(M\mathbf{I}+\mathbf{A}(\xi)\right)\mathbf{Z} &= \mathbf{Z}^{-1}M\mathbf{I}\mathbf{Z}+\mathbf{Z}^{-1}\mathbf{A}(\xi)\mathbf{Z}\\ &= M\mathbf{I}+\mathbf{Z}^{-1}\mathbf{A}(\xi)\mathbf{Z}\\ &= \mathrm{diag}(M,M,\ldots,M)\\ &\quad+\mathrm{diag}(\lambda_1,\lambda_2,\ldots,\lambda_m).\end{aligned}$$

Noting the formula (25), we conclude that the matrix $M\mathbf{I}+\mathbf{A}(\xi)$ has positive eigenvalues, which implies that it is a positive-definite matrix, and from the definition of positive-definiteness we obtain the following inequality

$$|\mathbf{u}|^2M+\mathbf{u}.\mathbf{A}(\xi)\mathbf{u}=\mathbf{u}.(M\mathbf{I}+\mathbf{A}(\xi))\mathbf{u}\geq 0.$$

Thus (30) becomes

$$\frac{1}{2}\int_{S(h)}|\mathbf{u}|^2dx-\frac{1}{2}\int_{S(0)}|\mathbf{u}|^2dx - \frac{1}{2}\int_{\Omega}\left\{\sum_{j=1}^{n}\mathbf{u}.\frac{\partial\widetilde{A}_j}{\partial x_j}\mathbf{u}-2\mathbf{u}.\widetilde{B}\mathbf{u}\right\}dxdt - \int_{\Omega}\mathbf{u}.\mathbf{f}dxdt\leq 0. \tag{31}$$

Remark. Let us denote

$$\frac{\partial\widetilde{A}_j}{\partial x_j}=\left(\frac{\partial a_{kl}^j}{\partial x_j}\right),$$

and

$$\max_j\max_{k,l}\max_{x\in S(0)}\left|\frac{\partial a_{kl}^j}{\partial x_j}\right|\leq L,$$

$$\max_{k,l}\max_{x\in S(0)}\left|b_{kl}(x)\right|\leq L.$$

Since

$$\sum_{j=1}^{n}\mathbf{u}.\frac{\partial\widetilde{A}_j}{\partial x_j}\mathbf{u}-2\mathbf{u}.\widetilde{B}\mathbf{u}=\left\langle\mathbf{u},\left(\sum_{j=1}^{n}\frac{\partial\widetilde{A}_j}{\partial x_j}-2\widetilde{B}\right)\mathbf{u}\right\rangle,$$

then

$$\left|\left\langle \mathbf{u}, \left(\sum_{j=1}^{n} \frac{\partial \widetilde{A}_j}{\partial x_j} - 2\widetilde{B}\right)\mathbf{u}\right\rangle\right| = \left|\left\langle \mathbf{u}, \sum_{j=1}^{n} \frac{\partial \widetilde{A}_j}{\partial x_j}\mathbf{u}\right\rangle - 2\left\langle \mathbf{u}, \widetilde{B}\mathbf{u}\right\rangle\right|,$$
$$\leq L\Big[\sum_{j=1}^{n}\left\langle \mathbf{u}, \mathbf{u}\right\rangle + 2\left\langle \mathbf{u}, \mathbf{u}\right\rangle\Big],$$
$$\leq L(n+2)\left\langle \mathbf{u}, \mathbf{u}\right\rangle,$$
$$\leq L(n+2)\left|\mathbf{u}(x,t)\right|^2.$$

Using previous remark, the inequality (31) becomes

$$\frac{1}{2}\int_{S(h)} |\mathbf{u}|^2 dx - \frac{1}{2}\int_{S(0)} |\mathbf{u}|^2 dx - \int_{\Omega} \mathbf{u}.\mathbf{f} dx dt \leq L(n+2)\int_0^h \int_{S(h)} \left|\mathbf{u}(x,t)\right|^2 dx dt.$$

Denoting

$$\frac{1}{2}\int_{S(\tau)} |\mathbf{u}(x,\tau)|^2 dx = w(\tau),$$

we have

$$w(h) \leq w(0) + 2(n+2)L\int_0^h w(t)dt + \int_0^h w(t)dt + \frac{1}{2}\int_0^h \int_{S(t)} |\mathbf{f}(x,t)|^2 dx dt.$$

Using Gronwall's Lemma we obtain

$$w(h) \leq \Big(w(0) + \frac{1}{2}\int_0^h \int_{S(t)} |\mathbf{f}(x,t)|^2 dx dt\Big)e^{Kh}.$$
$$(K = 2(n+2)L + 1)$$

Then we get the energy inequality

$$\int_{S(h)} |\mathbf{u}(x,h)|^2 dx \leq e^{Kh}\int_0^h \int_{S(t)} |\mathbf{f}(x,t)|^2 dx dt.$$

Thus, the stability estimate for solution of (20),(21) is

$$\int_{S(h)} |A_0^{\frac{1}{2}}\mathbf{U}(x,h)|^2 dx \leq e^{Kh}\int_0^h \Big(\int_{S(t)} |A_0^{-\frac{1}{2}}\mathbf{F}(x,t)|^2 dx\Big)dt.$$

Theorem. (Uniqueness Theorem for the IVP)
Let $x \in \mathbb{R}^n$, $t > 0$ and $\widetilde{A}_j(x)$ is an $m \times m$ symmetric matrix then following Initial Value Problem has unique solution

$$\frac{\partial \mathbf{u}}{\partial t} + \sum_{j=1}^{n} \widetilde{A}_j \frac{\partial \mathbf{u}}{\partial x_j} + \widetilde{B}(x)\mathbf{u} = \mathbf{f},$$
$$\mathbf{u}(x,0) = \varphi(x),$$

Proof. Assume that we have two solutions u and u^* corresponding to the same data φ and the same inhomogeneous term f. Let $\hat{\mathbf{u}} = \mathbf{u} - \mathbf{u}^*$. Then $\hat{\mathbf{u}}$ satisfies

$$\frac{\partial \hat{\mathbf{u}}}{\partial t} + \sum_{j=1}^{n} \widetilde{A}_j \frac{\partial \hat{\mathbf{u}}}{\partial x_j} + \widetilde{B}(x)\hat{\mathbf{u}} = 0,$$
$$\hat{\mathbf{u}}(x,0) = 0,$$

Applying energy inequality we have

$$\int_{S(h)} |\hat{\mathbf{u}}(x,h)|^2 dx \leq \int_{S(0)} |\hat{\mathbf{u}}(x,0)|^2 dx = 0,$$
$$0 \leq \int_{S(h)} |\hat{\mathbf{u}}(x,h)|^2 dx \leq 0, \text{ for all } h \in [0,T].$$

Hence

$$|\hat{\mathbf{u}}(x,h)|^2 \equiv 0, \text{ for all } h \in [0,T],\ x \in S(h),$$

then we have

$$\mathbf{u}(x,h) - \mathbf{u}^*(x,h) \equiv 0, \text{ for all } h \in [0,T],\ x \in S(h),$$

that is,

$$\mathbf{u}(x,h) \equiv \mathbf{u}^*(x,h), \text{ for all } h \in [0,T],\ x \in S(h).$$

This proves the uniqueness theorem.

6. Implementation of the method

In this section, our aim is to implement the method to a simplified form of the problem and sketch out how the method works.

For implementation of PS method, let us consider the IVP (9),(10) with $-\frac{\partial j}{\partial t} = (f,0,0)$, $\varepsilon = I_{3\times 3}$, $\mu^{-1} = \text{diag}\,(\mu_{11},\mu_{22},\mu_{33})$, $\sigma = \text{diag}\,(\sigma_{11},\sigma_{22},\sigma_{33})$. Let $f(x,t)$ has an approximation in the domain of dependence in the form

$$f(x,t) = \sum_{n=0}^{p} f^n(t)x^n, \tag{32}$$

where $x \in \mathbb{R}, t \in \mathbb{R}$ and $p \in \mathbb{N}$. The solution $\mathbf{E}(x,t) = (E_1(x,t), E_2(x,t), E_3(x,t))$ of the problem will be in the form

$$\mathbf{E}(x,t) = \sum_{n=0}^{p} \mathbf{E}(x,t)^n(t)x^n \tag{33}$$

Substituting (32) and (33) into the IVP (9),(10) we get

$$\frac{\partial^2 E_1^n}{\partial t^2} - \mu_{22}(n+2)(n+1)E_1^{n+2} + \sigma_{11}\frac{\partial E_1^n}{\partial t} = f_1^n(t)$$
$$E_1^n\big|_{t=0} = 0, \quad \frac{\partial E_1^n}{\partial t}\Big|_{t=0} = 0, \tag{34}$$

$$\frac{\partial^2 E_2^n}{\partial t^2} + \sigma_{22}\frac{\partial E_2^n}{\partial t} = 0, \qquad E_2^n\big|_{t=0} = 0, \quad \left.\frac{\partial E_2^n}{\partial t}\right|_{t=0} = 0, \tag{35}$$

$$\frac{\partial^2 E_3^n}{\partial t^2} + \sigma_{33}\frac{\partial E_3^n}{\partial t} = 0, \qquad E_3^n\big|_{t=0} = 0, \quad \left.\frac{\partial E_3^n}{\partial t}\right|_{t=0} = 0. \tag{36}$$

The solutions of IVPs (35),(36) are $E_2^n(t) = 0, E_3^n(t) = 0$. Also the IVP (34) for any $n > p$ we have $E_1^n(t) = 0$. Let us start PS method computation when $n = p$. For $n = p$ we have

$$\frac{\partial^2 E_1^p}{\partial t^2} - \mu_{22}(p+2)(p+1)E_1^{p+2} + \sigma_{11}\frac{\partial E_1^p}{\partial t} = f_1^p, \qquad E_1^P\big|_{t=0} = 0, \quad \left.\frac{\partial E_1^p}{\partial t}\right|_{t=0} = 0. \tag{37}$$

The solution of IVP (37) is of the form

$$E_1^p(t) = \frac{1}{\sigma_{11}}\int_0^t f_1^p(\tau)\left(1 - e^{\sigma_{11}(\tau - t)}\right) + \left(\mu_{22}(p+2)(p+1)E_1^{p+2}(\tau)\right)\left(1 - e^{\sigma_{11}(\tau-t)}\right)d\tau.$$

Since $E_1^{p+2} = 0$, the solution of problem (37) is

$$E_1^p(t) = \frac{1}{\sigma_{11}}\int_0^t f_1^p(\tau)\left[1 - e^{\sigma_{11}(\tau-t)}\right]d\tau.$$

Now, the computation will continue with $n = p - 1$ to calculate $E_1^{p-1}(t)$. When $n = p - 1$ we have

$$\frac{\partial^2 E_1^{p-1}}{\partial t^2} - \mu_{22}(p+1)pE_1^{p+1} + \sigma_{11}\frac{\partial E_1^{p-1}}{\partial t} = f_1^{p-1}, \qquad E_1^{p-1}\Big|_{t=0}^{p-1}, \left.\frac{\partial E_1^{p-1}}{\partial t}\right|_{t=0} = 0. \tag{38}$$

With the similar reasoning, the solution of (38) is

$$E_1^{p-1}(t) = \frac{1}{\sigma_{11}}\int_0^t f_1^{p-1}(\tau)\left[1 - e^{\sigma_{11}(\tau-t)}\right]d\tau.$$

Continuing calculation when $n = p - 2$ we have

$$\frac{\partial^2 E_1^{p-2}}{\partial t^2} - \mu_{22}p(p-1)E_1^p + \frac{\partial E_1^{p-2}}{\partial t} = f_1^{p-2}(t), \qquad E_1^{p-2}\Big|_{t=0} = 0, \quad \left.\frac{\partial E_1^{p-2}}{\partial t}\right|_{t=0} = 0. \tag{39}$$

Since $E_1^p(t)$ is calculated in previous steps, we get the solution of IVP (39) as

$$E_1^{p-2}(t) = \frac{1}{\sigma_{11}}\int_0^t f_1^{p-2}(\tau)\left(1 - e^{\sigma_{11}(\tau-t)}\right) + \left(\mu_{22}p(p-1)E_1^p(\tau)\right)\left(1 - e^{\sigma_{11}(\tau-t)}\right)d\tau.$$

Thus, the values of $E_1^i(t)$ $(0 \le i \le p)$ with decreasing i values can be calculated with the following formula

$$E_1^i(t) = \frac{1}{\sigma_{11}}\int_0^t f_1^i(\tau)\left(1 - e^{\sigma_{11}(\tau-t)}\right) + \left(\mu_{22}(i+2)(i+1)E^{i+2}(\tau)\right)\left(1 - e^{\sigma_{11}(\tau-t)}\right)d\tau.$$

The values of $E^{i+2}(\tau)$ are calculated with the previous steps. In this way all coefficients $E_1^i(t)$ of the solution $E_1(x,t)$ that is given with formula (33) can be calculated.

7. Computational examples

In this section, there are three examples. In the first example, all the components of non homogeneous term are in polynomial form. PS method is used to solve the problem and the solutions obtained by using Maple codes are checked by direct substitution to the problem. In example 2 and example 3 the components of non homogeneous term are chosen as smooth functions. Chebyshev polynomials are used for approximations of these smooth functions. Each example is chosen since we know the exact solutions of the problems with chosen matrices ε, μ and σ and inhomogeneous term. Aim is to compare the exact solution with the solution obtained by using Chebyshev polynomials and PS method.

Example 1: Let us consider a simple example for the IVP given with the equations (3)-(8). Let the matrices ε, μ and σ be identity matrices and let the inhomogeneous term $\mathbf{f}(x,t) = -\dfrac{\partial \mathbf{j}}{\partial t}$ be a vector function that has the components

$$f_1(x,t) = (x_1 + 4x_2^4 + 3x_3^2),$$
$$f_2(x,t) = x_3^2 t,$$
$$f_3(x,t) = (2x_1 + x_2)(t+2).$$

As we mention in Section 1, this problem can be written in the form of two IVPs (9),(10) and (11),(12). Our aim is to find electric and magnetic currents. Using PS method exact solution of IVP (9),(10) can be obtained.

The components of electric field $\mathbf{E}(x,t)$ are

$$\begin{aligned}
E_1(x,t) &= 942e^{-t} - 942 + 378e^{-t}t + 564t - 141t^2 \\
&\quad + 48e^{-t}t^2 + 16t^3 + (4e^{-t} - 4 + 4t)x_2^4 \\
&\quad + (3e^{-t} - 3 + 3t)x_3^2, \\
E_2(x,t) &= 7.99e^{-t} - 7.99e^{-t}e^t + .33e^{-t}t^3e^t + 5.99e^{-t}te^t \\
&\quad - 2e^{-t}t^2e^t + 2e^{-t}t + (.50t^2 - e^{-t} + 1 - t)x_3^2, \\
E_3(x,t) &= (t^2 + 2t + 2e^{-t} - 2)x_1 + (.50t^2 + t + e^{-t} - 1)x_2.
\end{aligned}$$

Using the solution of the IVP (9),(10), the solution of the IVP (11),(12) can be obtained. The components of magnetic filed $\mathbf{H}(x,t)$ are

$$\begin{aligned}
H_1(x,t) &= -.16t^3 - .50t^2 + e^{-t} + t + .33t^3x_3 + 2x_3e^{-t} \\
&\quad + 2x_3t - x_3t^2 - 2x_3 - 1, \\
H_2(x,t) &= -2t + 6x_3e^{-t} + 6x_3t - 3x_3t^2 + .33t^3 + t^2 \\
&\quad - 2e^{-t} - 6x_3 + 2, \\
H_3(x,t) &= 8x_2^3t^2 - 16x_2^3e^{-t} - 16x_2^3t - 96x_2t^2 + 288x_2t \\
&\quad + 384x_2e^{-t} + 96x_2e^{-t}t + 16x_2t^3 + 16x_2^3 - 384x_2.
\end{aligned}$$

By direct substitution of $\mathbf{E}(x,t)$ and $\mathbf{H}(x,t)$ that are obtained using PS method into the problem given in equations (3)-(8) the robustness of the method is checked.

Example 2: Let us consider the IVP (3)-(8) with the matrices ε, μ and σ that are identity matrices and let the inhomogeneous term $\mathbf{f}(x,t) = -\dfrac{\partial \mathbf{j}}{\partial t}$ be a vector function that has the components

$$\begin{aligned}
f_1(x,t) &= (x_1+1)^1 0 + (x_2+3)^3, \\
f_2(x,t) &= x_2^3(t-1), \\
f_3(x,t) &= (5x_2 + x_3^2)t.
\end{aligned}$$

As we mention in Section 1 and in the example 1, this problem can be written in the form of two IVPs (9),(10) and (11),(12). Similarly, our aim is to find electric and magnetic currents. Using PS method exact solution of IVP (9),(10) can be obtained.
The components of electric field $\mathbf{E}(x,t)$ are

$$\begin{aligned}
E_1(x,t) &= (x_1+1)^{10}\left(e^{-t} + t - 1\right) + (x_2+3)^3\left(e^{-t} + t - 1\right) \\
&\quad - 6(t+3)(x_2+3)\left(e^{-t} + t - 1\right) + 9(x_2+3)t^2 \\
E_2(x,t) &= \left(\frac{t^2}{2} - 2t - 2e^{-t} + 2\right)x_2^3 \\
E_3(x,t) &= (5x_2 + x_3^2)\left(\frac{t^2}{2} - e^{-t} + 1 - t\right).
\end{aligned}$$

Using the solution of the IVP (9),(10), the solution of the IVP (11),(12) can be obtained. The components of magnetic filed $\mathbf{H}(x,t)$ are

$$\begin{aligned}
H_1(x,t) &= -\frac{5t^3}{6} + \frac{5t^2}{2} - 5(e^{-t} + t - 1), \\
H_2(x,t) &= 0, \\
H_3(x,t) &= -\left(3x_2^2 + 6t + 18x_2 + 3\right)\left(e^{-t} + t - 1\right) \\
&\quad + \frac{3x_2^2t^2}{2} + t^3 + 9x_2t^2 + \frac{3t^2}{2}.
\end{aligned}$$

By direct substitution of $\mathbf{E}(x,t)$ and $\mathbf{H}(x,t)$ that are obtained using PS method into the problem given in equations (3)-(8) the robustness of the method is checked. It is not easy to compute the solutions of such examples. As the inhomogeneous terms order increase it becomes much more complicated. This method enables us to deal with these complicated problems.

Example 3: Now let us consider problem (9),(10) and (11),(12) when ε, μ and σ be identical matrices and let the non-homogeneous term $\mathbf{f}(x,t) = -\frac{\partial \mathbf{j}}{\partial t}$ be a vector function that is not polynomial. The components of non-polynomial smooth data $\mathbf{f} = (f_1, f_2, f_3)$ are

$$\begin{aligned}
f_1(x,t) &= \cos(x_1)\sin(2x_2)\sin(3x_3)\delta(t), \\
f_2(x,t) &= \sin(x_1)\cos(2x_2)\sin(3x_3)\delta(t), \\
f_3(x,t) &= \sin(x_1)\sin(2x_2)\cos(3x_3)\delta(t).
\end{aligned}$$

The exact solution of IVPs can be easily found without using PS method. The components of the solutions are

$$\begin{aligned}
E_1(x,t) &= \frac{165}{385}\left(1 - e^{-t}\right)\cos(x_1)\sin(2x_2)\sin(3x_3) \\
&\quad + \frac{8\sqrt{55}}{385}\left(e^{-\frac{t}{2}}\sin(\frac{\sqrt{55}t}{2})\right)\cos(x_1)\sin(2x_2)\sin(3x_3), \\
E_2(x,t) &= \frac{330}{385}\left(1 - e^{-t}\right)\sin(x_1)\cos(2x_2)\sin(3x_3) \\
&\quad + \frac{2\sqrt{55}}{385}\left(e^{-\frac{t}{2}}\sin(\frac{\sqrt{55}t}{2})\right)\sin(x_1)\cos(2x_2)\sin(3x_3), \\
E_3(x,t) &= -\frac{495}{385}\left(e^{-t} - 1\right)\sin(x_1)\sin(2x_2)\cos(3x_3) \\
&\quad - \frac{4\sqrt{55}}{385}\left(e^{-\frac{t}{2}}\sin(\frac{\sqrt{55}t}{2})\right)\sin(x_1)\sin(2x_2)\cos(3x_3),
\end{aligned} \tag{40}$$

and

$$
\begin{aligned}
H_1(x,t) &= -\frac{\sqrt{55}}{770}\sin(x_1)\cos(2x_2)\cos(3x_3)\left(e^{-\frac{t}{2}}\sin\left(\frac{\sqrt{55}t}{2}\right)\right)\\
&\quad -\frac{55}{770}\sin(x_1)\cos(2x_2)\cos(3x_3)\left(e^{-\frac{t}{2}}\cos\left(\frac{\sqrt{55}t}{2}\right)-1\right)\\
H_2(x,t) &= \frac{\sqrt{55}}{385}\cos(x_1)\sin(2x_2)\cos(3x_3)\left(e^{-\frac{t}{2}}\sin\left(\frac{\sqrt{55}t}{2}\right)\right)\\
&\quad +\frac{55}{385}\cos(x_1)\sin(2x_2)\cos(3x_3)\left(e^{-\frac{t}{2}}\cos\left(\frac{\sqrt{55}t}{2}\right)-1\right)\\
H_3(x,t) &= -\frac{\sqrt{55}}{770}\cos(x_1)\cos(2x_2)\sin(3x_3)\left(e^{-\frac{t}{2}}\sin\left(\frac{\sqrt{55}t}{2}\right)\right)\\
&\quad -\frac{55}{770}\cos(x_1)\cos(2x_2)\sin(3x_3)\left(e^{-\frac{t}{2}}\cos\left(\frac{\sqrt{55}t}{2}\right)-1\right).
\end{aligned}
\tag{41}
$$

Using PS method we obtain polynomial form of the solution of the IVPs (9),(10) and (11),(12) and these solutions are compared by the solutions given in (40),(41) at the same fixed points and the results of the comparison of $E_1(x,t)$ are presented in the table given below. The results obtained by the PS method are in good agreement with the exact solution.

Table 1: Values of E_1 and E_1^N for $N = 24$

t	x_1	x_2	x_3	Error
7/5	1	1	1	$0.1 * 10^{-10}$
1	2	1	2	$0.3 * 10^{-10}$
2	5	2	2	$0.2 * 10^{-10}$
14/10	0	2	3	$0.1 * 10^{-9}$
2	4	4	4	$0.3 * 10^{-9}$
2	5	5	5	$0.2 * 10^{-9}$

Using the method in Section 3, a polynomial solution $\mathbf{E}^N = (E_1^N, E_2^N, E_3^N)$ of the IVP (9), (10) is calculated. The graph of the comparison for the first component of the approximate function that is $E_1^N(x,t)$ and the the first component of the explicit formula $E_1(x,t)$ are presented below.

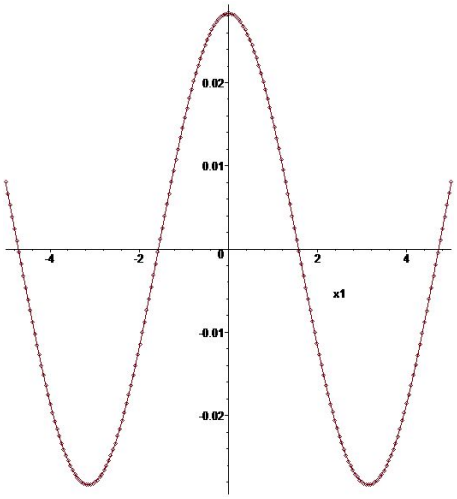

Figure 1: The graphs of the first component of the electric field $\mathbf{E}(x,t)$ computed by PS method and the explicit formula when $x_2 = 2, x_3 = 1, t = 1$.

8. Conclusion

Symbolic computations for constructing polynomial solutions for initial value problem of radiation from the electric current in electrically and magnetically anisotropic media is used for the case when ε, μ are arbitrary positive definite matrices and σ is a symmetric matrix with constant elements. Stability estimates (energy inequalities) for solutions of the system in a finite domain of dependence (a finite domain containing characteristic cones) is described. Using these stability estimates we justify that polynomial solutions are approximate solutions of the initial value problems with non-polynomial data. These theoretical results are confirmed by computational experiments which compares the exact solutions with polynomial solutions found by using polynomial solution method.

9. Acknowledgements

I would like to thank the anonymous referees for their comments, remarks and useful suggestions which I used in the revised version of this paper.

References

[1] Cohen, G. C. (2002). *Higher-order numerical methods for transient wave equations*. Scientific computation. Springer, Berlin, Heidelberg, New York.

[2] Courant, R. and Hilbert, D. (2008). *Methods of mathematical physics: partial differential equations*. John Wiley & Sons.

[3] Eom, H. J. (2004). *Electromagnetic Wave Theory For Boundary-Value Problems*. Springer-Verlag, Berlin.

[4] Goldberg, J. L. (1991). *Matrix Theory with Applications*. McGraw-Hill, New York.

[5] Ikawa, M. (2000). *Hyperbolic partial differential equations and wave phenomena*, volume 2. American Mathematical Soc.

[6] Ishimaru, A. (1991). *Electromagnetic wave propagation, radiation, and scattering*. Prentice Hall.

[7] Kong, J. A. (1990). *Electromagnetic Wave Theory, 2nd ed.* Wiley. John Wiley & Sons Inc., New York.

[8] Mizohata, S. (1973). *The theory of partial differential equations*. CUP Archive.

[9] Monk, P. (2003). *Finite Element Methods For Maxwell's Equations*. Numerical Mathematics and Scientific Computation. Oxford University Press, New York.

[10] Neittaanmäki, P., Joly, P., Heikkola, E., Cohen, G. C., national de recherche en informatique et en automatique (France), I., and of Jyväskylä (FI), U., editors (2003). *Mathematical and numerical aspects of wave propagation - WAVES 2003 : proceedings*, 6, Jyväskylä, FI. Springer.

[11] Ramo, S., Whinnery, J. R., and Duzer, T. (1994). *Fields and Waves in Communication Electronics*. Wiley. John Wiley & Sons Inc., New York.

[12] Stinson, D. C. (1976). *Intermediate mathematics of electromagnetics*. Electrical engineering series. Prentice-Hall, Englewood Cliffs.

[13] Taflove, A. (1995). *Computational electrodynamics : the finite-difference time-domain method*. Artech House, Boston.

[14] Yakhno, V. and Altunkaynak, M. (2009). Symbolic computation of an exact solution of the cauchy problem for the system of crystal optics with polynomial data. In *Numerical Analysis and Its Applications: 4th International Conference, NAA 2008, Lozenetz, Bulgaria, June 16-20, 2008. Revised Selected Papers 4*, pages 596–603. Springer.

[15] Yakhno, V. and Altunkaynak, M. (2016). A polynomial approach to determine the time-dependent electric and magnetic fields in anisotropic materials by symbolic computations. *COMPEL-The international journal for computation and mathematics in electrical and electronic engineering*, 35(3).

[16] Yakhno, V. and Altunkaynak, M. (2018). Symbolic computation of the time-dependent electric and magnetic fields in bi-anisotropic media with polynomial inputs. *International Journal of Numerical Modelling: Electronic Networks, Devices and Fields*, 31(5):e2339.

[17] Yakhno, V. G. and Altunkaynak, M. (2010). A new method for computing a solution of the Cauchy problem with polynomial data for the system of crystal optics. *Int. J. Comput. Math.*, 87(7):1469 – 1484.

[18] Yee, K. S. (1966). Numerical solution of initial boundary value problems involving Maxwell's equations inisotropic media. *IEEE Trans. Antennas Propag.*, 14:302 – 307.

[19] Zachmanoglou, E. C. and Thoe, D. W. (1986). *Introduction to partial differential equations with applications*. Courier Corporation.

[20] Zienkiewicz, O. C. and Taylor, R. L. (2000). *The Finite Element Method, 5 th ed.* Butterworth-Heinemann, Oxford.

MANAS Journal of Engineering
ISSN 1694-7398 | e-ISSN 1694-7398

Volume 12, Issue 1, (2024) Pages 88-103
https://doi.org/10.51354/mjen.1361736

Offshoring Location Decision in Fuzzy Environment

Mehmet Şahin[*,1]

[1]Department of Industrial Engineering, Iskenderun Technical University, 31200 Iskenderun, Turkey, mehmet.sahin@simon.rochester.edu, ORCID: 0000-0001-7078-7396

ABSTRACT

Offshoring location selection is a crucial decision for firms in terms of competitiveness, flexibility, productivity, and profitability. Determining an efficient and appropriate location for offshoring has been a substantial multicriteria decision-making (MCDM) problem. Considering that the outcome of an MCDM method alone can be misleading, a novel hybrid approach is presented in this study. Thus, five MCDM methods are utilized to solve the problem, and the results of four MCDM methods are integrated to assure an optimal offshoring location. A Fuzzy-AHP (analytical hierarchy process) integrated with the technique for order preference by similarity to ideal solution (TOPSIS), additive ratio assessment (ARAS), elimination et choix traduisant la realité (ELECTRE), and weighted sum method (WSM) methodology is proposed for the appraisal and selection of the optimal offshoring location. In this context, fifteen alternative locations are determined based on the attractiveness of the locations in terms of offshoring. Fuzzy-AHP is implemented to analyze the problem's structure and find the weights of the quantitative and qualitative criteria. Consistency tests are implemented to assess the quality of inputs of an expert. Then, TOPSIS, WSM, ARAS, and ELECTRE are used to evaluate and rank the candidate locations and present a comparative analysis. By considering fifteen countries and using real data, offshoring location selection is conducted through the proposed methodology. Moreover, sensitivity analysis is made to diminish the subjectivity and assess the robustness of the techniques. The results demonstrated that giving more weights to the labor characteristics and proximity to market criteria might improve the quality of the best offshoring country index.

ARTICLE INFO

Research article

Received: 17.09.2023
Accepted: 18.03.2024

Keywords:
Offshoring,
decision making,
fuzzy-AHP,
location selection,
comparative analysis.

[*]Corresponding author

1. Introduction

Offshoring has been one of the most fundamental and significant strategies for manufacturing companies worldwide because of the considerable forces of globalization and competition. It has become one of the most preferred tactics by manufacturing companies to preserve and advance their competitive advantage [1]. Offshoring can be described as the relocation of value-added processes across the national borders of a company [2]. It has the potential to help the firm to obtain the benefits namely lower cost, entering, penetrating, and growth in new markets, flexibility, access to skilled labor, higher productivity in terms of corporate innovativeness, and opportunities to focus on central skills, thus increasing innovation level by offshoring noncore activities [3, 4]. Offshoring is especially widespread in industries (i.e., electronics, auto parts, and machinery), in which manufacturing stages are physically separable, meaning that they can be made in different locations, and factor intensities vary sharply, meaning that fragmenting manufacture across borders is attractive [5].

Offshoring has become an economic interest, and appealing strategy for the industry worldwide as manufacturing location decision plays a vital role in the performance and future of firms. Thus, the number of studies regarding offshoring has been increasing. In this context, Kinkel and Maloca [6] state that manufacturing offshoring becomes an appealing choice for all-sized firms, mainly due to reduced labor costs. Michel and Rycx [7] examine the effect of offshoring on employment and address that no significant effect of offshoring on Belgium's total employment between 1995 and 2003 is observed. Ellram, Tate [8] use study data to determine the effective criteria for manufacturing location decisions of firms. Stentoft, Mikkelsen [9] evaluate performance outcomes of companies adopting back shoring, staying domestic, and

offshoring and reveal that organizations implementing offshored manufacturing strategy have reduced unit costs compared to companies implementing a staying-at-home strategy.

Location decision-making represents a multi-level hierarchy, in which effective varying parameters exist at each level [10]. This kind of decision requires considerable time and resources, special attention, and thorough data analysis as it involves a high level of uncertainty and impacts the competitiveness and profitability of a firm profoundly [9]. Thus, location decision has attracted considerable interest among practitioners and researchers [11, 12]. Multi-criteria decision-making (MCDM) approaches have been commonly utilized to solve location selection problems. Gupta, Mehlawat [13] present an extended VIKOR (VlseKriterijumska Optimizacija I Kompromisno Resenje) technique for solving a plant location problem. Lai [14] implements integrated simplified swarm optimization with the Analytical Hierarchy Process (AHP) for solving the location problem of the capacitated military logistic depot. Ishizaka, Nemery [15] use the Preference Ranking Organization Method for Enrichment Evaluation (PROMETHEE), Weighted Sum Method (WSM), and Technique for Order Preference by Similarity to Ideal Solution (TOPSIS) to determine the ideal location for a casino.

It can be inferred that even though there is an abundant quantity of research on location selection, only a few of them have concentrated on offshoring location selection problems. Liu, Berger [16] apply AHP for offshore outsourcing location decisions. Dou and Sarkis [17] propose an Analytical Network Process (ANP) model for strategic offshoring decisions. López and Ishizaka [18] examine the attributes impacting location criteria (attributes) on offshore outsourcing decisions and their impact on the supply chain resilience capabilities using AHP and fuzzy cognitive maps. De Felice, Petrillo [19] analyze captive offshoring criteria and apply Fuzzy AHP method to obtain the weight of each criterion and sub-criterion. Costanzo and Ahmed [20] propose an offshoring desirability index to determine the value of offshoring locations in the Eastern European. However, the hybridization of successful MCDM methods in the context of evaluating offshoring location decisions is not available in the extant literature except for a study [21]. Thus, addressing this research gap inspires this study to propose a hybrid approach grounded on Fuzzy-AHP with TOPSIS, WSM, additive ratio assessment (ARAS), and elimination et choix traduisant la realité (ELECTRE) approach to evaluate offshoring location decisions. The reason for choosing these methods is to use different MCDM methods to reveal a practical comparative analysis. Wu, Zhang [22] classify MCDM methods into three types that are outranking (ELECTRE), distance-based (TOPSIS), and utility-based (AHP and WSM) models. Hence, utilizing different methods from different family groups may be valuable. It is the first time to implement all these methods together for this purpose. Also, ARAS is used for offshoring for the first time in this study.

Another inspiration for this study can be explained as follows. A great deal of the studies conducted on offshoring qualitatively examines offshoring from a feasibility perspective and concentrates on reasons for offshoring, advantages, and disadvantages of offshoring, performance improvements, and influencing criteria [23, 24]. However, this study examines the multifaceted "where to offshore" question by implementing quantitative approaches, namely Fuzzy-AHP, TOPSIS, WSM, ARAS, and ELECTRE. It extends the literature in terms of evaluating and comparing different MCDM methods for the "where to offshore" problem. In this context, a novel hybrid approach for offshoring location selection is introduced. Also, a comprehensive analysis is presented.

The chief objective of this study is to reveal a comparative analysis for multicriteria offshoring location selection problems by utilizing Fuzzy-AHP, TOPSIS, WSM, ARAS, and ELECTRE methods. To do so, fifteen countries, which have been commonly preferred for offshoring, are ranked by considering seven main criteria (attributes), namely cost [25, 26], labor characteristics [17, 27], infrastructure [28], proximity to suppliers [29, 30], economic factors [17], quality of life [31], and proximity to market [32, 33] and thirty sub-criteria under these main criteria. These most effective attributes are selected after conducting a comprehensive literature review and utilizing expert knowledge. The criteria weights required by the TOPSIS, WSM, ARAS, and ELECTRE are obtained by utilizing the Fuzzy-AHP. The fifteen alternative countries are evaluated and ranked based on the criteria by TOPSIS, WSM, ARAS, and ELECTRE, respectively. Another reason to adopt more than one MCDM method is that using one MCDM method does not guarantee finding the most suitable solution. Sensitivity analysis is also conducted to minimize the effect of subjective assessments. Thus, a comparative analysis, which contributes to the literature and can be utilized for offshoring and outsourcing decisions, is introduced.

The rest of this research is organized as follows: A brief description of the methods utilized, the methodology and application of the methods, and sensitivity analysis are given in Section 2. In Section 3, the results of the applications and sensitivity analysis and discussions on the results are provided. Finally, the conclusions and possible future studies are presented in Section 4.

2. Materials and Methods

In this study, the Fuzzy-AHP is employed for finding the attribute weights, and TOPSIS, WSM, ARAS, and ELECTRE are used for ranking alternatives to designate the most appropriate offshoring location. The methodology of each method can be described as follows:

2.1. Fuzzy-AHP

The AHP, which was presented by Saaty [34], is capable of tackling complex systems regarding selecting an alternative

from among many candidates and providing a comparison of the considered alternatives. The Fuzzy-AHP is preferred over AHP because of several shortcomings of the AHP. First, the AHP ranking is rather vague. Second, the AHP generates and manages a highly unbalanced judgment scale. Third, the AHP is primarily applied in almost precise decision cases. Fourth, the AHP results are significantly affected by subjective judgment, preference, and selection of decision-makers. Last, the AHP ignores the uncertainty linked with mapping the expert's interpretation of a number [35, 36]. To overcome these shortcomings, an extended form of AHP fuzzy sets can be combined with the pairwise comparison, termed Fuzzy-AHP. The Fuzzy-AHP method permits a more specific explanation of the process of decision-making. This study suggests the use of Fuzzy-AHP for obtaining the criteria weights. The Fuzzy-AHP has been commonly utilized for different problems such as the assessment of solar farms locations [37], location selection for landfill of industrial wastes [38], optimal stock portfolio selection [39], green supply chain management [40], assessment of groundwater potential zones [41], and evaluation of healthcare service quality from the perspective of patients [42].

Even though there are several Fuzzy-AHP methods used in the literature, the Fuzzy-AHP, presented by Chang [43] was utilized in this study due to its computational efficiency and easiness.

Preliminaries:

Let a fuzzy number M on R be a triangular fuzzy number in case its membership function $\mu_M(x): R \to [0,1]$ is equal to the following equation [43].

$$\mu_M(x) = \begin{cases} \dfrac{(x-l)}{(m-l)}, & x \in [l,m] \\ \dfrac{(x-u)}{(m-u)}, & x \in [m,u] \\ 0, & otherwise \end{cases} \quad (1)$$

in which $l \le m \le u$, l and u represent the lower and upper value of the support of M, respectively, and m represents the modal value. The triangular fuzzy number may be denoted by (l, m, u). The operational laws of fuzzy triangular numbers $M_1 = (l_1, m_1, u_1)$ and $M_2 = (l_2, m_2, u_2)$ are given in the following equations.

$$(l_1, m_1, u_1) \oplus (l_2, m_2, u_2) = (l_1 + l_2, m_1 + m_2, u_1 + u_2) \quad (2)$$

$$(l_1, m_1, u_1) \otimes (l_2, m_2, u_2) \approx (l_1 l_2, m_1 m_2, u_1 u_2) \quad (3)$$

$$(\lambda, \lambda, \lambda) \otimes (l_1, m_1, u_1) = (\lambda l_1, \lambda m_1, \lambda u_1), \quad \lambda > 0, \quad \lambda \in R \quad (4)$$

$$(l_1, m_1, u_1)^{-1} \approx (1/u_1, 1/m_1, 1/l_1) \quad (5)$$

Assuming that an object set is represented by $X = \{x_1, x_2, x_3, \dots, x_n\}$ and a goal set by $U = \{u_1, u_2, u_3, \dots, u_n\}$. Each entity is considered, and extent analysis is made for every goal (g_i) sequentially. Thus, m extent analysis values for every entity are obtained with the signs:

$$M_{gi}^1, M_{gi}^2, \dots, M_{gi}^m, \qquad i = 1,2, \dots, n \quad (6)$$

in which $M_{gi}^j (j = 1,2, \dots, m)$ are triangular fuzzy numbers. The methodology of the Fuzzy-AHP [43] can be explained in the following steps.

1. The fuzzy synthetic extent value (S_i) regarding the ith entity is represented as:

$$S_i = \sum_{j=1}^{m} M_{gi}^j \otimes \left[\sum_{i=1}^{n} \sum_{j=1}^{m} M_{gi}^j \right]^{-1} \quad (7)$$

To find $\sum_{j=1}^{m} M_{gi}^j$, the fuzzy addition operation of m extent analysis values for a matrix is applied as follows:

$$\sum_{j=1}^{m} M_{gi}^j = \left(\sum_{j=1}^{m} l_j, \sum_{j=1}^{m} m_j, \sum_{j=1}^{m} u_j \right) \quad (8)$$

To find $\left[\sum_{i=1}^{n} \sum_{j=1}^{m} M_{gi}^j\right]^{-1}$, the fuzzy addition operation of $M_{gi}^j (j = 1,2, \dots, m)$ values is achieved as follows:

$$\sum_{i=1}^{n} \sum_{j=1}^{m} M_{gi}^j = \left(\sum_{i=1}^{n} l_i, \sum_{i=1}^{n} m_i, \sum_{i=1}^{n} u_i \right) \quad (9)$$

Next, the inverse of the vector given previously is calculated as follows:

$$\left[\sum_{i=1}^{n} \sum_{j=1}^{m} M_{gi}^j \right]^{-1} = \left(\frac{1}{\sum_{i=1}^{n} u_i}, \frac{1}{\sum_{i=1}^{n} m_i}, \frac{1}{\sum_{i=1}^{n} l_i} \right) \quad (10)$$

2. Since $M_1 = (l_1, m_1, u_1)$ and $M_2 = (l_2, m_2, u_2)$ are two triangular fuzzy numbers, the possibility degree of $M_2 = (l_2, m_2, u_2) \ge M_1 = (l_1, m_1, u_1)$ is represented as:

$$V(M_2 \ge M_1) = \sup_{y \ge x} (min(\mu_{M_1}(x), \mu_{M_2}(y))) \quad (11)$$

and is defined as follows:

$$V(M_2 \ge M_1) = hgt(M_1 \cap M_2) = \mu_{M_2}(d) = \begin{cases} 1 & if\ m_2 \ge m_1 \\ 0 & if\ l_1 \ge u_2 \\ \dfrac{l_1 - u_2}{(m_2 - u_2) - (m_1 - l_1)} & otherwise \end{cases} \quad (12)$$

This function is illustrated in Figure 1 [44], where d denotes the ordinate of the maximum intersection point D between μ_{M1} and μ_{M2}. Both $V(M_1 \ge M_2)$ and $V(M_2 \ge M_1)$ values are needed to compare M_1 and M_2.

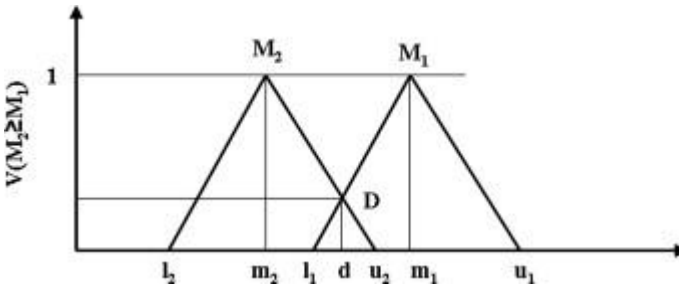

Figure 1. *The intersection between M_1 and M_2 [43].*

3. For a convex fuzzy number, the possibility degree, to be higher than k convex fuzzy $M_i(i = 1,2,\dots,k)$ numbers are represented by:

$$V(M \geq M_1, M_2, \dots, M_k) = V[(M \geq M_1)\ and\ (M \geq M_2)\ and \dots and\ (M \geq M_k)] = \min V(M \geq M_i), i = 1,2,3,\dots.k \quad (13)$$

Let $d(A_i) = \min V\,(S_i \geq S_k)\ for\ k = 1,2,\dots,n; k \neq i$. Then the vector of weight is specified by:

$$\acute{W} = (\acute{d}(A_1), \acute{d}(A_2), \dots, \acute{d}(A_n))^T \quad (14)$$

in which $A_i(i = 1,2,\dots,n)$ are n elements.

4. Through normalization, the normalized weight vectors are:

$$W = (d(A_1), d(A_2), \dots, d(A_n))^T \quad (15)$$

in which W is a non-fuzzy number.

2.2. TOPSIS

The TOPSIS, developed by Hwang and Yoon [45], has been one of the most frequently utilized MCDM methods to determine and rank alternatives for various decision-making problems [46]. It is implemented for location selection problems such as the storage location assignment problem [47], choosing wind farm installation locations [48], optimal solar energy sites identification [49], wave power plant site selection [50], and service apartment location selection [51]. The core principle of the TOPSIS involves selecting the candidate that has the shortest distance from the positive ideal solution (PIS) and the farthest distance from the negative ideal solution (NIS) [45]. It requires limited subjective input from the decision-maker. The structure of the TOPSIS is explained in steps as follows:

Step 1. Forming the evaluation matrix is displayed as follows:

$$Evaluation\ Matrix = \begin{bmatrix} a_{11} & \cdots & a_{1n} \\ \vdots & \ddots & \vdots \\ a_{m1} & \cdots & a_{mn} \end{bmatrix} \quad (16)$$

where a_{ij} represents the numerical value collected from the ith option with the jth index.

Step 2. Normalizing the evaluation matrix through the following equation.

$$r_{ij} = \frac{a_{ij}}{\sqrt{\sum_{i=1}^{m} a_{ij}^2}} \qquad for\ i = 1,2,\dots,m;\ j = 1,2,\dots,n \quad (17)$$

Step 3. Determining the weighted normalized decision matrix by using the equation given as follows.

$$v_{ij} = w_j * r_{ij} \quad (18)$$

Step 4. Determining the PIS and NIS for each attribute is as:

$$Positive\ Ideal\ Solution = V_j^+ = MAX_i(v_{ij}) \quad (19)$$

$$Negative\ Ideal\ Solution = V_j^- = MIN_i(v_{ij}) \quad (20)$$

Step 5. Computing the geometric distance of each candidate from PIS and NIS through the following functions, respectively.

$$S_i^+ = \sqrt{\sum_{j=1}^{n} \left(V_j^+ - v_{ij}\right)^2} \quad (21)$$

$$S_i^- = \sqrt{\sum_{j=1}^{n} \left(V_j^- - v_{ij}\right)^2} \quad (22)$$

Step 6. Computing the relative closeness to the ideal solution as:

$$C_i = \frac{S_i^-}{S_i^- + S_i^+} \qquad 0 < C_i < 1 \quad (23)$$

The optimal selection is the one that has the maximum relative closeness.

2.3. ELECTRE

ELECTRE was presented by Roy [52]. It is among the most common and effective MCDM methods. ELECTRE III is broadly utilized to deal with ambiguous and uncertain information [53]. Thus, ELECTRE III is adopted for the structure and scope of the present study. It is implemented successfully in tackling MCDM problems such as assessing different kinds of energy generation technologies [54], machine tool remanufacturing [55], optimal site selection [56], autonomous vehicles project [57], site selection for offshore wind power stations [58], and evaluating the optimal location for a construction and demolition waste management facility [59].

The ELECTRE-III method comprises two main phases: forming an outranking association over all the probable candidate pairs and utilizing the outranking association to attain a ranking of the selections in the partial pre-order form [60]. Forming the outranking relation needs the credibility index description that characterizes the credibility of the statement "*a* outranks *b*", *aSb*, where the index is denoted by σ(*aSb*). It involves the concordance index, *c*(*aSb*), and the discordance index for each criterion g_j in *F*, which is $d_j(aSb)$ [61]. The partial concordance index $c_j(a,b)$ is represented as follows:

$$c_j(a,b) = \begin{cases} 1 & if\ g_j(a) \geq g_j(b) - q_j(b) \\ 0 & if\ g_j(a) \leq g_j(b) - p_j(b) \\ \dfrac{g_j(a) - g_j(b) + p_j(b)}{p_j(b) - q_j(b)} & otherwise \end{cases} \quad (24)$$

The general concordance index is computed for every ordered pair $(a, b) \in A$ as:

$$c(a,b) = \frac{1}{W}\sum_{j=1}^{m} w_j c_j(a,b) \quad (25)$$

The partial discordance index $d_j(a, b)$ is represented as:

$$d_j(a,b) = \begin{cases} 1 & if\ g_j(a) - g_j(b) \leq -v_j(a) \\ 0 & if\ g_j(a) - g_j(b) \geq -p_j(a) \\ \dfrac{g_j(b) - g_j(a) + p_j(a)}{v_j(a) - p_j(a)} & otherwise \end{cases} \quad (26)$$

Consequently, to attain a valued outranking relation with credibility σ (a, b), the general concordance and partial discordance indexes are joined as:

$$\sigma(a,b) = \begin{cases} c(a,b) & if\ d_j(a,b) \leq c(a,b), \forall_j \\ c(a,b) \cdot \prod_{j \in \bar{F}} \dfrac{1 - d_j(a,b)}{1 - c(a,b)} & otherwise \end{cases} \quad (27)$$

where $\bar{F} = \{j \in F : d_j(a,b) > c(a,b)\}$.

2.4. WSM

The WSM has been a reference MCDM method. A score for each alternative A_i is calculated by summing the products of each decision variable with its corresponding criterion weight. The most appropriate alternative that has the highest total score is determined via the following equation.

$$A_i = \sum_{j=1}^{n} a_{ij} w_j \quad \text{for } i = 1,2,3,\dots,m \quad (28)$$

The letters represent the following terms: *m:* the alternatives; *n*: the criteria; w_j: the criterion weight; a_{ij}: the score for the *i*th alternative regarding the *j*th criterion.

2.5. ARAS

ARAS was presented by Zavadskas and Turskis [62] as a new MCDM method. It is successfully applied to MCDM problems such as evaluation of the blockchain technology strategies [63], evaluation of the e-commerce last-mile logistics' hidden risk hurdles [64], and identification proper process parameters [65]. The procedure of ARAS is described as follows.

Step 1. The decision matrix is normalized through the following equation. The cost attributes are transformed, and then their values are normalized.

$$r_{ij}^* = \frac{r_{ij}}{\sum_{i=0}^{m} r_{ij}} \qquad for\ j = 1,2,\dots,n \quad (29)$$

Step 2. The weighted normalized decision matrix is determined through the following function. The weights of criteria ($w_1, w_2, \dots, w_n$) are provided by FAHP.

$$\widehat{r_{ij}} = r_{ij}^* * w_j \qquad for\ i = 0,1,2,\dots,m \quad j = 1,2,\dots,n \quad (30)$$

Step 3. The optimality function (S_i) is calculated through the following equation. The higher value indicates the better.

$$S_i = \sum_{j=1}^{n} \widehat{r_{ij}} \qquad for\ i = 0,1,2,\dots,m \quad (31)$$

Step 4. The utility degree is calculated to rank alternatives. The utility degree (k_i) for the *i*th alternative is calculated through the following equation. The alternative with the highest utility degree is optimal.

$$k_i = \frac{S_i}{V_0} \qquad for\ i = 0,1,2,\dots,m \quad (32)$$

where V_0 is the optimality value of S_i.

2.6. Methodology and Application of the Methods

The framework of the methodology is given in Figure 2. The methodology of the present study and the application of the models can be described as follows. First, a two-level hierarchy of criteria was developed. The first level of the offshoring location evaluation hierarchy consists of seven main criteria: cost, labor characteristics, infrastructure, proximity to suppliers, economic factors, quality of life, and proximity to market. The second level involves thirty sub-criteria under these main criteria (Table 1). All the criteria are determined based on a thorough literature review and expert knowledge.

Then, the Fuzzy-AHP is utilized to obtain the criteria weights since it is commonly used in the literature and provides consistent results. The pairwise comparisons of the criteria are made through the fuzzy scale, as shown in Table 2. The evaluations are provided by an expert decision-maker with twelve years of experience in the field.

The pairwise comparison matrix of the main criteria is given in Table 3. Likewise, the pairwise comparison matrices of all sub-criteria are shown in Table 4.

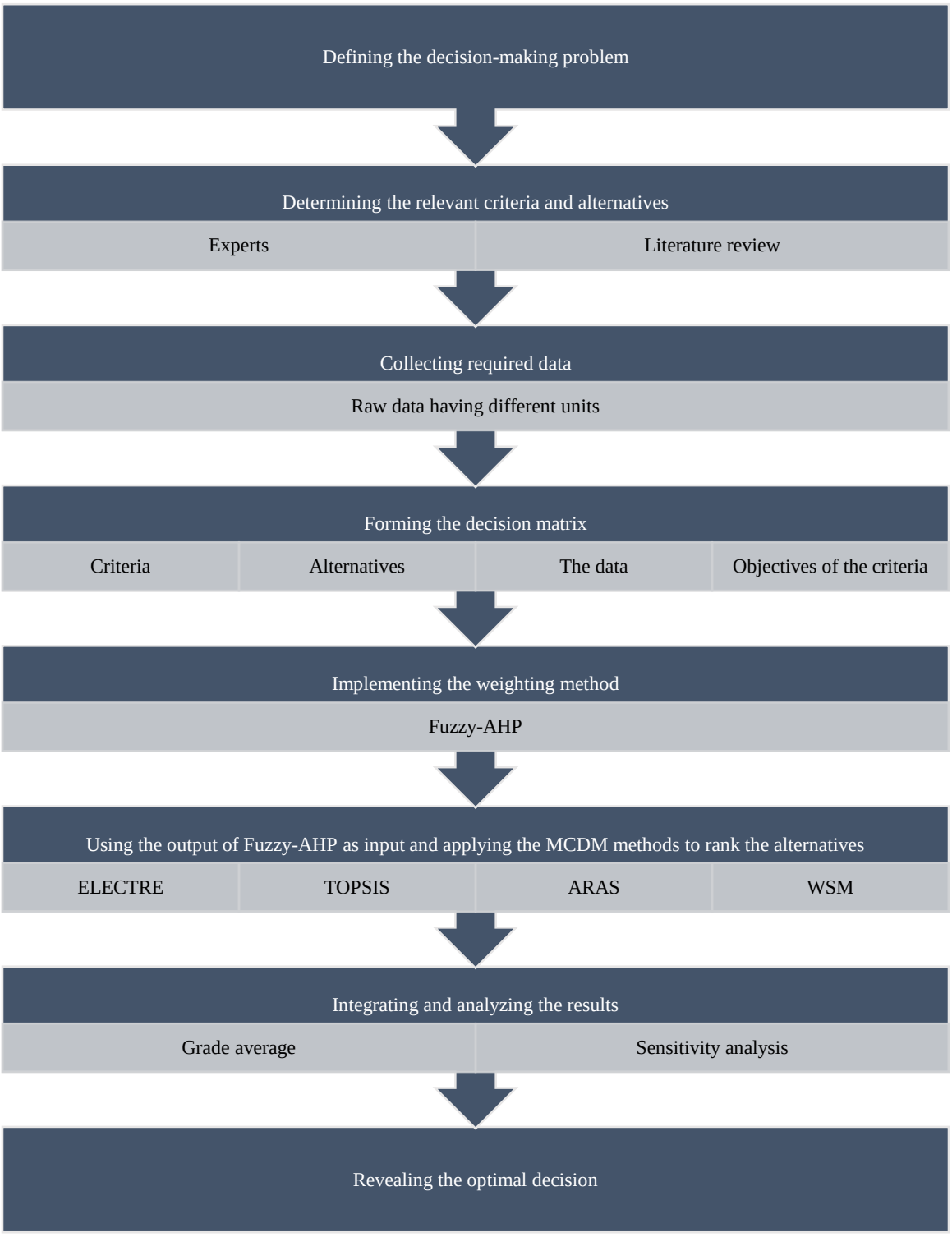

Figure 2. *The framework of the methodology.*

Table 1. *Summary of offshoring location evaluation criteria.*

Criteria	Sub-criteria	Description	Objective
Cost (C1)	Cost of labor (C11)	Labor cost	min
	Cost of power (C12)	Electricity rates	min
	Cost of land (C13)	Land cost	min
	Other manufacturing costs (C14)	Cost of starting a business	min
Labor characteristics (C2)	Existence of labor force (C21)	Total labor force	max
	Quality of labor force (C22)	Ease of finding skilled employees	max
	Unemployment rate (C23)	Unemployment rate	min
	Quality of vocational training (C24)	Quality of vocational training	max
Infrastructure (C3)	Existence of airports (C31)	Airport connectivity	max
	Existence of railroads (C_{32})	Railroad density	max
	Existence of roads (C_{33})	Road connectivity index	max
	Existence of seaports (C_{34})	Efficiency of seaport services	max
	Quality and reliability of utilities (C_{35})	Reliability of water supply	max
	Telecommunication systems (C_{36})	Percentage of individuals using the internet	max
Proximity to suppliers (C_4)	Supplier quality (C_{41})	Local supplier quality	max
	Supplier quantity (C_{42})	Local supplier quantity	max
	Existence of international suppliers (C_{43})	Manufacturing, value added (current US$)	max
Economic factors (C_5)	Tariffs (C_{51})	Trade tariffs	min
	Inflation (C_{52})	Inflation annual % change	min
	GDP growth (C_{53})	GDP growth (annual %)	max
	Income per capita (C_{54})	Adjusted net national income per capita (current US$)	max
	Country risk (C_{55})	Country Risk	min
Quality of life (C_6)	Quality of environment (C_{61})	Pollution index	min
	Climate (C_{62})	Climate index	max
	Quality of the education system (C_{63})	Quality of the education system	max
	Health services (C_{64})	Health index	max
	Crime rate (C_{65})	Crime index for the country	min
	Standard of living (C_{66})	Human development index	max
Proximity to markets (C_7)	Size of market that can be served (C_{71})	Population of the country	max
	Population trends (C_{72})	Population growth rate	max

Table 2. *Linguistic scale for the Fuzzy-AHP.*

Linguistic variables	Triangular fuzzy scale	Reciprocal of triangular fuzzy scale
Exactly the same	(1, 1, 1)	(1, 1, 1)
Equally important	(0.5, 1, 1.5)	(0.667, 1, 2)
Slightly important	(1, 1.5, 2)	(0.5, 0.667, 1)
Strongly important	(1.5, 2, 2.5)	(0.4, 0.5, 0.667)
Very strongly important	(2, 2.5, 3)	(0.333, 0.4, 0.5)
Extremely important	(2.5, 3, 3.5)	(0.286, 0.333, 0.4)

Table 3. *Pairwise comparison concerning goal.*

Criteria	C_1	C_2	C_3	C_4	C_5	C_6	C_7
C_1	(1,1,1)	(1.5,2,2.5)	(1,1.5,2)	(1,1.5,2)	(1,1.5,2)	(2.5,3,3.5)	(2,2.5,3)
C_2	(0.4,0.5,0.667)	(1,1,1)	(0.667,1,2)	(0.5,0.667,1)	(0.667,1,2)	(1.5,2,2.5)	(1,1.5,2)
C_3	(0.5,0.667,1)	(0.5,1,1.499)	(1,1,1)	(0.5,0.667,1)	(0.667,1,2)	(1,1.5,2)	(0.5,1,1.5)
C_4	(0.5,0.667,1)	(1,1.499,2)	(1,1.499,2)	(1,1,1)	(0.5,1,1.5)	(2,2.5,3)	(1.5,2,2.5)
C_5	(0.5,0.667,1)	(0.5,1,1.499)	(0.5,1,1.499)	(0.667,1,2)	(1,1,1)	(1,1.5,2)	(0.5,1,1.5)
C_6	(0.286,0.333,0.4)	(0.4,0.5,0.667)	(0.5,0.667,1)	(0.333,0.4,0.5)	(0.5,0.667,1)	(1,1,1)	(0.667,1,2)

C_7	(0.333,0.4,0.5)	(0.5,0.667,1)	(0.667,1,2)	(0.4,0.5,0.667)	(0.667,1,2)	(0.5,1,1.499)	(1,1,1)

Table 4. *Pairwise comparison matrices of sub-criteria of cost (a), labor characteristics (b), infrastructure (c), proximity to suppliers (d), economic factors (e), quality of life (f), and proximity to market (g)*

(a)

Sub-criteria	C_{11}	C_{12}	C_{13}	C_{14}
C_{11}	(1,1,1)	(1.5,2,2.5)	(1,1.5,2)	(1,1.5,2)
C_{12}	(0.4,0.5,0.667)	(1,1,1)	(0.5,0.667,1)	(0.4,0.5,0.667)
C_{13}	(0.5,0.667,1)	(1,1.499,2)	(1,1,1)	(0.5,0.667,1)
C_{14}	(0.5,0.667,1)	(1.499,2,2.5)	(1,1.499,2)	(1,1,1)

(b)

Sub-criteria	C_{21}	C_{22}	C_{23}	C_{24}
C_{21}	(1,1,1)	(0.667,1,2)	(1,1.5,2)	(1.5,2,2.5)
C_{22}	(0.5,1,1.499)	(1,1,1)	(1,1.5,2)	(1.5,2,2.5)
C_{23}	(0.5,0.667,1)	(0.5,0.667,1)	(1,1,1)	(1,1.5,2)
C_{24}	(0.4,0.5,0.667)	(0.4,0.5,0.667)	(0.5,0.667,1)	(1,1,1)

(c)

Sub-criteria	C_{31}	C_{32}	C_{33}	C_{34}	C_{35}	C_{36}
C_{31}	(1,1,1)	(1.5,2,2.5)	(2,2.5,3)	(0.5,1,1.5)	(2,2.5,3)	(1,1.5,2)
C_{32}	(0.4,0.5,0.667)	(1,1,1)	(0.5,1,1.5)	(0.5,0.667,1)	(1,1.5,2)	(0.5,0.667,1)
C_{33}	(0.333,0.4,0.5)	(0.667,1,2)	(1,1,1)	(0.4,0.5,0.667)	(1,1.5,2)	(0.5,0.667,1)
C_{34}	(0.667,1,2)	(1,1.499,2)	(1.499,2,2.5)	(1,1,1)	(1.5,2,2.5)	(1,1.5,2)
C_{35}	(0.333,0.4,0.5)	(0.5,0.667,1)	(0.5,0.667,1)	(0.4,0.5,0.667)	(1,1,1)	(0.4,0.5,0.667)
C_{36}	(0.5,0.667,1)	(1,1.499,2)	(1,1.499,2)	(0.5,0.667,1)	(1.499,2,2.5)	(1,1,1)

(d)

Sub-criteria	C_{41}	C_{42}	C_{43}
C_{41}	(1,1,1)	(1,1.5,2)	(0.667,1,2)
C_{42}	(0.5,0.667,1)	(1,1,1)	(0.5,0.667,1)
C_{43}	(0.5,1,1.499)	(1,1.499,2)	(1,1,1)

(e)

Sub-criteria	C_{51}	C_{52}	C_{53}	C_{54}	C_{55}
C_{51}	(1,1,1)	(1,1.5,2)	(2,2.5,3)	(1.5,2,2.5)	(0.667,1,2)
C_{52}	(0.5,0.667,1)	(1,1,1)	(1,1.5,2)	(1,1.5,2)	(0.5,0.667,1)
C_{53}	(0.333,0.4,0.5)	(0.5,0.667,1)	(1,1,1)	(0.5,0.667,1)	(0.4,0.5,0.667)
C_{54}	(0.4,0.5,0.667)	(0.5,0.667,1)	(1,1.499,2)	(1,1,1)	(0.5,0.667,1)
C_{55}	(0.5,1,1.499)	(1,1.499,2)	(1.499,2,2.5)	(1,1.499,2)	(1,1,1)

(f)

Sub-criteria	C_{61}	C_{62}	C_{63}	C_{64}	C_{65}	C_{66}
C_{61}	(1,1,1)	(1,1.5,2)	(0.5,1,1.5)	(1.5,2,2.5)	(0.667,1,2)	(0.5,0.667,1)
C_{62}	(0.5,0.667,1)	(1,1,1)	(0.667,1,2)	(0.5,1,1.5)	(0.5,0.667,1)	(0.333,0.4,0.5)
C_{63}	(0.667,1,2)	(0.5,1,1.499)	(1,1,1)	(1,1.5,2)	(0.5,0.667,1)	(0.4,0.5,0.667)
C_{64}	(0.4,0.5,0.667)	(0.667,1,2)	(0.5,0.667,1)	(1,1,1)	(0.4,0.5,0.667)	(0.286,0.333,0.4)
C_{65}	(0.5,1,1.499)	(1,1.499,2)	(1,1.499,2)	(1.499,2,2.5)	(1,1,1)	(0.5,0.667,1)
C_{66}	(1,1.499,2)	(2,2.5,3.3)	(1.499,2,2.5)	(2.5,3.3,3.497)	(1,1.499,2)	(1,1,1)

(g)

Sub-criteria	C_{71}	C_{72}
C_{71}	(1,1,1)	(0.5,1,1.5)
C_{72}	(0.667,1,2)	(1,1,1)

The consistency ratios for the comparison matrices are computed to determine the accuracy of expert assessments. Once it is assured that the ratio values are accepted values, the subsequent step, in which the alternatives are ranked, is

performed. In this context, fifteen location alternatives, which are Brazil (A1), Canada (A2), Chile (A3), China (A4), Czech Republic (A5), Hungary (A6), India (A7), Malaysia (A8), Mexico (A9), Philippines (A10), Poland (A11), Russia (A12), Singapore (A13), Thailand (A14), and Turkey (A15), are determined based on offshoring location preferences worldwide. The data of each criterion for each country are collected from [66-74]. The data is the input for the TOPSIS, WSM, ARAS, and ELECTRE methods. The alternatives are evaluated against each criterion using the TOPSIS, WSM, ARAS, and ELECTRE methods, for whom the equations mentioned before are employed, respectively. Then, the ranks of alternatives are obtained for each method, and they are compared to each other. Also, an integrated rank of alternatives is presented.

3. Results and Discussion

The Fuzzy-AHP results indicate that the cost criterion has the highest weight, followed by proximity to suppliers, labor characteristics, economic factors, infrastructure, proximity to markets, and quality of life, as shown in Table 5. The consistency ratios of all comparison matrices are less than 10%, which is within a reasonable limit. Table 5 also provides the sub-criteria weights and indicates that labor cost has the highest weight.

Table 5. *Weights provided by the Fuzzy-AHP.*

Main criteria	Weights of main criteria	Sub-criteria	Local weights of sub-criteria	Global weights of sub-criteria	Rank
C_1	0.250	C_{11}	0.386	0.0965	1
		C_{12}	0.068	0.0170	19
		C_{13}	0.219	0.0548	5
		C_{14}	0.328	0.0820	2
C_2	0.150	C_{21}	0.339	0.0509	6
		C_{22}	0.339	0.0509	6
		C_{23}	0.225	0.0338	14
		C_{24}	0.097	0.0146	21
C_3	0.127	C_{31}	0.299	0.0380	13
		C_{32}	0.117	0.0149	20
		C_{33}	0.114	0.0145	22
		C_{34}	0.259	0.0329	15
		C_{35}	0.011	0.0014	30
		C_{36}	0.200	0.0254	17
C_4	0.197	C_{41}	0.381	0.0751	3
		C_{42}	0.237	0.0467	10
		C_{43}	0.381	0.0751	3
C_5	0.137	C_{51}	0.327	0.0448	11
		C_{52}	0.204	0.0279	16
		C_{53}	0.043	0.0059	26
		C_{54}	0.138	0.0189	18
		C_{55}	0.287	0.0393	12
C_6	0.042	C_{61}	0.198	0.0083	25
		C_{62}	0.093	0.0039	28
		C_{63}	0.137	0.0058	27
		C_{64}	0.038	0.0016	29
		C_{65}	0.208	0.0087	24
		C_{66}	0.327	0.0137	23
C_7	0.095	C_{71}	0.500	0.0475	8
		C_{72}	0.500	0.0475	8

To ensure that all criteria can be easily compared concerning the importance levels, the following figure is given. Figure 3 shows that the quality and reliability of utilities is the least important criteria.

Then, the rankings of the offshoring location alternatives are determined through algorithms of TOPSIS, ELECTRE III, ARAS, and WSM methods, as given in Table 6.

Table 6. *Rankings of the alternatives by proposed methods.*

Alternative	Rankings			
	TOPSIS	ELECTRE III	WSM	ARAS
Brazil	9	13	15	14
Canada	14	1	2	4
Chile	4	9	6	9
China	1	5	1	1
Czech Republic	5	4	4	5
Hungary	7	15	13	15
India	2	6	8	3
Malaysia	6	8	3	11
Mexico	11	2	10	8
Philippines	8	14	11	7
Poland	13	11	7	13
Russia	3	3	9	6
Singapore	15	10	5	2
Thailand	10	12	12	12
Turkey	12	7	14	10

To observe the results clearly and make comparisons, Figure 4 is presented. The TOPSIS results reveal that China is the optimal offshoring location. The ELECTRE results indicate that Canada is the optimal offshoring location. The WSM results reveal that China is the optimal offshoring location. Similarly, the results of the ARAS designate that China is the best option. It is understood that TOPSIS, ARAS, and WSM recommend the same alternative location as the best. This result may indicate that these three methods provide a more consistent result than the ELECTRE, as China has been one of the leading offshoring locations for years. However, this may not be enough to generalize this statement for the whole case. India has also been one of the most preferred offshoring locations. The rankings of India are second, sixth, eighth, and third for TOPSIS, ELECTRE, WSM, and ARAS, respectively. This result indicates that TOPSIS, followed by ARAS, provided a more realistic result than the WSM and ELECTRE. It can also be seen that the ELECTRE ranks India higher than the WSM, meaning that the outcome of the ELECTRE is more realistic for this case. Also, Malaysia, which was ranked third by the WSM, and Mexico, which was

ranked second by the ELECTRE, are two of the most chosen countries for offshoring in real life. Therefore, it can be understood that each method provides effective results for different situations. Considering the overall results of all methods, the Czech Republic is ranked similarly by all the approaches.

To extend the analysis and demonstrate an integrated result, the average ranks of the four methods are calculated and ranked, as shown in Table 7. The integrated results reveal that China is the most suitable offshoring location, followed by the Czech Republic and India. The rank of the Czech Republic might be unexpected. In this regard, to reveal the impact of criteria weights and test the methods' robustness, a sensitivity analysis is conducted.

Table 7. *Average ranks of four methods and integrated ranks of alternatives.*

Alternative	Average Rank	Integrated Rank
Brazil	12.75	15
Canada	5.25	4
Chile	7	6
China	2	1
Czech Republic	4.5	2
Hungary	12.5	14
India	4.75	3
Malaysia	7	6
Mexico	7.75	8
Philippines	10	10
Poland	11	12
Russia	5.25	4
Singapore	8	9
Thailand	11.5	13
Turkey	10.75	11

As the criteria weights prominently affect the ranking of alternatives, the value change of the weights should be examined. Thus, the impact of subjective evaluation can be observed. Different scenarios are constructed to reveal an overall evaluation. In this context, the main criterion is assigned 90% weight, and the rest 10% of the weight is distributed to the remaining criteria in the ratio of the weights assigned in the beginning. Likewise, the weights of the sub-criteria are allocated in the same way. This process is fulfilled for all criteria, respectively. Additionally, equal weights are assigned to all the criteria as an additional scenario. Sensitivity analysis is performed for the TOPSIS, ELECTRE, ARAS, and WSM methods, so 8×4 = 32 cases are examined altogether. The results of the calculations are obtained for all methods. The sensitivity analysis outcomes demonstrated that the outcomes of the ELECTRE, ARAS, and WSM are more robust than the TOPSIS, as shown in Table 8. The rankings of these three models are more stable than the TOPSIS as they provide the same rankings under different scenarios. To be noted, scenario "0" represents the original case in this table. Considering all scenarios, it can be inferred that all the approaches provide the closest results in Scenario 5.

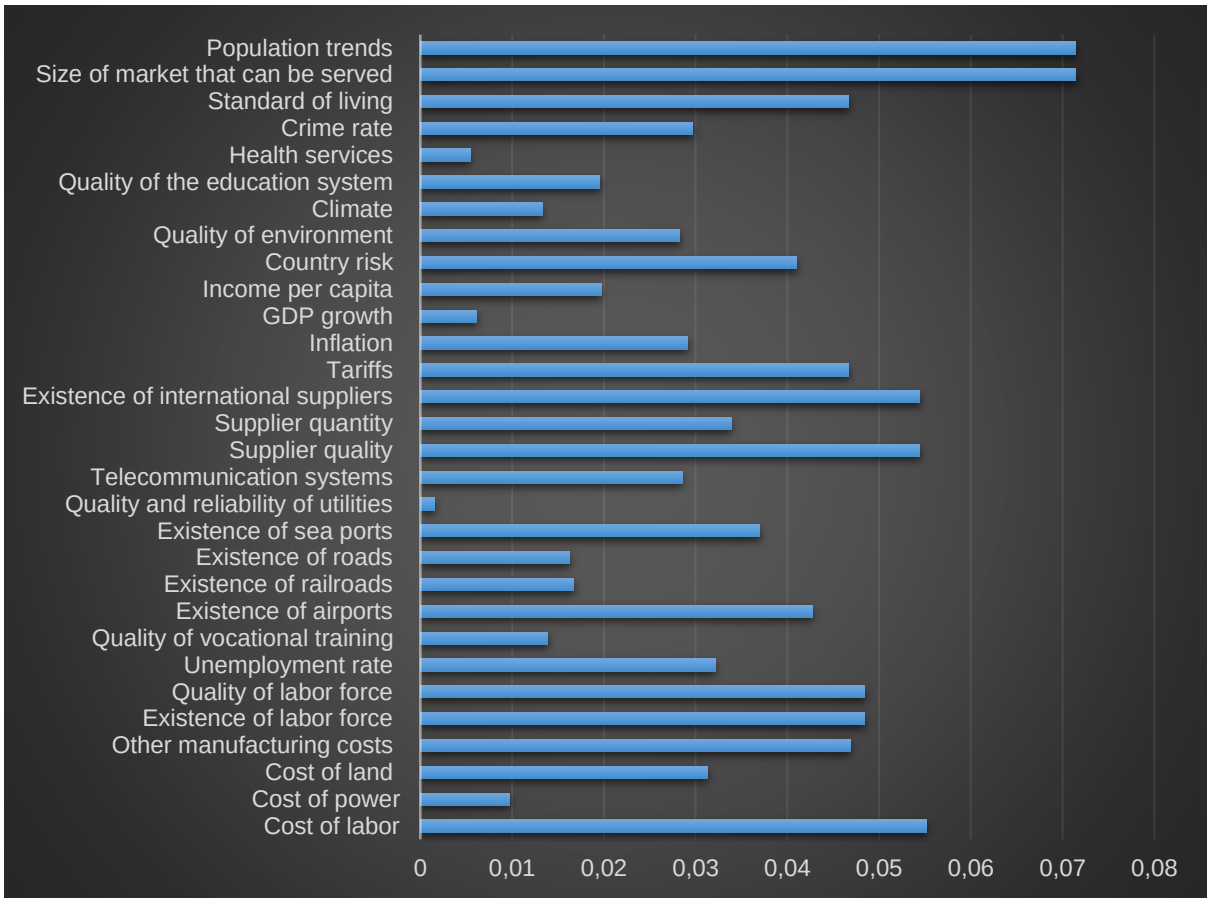

Figure 3. *Comparison of weights of criteria.*

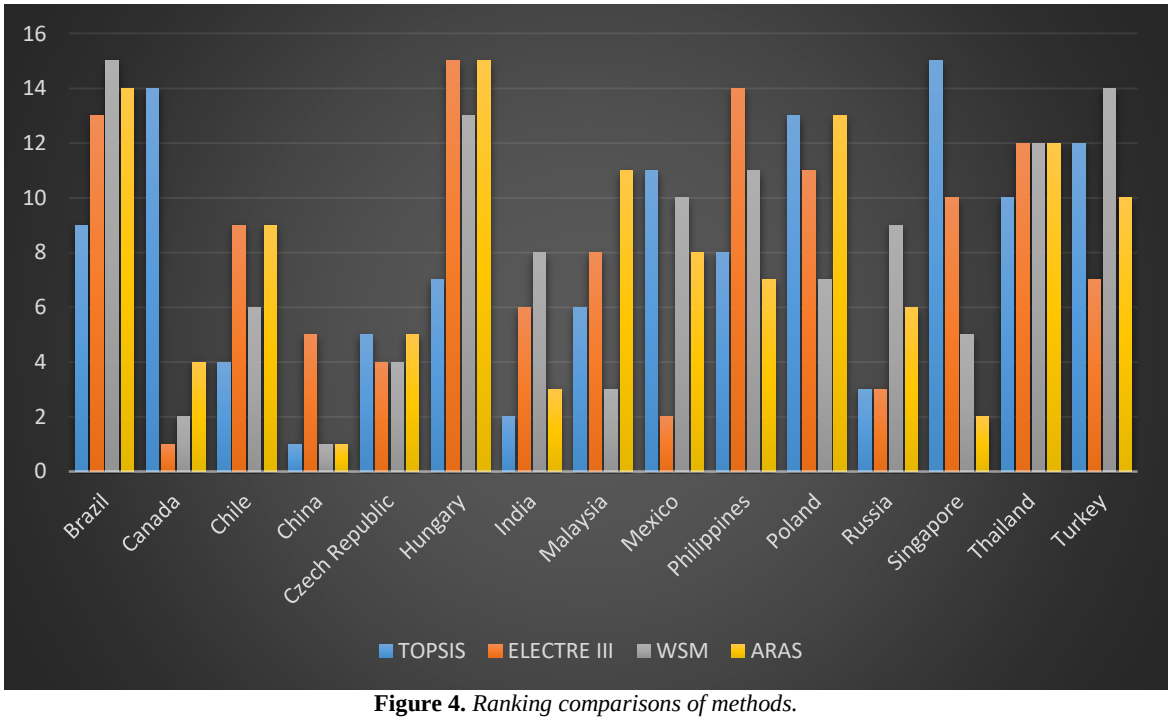

Figure 4. *Ranking comparisons of methods.*

Table 8. *Ranking of locations under different scenarios.*

Scenario	Method	Location Ranks														
		A1	A2	A3	A4	A5	A6	A7	A8	A9	A10	A11	A12	A13	A14	A15
0	TOPSIS	9	14	4	1	5	7	2	6	11	8	13	3	15	10	12
	WSM	15	2	6	1	4	13	8	3	10	11	7	9	5	12	14
	ELECTRE	13	1	9	5	4	15	6	8	2	14	11	3	10	12	7
	ARAS	14	4	9	1	5	15	3	11	8	7	13	6	2	12	10
1	TOPSIS	3	14	2	8	6	4	11	5	13	12	10	1	15	7	9
	WSM	6	9	3	7	5	4	11	2	13	14	12	1	15	10	8
	ELECTRE	4	2	11	6	14	8	9	3	12	10	13	1	15	7	5
	ARAS	10	1	12	2	8	13	7	11	9	5	15	4	3	14	6
2	TOPSIS	14	12	13	1	7	11	2	5	6	4	10	9	8	3	15
	WSM	15	6	7	1	12	13	2	3	8	5	11	9	4	10	14
	ELECTRE	12	1	10	4	2	14	5	6	3	9	11	8	15	7	13
	ARAS	11	9	13	1	10	15	2	6	7	4	12	8	5	3	14
3	TOPSIS	14	4	12	1	2	5	3	8	11	15	7	10	6	13	9
	WSM	14	3	4	1	5	11	12	7	9	15	6	8	2	13	10
	ELECTRE	12	1	9	8	2	15	11	3	6	14	13	5	4	10	7
	ARAS	14	5	13	1	2	6	4	12	9	15	7	10	3	11	8
4	TOPSIS	7	3	12	1	4	15	2	5	6	14	11	9	10	13	8
	WSM	11	2	7	1	3	15	10	4	8	13	6	12	5	14	9
	ELECTRE	13	1	8	5	4	15	11	7	2	14	10	3	9	12	6
	ARAS	8	3	13	1	6	15	2	7	5	14	11	10	4	12	9
5	TOPSIS	15	2	6	12	3	5	14	7	10	8	4	11	1	9	13
	WSM	15	2	6	10	4	5	13	7	11	8	3	12	1	9	14
	ELECTRE	15	1	3	8	5	7	13	9	10	11	6	4	2	12	14
	ARAS	15	2	6	7	3	5	8	9	13	12	4	10	1	14	11
6	TOPSIS	15	2	10	7	3	4	12	14	11	9	5	8	1	13	6
	WSM	15	2	6	11	3	5	14	8	10	13	4	7	1	12	9
	ELECTRE	13	1	8	10	3	6	15	12	9	11	4	5	2	14	7
	ARAS	15	2	10	4	3	5	9	12	7	13	6	11	1	14	8
7	TOPSIS	8	9	7	2	12	15	1	5	6	3	14	13	10	11	4
	WSM	9	8	6	2	12	15	1	4	7	3	14	13	10	11	5
	ELECTRE	12	3	9	5	4	15	6	8	1	13	10	2	14	11	7
	ARAS	8	9	7	2	13	15	1	5	6	3	14	12	10	11	4
8	TOPSIS	15	6	3	1	8	11	2	4	9	5	12	13	7	14	10
	WSM	15	1	6	2	5	12	7	4	9	11	8	10	3	14	13
	ELECTRE	14	1	9	4	2	15	7	11	3	13	10	5	6	12	8
	ARAS	14	4	6	1	5	15	3	10	7	8	12	11	2	13	9

The changes in the rankings provided by the methods can be observed well in Figure 5. The changes in the ranking of alternatives are seen more often in TOPSIS than the WSM, ARAS, and ELECTRE under different scenarios. This observation can be an indicator of the robustness of the WSM, ARAS, and ELECTRE. However, the results of the TOPSIS suggest China and India as the most optimal offshoring locations, as they are in real life, in several scenarios. Thus, the TOPSIS was distinguished from the WSM and ELECTRE in terms of providing the most realistic outcome for this case. However, all the MCDM approaches suggested in this study provide competitive and effective results.

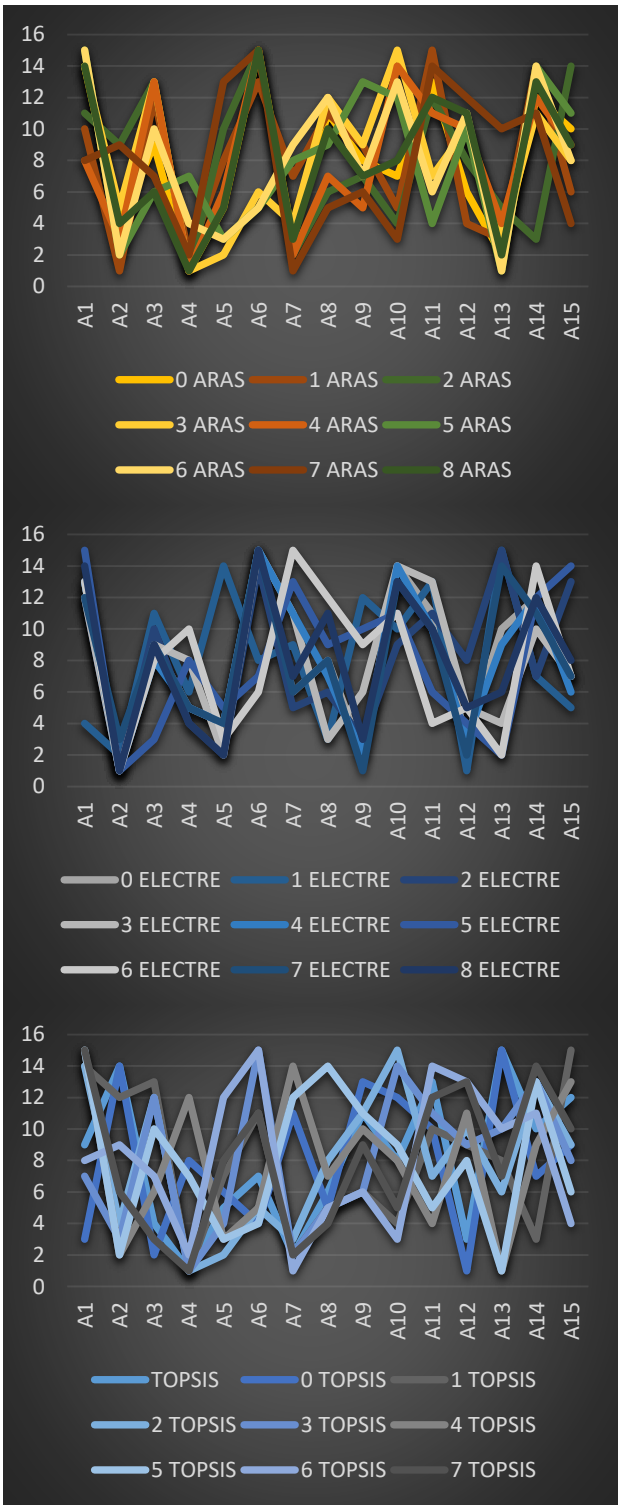

Figure 5. *Rank changes of ARAS, ELECTRE, TOPSIS, and WSM.*

To sum up, the sensitivity analysis results indicated that the situation in Scenario 2 is close to the case in real life in terms of providing the best offshoring locations, China, and India. It can be inferred that more weights need to be allocated to labor characteristics, namely the existence of labor force, unemployment rate, quality of labor force, and quality of vocational training. Also, Scenario 7 indicated that allocating more weights to proximity to markets criteria, namely the size of market that can be served and population trends, might improve the accuracy of the proposed methodology. Furthermore, if these changes were made, excluding the ELECTRE method might improve the accuracy of the rank result of the integrated rank results.

4. Conclusions

Unlike other studies, this study presented integrated models and a comparative analysis for optimizing decisions of offshoring location that represents a real-life problem. An integrated MCDM-based methodology was proposed for determining the best offshoring location. Thus, a practical approach that can be used by decision-makers in real life was presented. In this context, the Fuzzy-AHP was combined with the TOPSIS, WSM, ARAS, and ELECTRE. Fuzzy-AHP was applied to determine the weights of the criteria obtained from relevant literature and expert knowledge. Then, the alternative offshoring locations were ranked based on TOPSIS, WSM, ARAS, and ELECTRE. ARAS was utilized for the offshoring problem for the first time in this study.

Using actual data, the TOPSIS, WSM, ARAS, and ELECTRE methods provided competitive and effective results for the problem. Moreover, the comparative analysis, which is also a valuable contribution, revealed that the results of the TOPSIS might be assessed as more successful considering the preference rates of the offshoring locations in real life. Additionally, by conducting sensitivity analysis, the robustness of the methods was evaluated, and the subjectivity of evaluations was diminished. The ELECTRE III, ARAS,

and WSM methods were found to be more robust than the TOPSIS as their rankings were more stable compared to the priority ranking in general. However, the TOPSIS was robust in suggesting the best location (A4) in different scenarios. In addition, the results of the sensitivity analysis revealed that allocating more weights to the labor characteristics and proximity to market criteria might improve the quality of the results. Thus, it can be concluded that these methods can be effectively utilized for the offshoring location decision problem. However, the use of ELECTRE might be unnecessary for the purpose of the study if these changes were made. Compared to other studies, MCDM methods were applied to offshoring location selection problems like previous studies. However, the integration of the methods used in this study differs from previous studies.

Subsequently, considerable contributions were made in this study. However, there are some limitations. First, using more MCDM methods could improve the accuracy of the result. Second, implementing objective weighting methods such as entropy and standard deviation might contribute to the analysis. Third, a group decision-making approach could increase reliability. Last, not considering all countries might limit the generalization of the analysis. Thus, future studies can extend the literature by concentrating on utilizing other MCDM methods. Methods of weighting objective criteria for group decision-making can be incorporated into the model. It may also be worth examining more locations and adding additional criteria.

REFERENCES

[1]. Contractor, F.J., et al. 2010. "Reconceptualizing the Firm in a World of Outsourcing and Offshoring: The Organizational and Geographical Relocation of High-Value Company Functions". *Journal of Management Studies*. **47**(8): p. 1417-1433.

[2]. Roza, M., F.A.J. Van den Bosch, and H.W. Volberda. 2011. "Offshoring strategy: Motives, functions, locations, and governance modes of small, medium-sized and large firms". *International Business Review*. **20**(3): p. 314-323.

[3]. Grossman, G.M. and E. Helpman. 2005. "Outsourcing in a Global Economy". *The Review of Economic Studies*. **72**(1): p. 135-159.

[4]. Mihalache, M. and O.R. Mihalache. 2016. "A Decisional Framework of Offshoring: Integrating Insights from 25 Years of Research to Provide Direction for Future*". *Decision Sciences Journal*. **47**(6): p. 1103-1149.

[5]. Bergin, P.R., R.C. Feenstra, and G.H. Hanson. 2011. "Volatility due to offshoring: Theory and evidence". *Journal of International Economics*. **85**(2): p. 163-173.

[6]. Kinkel, S. and S. Maloca. 2009. "Drivers and antecedents of manufacturing offshoring and backshoring—A German perspective". *Journal of Purchasing and Supply Management*. **15**(3): p. 154-165.

[7]. Michel, B. and F. Rycx. 2011. "Does offshoring of materials and business services affect employment? Evidence from a small open economy". *Applied Economics*. **44**(2): p. 229-251.

[8]. Ellram, L.M., W.L. Tate, and K.J. Petersen. 2013. "Offshoring and Reshoring: An Update on the Manufacturing Location Decision". *Journal of Supply Chain Management* **49**(2): p. 14-22.

[9]. Stentoft, J., et al. 2018. "Performance outcomes of offshoring, backshoring and staying at home manufacturing". *International Journal of Production Economics*. **199**: p. 199-208.

[10]. Schmenner, R.W., J.C. Huber, and R.L. Cook. 1987. "Geographic differences and the location of new manufacturing facilities". *Journal of Urban Economics*. **21**(1): p. 83-104.

[11]. Buckley, P.J. and M.C. Casson. 2009. "The internalisation theory of the multinational enterprise: A review of the progress of a research agenda after 30 years". *Journal of International Business Studies*. **40**(9): p. 1563-1580.

[12]. Dunning, J.H. 1998. "Location and the Multinational Enterprise: A Neglected Factor?". *Journal of International Business Studies*. **29**(1): p. 45-66.

[13]. Gupta, P., M.K. Mehlawat, and N. Grover. 2016. "Intuitionistic fuzzy multi-attribute group decision-making with an application to plant location selection based on a new extended VIKOR method". *Information Sciences*. **370-371**: p. 184-203.

[14]. Lai, C.-M. 2019. "Integrating simplified swarm optimization with AHP for solving capacitated military logistic depot location problem". *Applied Soft Computing*. **78**: p. 1-12.

[15]. Ishizaka, A., P. Nemery, and K. Lidouh. 2013. "Location selection for the construction of a casino in the Greater London region: A triple multi-criteria approach". *Tourism Management*. **34**: p. 211-220.

[16]. Liu, L.B., et al. 2008. "Applying the analytic hierarchy process to the offshore outsourcing location decision". *Supply Chain Management-an International Journal*. **13**(6): p. 435-449.

[17]. Dou, Y. and J. Sarkis. 2010. "A joint location and outsourcing sustainability analysis for a strategic offshoring decision". *International Journal of Production Research*. **48**(2): p. 567-592.

[18]. López, C. and A. Ishizaka. 2017. "A hybrid FCM-AHP approach to predict impacts of offshore outsourcing location decisions on supply chain resilience". *Journal of Business Research*.

[19]. De Felice, F., A. Petrillo, and L. Petrillo. 2021. "Captive offshoring drivers in the manufacturing industry: criteria and sub-criteria that influence the location choice". *International Journal of Production Research*. **59**(1): p. 76-94.

[20]. Costanzo, A.M. and S.A. Ahmed. 2021. "Eastern European Offshoring: Determining The Value of Offshoring Locations in Eastern Europe Using Desirability Index". *Performance Improvement*. **60**(4): p. 14-20.
[21]. Şahin, M. 2020. "Hybrid Multicriteria Group Decision-Making Method for Offshore Location Selection Under Fuzzy Environment". *Arabian Journal for Science and Engineering*.
[22]. Wu, Y., et al. 2019. "Location selection of seawater pumped hydro storage station in China based on multi-attribute decision making". *Renewable Energy*. **139**: p. 410-425.
[23]. Johansson, M. and J. Olhager. 2018. "Comparing offshoring and backshoring: The role of manufacturing site location factors and their impact on post-relocation performance". *International Journal of Production Economics*. **205**: p. 37-46.
[24]. Kaur, H., S.P. Singh, and A. Majumdar. 2019. "Modelling joint outsourcing and offshoring decisions". *International Journal of Production Research*: p. 1-32.
[25]. Ngwenyama, O.K. and N. Bryson. 1999. "Making the information systems outsourcing decision: A transaction cost approach to analyzing outsourcing decision problems". *European Journal of Operational Research*. **115**(2): p. 351-367.
[26]. Swenson, D.L. 2005. "Overseas assembly and country sourcing choices". *Journal of International Economics*. **66**(1): p. 107-130.
[27]. Feldmann, A. and J. Olhager. 2013. "Plant roles: site competence bundles and their relationships with site location factors and performance". *International Journal of Operations & Production Management*. **33**(6): p. 722-744.
[28]. McMillan, T.E. 1965. "Why Manufacturers Choose Plant Locations vs. Determinants of Plant Locations". *Land Economics*. **41**(3): p. 239-246.
[29]. Schmenner, R.W., "*Making business location decisions"*. 1982: Prentice Hall.
[30]. Wheeler, D. and A. Mody. 1992. "International investment location decisions: The case of US firms". *Journal of international economics*. **33**(1-2): p. 57-76.
[31]. Coughlin, C.C., J.V. Terza, and V. Arromdee. 1991. "State characteristics and the location of foreign direct investment within the United States". *The Review of Economics and Statistics*: p. 675-683.
[32]. MacCarthy, B.L. and W. Atthirawong. 2003. "Factors affecting location decisions in international operations – a Delphi study". *International Journal of Operations & Production Management*. **23**(7): p. 794-818.
[33]. Maritan, C.A., T.H. Brush, and A.G. Karnani. 2004. "Plant roles and decision autonomy in multinational plant networks". *Journal of Operations Management*. **22**(5): p. 489-503.
[34]. Saaty, T.L. 1977. "A scaling method for priorities in hierarchical structures". *Journal of Mathematical Psychology*. **15**(3): p. 234-281.
[35]. Deng, H. 1999. "Multicriteria analysis with fuzzy pairwise comparison". *International Journal of Approximate Reasoning*. **21**(3): p. 215-231.
[36]. Wang, T.-C. and Y.-H. Chen. 2007. "Applying consistent fuzzy preference relations to partnership selection". *Omega*. **35**(4): p. 384-388.
[37]. Asakereh, A., M. Soleymani, and M.J. Sheikhdavoodi. 2017. "A GIS-based Fuzzy-AHP method for the evaluation of solar farms locations: Case study in Khuzestan province, Iran". *Solar Energy*. **155**: p. 342-353.
[38]. Hanine, M., et al. 2017. "An application of OLAP/GIS-Fuzzy AHP-TOPSIS methodology for decision making: Location selection for landfill of industrial wastes as a case study". *KSCE Journal of Civil Engineering*. **21**(6): p. 2074-2084.
[39]. Vasantha Lakshmi, K. and K.N. Udaya Kumara. 2024. "A novel randomized weighted fuzzy AHP by using modified normalization with the TOPSIS for optimal stock portfolio selection model integrated with an effective sensitive analysis". *Expert Systems with Applications*. **243**: p. 122770.
[40]. Dhumras, H. and R.K. Bajaj. 2024. "On potential strategic framework for green supply chain management in the energy sector using q-rung picture fuzzy AHP & WASPAS decision-making model". *Expert Systems with Applications*. **237**: p. 121550.
[41]. Ally, A.M., et al. 2024. "Assessment of groundwater potential zones using remote sensing and GIS-based fuzzy analytical hierarchy process (F-AHP) in Mpwapwa District, Dodoma, Tanzania". *Geosystems and Geoenvironment*. **3**(1): p. 100232.
[42]. Singh, A. and A. Prasher. 2019. "Measuring healthcare service quality from patients' perspective: using Fuzzy AHP application". *Total Quality Management & Business Excellence*. **30**(3-4): p. 284-300.
[43]. Chang, D.-Y. 1996. "Applications of the extent analysis method on fuzzy AHP". *European Journal of Operational Research*. **95**(3): p. 649-655.
[44]. Zhu, K.-J., Y. Jing, and D.-Y. Chang. 1999. "A discussion on Extent Analysis Method and applications of fuzzy AHP". *European Journal of Operational Research*. **116**(2): p. 450-456.
[45]. Hwang, C.-L. and K. Yoon, "*Methods for multiple attribute decision making"*, in *Multiple attribute decision making*. 1981, Springer. p. 58-191.
[46]. Ho, W. and X. Ma. 2018. "The state-of-the-art integrations and applications of the analytic

hierarchy process". *European Journal of Operational Research*. **267**(2): p. 399-414.
[47]. Micale, R., C.M. La Fata, and G. La Scalia. 2019. "A combined interval-valued ELECTRE TRI and TOPSIS approach for solving the storage location assignment problem". *Computers & Industrial Engineering*. **135**: p. 199-210.
[48]. Konstantinos, I., T. Georgios, and A. Garyfalos. 2019. "A Decision Support System methodology for selecting wind farm installation locations using AHP and TOPSIS: Case study in Eastern Macedonia and Thrace region, Greece". *Energy Policy*. **132**: p. 232-246.
[49]. Jong, F.C. and M.M. Ahmed. 2024. "Novel GIS-based fuzzy TOPSIS and filtration algorithms for extra-large scale optimal solar energy sites identification". *Solar Energy*. **268**: p. 112274.
[50]. Shao, M., et al. 2024. "A novel framework for wave power plant site selection and wave forecasting based on GIS, MCDM, and ANN methods: A case study in Hainan Island, Southern China". *Energy Conversion and Management*. **299**: p. 117816.
[51]. Chang, K.-L., et al. 2015. "An ANP based TOPSIS approach for Taiwanese service apartment location selection". *Asia Pacific Management Review*. **20**(2): p. 49-55.
[52]. Roy, B. 1978. "ELECTRE III: Un algorithme de classements fondé sur une représentation floue des préférences en présence de critères multiples". *Cahiers du CERO*. **20**(1): p. 3-24.
[53]. Govindan, K. and M.B. Jepsen. 2016. "ELECTRE: A comprehensive literature review on methodologies and applications". *European Journal of Operational Research*. **250**(1): p. 1-29.
[54]. Martínez-García, M., et al. 2018. "A semantic multi-criteria approach to evaluate different types of energy generation technologies". *Environmental Modelling & Software*. **110**: p. 129-138.
[55]. Akram, M., F. Ilyas, and M. Deveci. 2024. "Interval rough integrated SWARA-ELECTRE model: An application to machine tool remanufacturing". *Expert Systems with Applications*. **238**: p. 122067.
[56]. Seyed Alavi, S.M., et al. 2024. "Simultaneous optimal site selection and sizing of a grid-independent hybrid wind/hydrogen system using a hybrid optimization method based on ELECTRE: A case study in Iran". *International Journal of Hydrogen Energy*. **55**: p. 970-983.
[57]. Akram, M., K. Zahid, and C. Kahraman. 2024. "A new ELECTRE-based decision-making framework with spherical fuzzy information for the implementation of autonomous vehicles project in Istanbul". *Knowledge-Based Systems*. **283**: p. 111207.
[58]. Wu, Y., et al. 2016. "Study of decision framework of offshore wind power station site selection based on ELECTRE-III under intuitionistic fuzzy environment: A case of China". *Energy Conversion and Management*. **113**: p. 66-81.
[59]. Banias, G., et al. 2010. "Assessing multiple criteria for the optimal location of a construction and demolition waste management facility". *Building and Environment*. **45**(10): p. 2317-2326.
[60]. Figueira, J.R., et al. 2013. "An Overview of ELECTRE Methods and their Recent Extensions". *Journal of Multi-Criteria Decision Analysis*. **20**(1-2): p. 61-85.
[61]. Figueira, J., V. Mousseau, and B. Roy, "*Electre Methods"*, in *Multiple Criteria Decision Analysis: State of the Art Surveys*. 2005, Springer New York: New York, NY. p. 133-153.
[62]. Zavadskas, E.K. and Z. Turskis. 2010. "A new additive ratio assessment (ARAS) method in multicriteria decision-making". *Technological and Economic Development of Economy*. **16**(2): p. 159-172.
[63]. Hosseini Dehshiri, S.J., M. Amiri, and S.M. Hosseini Bamakan. 2024. "Evaluating the blockchain technology strategies for reducing renewable energy development risks using a novel integrated decision framework". *Energy*. **289**: p. 129987.
[64]. Raj, R., et al. 2024. "Assessing the e-commerce last-mile logistics' hidden risk hurdles". *Cleaner Logistics and Supply Chain*. **10**: p. 100131.
[65]. Kannan, S., et al. 2023. "Identification of the effect of strontium and ytterbium addition over magnesium zinc alloy during the drilling process with ARAS and WASPAS techniques". *Materials Chemistry and Physics*. **309**: p. 128320.
[66]. Global Petrol Prices. 2019 [cited 2019 9/4/2019]; Available from: https://www.globalpetrolprices.com/.
[67]. International Telecommunication Union. 2019 [cited 2019 9/4/2019]; Available from: www.itu.int.
[68]. Numbeo. 2019 [cited 2019 9/4/2019]; Available from: https://www.numbeo.com.
[69]. OECD. 2019 [cited 2019 9/4/2019]; Available from: http://www.oecd.org/.
[70]. United Nations Development Programme. *Human Development Reports*. 2019 [cited 2019 9/4/2019]; Available from: http://hdr.undp.org/en.
[71]. World Bank. 2019 [cited 2019 9/4/2019]; Available from: https://data.worldbank.org/.
[72]. World Data. 2019 [cited 2019 9/4/2019]; Available from: https://www.worlddata.info/.
[73]. World Economic Forum. 2019 [cited 2019 9/4/2019]; Available from: https://www.weforum.org.
[74]. World Population Review. 2019 [cited 2019 9/4/2019]; Available from: http://worldpopulationreview.com/.

MANAS Journal of Engineering
ISSN 1694-7398 | e-ISSN 1694-7398

Volume 12, Issue 1, (2024) Pages 104-115
https://doi.org/10.51354/mjen.1375211

Circulating tumor DNA (ctDNA) Detection via electrochemical Biosensing Tools

Sonya Sahin[1], Nimet Yıldırım-Tirgil[2,*]

[1]Biomedical Engineering Department, Ankara Yildirim Beyazit University, Ankara, Turkey , sonyashaheen99@gmail.com, ORCID: 0009-0002-7722-3520

[2]Biomedical Engineering Department, Ankara Yildirim Beyazit University, Ankara, Turkey , nyildirimtirgil@ybu.edu.tr, ORCID: 0000-0002-5973-8830

ABSTRACT

Cancer is characterized by the presence of mutated alleles in DNA, leading to the formation of tumors. A delayed diagnosis of this condition can result in fatal outcomes, making it a significant global cause of mortality. WHO has emphasized that early detection could significantly increase the chances of successful treatment and recovery. Traditional cancer diagnosis relies on invasive tissue biopsies, which pose risks to both patient's and healthcare professionals due to the use of formaldehyde, a known carcinogenic agent, for specimen preservation. In recent times, liquid biopsies have emerged as a promising alternative, particularly for the analysis of circulating tumor DNA (ctDNA), a fraction of which originates from tumor cells and circulates in the bloodstream. However, conventional molecular genetic tests for ctDNA analysis are often costly and time-consuming. Advancements in technology and the field of nanoscience offer the potential to develop cost-effective, rapid, highly sensitive, and selective diagnostic tools. Among these, biosensors stand out as a promising option. In this article, we delve into the quantification of ctDNA in plasma, discuss amplification techniques for ctDNA, and explore the development of electrochemical-based biosensors tailored for ctDNA detection. Finally, we highlight recent studies and innovations in the field of ctDNA detection.

ARTICLE INFO

Research article

Received: 16.10.2023
Accepted: 08.01.2024

Keywords:

Liquid biopsies, Circulating tumor DNA, ctDNA, Amplification techniques, Biosensors, Electrochemical detection

**Corresponding author*

1. Introduction

Circulating tumor DNA (ctDNA) is a fraction of cell-free DNA (cfDNA) present in the bloodstream of cancer patients. Malignant tumors release ctDNA into the blood, typically in low quantities, either at the onset of the disease or following successful therapy [1]. In the year 2020, 19.3 million new cases of cancer worldwide were diagnosed (18.1 million excluding non-melanoma skin cancer) and around 10.0 million cancer-related deaths (9.9 million excluding non-melanoma skin cancer). All over the world, female breast cancer (2.26 million cases), lung cancer (2.21), and prostate cancer (1.41 million cases) were the most widely diagnosed cancers. Lung, liver, and stomach cancers were the most frequently reported causes of cancer-related deaths[2], WHO has underscored that early detection could enhance the curability of cancer, potentially saving 40 percent of affected individuals if diagnose at an earlier stage [3].

While numerous sensitive diagnostic methods and specimens have been employed for cancer detection, many of them pose risks to the patient's physical health. For instance, imaging techniques like tomography involve excessive ionizing radiation exposure. Solid biopsy methods, which analyze tissue samples, struggle to accurately capture dynamic tumor changes due to the heterogeneity of tumors and are inadequate for diagnosing brain and lung tumors [4]. Hence, liquid biopsies, utilizing bodily fluids such as peripheral blood, saliva, cerebrospinal fluid, and urine, depending on the tumor's. location, offer a safer alternative, as they contain cell-free DNA with quantifiable ctDNA levels. However, liquid biopsies still have certain limitations [5].

Liquid biopsies have emerged as a contemporary approach for diagnosing various diseases, ranging from genetic conditions to cancers, owing to their patient safety and ease of sampling [5]. Furthermore, liquid biopsies can be employed for diagnosing cancer and monitoring treatment efficacy by assessing cancer biomarkers (CB). These biomarkers encompass biologically active molecules, including proteins such as enzymes, nucleic acids like RNA and microRNA, immunoglobulins like IgG, or short amino acid chains. Notable examples include the identification of immunoglobulin IgG in 1847 as an indicator for multiple myeloma, elevated amylase enzyme levels in 1867 as an indicator for pancreatic cancer, and the discovery of

carcinoembryonic antigen (CEA) in 1965 as a marker for colon cancer. Subsequent biomarkers were developed in 1975. Testing these biomarkers allows differentiation between healthy and diseased tissues, early disease detection, and assessment of disease risk [5].

Liquid biopsies utilizing whole blood, serum, plasma, urine, sputum, or milk have gained prominence in recent years, particularly blood-based liquid biopsies for tumor localization, with plasma being the preferred choice for detecting solid tumor malignancies due to its higher cfDNA concentration [6]. Mandel and Metais published the first study on circulating cell-free DNA (cfDNA) in human blood in 1948. In 1970s notified that cfDNA in plasma rises during inflammation and injuries. Then, they know there will be a connection between cfDNA and tumors. ctDNA can be detected within the pool of cfDNA in plasma, where concentrations are higher than in serum, owing to its coagulation characteristics [7]. Table 1.1 below illustrates cfDNA concentrations for healthy persons and various cancer types, noting that these values may vary depending on the disease prognosis. These quantities are instrumental in cancer diagnosis and assessing the success of cancer therapies [8].

ctDNA offers several advantages, including straightforward sampling through a non-invasive approach, the ability to detect novel mutations, assess therapy effectiveness, surgical outcomes, and cost-effectiveness. ctDNA serves as a valuable molecular analysis tool for diagnostic, predictive, and prognostic purposes. Liquid biopsies, in particular, play a pivotal role in enhancing therapy response and identifying the development of resistance mutations.

Table 1: Comparison of cfDNA Concentration in Plasma Between Cancer Patient's and Healthy Individuals

Cancer type	cfDNA amount in total blood plasma
prostate cancer	115 ng/ml (range 13–339)
breast cancer	83-1414 ng/ml
lung cancer	35-173 ng/ml
stomach cancer	0-527 ng/ml
colon cancer	0-297 ng/ml
healthy women	15±13 ng/ml
healthy men	16±7 ng/ml

The identification of non-cancerous mutations in circulating tumor DNA (ctDNA) can be affected by the presence of mutant alleles in the DNA of hematopoietic stem cells or other early blood cells. In June 2016, the FDA approved the use of liquid biopsy in clinical practice for detecting EGFR mutations. Typically, an average concentration of ~10 ng/ml of cell-free DNA (cfDNA) in human plasma is considered realistic for diagnostic applications. Consequently, ctDNA accounts for less than 0.01% of the total cfDNA. The quantity of ctDNA can vary depending on factors such as tumor burden, proliferation rate, and disease stage. These variables must be taken into account when developing diagnostic systems or discussing the biological significance of ctDNA. As a result, considerable amounts of DNA from other sources frequently dilute ctDNA in the biofluids of cancer patients, which typically makes up 0.01-2% of the total cfDNA. Elevated cfDNA concentration is a sign of disease progression since it also tends to rise in advanced cancer stages and is noticeably higher in patients with metastatic cancer or big tumors [9].

Only 48% to 73% of patients with localized malignancies, such as colorectal cancer, gastroesophageal cancer, pancreatic cancer, and breast adenocarcinoma, have had ctDNA found in them. Despite being notable, these detection rates are not yet thought to be adequate for early cancer detection [10].

This information underscores the variability in ctDNA levels in plasma, which depends on factors such as cancer type, tumor location, disease stage, and whether the patient has undergone successful therapy. As an example, one study examined the concentration of ctDNA in plasma, focusing on colorectal cancer and considering disease prognosis. Only 48% to 73% of patients with localized malignancies, such as colorectal cancer, gastroesophageal cancer, pancreatic cancer, and breast adenocarcinoma, have had ctDNA found in them. Despite being notable, these detection rates are not yet thought to be adequate for early cancer detection as detailed in Table 2.

Circulating tumor DNA (ctDNA) is used to diagnose, treat, and predict the prognosis of numerous malignant illnesses and has undergone thorough analysis. ctDNA levels in blood plasma are typically low, with mutant allele fractions in locally advanced non-metastatic disease less than 1% and below 10% in cases of advanced metastatic disease, respectively. Furthermore, early-stage malignancies and those treated to cure them have substantially lower quantities of ctDNA, which frequently results in mutant allele fractions of less than 0.1%. Highly sensitive techniques are needed to detect ctDNA both during and after therapy [11].

The detection of aqueous solution samples can be accomplished through electrochemical transduction methods, which involve devices that convert information from one system (chemical) into another (physical). Electrochemistry techniques rely on ion transport, ion distribution, and redox reactions on solid conductors (electrodes).

In this review, we emphasize the utilization of electrochemical methods for ctDNA detection. Additionally, we touch upon biorecognition methods for ctDNA, amplification sequences, and the materials employed in designing electrodes for electrochemical techniques.

Table 2. ctDNA levels in various cancer types before and after surgery operations.

Stage	Surgery Number	Surgical procedure	Resection	Gene	Pre-surgery day 0	Post-operative days 13-56
IV	1	Hepatic metastasectomy	Complete	APC KRAS	99 ± 38 79 ± 35	16 ± 2.3 5.6 ± 0.9
IV	1	Hepatic metastecomy (First stage)	Incomplete	APC	2,952 ± 773	1,049 ± 254
IV	1	Sigmoid colectomy with hepatic metastectomy	Incomplete	TP53	14 ± 3	295 ± 71
	2	Hepatic metastectomy	complete	TP53	2,713 ± 775	1.8 ± 0.4
	3	RFA to hepatic metastases	complete	TP53	1,267 ± 243	39 ± 2
II	1	Sigmoid colectomy	complete	APC	2 ± 0.7	Neg
III	1	Sigmoid colectomy	complete	TP53	2 ± 0.6	Neg

2. Biorecognition Elements for Detection of ctDNA

Biosensors are specialized sensing devices designed to detect specific molecules, often referred to as biomarkers. Molecular recognition, also known as biorecognition, plays a crucial role in the detection of these biomarkers within the biosensor. The process commences with the recognition step, during which biomarkers or analytes bind to recognition molecules, resulting in the generation of signals within the sensor device. Biorecognition can be finely tailored for specific analytes, ensuring a high level of specificity in target detection.

The biomolecular recognition elements utilized in electrochemical biosensors for ctDNA can be classified into various categories, including enzymes, nucleic acids (such as aptamers), organelles, immune substances (antibody-antigen reactions), and more. These biomolecular receptors can be immobilized on the biosensor's surface through physical adsorption, covalent bonding, or embedding techniques [12].The recognition or sensing element, which has a strong affinity for the analyte, selectively interacts with the analyte. The sensing component might be made up of many molecular entities called recognition receptors [13].

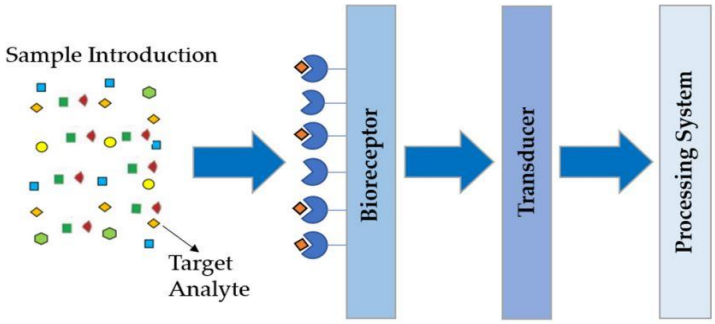

Figure 1. The pivotal role of the biorecognition element on the electrode surface. Various components, including antibodies, enzymes, nucleic acids, microorganisms, and cells, can be immobilized onto the electrode surface. When a target analyte is present, the electrode generates a physical signal, such as an electrochemical or optical signal.

In the following sections of this article, we delve into the biorecognition elements employed for the detection of ctDNA, specifically focusing on nucleic acids and antibodies. These recognition elements are immobilized on the electrode surface and interact with the target analyte to facilitate the detection process.

2.1 Nucleic Acid Probe-Based Detection

Palecek first noticed the electrochemical activity of nucleic acids using a mercury electrode. The electrical response, according to later research, results from the reduction of adenine and cytosine residues [14].

Nucleotide probes, comprising RNA and DNA oligonucleotide sequences, can be designed to target specific DNA or RNA sequences through Watson-Crick base pairing. There are two types of nucleotide probes: RNA probes and DNA probes. These probes are integral to hybridization techniques. In this process, a complementary DNA sequence to the target sequence is obtained and labeled. The label can be radioactive, a fluorescent tag, or an enzyme, referred to as a probe. When this probe is introduced to the analyte sequence, it leads to hybridization. The presence of the label allows for the detection of hybrids. For instance, if the probe is labeled with an enzyme, detection occurs through a color or light-producing reaction catalyzed by the enzyme [15].

Nucleic acid hybridization-based electrochemical biosensors are predominantly employed in clinical and microbial diagnosis due to their high sensitivity, rapid response, ease of use, and cost-effectiveness. After designing the probe, it is immobilized onto an electrode. When the analyte is introduced, hybridization occurs, converting the chemical reaction into an electrical signal.

There are three types of nucleic acid probes: PNA (peptide nucleic acid), DNA probes, and RNA probes, all of which can be utilized for DNA detection. By employing different probes and techniques, highly sensitive detection can be achieved. PNA is a synthetic organic polymer similar to DNA and RNA, but its sugar backbone is replaced by glycine linked through a peptide bond. This unique structure reduces electrostatic repulsion when hybridized with DNA, resulting in superior hybridization capability compared to DNA/DNA interactions. Consequently, using PNA probes in electrochemical methods is important. Through covalent bonding, significant amounts of PNA can be immobilized on a screen-printed electrode (SPE) surface that has been treated with gold nanoparticles. The working electrode, auxiliary electrode, and reference electrode are the three electrodes that make up the SPE. Both serum and peripheral blood can be used as sample matrices, with serum often exhibiting higher sensitivity. When the sample is applied to the working electrode, mutants bind to the complementary PNA probe, leading to a potential change [16].

Alternatively, DNA or RNA probes can be employed for ctDNA detection. For example, graphene-oxide-coated gold nanoparticles can be modified onto a glassy carbon electrode, with probes fixed through affinity interactions. The introduction of the analyte leads to hybridization, resulting in a change in current. Sensitivity can be enhanced by altering the surface material, dimensions, size, and physical transduction methods, such as the type of electrochemical signal utilized [15]

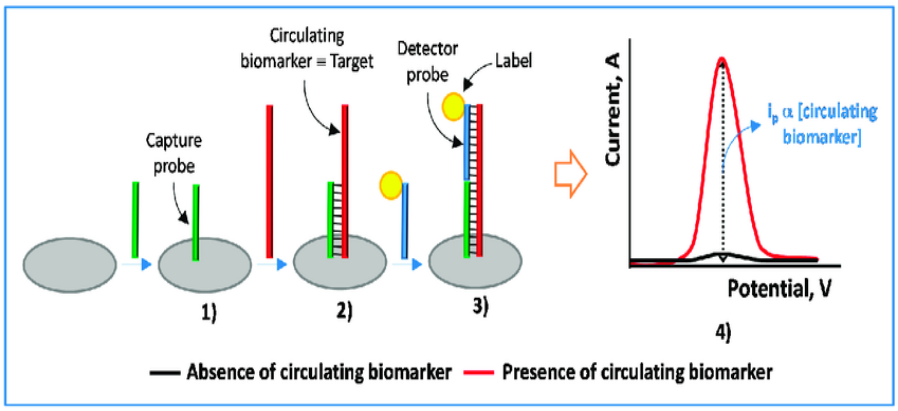

Figure 2: The Immobilized Green Capture Probe on the Electrode, Binding to the Target, resulting in a Current Change on the Electrode, Visualized in the Voltammogram [17]

2.2 Antibody Probe-Based Detection

The antibody-antigen reaction is a widely employed method in both diagnosis and treatment. Antibodies exhibit specific binding capabilities for various antigens, including pathogens, micro-molecules, cells, bacteria, and other molecules. Utilizing this principle for detection offers advantages such as achieving lower limits of detection. In the context of ctDNA detection, specific antibodies can be immobilized on an electrode surface [18]. A binding event between the antibody and antigen takes place when the antigen is added, leading to physical effects like a mass change or the usage of signaling tags, like fluorescent labels affixed to one of the reactants. These complexes can then be detected through signal transduction, either via electrochemical methods or through techniques like ELISA (enzyme-linked immunosorbent assay).

At present, DNA site-specific methylation is becoming increasingly popular as a biomarker [19]. Additionally, ctDNA methylation plays a vital role in regulating tumors, and evaluating the level of ctDNA methylation can effectively gauge the tumor's degree of malignancy [20]. Methods for analyzing ctDNA methylation primarily encompass PCR, sequencing, and microarray techniques, among others. However, it's worth noting that all these methodologies

require prior ctDNA pretreatment [21]. In contrast, 5-methylcytosine (5-mC) monoclonal antibodies can be directly attached to the electrode through covalent coupling. This approach enables the capture of methylated ctDNA without necessitating sample pre-treatment.

3. Electrochemical Methods for ctDNA Biosensors

Electrochemistry, as the name suggests, involves chemical reactions and the exchange of electrons. In this process, chemical reactions yield physical signals such as changes in voltage, current, or impedance. These signals can indicate the occurrence of a chemical reaction and allow for the measurement of molecule concentrations within the reaction. This technique has enabled the development of cost-effective, rapid-response, highly sensitive, and selective biosensors.

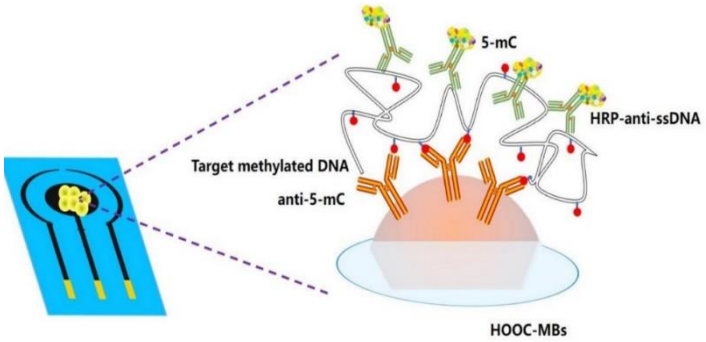

Figure 3. Schematic display of the immunosensor and ctDNA detection. Anti-5-mC immobilized on the electrode as a bioreceptor to capture methylated ctDNA. [19]

The inception of electrochemical biosensors dates back to 1950 when they were first designed to monitor oxygen (O2) levels in industrial settings, with Leland C. Clark leading the way. These early O2 sensors employed a two-electrode system with an O2-permeable membrane that separated the electrode from the electrolytic solution. When O2 diffused through the permeable membrane, it interacted with the electrode, resulting in a change in current. This change in current is directly correlated with alterations in the oxygen levels. Over time, this technique found applications in environmental monitoring, industrial processes, and medical diagnostics [22].

For aqueous solution samples, electrochemical transduction methods are frequently employed to create biosensors for detecting molecules like ctDNA. These biosensors convert biological signals, generated by the binding of an analyte to a biorecognition molecule, into electrical signals for detection. In the context of ctDNA detection, two commonly used electrochemical techniques are Differential Pulse Voltammetry (DPV) and Electrochemical Impedance Spectroscopy (EIS). This review focuses on these two types of electrochemical cells for the detection of ctDNA.

3.1. Differential Pulse Voltammetry

Voltammetry is an analytical method used to measure the current in electrochemical cells after applying a potential. One specific technique within voltammetry is Differential Pulse Voltammetry (DPV), which involves the application of small amplitude potential perturbations that gradually slow down. The current is measured at two points for each pulse, both before the pulse is applied and at the end of the pulse. DPV is particularly effective for measuring short intervals after the current has dropped. In this technique, potential readings are taken after adding each sample, and as subsequent samples are added, the potential decreases. DPV is highly sensitive, allowing for direct analysis at the parts per billion level. It detects the current response of a chemical under an applied potential difference, providing insights into the behavior of ions, molecules, or atoms undergoing oxidation or reduction reactions in a solution.

The voltammetric method family includes differential pulse voltammetry, which is used as an electrochemical detection method that may amplify signals more than 30 times. Longer pulse periods, which allow for the collection of a full charge current and improve the signal-to-noise ratio (SNR), are used to achieve this amplification. DPV excels in measuring trace substances, making it particularly advantageous when detecting low-abundance molecules [24].

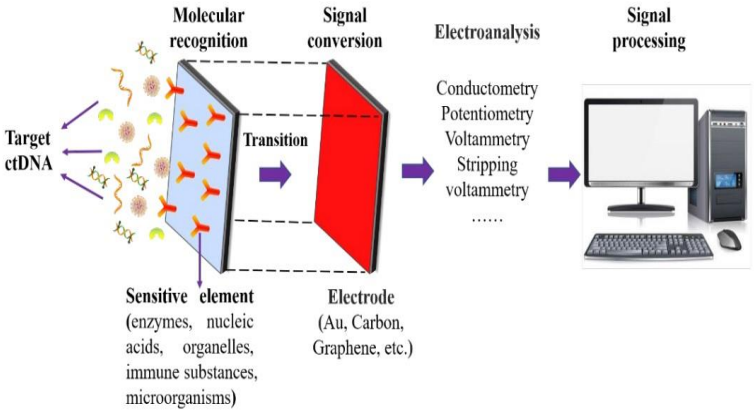

Figure 4. Schematic Representation of a ctDNA Electrochemical Biosensor Detection System. The biosensor components include molecular recognition elements such as enzymes, acids, organelles, and more. Additionally, it features a signal conversion electrode that has been enhanced through the use of various nanomaterials. Various electrochemical techniques, including potentiometric and voltammetric methods, are employed for signal detection [23].

As another example, a carbon electrode is enhanced by modification with nanomaterials to boost its catalytic activity. This modified electrode is then immobilized with single-strand DNA probes designed to specifically recognize mutant ctDNA. Hybridization between the two strands, the probe, and the ctDNA, initiates. By monitoring Differential Pulse Voltammetry (DPV), changes in current are observed, indicating the presence of a mutant analyte [25]

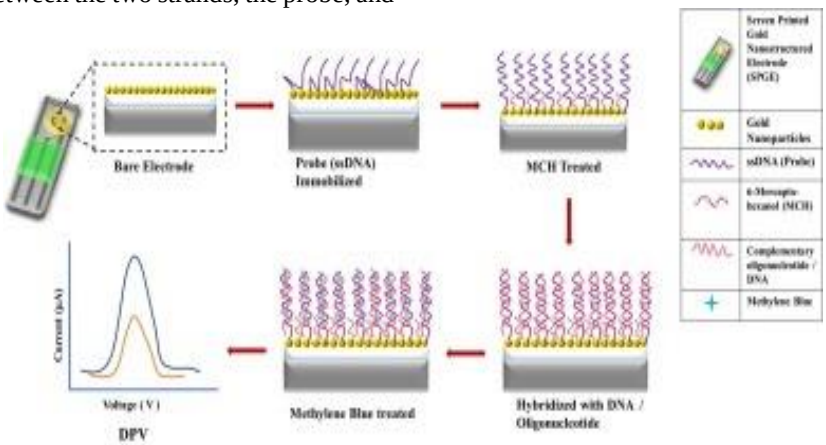

Figure 5. Principle of Differential Pulse Voltammetry (DPV) for Detecting DNA from a Specific Bacterial Strain. The biosensor employs a synthesized probe called sgDNA as the biorecognition element, which is immobilized on gold nanoparticles. Following the introduction of the target DNA, hybridization occurs, and the resulting hybridization is depicted on the plot by observing changes in the DPV, which yield varying current values [24]

3.2. Electrochemical Impedance Spectroscopy (EIS)

Electrical Impedance Spectroscopy is an exceptionally sensitive technique employed in electrochemical biosensors to detect and quantify physical changes resulting from chemical interactions between analytes and biorecognition elements. In this method, an alternating voltage is applied to the working electrode at various frequencies, inducing alternating current responses due to the REDOX (charge transfer) reactions of electrochemical species at the electrode's surface.

Electronic Impedance Spectroscopy can detect single-base variations or mismatched hybridization signals in addition to identifying DNA hybridization signals. The basic idea is based on the fact that DNA molecules have a negative charge, causing a coating of negatively charged material to build on the electrode's surface. Electrostatic repulsion happens when an oxidation-reduction electrode is present, increasing resistance. By measuring changes in resistance, impedance can be quantified following Ohm's law [26]

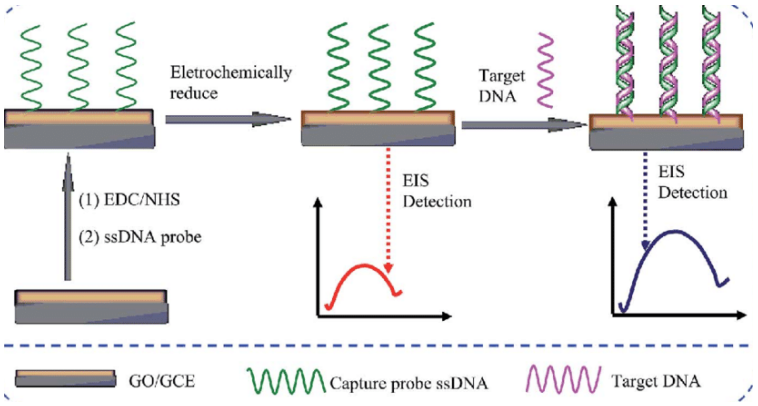

Figure 6. Illustration of the EIS Principle for Detecting Target DNA Hybridization Utilizing an ssDNA Probe Synthesized on the Electrode Surface. The presence of an analyte results in impedance changes on the electrode, which is visualized on the plot through the measurement of peaks [27]

4. Current novel Studies for ctDNA detection

Here, we will elaborate on several innovative techniques that have been explored for the detection of ctDNA, utilizing various biosensors in conjunction with distinct amplification methods.

4.1. Utilization of the CRISPR-dCas9 Enzyme Principle for ctDNA Detection

In this study, a highly sensitive, selective, cost-effective, and rapid-response biosensor was developed. The biosensor design involved the modification of an electrode with graphene oxide (GPHOXE), a carbon nanomaterial known for its high electron mobility, strength, and flexibility, all of which are crucial in biological sensing applications.

To create the biorecognition receptors, deactivated Cas9 (dCas9, endonuclease deficient Cas9) protein and synthetic guide

RNA (sgRNA) was immobilized on the electrode. This modification effectively eliminated the endonuclease activity of dCas9 by mutating its endonuclease domains. As a result, dCas9 was capable of binding to sgRNA and the specific DNA strand targeted by sgRNA. This catalytically inactive Cas9 is only bound to the predetermined region on the DNA.

The PIK3CA exon 9 mutation was chosen as the tumor-related mutation that the biosensor was developed to identify utilizing electrochemical impedance spectroscopy (EIS) as the electrochemical technique. The subjects were women with newly diagnosed breast cancer who had not undergone treatment.

The biosensor's performance was assessed through a series of tests conducted after the modification of the nanomaterial and immobilization of the biorecognition elements. The Limit of Detection (LOD) was determined to be 0.65 nM, and the Limit of Quantification (LOQ) was found to be 1.92 nM. Various concentrations of 120bp ctDNA fragments were generated and used to enhance the GPHOXE-dCas9-sgRNA electrode for chronoimpedimetric detection.

Chronoimpedance measurements were used to keep track of the biosensor surface's ctDNA saturation. Following the initial linear increase in signal, the biosensor's detection time was set at 40 seconds. The detection time was determined, and a linear calibration range was created using 120bp ctDNA standards. The circuit model shown in Figure 13 is the result of plotting the concentration-binding time (the length of time it takes for ctDNA to attach to the electrode) against the EIS spectra [28]

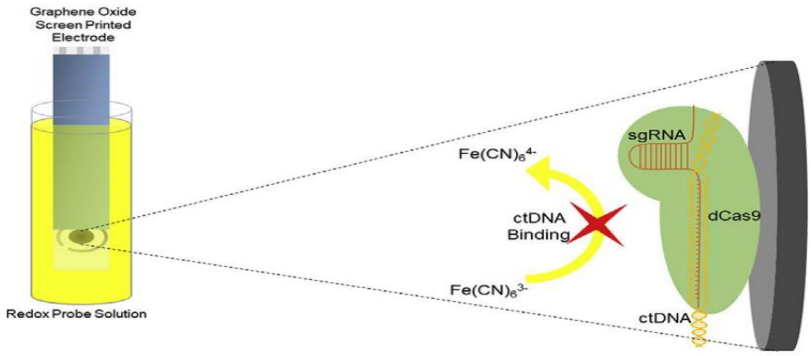

Figure 7. Utilizing a Graphene Oxide Screen Printed Electrode Modified with CRISPR dCas9 and sgRNA for ctDNA Detection. Upon the addition of ctDNA, a conversion of $Fe(CN)63^{-}$ to $Fe(CN)64^{-}$ occurs, resulting in the generation of a detectable signal.

4.2. Investigating the Use of AuPt Alloy Nanoparticles as an Amplification Strategy for the Detection of Circulating Tumor DNA (ctDNA)

The detection of circulating tumor DNA (ctDNA) as a liquid biopsy for cancer diagnosis and treatment monitoring has garnered significant attention. However, designing an effective biosensor for this purpose comes with its challenges. In this article, a solution was developed using improved nanocomposites with high carbon activity, which enhances conductivity. Additionally, Au-Pt (gold-platinum) nanoparticles were synthesized and utilized as a signal amplification strategy to create a sandwich-type biosensor.

Due to the strong electrochemical characteristics of HAC-AuPt (high carbon activity Au-Pt), the current response is considerably increased in this biosensor design when an analyte is present. As biorecognition components, DNA probes, and capture probes were mounted on the electrode surface. To detect ctDNA, the target DNA and DNA probe were incubated on capture probes in a sandwich-like shape.

With an incredibly low detection limit of 3.6 x 10-17 mol/L (S/N 1/4), this biosensor displayed a wide linear detection range from 10-8 mol/L to 10-16 mol/L. A conventional three-electrode system, consisting of the modified working electrode, counter electrode, and reference Ag/AgCl electrode, with a potential of 0.4 V, was used to perform amperometric current-time (i-t) measurements. To learn more about the electrode's interface properties, more cyclic voltammetry (CV) and electrochemical impedance spectroscopy (EIS) tests were made.

H2O2 was added to phosphate-buffered saline (PBS) to start the current response after the sandwich structure was formed by the hybridization of the target DNA and SPs-label. Due to its exceptional catalytic properties, the addition of the label HAC-AuPt considerably enhanced the current signal. As a result, the biosensor created for this work has a high sensitivity for detecting ctDNA [29]

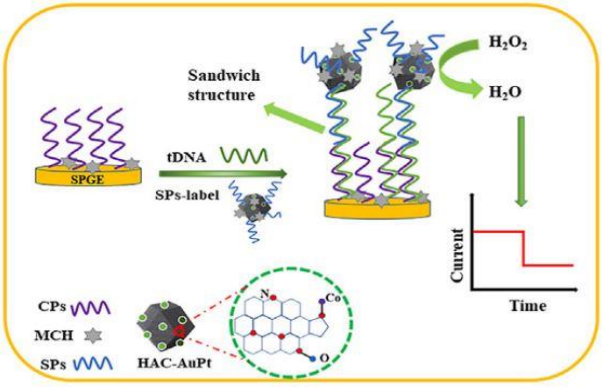

Figure 8. Utilization of a Gold Electrode Immobilized with SPs-Label for ctDNA Detection. In the presence of target DNA (mtDNA), the conversion of H_2O_2 to H_2O occurs, resulting in a signal represented by changes in current over time [29]

4.3. Leveraging Hybridization Chain Reaction for Enhanced Sensitivity in Detecting Circulating Tumor DNA

This study established a novel electrochemical biosensor for the extremely sensitive detection of ctDNA bearing the PIK3CA E545K allele mutation, employing the hybridization chain reaction (HCR) approach as a biorecognition mechanism. The biosensor's construction required the hybridization of two dumbbell-shaped DNA units that were put together using two different classes of painstakingly

created DNA probes. This complex structure started a chain reaction of nested hybridization.

In the presence of the particular allele mutation, the amplification products produced during the hybridization chain reaction were successfully caught by the target ctDNA. This interaction greatly enhanced the electrochemical signal. The main element of the biosensor was a 2mm gold electrode. Three dumbbell-shaped DNA units (U10, U1, and U2), capture probes, and gold electrodes made up the novel HCR sensing apparatus. The system's extraordinary amplification made it possible to use differential pulse voltammetry (DPV) to measure the electrochemical signal. As a result, the detection of an electrochemical signal was made possible by the presence of HCR products, offering a stable foundation for the detection of sensitive ctDNA [30]

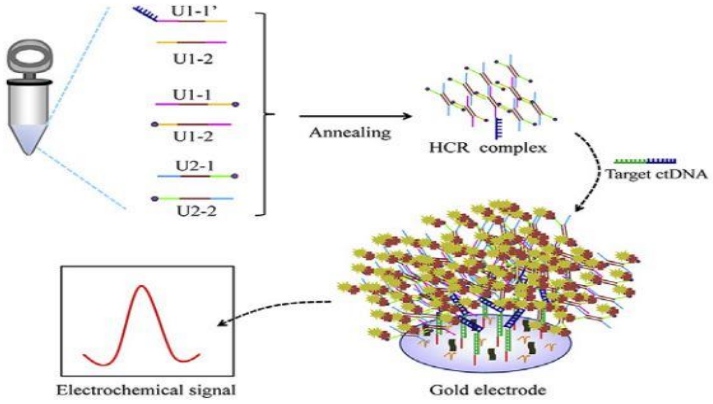

Figure 9. illustrates the underlying principle of the reaction involving target DNA and the utilization of the HCR amplification technique before immobilization onto the gold electrode. Additionally, it presents a differential pulse voltammetry (DPV) graph that discerns the presence or absence of the analyte [30]

Leveraging a Dual Enzyme Multiple Amplification Strategy for the Detection of Circulating Tumor DNA

In this study, electrode biosensors were amplified using a wide range of amplification strategies. A triple-helix molecular switch (THMS) was used in the design of the biosensor as the molecular recognition and signal transduction probe. To enable different amplification pathways, ribonuclease HII (RNase HII) and terminal deoxynucleotidyl transferase (TdT) were added as dual enzymes.

Target ctDNA caused the THMS to open, which started RNase HII-assisted homogeneous target recycling amplification. A significant signal transduction probe (STP) was produced because of this technique. The captured probe was then hybridized with the released STP using an electrode made of gold. To facilitate TdT-mediated cascade extension and ultimately the production of stable DNA dendritic nanostructures, TdT, and an assistance probe were used.

EIS was used in this study to analyze the electrochemical production and amplification processes since it has shown to be a highly effective method for examining the interfacial reaction mechanism of electrode surfaces [31]

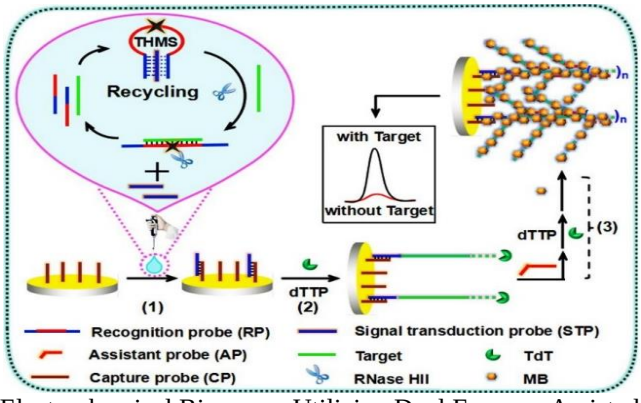

Figure 10. Depiction of the Electrochemical Biosensor Utilizing Dual Enzyme-Assisted Multiple Amplification [31]

5. Future perspective and conclusion

In recent years, advancements in technology and nanoscience have led to the development of portable, sensitive, quick-response, and cost-effective diagnostic tools. Electrochemical-based biosensors have emerged as crucial instruments for detecting circulating tumor DNA (ctDNA), aiding in the diagnosis and treatment monitoring of patient's. However, current electrochemical biosensors can typically only detect a single analyte, whereas clinical diagnosis often requires the detection of multiple analytes. Therefore, further research is needed to enhance ctDNA detection capabilities.

The diverse biosensor methods presented in the table 3 exhibit distinctive characteristics in terms of sensitivity, response time, and linear range, catering to a range of applications. From the ultra-sensitive label-free electrochemical biosensor with a LOD of 2.4 aM to the versatile LAMP electrochemical biosensors designed for cervical precancerous lesions, each method offers unique advantages in sample testing and biorecognition elements. The innovative use of CRISPR-dCas9, AuPt alloy nanoparticles, triple-helix molecular switches (THMS), DNA probes, and SPs-label showcases the evolving landscape of biosensor technologies. Researchers and practitioners can leverage this comprehensive overview to select the most suitable biosensor method for their specific analytical needs, considering factors such as LOD, response time, and linear range in real sample testing scenarios.

CtDNA levels are typically low in the early stages of cancer, and their concentration varies among different types of cancer lesions. As a result, sensors must possess a lower detection limit, as well as high sensitivity and specificity. By harnessing various nanoscale materials, electrode conductivity and surface area can be increased, leading to more sensitive electrodes. Additionally, it is essential to integrate biosensors with other analytical methods to minimize harm to the human body during sample collection, such as employing liquid biopsy techniques instead of invasive tissue biopsies.

This paper provides an overview of novel methods for ctDNA detection using electrochemical biosensors while also discussing traditional approaches like PCR and their associated drawbacks, such as high costs, complex procedures, and frequent false positives. The trend in ctDNA detection is shifting towards portable, cost-effective solutions. Furthermore, the paper explores the various types of electrochemical sensors used for ctDNA detection and highlights recent studies in this field. Introducing these methods into clinical diagnosis and mobile health applications offers both opportunities and challenges, which must be addressed as we move forward in the field of ctDNA detection.

Table 3. Comparing electrochemical biosensors

Biosensor Method	LOD	Response Time	linear Range	Electrochemical method	Sample testing	Biorecognition element
Impedimetric biosensor[28]	0.65 nM	40 Seconds	2-20 nM	EIS	Real Blood Sample (Serum)	CRISPR-dCas9
AuPt alloy nanoparticles electrochemical Biosensor[29]	3.6-10^{17}mol/L	quick response	10^{8}mol/L - 10^{16}mol/L	EIS/CV	Real serum sample	capture probes (CPs)
label-free electrochemical biosensor[32]	2.4 aM	Response in 30 seconds	0.01 fM to 1 pM	EIS	Real plasma sample	triple-helix molecular switch (THMS)
HCR electrochemical biosensor[30]	3 pM	Response time in seconds	5 pM to 0.5 nM	EIS/SWV	Real serum samples	DNA probes
gold-coated magnetic nanoparticles electrochemical biosensor[33]	3.3 aM	20 min response time	200 aM to 20 nM	SWV	whole blood	probe DNA
LAMP electrochemical biosensors[34]	10 pg and 150 ng	40 min	150 ng	amperometry measurement and CV	cervical precancerous lesions	Probe DNA
sandwich-type electrochemical biosensor[35]	5×10^{-16} mol/L	Rapid responce	$1 \times 10^{-15}$to 1 x 10^{-8} mol/L	CV/EIS	Real serum sample	SPs-label

References

[1]. M. N. Islam and R. B. Channon, "Electrochemical sensors," in Bioengineering Innovative Solutions for Cancer, Elsevier, 2019, pp. 47–71. doi: 10.1016/B978-0-12-813886-1.00004-8.

[2]. J. Ferlay et al., "Cancer statistics for the year 2020: An overview," Int J Cancer, vol. 149, no. 4, pp. 778–789, Aug. 2021, doi: 10.1002/ijc.33588.

[3]. F. Diehl et al., "Circulating mutant DNA to assess tumor dynamics," Nat Med, vol. 14, no. 9, pp. 985–990, Sep. 2008, doi: 10.1038/nm.1789.

[4]. X. Li et al., "Liquid biopsy of circulating tumor DNA and biosensor applications," Biosensors and Bioelectronics, vol. 126. Elsevier Ltd, pp. 596–607, Feb. 01, 2019. doi: 10.1016/j.bios.2018.11.037.

[5]. D. W. Cescon, S. V. Bratman, S. M. Chan, and L. L. Siu, "Circulating tumor DNA and liquid biopsy in oncology," Nature cancer, vol. 1, no. 3. NLM (Medline), pp. 276–290, Mar. 01, 2020. doi: 10.1038/s43018-020-0043-5.

[6]. J. Das and S. O. Kelley, "High-Performance Nucleic Acid Sensors for Liquid Biopsy Applications," Angewandte Chemie - International Edition, vol. 59, no. 7. Wiley-VCH Verlag, pp. 2554–2564, Feb. 10, 2020. doi: 10.1002/anie.201905005.

[7]. H. Schwarzenbach, D. S. B. Hoon, and K. Pantel, "Cell-free nucleic acids as biomarkers in cancer patients," Nature Reviews Cancer, vol. 11, no. 6. pp. 426–437, Jun. 2011. doi: 10.1038/nrc3066.

[8]. A. Kustanovich, R. Schwartz, T. Peretz, and A. Grinshpun, "Life and death of circulating cell-free DNA," Cancer Biology and Therapy, vol. 20, no. 8. Taylor and Francis Inc., pp. 1057–1067, Aug. 03, 2019. doi: 10.1080/15384047.2019.1598759.

[9]. Z. Qin, V. A. Ljubimov, C. Zhou, Y. Tong, and J. Liang, "Cell-free circulating tumor DNA in cancer," Chinese Journal of Cancer, vol. 35, no. 5. Landes Bioscience, May 01, 2016. doi: 10.1186/s40880-016-0092-4.

[10]. X. Wen, H. Pu, Q. Liu, Z. Guo, and D. Luo, "Circulating Tumor DNA—A Novel Biomarker of Tumor Progression and Its Favorable Detection Techniques," Cancers, vol. 14, no. 24. MDPI, Dec. 01, 2022. doi: 10.3390/cancers14246025.

[11]. R. I. Chin et al., "Detection of Solid Tumor Molecular Residual Disease (MRD) Using Circulating Tumor DNA (ctDNA)," Molecular Diagnosis and Therapy. Springer International Publishing, 2019. doi: 10.1007/s40291-019-00390-5.

[12]. M. A. Morales and J. M. Halpern, "Guide to Selecting a Biorecognition Element for Biosensors," Bioconjug Chem, vol. 29, no. 10, pp. 3231–3239, Oct. 2018, doi: 10.1021/acs.bioconjchem.8b00592.

[13]. L. S. Pessoa, M. Heringer, and V. P. Ferrer, "ctDNA as a cancer biomarker: A broad overview," Critical Reviews in Oncology/Hematology, vol. 155. Elsevier Ireland Ltd, Nov. 01, 2020. doi: 10.1016/j.critrevonc.2020.103109.

[14]. K. Wang, Z. Peng, X. Lin, W. Nian, X. Zheng, and J. Wu, "Electrochemical Biosensors for Circulating Tumor DNA Detection," Biosensors (Basel), vol. 12, no. 8, Aug. 2022, doi: 10.3390/bios12080649.

[15]. Y. Krishnan and M. Bathe, "Designer nucleic acids to probe and program the cell," Trends in Cell Biology, vol. 22, no. 12. pp. 624–633, Dec. 2012. doi: 10.1016/j.tcb.2012.10.001.

[16]. C. Alix-Panabières, H. Schwarzenbach, and K. Pantel, "Circulating tumor cells and circulating tumor DNA," Annual Review of Medicine, vol. 63. pp. 199–215, 2012. doi: 10.1146/annurev-med-062310-094219.

[17]. S. Campuzano, P. Yáñez-Sedeño, and J. M. Pingarrón, "Electrochemical genosensing of circulating biomarkers," Sensors (Switzerland), vol. 17, no. 4, Apr. 2017, doi: 10.3390/s17040866.

[18]. D. Saerens, L. Huang, K. Bonroy, and S. Muyldermans, "Antibody fragments as probe in biosensor development," Sensors, vol. 8, no. 8. pp. 4669–4686, Aug. 2008. doi: 10.3390/s8084669.

[19]. K. Wang, Z. Peng, X. Lin, W. Nian, X. Zheng, and J. Wu, "Electrochemical Biosensors for Circulating Tumor DNA Detection," Biosensors (Basel), vol. 12, no. 8, Aug. 2022, doi: 10.3390/bios12080649.

[20]. C. Whalley et al., "Ultra-low DNA input into whole genome methylation assays and detection of oncogenic methylation and copy number variants in circulating tumour DNA," Epigenomes, vol. 5, no. 1, p. 6, 2021.

[21]. F. Khatami et al., "Circulating ctDNA methylation quantification of two DNA methyl transferases in papillary thyroid carcinoma," J Cell Biochem, vol. 120, no. 10, pp. 17422–17437, 2019.

[22]. E. J. H. Wee, M. J. A. Shiddiky, M. A. Brown, and M. Trau, "eLCR: Electrochemical detection of single DNA base changes viaLigase Chain Reaction," Chemical Communications, vol. 48, no. 98, pp. 12014–12016, Nov. 2012, doi: 10.1039/c2cc35841g.

[23]. K. Wang, Z. Peng, X. Lin, W. Nian, X. Zheng, and J. Wu, "Electrochemical Biosensors for Circulating

Tumor DNA Detection," Biosensors (Basel), vol. 12, no. 8, Aug. 2022, doi: 10.3390/bios12080649.

[24]. V. Manohar Raju et al., "A novel disposable electrochemical DNA biosensor for the rapid detection of Bacillus thuringiensis," Microchemical Journal, vol. 159, Dec. 2020, doi: 10.1016/j.microc.2020.105434.

[25]. M. N. Islam and R. B. Channon, "Electrochemical sensors," in Bioengineering Innovative Solutions for Cancer, Elsevier, 2019, pp. 47–71. doi: 10.1016/B978-0-12-813886-1.00004-8.

[26]. E. Cano, D. Lafuente, and D. M. Bastidas, "Use of EIS for the evaluation of the protective properties of coatings for metallic cultural heritage: A review," Journal of Solid State Electrochemistry, vol. 14, no. 3. pp. 381–391, 2010. doi: 10.1007/s10008-009-0902-6.

[27]. Q. Gong, H. Yang, Y. Dong, and W. Zhang, "A sensitive impedimetric DNA biosensor for the determination of the HIV gene based on electrochemically reduced graphene oxide," Analytical Methods, vol. 7, no. 6, pp. 2554–2562, Mar. 2015, doi: 10.1039/c5ay00111k.

[28]. Z. O. Uygun, L. Yeniay, and F. Girgin Sağın, "CRISPR-dCas9 powered impedimetric biosensor for label-free detection of circulating tumor DNAs," Anal Chim Acta, vol. 1121, pp. 35–41, Jul. 2020, doi: 10.1016/j.aca.2020.04.009.

[29]. K. Chen, H. Zhao, Z. Wang, and M. Lan, "A novel signal amplification label based on AuPt alloy nanoparticles supported by high-active carbon for the electrochemical detection of circulating tumor DNA," Anal Chim Acta, vol. 1169, Jul. 2021, doi: 10.1016/j.aca.2021.338628.

[30]. Y. F. Huang et al., "A novel nest hybridization chain reaction based electrochemical assay for sensitive detection of circulating tumor DNA," Anal Chim Acta, vol. 1107, pp. 40–47, Apr. 2020, doi: 10.1016/j.aca.2020.02.006.

[31]. H. F. Wang et al., "A versatile label-free electrochemical biosensor for circulating tumor DNA based on dual enzyme assisted multiple amplification strategy," Biosens Bioelectron, vol. 122, pp. 224–230, Dec. 2018, doi: 10.1016/j.bios.2018.09.028.

[32]. H. F. Wang et al., "A versatile label-free electrochemical biosensor for circulating tumor DNA based on dual enzyme assisted multiple amplification strategy," Biosens Bioelectron, vol. 122, pp. 224–230, Dec. 2018, doi: 10.1016/j.bios.2018.09.028.

[33]. D. Chen, Y. Wu, S. Hoque, R. D. Tilley, and J. J. Gooding, "Rapid and ultrasensitive electrochemical detection of circulating tumor DNA by hybridization on the network of gold-coated magnetic nanoparticles," Chem Sci, vol. 12, no. 14, pp. 5196–5201, Apr. 2021, doi: 10.1039/d1sc01044a.

[34]. R. Sebuyoya et al., "Electrochemical DNA biosensor coupled to LAMP reaction for early diagnostics of cervical precancerous lesions," Biosens Bioelectron X, vol. 12, Dec. 2022, doi: 10.1016/j.biosx.2022.100224.

[35]. H. Zhao et al., "A novel sandwich-type electrochemical biosensor enabling sensitive detection of circulating tumor DNA," Microchemical Journal, vol. 171, Dec. 2021, doi: 10.1016/j.microc.2021.106783.

MANAS Journal of Engineering
ISSN 1694-7398 | e-ISSN 1694-7398

Volume 12, Issue 1, (2024) Pages 116-128
https://doi.org/10.51354/mjen.1407291

Treatment of cattle slaughterhouse wastewater by sequential coagulation-flocculation/electrooxidation process

Nawid Ahmad Akhtar[1,*], Mehmet Kobya[1,2]

[1]Kyrgyz-Turkish Manas University, Faculty of Engineering, Department of Environmental Engineering, 720044, Bishkek-Kyrgyzstan, nawidahmad.akhtar@manas.edu.kg, ORCID: 0009-0006-5390-7505.

[2]Gebze Technical University, Faculty of Engineering, Department of Environmental Engineering, 41400, Gebze-Turkey, kobya@gtu.edu.tr, ORCID: 0000-0001-5052-7220.

ABSTRACT

This study aimed to investigate the applicability and efficiency of sequential coagulation-flocculation (CF) and electrooxidation (EO) processes for cattle slaughterhouse wastewater by evaluating treatment efficiency and total operating cost values together. The effect of two different coagulant dosages ($FeCl_3$ and alum) in the CF process and operating parameters such as current density (5 to 30 mA/cm^2), wastewater flow rate (0.9 to 3.6 L/h), and supporting electrolyte concentration (1 to 3 g NaCl/L) in the EO process on chemical oxygen demand (COD) and turbidity removal were investigated. During the first part of the study, the $FeCl_3$ coagulant dosage worked better than other coagulants, eliminating 50% of the COD and 68% of the turbidity. Due to the insufficient removal efficiencies of COD and turbidity, a secondary treatment was required. In the second part of the study, a boron-doped diamond (BDD) electrode was used to treat the coagulated effluent in a continuous EO reactor. The COD and turbidity removal efficiency under optimum treatment conditions (j = 30 mA/cm^2, Q = 0.9 L/h, pH = 8.5, SE = 3.0 g NaCl/L, and hydraulic retention time = 1 hour) were calculated as 97.2% and 99.9%, respectively. At these optimum conditions, the energy consumption and total operating cost were calculated as 91.1 kWh/m^3 (73.5 kWh/kg COD) and 3.50 US $/m^3 (1.5 US $/kg COD), respectively. As a result, combined coagulation-flocculation and electrooxidation processes have proven to be very successful and cost-efficient for treating cattle slaughterhouse wastewater.

ARTICLE INFO

Research article

Received: 20.12.2023
Accepted: 23.05.2024

Keywords:

Continuous electrooxidation reactor, Coagulation-flocculation, cattle Slaughterhouse, Treatment

**Corresponding author*

1. Introduction

The United States Environmental Protection Agency (USEPA) has identified effluent from slaughterhouses as one of the most dangerous types of wastewater. The Organization for Economic Co-operation and Development has projected that the annual meat output will reach 366 million metric tons by 2029 [1]. A slaughterhouse produces wastewater from both the slaughtering process and the cleaning of the intestines. This wastewater contains high levels of organic substances, including chemical oxygen demand (COD), biological oxygen demand (BOD), total phosphorus (TP), total nitrogen (TN), total suspended solids (TSS), and oil and greases [2,3].

Efficiently treating slaughterhouse wastewater is crucial for both human well-being and environmental preservation. Commonly, slaughterhouse wastewater treatment approaches use a physicochemical treatment process [4,5], a biological (aerobic and anaerobic) treatment process [6-8], and an advanced treatment process [9,10]. Typically, biological processes are the primary techniques used to treat slaughterhouse effluent. Nevertheless, aerobic treatment requires a substantial oxygen supply of >100 mg O_2/L h, generates excessive quantities of biomass at around 8 kg/m^3, and demands significant energy consumption. The accumulation of suspended particles and floating oils in the anaerobic treatment reactor has a negative impact on SWW

treatment, making the aerobic and anaerobic processes for SWW treatment costly and time-consuming [11-13].

Among physicochemical processes, the coagulation-flocculation (CF) process is often used in slaughterhouse wastewater treatment due to its notable efficiency and low cost, proving to be effective in removing COD, BOD, TSS, and turbidity [2]. Three distinct steps, namely coagulation, flocculation, and sedimentation, comprise the CF process. The coagulation phase's objective is to induce colloidal suspension destabilization by introducing coagulant chemicals. This is achieved by disrupting the repulsive forces arising from the presence of similar polarity charges on the colloids' surface. Flocculation makes colloidal substances even less stable, mostly by bringing together particles that aren't stable, which makes micro-flakes and then bigger flakes that settle. The often used coagulants in the CF process are aluminum and iron salts, namely aluminum chloride ($AlCl_3$), aluminum sulfate ($Al_2(SO_4)_3$), ferric chloride ($FeCl_3$), and ferric sulfate ($Fe_2(SO_4)_3$), due to their effectiveness, cost-effectiveness, and ease of use. Nevertheless, the CF process alone may not be sufficiently effective in eliminating organic compounds from slaughterhouse effluent, necessitating additional procedures to eliminate the residual organic matter down [14].

At present, electrochemical oxidation has emerged as a very effective approach for the treatment of several categories of wastewater. Electrooxidation (EO) offers several benefits as compared to traditional and alternative advanced oxidation process (AOP) treatment procedures. These steps prevent the production of extra wastes such as used sorbents, contaminated retentate, waste ferric hydroxide, or waste-activated sludge, which typically occur during adsorption, filtering, Fenton reactions, and biological processes, respectively. EO has the advantage of being easy to examine during operation and does not require additional chemicals for process control [15]. When exposed to an electric current, dangerous or non-biodegradable chemicals experience oxidation, leading to their transformation into biodegradable substances or complete oxidation into water (H_2O), carbon dioxide (CO_2), and simpler organic molecules [16]. In environmental science, the degradation of organic compounds occurs primarily via direct and/or indirect oxidation. The EO process generates hydroxyl radicals (•OH) and other reactive oxidant species (H_2O_2, Cl_2, and O_3) that are produced at the anode surface (A) during the treatment. These species then proceed to oxidize the contaminants directly at the anode surface. Anodes with high reactivity, such as RuO_2, IrO_2, or Pt, promote the partial and selective oxidation of pollutants. In contrast, anodes with low reactivity, such as BDD, PbO_2, or SnO_2, may achieve total combustion. As a result, inactive anodes are considered favorable electrodes for the full conversion of organic compounds into CO_2 during the wastewater treatment process [17]. There has been a notable surge of interest in using BDD electrodes for chemically degrading pollutants in recent years. The BDD electrode exhibits a wide range of potential values in both water-based and non-water-based solutions, demonstrating good stability and corrosion resistance. Furthermore, it has a non-reactive surface that exhibits little adsorption and a low baseline current [18]. However, as with other procedures, EO has drawbacks. The mentioned phenomena include abrasion, passivation, polarization of electrodes, and significant energy consumption. Electrochemical technologies exhibit much higher energy consumption as compared to other technologies. To reduce the excessive energy consumption of the EO process, it is advantageous to treat the wastewater beforehand using other methods. There are many studies in the existing literature on single and sequential electrochemical processes for the treatment of cattle SWW; to the authors' knowledge, there is no research in the existing literature on the use of sequential coagulation-flocculation/electrooxidation processes for cattle SWW treatment.

Therefore, in light of the existing research gap, this study investigates the treatment of cattle slaughterhouse plant wastewater by pre-treatment, including coagulation-flocculation (CF), in a continuous electrooxidation reactor using BDD electrodes. Initially, we used the CF process to remove colloidal and suspended particles from the cattle SWW. Then, a continuous electrooxidation reactor was used to remove the remaining persistently dissolved organic compounds. The CF process involved testing two types of coagulant dosages to investigate their effect on COD and turbidity removal. The effectiveness of the BDD anode was investigated in the CEO process. In particular, the impact of the applied current density, wastewater flow rate, and supporting electrolyte concentration on the treatment performance was studied. Furthermore, the specific energy consumption for COD, the energy consumption of the process, and the total operating costs were calculated.

2. Materials and methods

2.1. The Bishkek slaughterhouse plants

Bishkek serves as the capital and most populous city of Kyrgyzstan (Kyrgyz Republic). The city is located at

coordinates 42°52′29″N and 74°36′44″E, with an altitude of around 800 meters. It is positioned at the northern edge of the Kyrgyz Ala-Too Range, which is an extension of the Tian-Shan mountain range. The elevation of these mountains reaches 4,895 meters. The city spans a total area of 170 square kilometers. The mean annual precipitation is around 440 mm. The average daily maximum temperatures vary from 3 °C in January to around 31 °C in July (almost -10°C in winter). The official population of Bishkek in 2021 is about 110,472 individuals, with a population growth rate of roughly 2.1%, above the national average of 1.7%. Nevertheless, a significant number of individuals (~400.000 people) reside in Bishkek without formal recognition. The meat industry has a prominent position in Kyrgyzstan, similar to other Central Asian nations. The rural population relies heavily on livestock farming as their primary source of income and subsistence. In 2020, the per capita consumption of beef in Kyrgyzstan was 14.9 kilograms. The present number signifies a decline of 3.19% in comparison to the value seen in the preceding year. Within the historical framework, the average individual consumption of beef in Kyrgyzstan reached its highest level at 21.0 kg in 2002 and then dropped to its lowest point at 14.0 kg in 2010. Kyrgyzstan ranks 42nd out of 165 countries in terms of per capita consumption of beef. Currently, there are about 12 functioning slaughterhouses in Bishkek. These slaughterhouses have a daily average of slaughtering about 70 cattle and over 410 sheep and goats. The slaughterhouses produce an estimated volume of 80 m^3 of effluent every day.

2.2. Materıals

The cattle slaughterhouse wastewater was obtained from the slaughterhouse plant located in Bishkek City (Kyrgyzstan). The slaughterhouse plant has a daily slaughter capacity of 20 cattle and produces an average of 10-15 m^3 of wastewater. Samples were collected in polypropylene bottles, following the protocols outlined in the Standard Method [19]. The obtained samples were then transported under cold conditions and thereafter kept at a temperature of 4 °C until they were ready for use. The characteristics of dissolved oxygen, pH, electrical conductivity, and temperature were investigated while collecting wastewater from the slaughterhouse plant. (Table 1) presents the primary characteristics of cattle slaughterhouse wastewater. In the CF process, two different coagulant dosages were used ($FeCl_3$ and $Al_2(SO_4)_3$). All chemicals used in this study were analytical quality Merck products. The BDD, which consists of a layer of boron diamond film applied over a 1.5 mm niobium plate, was acquired from DiaCCon GmbH in Germany. Also, the cathode was comprised of a rectangular electrode made of stainless steel (316 AISI).

Table 1. *Characteristics of the wastewater used in this study.*

Parameters	**SWW**	**Effluent of CF + CEO**
pH	7.4 ± 0.20	8.35 ± 0.10
Temperature (T, ℃)	17 ± 2	<30
Turbidity (NTU)	175 ± 5	<1
Dissolved Oxygen (DO, mg/L)	7.25 ± 0.25	7.85 ± 0.10
Electrical Conductivity (EC, µS/cm)	1800 ± 10	11000 ± 100
Total dissolved solids (TSS, mg/L)	2350 ± 30	<3
Volatile suspended solids (VSS, mg/L)	450 ± 10	<1
Total dissolved solids (TDS, mg/L)	1100 ± 20	6000 ± 100
Oil and grease (mg/L)	250 ± 10	
Chemical oxygen demand (COD, mg/L)	4100 ± 100	<100
Total phosphorus (TP, mg/L)	110 ± 5	
Total nitrogen (TN, mg/L)	330 ± 10	

2.3. Experimental apparatus and procedure

A series of standard jar test tests evaluated the coagulation-flocculation (CF)process. Six beakers, each with a volume of 1000 mL, were used for this purpose. The experiments were conducted under controlled conditions at a room temperature of 25 ± 1 ºC. In this experimental study, a total of six distinct coagulant dosages (100, 500, 800, 1000, 2000, and 3000

mg/L) were examined for each coagulant to ascertain the optimum coagulant dosage. In CF studies, after adding a coagulant dosage to wastewater, pH was adjusted to 6.5 for alum and 8.5 for $FeCl_3$. pH levels were adjusted using 1 M HCl and NaOH solutions. The CF included three consecutive stages: an initial phase of quick mixing at a speed of 220 rpm for 3 minutes, which was then followed by a gradual mixing stage lasting for 25 minutes at a speed of 40 rpm. Finally, the process concluded with a settling step that lasted for an additional hour. Subsequently, water samples were collected from the water surface (supernatant) to analyze COD and turbidity. These samples were then subjected to filtration using a membrane filter with a pore size of 0.45 µm. The determination of the volume and quantity of the settled sludge was also conducted.

The experimental investigation included the use of a cylindrical plastic reactor for conducting experiments on the CEO reactor. The capacity of the reactor was 0.9 L, while the diameter and height were 110 mm and 140 mm, respectively. In each experimental trial, a volume of 0.8 L of wastewater was introduced into the reactor. The wastewater was then consistently supplied to the reactor using a peristaltic pump (Masterflex, Model NO: 7553-76). The wastewater was subjected to continuous stirring at a rate of 250 rpm using a magnetic stirrer of the (Heidolph MR Hei-End) type to achieve a homogenous solution in the reactor. In CEO reactor investigations, the anode used was BDD and the cathode was stainless steel. The dimensions of the used anode and cathode electrodes were as follows: 200 mm (length) x 60 mm (width) x 3 mm (thickness). The electrodes were arranged in a vertical parallel configuration inside the reactor. In the CEO reactor, the contact area between the electrodes in the effluent is measured to be 100 mm, with a separation distance of 15 mm. The positioning of the electrodes in the CEO reactor was set at a distance of 15 mm from the bottom. The anode electrode has an active surface area of 120 cm^2. The electrodes were linked to a digital (DC) power source (Gwinstek DC SPS-60: 0-60 V, 0-6 A) via the galvanostatic connection. The direct current (DC) power source was used to establish the specific electrical currents required for each experimental procedure. The CEO reactor output was sampled at various time intervals, and each sample underwent filtration using a 0.45 µm filter paper before analysis. Subsequently, studies were conducted to determine the levels of COD and turbidity.

2.4. Analytical methods

The analysis of all samples was conducted by the Standard Method [19]. The dichromate open reflux technique (5220-B standard) was used for COD analysis, (ZBK Turb 550 IR) for turbidity, (Thermo Scientific Eutech pH 150) for pH, and (YSI 30) for conductivity.

The assessment of total operating cost (OC) is important in evaluating a wastewater treatment methodology. The energy consumption for the CEO reactor and specific energy consumption for removed kg COD from 1 m^3 wastewater was determined by the use of Eqs (1) and (2), respectively. The energy consumption of the peristaltic pump was determined using Eq (3), while the energy consumption of the magnetic stirrer was determined using Eq (4), and the overall energy consumption was computed by using Eq (5) [20].

$$C_{CEO,\ energy}\ (kWh/m^3) = \frac{i \times t_{CEO} \times U}{v} \quad (1)$$

$$C_{CEO,\ energy}\ (kWh/kg\ COD) = \frac{V \times t_{CEO} \times i}{\Delta C \times v} \quad (2)$$

$$C_{CEO,\ pump\ energy}\ (kWh/m^3) = \frac{P.t_{CFEO}}{v} \quad (3)$$

$$C_{magnetic\ stirrer,\ energy}\ (kWh/m^3) = \frac{N \times t}{\eta\ (\%) \times v} \quad (4)$$

$$C_{total,\ energy} = C_{CEO,\ energy} + C_{magnetic\ stirrer,\ energy} + C_{CEO,\ pump\ energy} \quad (5)$$

In this context, the variable (i) represents the applied current in amperes (A), U denotes the cell voltage in volts (V), t_{CEO} signifies the operating duration of the CEO reactor in hours, v represents the volume of treated wastewater in the CEO reactor in cubic meters (m^3), and ΔC denotes the difference in COD between the influent and effluent to the reactor, measured in kg/m^3, the variable P (kW) represents the power of the peristaltic pump, with the motor power of the pump utilized denoted as 760 W, and N representing the magnetic stirrer power, η is the magnetic stirrer power efficiency.

The total operating cost for the CF, CEO, and CF+CEO processes was determined by using Eqs (6), (7), and (8) [20].

$$OC_{CF}\ (US\ \$/m^3) = \alpha C_{energy} + \beta C_{chemical} + \gamma C_{sludge} \quad (6)$$

$$OC_{CEO}\ (US\ \$/m^3) = \alpha_{Cenergy} + \beta C_{chemical} \quad (7)$$

$$OC_{total}\ (US\ \$/m^3) = OC_{CF} + OC_{CEO} \quad (8)$$

In this context, α represents the unit cost of electrical energy, C_{energy} denotes the total energy consumption associated with the processes, β signifies the unit prices of chemicals used in the CF and CEO processes, $C_{chemical}$ represents the dosage of coagulant (measured in kg), and γ denotes the unit cost of created sludge, with C_{sludge} representing the quantity of sludge formed per unit volume (kg/m^3). In December 2023, the Kyrgyzstan market reported an electrical energy (α) price of 0.033 US $/kWh. The unit prices for the chemicals employed in the study were as follows: $FeCl_3$ had a unit price of 0.15 US $/kg, alum had a unit price of 0.22 US $/kg, NaOH had a unit price of 0.40 US $/kg, HCl had a unit price of 0.45 US $/kg, and NaCl had a unit price of 0.05 US $/kg. The cost of disposing of the CF process sludge, with a moisture content of 25%, in a typical landfill location is estimated to be 0.15 US $/kg of sludge.

The COD and turbidity removal efficiency (Re), are calculated by using Eq (9).

$$\text{Removal efficiency (Re, \%)} = \frac{C_i - C_t}{Ci} \times 100 \quad (9)$$

Where C_i is the initial concentration of COD (mg/L) and turbidity (NTU) and C_t is the final concentration of COD and turbidity.

3. Results and discussion

The present research aimed to examine the removal of COD and turbidity from slaughterhouse wastewater (SWW). The investigation was conducted in two distinct stages. During the first stage, the SWW underwent coagulation-flocculation treatment to eliminate suspended organic matter. This process included the use of two distinct coagulant dosages (alum and $FeCl_3$) to identify the most efficient one. During the second part of the study, different current densities (5-30 mA/cm^2), different wastewater flow rates (0.9-3.6 L/h), and different supporting electrolyte concentrations (1-3 g/L) were used in the continuous electrooxidation reactor to determine the most efficient one in terms of removing COD and turbidity from SWW.

3.1. The impact of coagulant dosage on the COD and turbidity removal efficiency

Coagulation-flocculation (CF) is a chemical-physical treatment process that is extensively used for the treatment of wastewater generated by slaughterhouses. The use of precise amounts of coagulants enables the precipitation of colloidal suspended particles that do not settle naturally, as well as the removal of small sedimentable solids that are difficult to eradicate by conventional physical treatment methods because of their prolonged sedimentation rate [21]. In the CF process, metal salts for hydrolysis, such as aluminium and iron, are prevalent as key coagulants in the treatment of wastewater. These coagulants play a crucial role in diminishing the levels of particulate matter and dissolved organic compounds within the wastewater. Upon dissolution in water, the aluminium and iron salts undergo a process whereby the metal (M) ions undergo hydration and hydrolysis, resulting in the formation of both monomeric and polymeric species, as well as the precipitation of solid compounds: MOH^{2+}, $M(OH)_2^{+}$, $M_2(OH)_2^{4+}$, $M(OH)_4^{5+}$, $M(OH)_3(s)$, $M(OH)_4^{-}$. The quality of treated wastewater is influenced by the quantity of coagulant used and the appropriate pH level. Consequently, these elements have significant importance in the coagulation process, since each coagulant necessitates a certain pH range to facilitate effective coagulation [22].

This study conducted jar tests to examine the effects of various coagulant dosages (alum and $FeCl_3$), including 100, 500, 800, 1000, 2000, and 3000 mg/L, at constant pH levels (8.5 for $FeCl_3$ and 6.5 for alum), on the removal efficiencies of COD and turbidity from cattle slaughterhouse effluent. As shown in (Figure 1(a)), the effluent COD concentration was found to be 2000-2500 mg/L for $FeCl_3$ and 2100-2800 mg/L for alum, respectively. On the other hand, the effluent turbidity concentration was found to be 56-102 NTU for $FeCl_3$ and 73-109 NTU for alum, respectively (Figure 1(b)). The effluent COD and turbidity concentrations under optimum coagulant dosages were determined to be 2100 mg/L and 79 NTU for alum and 2000 mg/L and 65 NTU for $FeCl_3$, respectively. The removal effectiveness of both coagulants remained rather stable for COD and turbidity at coagulant doses above 800 mg/L. According to these results, the optimum coagulant dosage for $FeCl_3$ and alum in the CF process was taken at 800 mg/L because they hypothesized that a portion of the dissolved COD would become adsorbed onto the metal hydroxyl flocs. However, they observed minimal variation in the COD elimination effectiveness after a specific coagulant dosage.

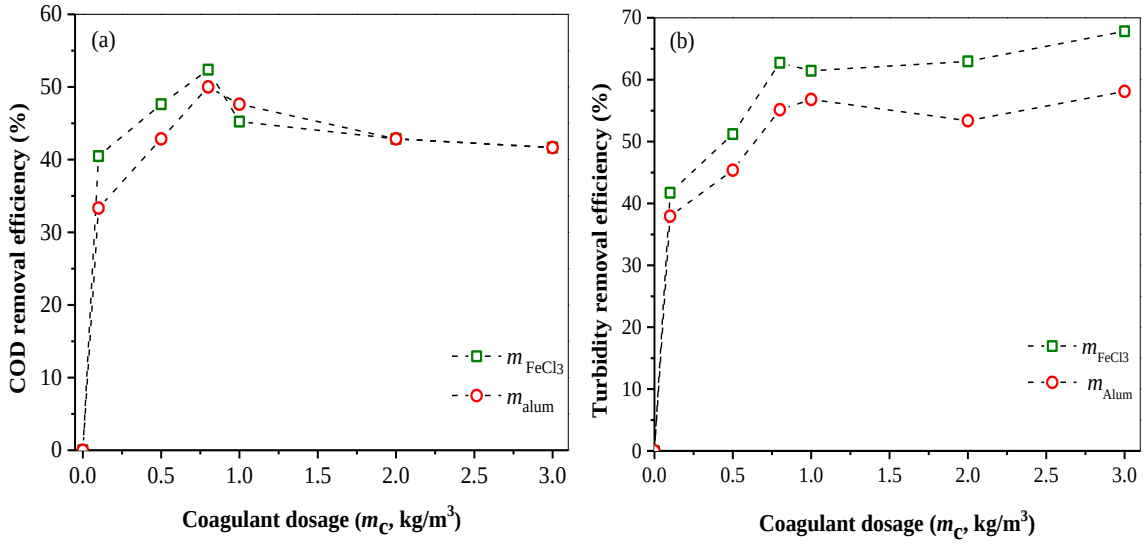

Figure 1. *(a) The COD removal efficiency for $FeCl_3$ and alum coagulant dosages (b) The turbidity removal efficiency for $FeCl_3$ and alum coagulant dosages (conditions; pH = 6.5 for alum and 8.5 for $FeCl_3$).*

The total operating cost for electrical energy (the energy consumption of the magnetic stirrer), chemicals ($FeCl_3$ and alum coagulant dosages, HCl, and NaOH), and sludge disposal were calculated with Eq (6). for the CF process. The total operating costs for the optimum coagulant dosages for the CF process were calculated as 0.45 US \$/m^3 (0,43 US \$/kg COD) for $FeCl_3$ and 0.53 US \$/m^3 (0,49 US \$/kg COD) for alum, respectively. Based on the findings, it is evident that the $FeCl_3$ dosage used in the CF process was determined to be the optimum coagulant dosage for treating SWW wastewater, considering both treatment effectiveness and minimal overall operating cost.

The quantity and properties of the sludge generated during the coagulation-flocculation (CF) process are primarily influenced by the particular coagulant used and the operational parameters. The volume of wet sludge at the base of the vertical-graded glass sedimentation columns, which had an internal diameter of 55 mm and a height of 350 mm, was measured to determine the amount of sludge produced in this research after the CF process. The measurements were taken at an ambient temperature of 20 ℃. The height of the liquid/sludge contact was measured at regular time intervals. Figure 2 shows the mean height fluctuations at the interface between the suspension and the supernatant, represented as the volume (mL) of settled sludge. The process of sludge settling was observed for one hour. This specific time frame was chosen to ensure that the settling process was close to completion after the observation period. A flat horizontal interface is seen in each coagulation process, exhibiting a clear discontinuity between the suspension and supernatant phases that are created after 1 hour (referred to as SV60, representing the sludge volume in mL at the 1-hour mark). The optimum coagulant dosage for SV60 was discovered to be 15 mL for both $FeCl_3$ and alum sludge (Figure 2). The settling speed of sludge was determined to be 0.0236 cm/s for both $FeCl_3$ sludge and alum sludge when a coagulant dosage concentration of 800 mg/L was used.

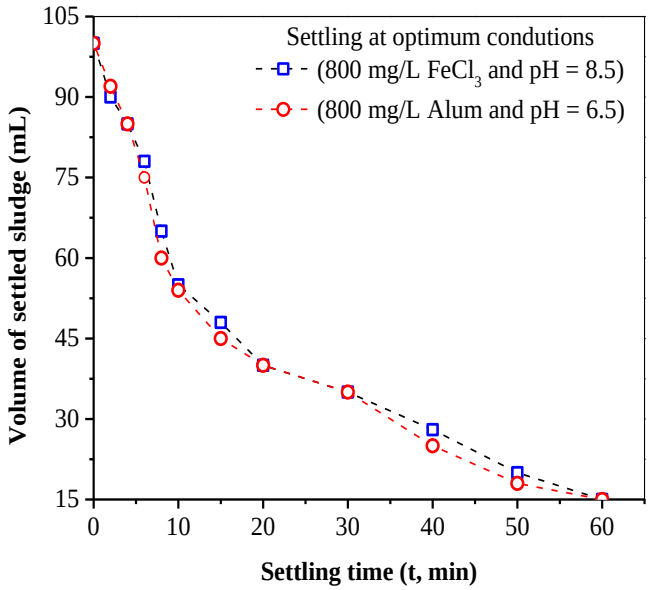

Figure 2. *Sludge settling for the coagulation-flocculation process (conditions; 800 mg/L $FeCl_3$, and alum coagulant dosages, pH = 6.5 for alum and 8.5 for $FeCl_3$).*

3.2. The impact of current density on the COD and turbidity removal efficiency

Significant advancements have been achieved in recent decades in the field of electrochemical technology used for the treatment of effluents that include organic contaminants. Electrochemical technologies are a viable alternative for addressing several environmental challenges within the process sector. This is mostly due to the diverse nature of electrons, which offer efficient, cost-effective, readily automatable, and environmentally friendly reagent options [10,23].

Current density has a significant impact on the formation rate of oxidizing species, making it a significant factor in all electrochemical processes. Due to its ability to regulate the reaction rate, electrooxidation procedures often regard the current density as the primary variable to manipulate (Can et al., 2019). The resulting data showed a COD output of 2000 mg/L and a turbidity output of 65 NTU when determining the optimum coagulant dosage in the CF process. The results show that the best coagulant dosage (800 mg/L of $FeCl_3$) used for coagulation-flocculation (CF) before the CEO reactor had a big effect on how well the BDD anode electrode worked. An investigation was conducted to analyze the influence of current density on the treatment of SWW using the CEO reactor, which was examined at four different current densities (5, 10, 20, and 30 mA/cm^2) under optimum conditions: a wastewater pH value of 8.5, a treatment duration of 3 hours (hydraulic retention time ($HRT = \frac{V_{reactor}}{Q}$) = 1 hour), a supporting electrolyte concentration of 3 g/L NaCl, and a wastewater constant flow rate of 0.9 L/h. The effluent COD concentrations achieved were 600 mg/L (70.0%) for 5 mA/cm^2, 480 mg/L (76.1%) for 10 mA/cm^2, 280 mg/L (86.0%) for 20 mA/cm^2, and 50 mg/L for mg/L (97.2%) for 30 mA/cm^2, respectively (Figure 3(a)). The effluent turbidity concentration exceeding <1 NTU (100%) was observed across all current densities, as illustrated in (Figure 3(b)).

As shown in Figure 3, there is a direct correlation between an increase in current density and an increase in the effectiveness of removing COD and turbidity. This phenomenon suggests That a higher current density significantly enhances the elimination of contaminants by generating a greater quantity of electrons in the SWW. However, many factors, such as the composition of the pollutants, the density of the electric current, the anode materials, and the pH level of the wastewater, influence the process of mineralization and/or oxidation of pollutants in electrooxidation [24].

In recent years, there has been a significant focus on the utilization of BDD electrodes to chemically eliminate pollutants. The distinguishing characteristic of a BDD electrode compared to conventional anodes is its high oxygen evolution potential [25]. The electrochemical incineration procedure for organic contaminants in wastewater utilizing a BDD electrode is often explained by Eqs. (10-12).

$$BDD + H_2O \rightarrow BDD(\bullet OH) + H^+ + e^- \quad (10)$$

$$BDD(\bullet OH) + R \rightarrow BDD + \textit{oxidation products} + H^+ + e^- \quad (11)$$

$$BDD(\bullet OH) \rightarrow BDD + H^+ + O_2 + e^- \quad (12)$$

The first step in the process entails the generation of hydroxyl radicals (•OH) through the electrolysis of SWW molecules. Organic oxidation is indirectly facilitated by the hydroxyl radical (•OH), which exhibits weak adsorption onto the BDD electrode surface. This adsorption leads to subsequent oxidative degradation as a result of the hydroxyl radical's exceptionally high reactivity. The reaction competes with the side reaction of oxygen evolution that is generated from the adsorbed hydroxyl radical (•OH). Therefore, the quantification of electrogenerated oxidation radicals, specifically the reactive BDD(•OH), has the potential to serve as an indicator of the indirect electrochemical oxidation capability of the electrode materials [26]

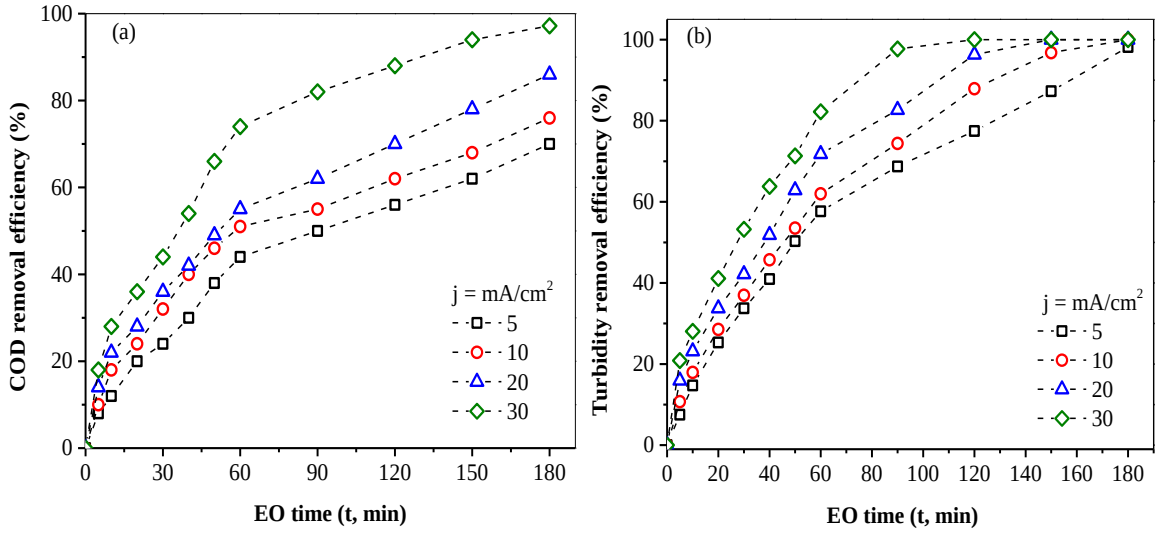

Figure 3. *(a) COD removal efficiency for BDD electrodes (b) The turbidity removal efficiency for BDD electrodes (conditions, initial COD C_0 = 2000 mg/L, initial turbidity C_0 = 65 NTU, initial pH = 8.5, HRT = 1 hour, Q = 0.9 L/h, SE = 3 g/L NaCl, stirring speed = 300 rpm, and distance between the electrodes = 15 mm).*

3.3. The impact of effluent flow rate on the COD and turbidity removal efficiency

The wastewater flow rate (FR) is a crucial factor. FR calculates the duration of time that effluent remains in the EO process. To comprehend An investigation was conducted to examine the effect of different wastewater flow rates on the COD and turbidity removal from the SWW. The study included a flow rate range of 0.9 L/h to 3.6 L/h while maintaining a constant current density of 30 mA/cm^2. The pH value of the wastewater was 8.50, the supporting electrolyte concentration was 3 g/L NaCl, and the reaction duration was 3 hours. According to (Figure 4(a)), the removal efficiencies increased as the FR decreased. The effluent COD concentrations for wastewater flow rates of 0.9, 1.5, 2.5, and 3.6 L/h were determined as 50 mg/L (97.2%) for 0.9 L/h, 100 mg/L (95.2%) for 1.5 L/h, 152 mg/L (92.4%) for 2.1 L/h, and 216 mg/L (89.2%) for 3.6 L/h, respectively, as shown in Figure 4 (a). Conversely, the turbidity concentration for all FR was determined to be <1 NTU (~99.9 %) according to (Figure 4(b)). The maximum removal effectiveness for COD and turbidity parameters was recorded at the wastewater flow rate of 0.9 L/h.

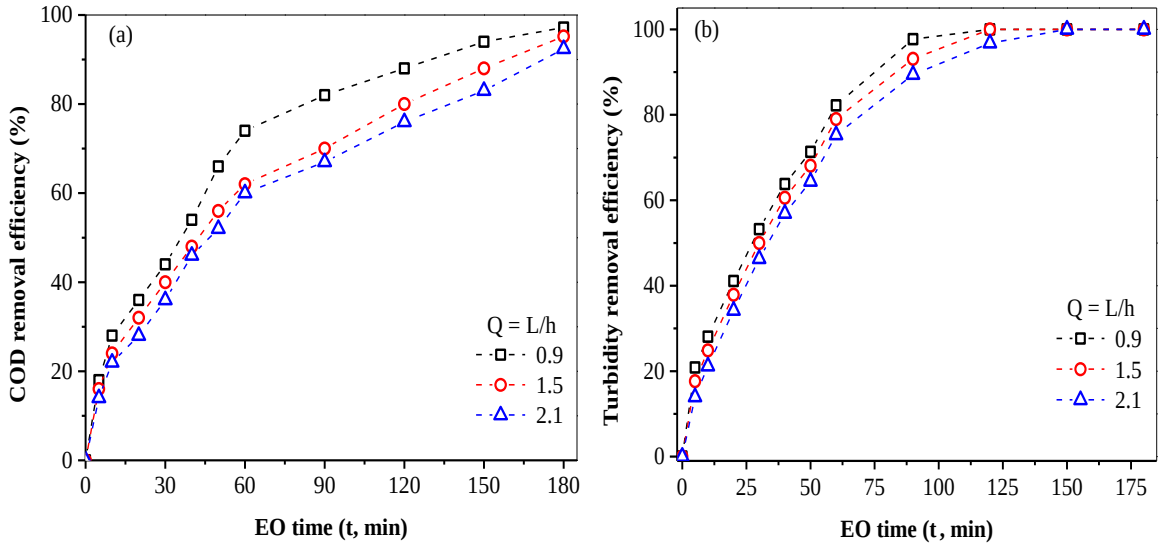

Figure 4. *(a) COD removal efficiency for BDD electrodes (b) The turbidity removal efficiency for BDD electrodes (conditions, initial COD C_0 = 2000 mg/L, initial turbidity C_0 = 65 NTU, j = 30 mA/cm^2, initial pH = 8.5, HRT = 1 hour, SE = 3 g/L NaCl, stirring speed = 300 rpm, and distance between the electrodes = 15 mm).*

3.4. The impact of supporting electrolyte concentration on the COD and turbidity removal efficiency

Supporting electrolytes (SE) in the electrochemical process may generate oxidation species and interact with organic contaminants in solutions, significantly impacting the oxidation capacity. Conversely, the addition of supportive electrolytes to wastewater is often seen to result in a reduction in electrical consumption and a significant improvement in removal efficiencies. This is achieved by the formation of radicals and stable oxidants [27,28]. Electrolysis was facilitated by the use of electrolytes since SWW typically includes a certain amount of salt. Electrolytes serve the purpose of facilitating electron transport and ionic conduction. The solution was subjected to different amounts of NaCl (1, 2, and 3 g/L) to examine the impact on COD and turbidity removal.

The oxidation procedure was conducted under optimum conditions, applying a wastewater pH value of 8.5, a current density of 30 mA/cm^2, using a BDD anode, a treatment duration of 3 hours, and a wastewater constant flow rate of 0.9 L/h. The effluent COD concentrations were determined to be 300 mg/L (85.0%) for 1 g/L of NaCl, 180 mg/L (91.1%) for 2 g/L of NaCl, and 50 mg/L (97.2%) for 3 g/L of NaCl, respectively, as shown in (Figure 5(a)). Furthermore, the turbidity concentration was determined to be <1 NTU (~99.9 %) using the same optimum conditions shown in (Figure 5(b)). The results show that a supporting electrolyte concentration of 3 g/L NaCl achieved the highest COD and turbidity removal efficiency The process of indirect electrochemical oxidation involves the degradation of contaminants by the use of a very potent oxidant on the surface of the anode. The current study included conducting CEO experiments with the incorporation of a concentration of 1-3 g/L NaCl into the SWW. Chlorine is often used as a potent oxidizing agent, derived from the anodic oxidation of chloride. The chloride reactions that occur during electrochemical oxidation are elucidated in Eqs (13-14). Hypochlorous acid (HOCl), chlorine (Cl_2), and hypochlorite (ClO^-) are recognized as potent oxidizing agents often known as active chlorine species. Hypochlorite acid may facilitate the indirect elimination of organic substances Eq (15) [18]. During indirect oxidation, increasing the concentration of NaCl leads to a gradual shift in the oxygen alteration process towards more favorable potentials, as compared to electrolysis performed without an SE [10,29].

$$2Cl \rightarrow Cl_2 + 2e^- \quad (13)$$

$$Cl_2 + H_2O \rightarrow HOCl + H^+ + Cl^- \quad (14)$$

$$HOCl \rightarrow ClO^- + H^+ \quad (15)$$

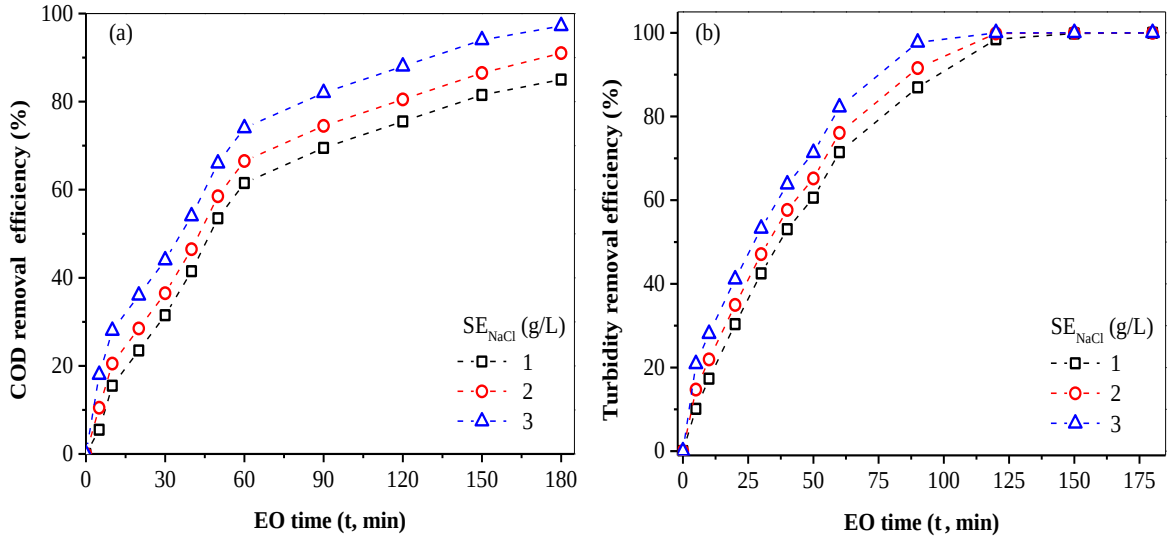

Figure 5. *(a) COD removal efficiency for BDD electrodes (b) The turbidity removal efficiency for BDD electrodes (conditions, initial COD C_0 = 2000 mg/L, initial turbidity C_0 = 65 NTU, j = 30 mA/cm^2, initial pH = 8.5, HRT = 1 hour, Q = 0.9 L/h, stirring speed = 300 rpm, and distance between the electrodes = 15 mm).*

3.5. Operating cost and kinetic analysis for CF+CEO reactor

The attainment of cost-effectiveness is a fundamental prerequisite for the practical implementation of wastewater treatment technologies within industrial contexts. Hence, the assessment of the treatment expenses associated with the SWW was conducted to ascertain the viability of the suggested treatment approach. The total operating costs for the CF+CEO reactor include the expenses associated with electrical energy, chemicals, and sludge dewatering and disposal. (Table 2) presents a summary of the relationship between the parameters of the electrooxidation process, such as removal efficiency, energy consumption for the process, overall operating cost, and the effect of the current density, wastewater flow rate, and supporting electrolyte concentration. It is evident that when the current density rises, the removal efficiencies also improve. However, this has a detrimental impact on energy consumption and performance characteristics. Increasing the current density from 5 mA/cm^2 to 30 mA/cm^2 results in a 2.5-3.0 times drop in the BBD anode efficiency (η). Conversely, energy consumption and total operating costs rise by 5.5-6.0 times and 3.0-3.5 times, respectively. When the flow rate of wastewater is raised from 0.9 L/h to 3.6 L/h, the efficiency of the anode (η) decreases by a factor of 1.0-1.5. Additionally, energy consumption and total operating costs rise by a factor of 0.5-1.0 and 1.0-1.5, respectively. On the contrary, when the concentration of the supporting electrolyte is raised from 1 g/L to 3 g/L, the anode efficiency (η) rises by a factor of 1.5–2.0. In contrast, energy consumption and total operating costs fall by a factor of 1.5–2.0 and 1.5–2.0, respectively. The findings suggest that operating at a lower current density is more advantageous in terms of energy efficiency and anode performance. Table 2. Table 2 demonstrates a strong association between the decline in COD concentration with time and the first-order reaction kinetics, as seen by the ideal linear correlations. The study's optimum conditions had an r^2 value of 0.99 and a k value of 18.7 × 10^{-3}(min^{-1}), respectively.

Table 2. *The total operating cost and kinetic analysis for the operation parameters.*

j	COD_{rem}	$Turbidity_{rem}$	SEC		Total OC		η	First order kinetic $(-\frac{dC}{dt} = k(Ct))$	
mA/cm^2	%	%	kWh/kg COD	kWh/m^3	US \$/m^3	US \$/kg COD	gCOD/Ahm^2	r^2	k (min^{-1})
5	70.0	98.0	10.2	15.1	1.1	0.27	35.5	0.98	6.3×10^{-3}
10	76.1	99.9	26.4	32.7	1.7	0.54	21.5	0.96	7.2×10^{-3}
20	86.0	99.9	52.3	65.3	2.7	1.10	13.5	0.98	9.8×10^{-3}
30	97.2	99.9	73.5	91.1	3.5	1.50	11.9	0.99	18.7×10^{-3}
Q	COD_{rem}	$Turbidity_{rem}$	SEC		Total OC		η	First order kinetic $(-\frac{dC}{dt} = k(Ct))$	
L/h	%	%	kWh/kg COD	kWh/m^3	US \$/m^3	US \$/kg COD	gCOD/Ahm^2	r^2	k (min^{-1})
0.9	97.2	99.9	73.5	91.2	3.5	1.5	11.9	0.99	18.7×10^{-3}
1.5	95.0	99.9	74.8	91.7	3.5	1.6	11.7	0.97	14.8×10^{-3}
2.1	92.4	99.9	85.2	105.3	4.1	1.8	10.2	0.97	12.6×10^{-3}
3.6	89.2	99.9	97.1	121.4	4.6	2.1	8.9	0.98	11.1×10^{-3}
SE	COD_{rem}	$Turbidity_{rem}$	SEC		Total OC		η	First order kinetic $(-\frac{dC}{dt} = k(Ct))$	
g/L	%	%	kWh/kg COD	kWh/m^3	US \$/m^3	US \$/kg COD	gCOD/Ahm^2	r^2	k (min^{-1})
1	85.0	99.9	110.4	136.4	5.0	2.33	7.9	0.97	10.8×10^{-3}
2	91.0	99.9	86.8	106.5	4.1	1.82	11.2	0.99	13.1×10^{-3}
3	97.2	99.9	73.5	91.2	3.5	1.50	12.0	0.99	18.7×10^{-3}

4. Conclusion

In this study, the aim was to treat cattle slaughterhouse wastewater (SWW) with sequential coagulation-flocculation (CF) + continuous electrooxidation reactor (CEO) using a BDD anode under different operation conditions.

The prior application of CF eliminated the presence of suspended organic matter and facilitated the achievement of effective electrooxidation. The pre-treatment stage successfully removed 50% of the COD and 68% of the turbidity from the effluent. The COD and turbidity removal efficiencies in the CEO reactor under optimum treatment conditions (j = 30 mA/cm^2, Q = 0.9 L/h, pH = 8.5, SE = 3.0 g NaCl/L and HRT = 1 h) were calculated to be 97.2% and ~99.9%, respectively. Therefore, using a CF + EO reactor with BDD electrodes was the most suitable method to meet the discharge limit of >125 mg/L COD for SWW. The specific energy consumption, process energy consumption, and total operating cost were 73.5 kWh/kg COD, 91.1 kWh/m^3, and 3.5 US \$/m^3, respectively. Current density and operating time significantly affected the EO process's removal efficiency. Moreover, both processes showed optimum removal efficiency at near-neutral pH. Therefore, under optimum process conditions, there is no need for much chemical addition for pH regulation in both systems. However, the addition of electrolytes during EO was necessary as it led to a reduction in electricity consumption. This study demonstrated that the combination of CF and EO processes is a powerful alternative for the treatment of wastewater with high turbidity and organic content, with many advantages such as easy-to-operate equipment, a short operating time, and low chemical requirements. In addition, future studies can be carried out using the initial pH of the wastewater, type of supporting electrolytes, and different anode materials, where some of the parameters investigated in this study (current density, wastewater flow rate, concentration of supported electrolyte) are kept at optimum values. The authors are planning such a study.

Acknowledgments

The publication in question originated from part of the master's degree thesis authored by Nawid Ahmad Akhtar under the advice of Prof. Dr. Mehmet Kobya. The authors

express their gratitude to Prof. Dr. Mustafa Dolaz for helping provide the wastewater, also the authors would like to thank Kyrgyz-Turkish Manas University for their support and assistance.

References

[1] C. F. Bustillo-Lecompte and M. Mehrvar, "Slaughterhouse wastewater characteristics, treatment, and management in the meat processing industry: A review on trends and advances," *J Environ Manage*, vol. 161, pp. 287–302, Sep. 2015, doi: 10.1016/j.jenvman.2015.07.008.

[2] E. Bazrafshan, F. Kord Mostafapour, M. Farzadkia, K. A. Ownagh, and A. H. Mahvi, "Slaughterhouse Wastewater Treatment by Combined Chemical Coagulation and Electrocoagulation Process," *PLoS One*, vol. 7, no. 6, p. e40108, Jun. 2012, doi: 10.1371/journal.pone.0040108.

[3] R. Terán Hilares, D. F. Atoche-Garay, D. A. Pinto Pagaza, M. A. Ahmed, G. J. Colina Andrade, and J. C. Santos, "Promising physicochemical technologies for poultry slaughterhouse wastewater treatment: A critical review," *J Environ Chem Eng*, vol. 9, no. 2, p. 105174, Apr. 2021, doi: 10.1016/j.jece.2021.105174.

[4] Ü. Tezcan Ün, A. S. Koparal, and Ü. Bakir Öğütveren, "Hybrid processes for the treatment of cattle-slaughterhouse wastewater using aluminum and iron electrodes," *J Hazard Mater*, vol. 164, no. 2–3, pp. 580–586, May 2009, doi: 10.1016/j.jhazmat.2008.08.045.

[5] P. V. Ngobeni, M. Basitere, and A. Thole, "Treatment of poultry slaughterhouse wastewater using electrocoagulation: a review," *Water Pract Technol*, vol. 17, no. 1, pp. 38–59, Jan. 2022, doi: 10.2166/wpt.2021.108.

[6] P. W. Harris and B. K. McCabe, "Review of pre-treatments used in anaerobic digestion and their potential application in high-fat cattle slaughterhouse wastewater," *Appl Energy*, vol. 155, pp. 560–575, Oct. 2015, doi: 10.1016/j.apenergy.2015.06.026.

[7] T. Schmidt, B. K. McCabe, P. W. Harris, and S. Lee, "Effect of trace element addition and increasing organic loading rates on the anaerobic digestion of cattle slaughterhouse wastewater," *Bioresour Technol*, vol. 264, pp. 51–57, Sep. 2018, doi: 10.1016/j.biortech.2018.05.050.

[8] M. A. Musa and S. Idrus, "Physical and Biological Treatment Technologies of Slaughterhouse Wastewater: A Review," *Sustainability*, vol. 13, no. 9, p. 4656, Apr. 2021, doi: 10.3390/su13094656.

[9] R. Davarnejad, K. Sarvmeili, and M. Sabzehei, "Car Wash Wastewater Treatment Using an Advanced Oxidation Process: A Rapid Technique for the COD Reduction of Water Pollutant Sources," *J Mex Chem Soc*, vol. 63, no. 4, Dec. 2019, doi: 10.29356/jmcs.v63i4.786.

[10] D. Ozturk and A. E. Yilmaz, "Treatment of slaughterhouse wastewater with the electrochemical oxidation process: Role of operating parameters on treatment efficiency and energy consumption," *Journal of Water Process Engineering*, vol. 31, p. 100834, Oct. 2019, doi: 10.1016/j.jwpe.2019.100834.

[11] S. Keskes, F. Hmaied, H. Gannoun, H. Bouallagui, J. J. Godon, and M. Hamdi, "Performance of a submerged membrane bioreactor for the aerobic treatment of abattoir wastewater," *Bioresour Technol*, vol. 103, no. 1, pp. 28–34, Jan. 2012, doi: 10.1016/j.biortech.2011.09.063.

[12] D. I. Massé and L. Masse, "The effect of temperature on slaughterhouse wastewater treatment in anaerobic sequencing batch reactors," *Bioresour Technol*, vol. 76, no. 2, pp. 91–98, Jan. 2001, doi: 10.1016/S0960-8524(00)00105-X.

[13] M. Pronk, M. K. de Kreuk, B. de Bruin, P. Kamminga, R. Kleerebezem, and M. C. M. van Loosdrecht, "Full scale performance of the aerobic granular sludge process for sewage treatment," *Water Res*, vol. 84, pp. 207–217, Nov. 2015, doi: 10.1016/j.watres.2015.07.011.

[14] P. Bruno, R. Campo, M. G. Giustra, M. De Marchis, and G. Di Bella, "Bench scale continuous coagulation-flocculation of saline industrial wastewater contaminated by hydrocarbons," *Journal of Water Process Engineering*, vol. 34, p. 101156, Apr. 2020, doi: 10.1016/j.jwpe.2020.101156.

[15] M. Shestakova and M. Sillanpää, "Electrode materials used for electrochemical oxidation of organic compounds in wastewater," *Rev Environ Sci Biotechnol*, vol. 16, no. 2, pp. 223–238, Jun. 2017, doi: 10.1007/s11157-017-9426-1.

[16] T. Le Luu, "Tannery wastewater treatment after activated sludge pre-treatment using electro-oxidation on inactive anodes," *Clean Technol Environ Policy*, vol. 22, no. 8, pp. 1701–1713, Oct. 2020, doi: 10.1007/s10098-020-01907-x.

[17] C. A. Martínez-Huitle and S. Ferro, "Electrochemical oxidation of organic pollutants for the wastewater

treatment: direct and indirect processes," *Chem. Soc. Rev.*, vol. 35, no. 12, pp. 1324–1340, 2006, doi: 10.1039/B517632H.

[18] B. A. Fil and S. Günaslan, "Electrooxidation treatment of slaughterhouse wastewater: investigation of efficiency of Ti/Pt anode," *Particulate Science and Technology*, vol. 41, no. 4, pp. 496–505, May 2023, doi: 10.1080/02726351.2022.2119905.

[19] APHA, *Standard Methods for the Examination of Water and Wastewater*, 19th ed. Washington, DC., 1998.

[20] M. Kobya and E. Demirbas, "Evaluations of operating parameters on treatment of can manufacturing wastewater by electrocoagulation," *Journal of Water Process Engineering*, vol. 8, pp. 64–74, Dec. 2015, doi: 10.1016/j.jwpe.2015.09.006.

[21] S. Verma, B. Prasad, and I. M. Mishra, "Pretreatment of petrochemical wastewater by coagulation and flocculation and the sludge characteristics," *J Hazard Mater*, vol. 178, no. 1–3, pp. 1055–1064, Jun. 2010, doi: 10.1016/j.jhazmat.2010.02.047.

[22] Ö. B. Gökçek and S. Özdemir, "Optimization of the Coagulation–Flocculation Process for Slaughterhouse Wastewater Using Response Surface Methodology," *Clean (Weinh)*, vol. 48, no. 7–8, Aug. 2020, doi: 10.1002/clen.202000033.

[23] D. Ozturk, A. E. Yilmaz, and Z. Sapci Ayas, "Electrochemical mineralization of abattoir wastewater with continuous system," *International Journal of Environmental Science and Technology*, vol. 18, no. 12, pp. 3761–3776, Dec. 2021, doi: 10.1007/s13762-020-03109-w.

[24] O. T. Can, E. Gengec, and M. Kobya, "TOC and COD removal from instant coffee and coffee products production wastewater by chemical coagulation assisted electrooxidation," *Journal of Water Process Engineering*, vol. 28, pp. 28–35, Apr. 2019, doi: 10.1016/j.jwpe.2019.01.002.

[25] S. O. Ganiyu, N. Oturan, S. Raffy, M. Cretin, C. Causserand, and M. A. Oturan, "Efficiency of plasma elaborated sub-stoichiometric titanium oxide (Ti4O7) ceramic electrode for advanced electrochemical degradation of paracetamol in different electrolyte media," *Sep Purif Technol*, vol. 208, pp. 142–152, Jan. 2019, doi: 10.1016/j.seppur.2018.03.076.

[26] H. Hai, X. Xing, S. Li, S. Xia, and J. Xia, "Electrochemical oxidation of sulfamethoxazole in BDD anode system: Degradation kinetics, mechanisms and toxicity evaluation," *Science of The Total Environment*, vol. 738, p. 139909, Oct. 2020, doi: 10.1016/j.scitotenv.2020.139909.

[27] E. Gengec, "Treatment of highly toxic cardboard plant wastewater by a combination of electrocoagulation and electrooxidation processes," *Ecotoxicol Environ Saf*, vol. 145, pp. 184–192, Nov. 2017, doi: 10.1016/j.ecoenv.2017.07.032.

[28] S. Periyasamy and M. Muthuchamy, "Electrochemical oxidation of paracetamol in water by graphite anode: Effect of pH, electrolyte concentration and current density," *J Environ Chem Eng*, vol. 6, no. 6, pp. 7358–7367, Dec. 2018, doi: 10.1016/j.jece.2018.08.036.

[29] P. Alfonso-Muniozguren, A. I. Gomes, D. Saroj, V. J. P. Vilar, and J. Lee, "The role of ozone combined with UVC/H2O2 process for the tertiary treatment of a real slaughterhouse wastewater," *J Environ Manage*, vol. 289, p. 112480, Jul. 2021, doi: 10.1016/j.jenvman.2021.112480.

MANAS Journal of Engineering
ISSN 1694-7398 | e-ISSN 1694-7398

Volume 12, Issue 1, (2024) Pages 129-134
https://doi.org/10.51354/mjen.1449637

The Analitical Solution of Linear and Non-Linear Differential-Algebraic Equations (DAEs) with Laplace-Padé Series Method

Nooriza Mirzabekova , Ercan Çelik*

Department of Applied Mathematics and Informatics, Kyrgyz-Turkish Manas University, Bishkek-Kyrgyzstan

noorizamirzabekova@gmail.com, ORCID: 0009-0004-9921-0696
ercan.celik@manas.edu.kg, ORCID: 0000-0001-5971-7653

ABSTRACT

In this paper, we apply Laplace-Padé Series method to solve linear and non-linear differential-algebraic equations (DAEs). Firstly, The basic properties of the Laplace-Padé Series method are given. Secondly, we calculate the arbitrary order power series of differential-algebraic equations (DAEs), then convert it to the series form Laplace-Padé. Then, the three differential-algebraic equations (DAEs) are solved by Laplace-Padé Series method. It was seen that the method gave effective and fast results. Therefore, the method can be easily applied to linear and non-linear differential-algebraic equations (DAEs) problems in different fields.

ARTICLE INFO

Research article

Received: 09.03.2024
Accepted: 29.04.2024

Keywords:
Differential-Algebraic Equations (DAEs), Power Series, Padé Series, Laplace-Padé Series Method
*Corresponding author

1. Introduction

Today, there are many mathematical models that can be expressed with differential-algebraic equations (DAEs). It is very difficult to solve such models analytically. Recently, researchers have begun to work on numerical solutions of systems of differential-algebraic equations (DAEs). Circuit analysis, computer aided design and real-time simulation of mechanical systems, power systems, chemical process simulation and optimum control are some of these systems in many fields. Researchers have developed some numerical methods using Backward Differentiation Formula (BDF) [1-5] and implicit Runge–Kutta methods [6] methods to solve these systems. This type of method is suitable for problems with small indexes and have a special structure. Many problems are solved by these methods. However, more general methods are needed. Many methods have been proposed by researchers[9-14], and so on[16-21]. In this article, we presented a new method for solving differential-algebraic equations (DAEs). We have applied the method to three examples. the first of the examples is linear, the second is non-linear, and the third is a physically modeled differential algebraic equations(DAEs). The difference of our method from other methods presented in the references in solving problems modeled as differential-algebraic equations (DAEs) in science and engineering is that the method we present gives fast results.

2. The Method

A system of general non-linear differential algebraic equations with initial conditions is denoted

$$G(t, y, y') = 0,\ y(t) = y_0 \quad (1)$$

where $G \in R^n, y \in R^n$ and $t \in R$.

Let us assume that the solutions of equation (1) are of the form

$$y = y_0 + at, \quad (2)$$

where a is a vector function. Equation (2) and its derivatives are substituted in equation (1), and if higher order terms are neglected, equation

$$\mathcal{M}a = \mathcal{N}, \quad (3)$$

is obtained. Where $\mathcal{M}$ and $\mathcal{N}$ are constant matrixes. The a values are found by solving equation (3). Then, by applying the above process to higher order terms, arbitrary order power series of equation (1) are obtained[7,8].

3. General Power Series Solution for Differential-Algebraic Equations(DAEs)

Now let's define another kind of power series in the form following:

$$f(t) = f_0 + f_1 t + f_2 t^2 + \ldots + (f_n + q_1 a_1 + \ldots + q_m a_m) t^n \quad (4)$$

Where $q_1, q_2, \cdots, q_m$ are constants. $a_1, a_2, \cdots, a_m$ are bases of vector a. Let's represent each element with the Power series in (4). Then

$y_i = y_{i,0} + y_{i,1}t + y_{i,2}t^2 + \ldots + a_i t^n$ (5)

is also generally of the form. Substituting equation (5) into equation (1), we get the following:

$f_i = (f_{i,n} + q_{i,1}a_1 + \ldots + q_{i,m}a_m)t^{n-j} + O(t^{n-j+1})$, (6)

If (1) have y', j is 0. If (1) not have y', j is 1. From equation (6) and (3), we get the linear equation following:

$\mathcal{M}_{i,j} = P_{i,j}$ (7)

$\mathcal{N}_i = -f_{i,n}$, (8)

When the linear equation (7) and (8) is solved, a_i $(i = 1, \ldots, m)$ is obtained. Substituting a_i in equation (5), we get y_i $(i = 1, \ldots, m)$ polynomials of degree n. If these process are repeated from equation (5) to equation (8), arbitrary order power series are obtained for equation (1).

4. Padé Series

The Padé series, in the form of a rational function, is defined as following:

$c_0 + c_1 x + c_2 x^2 + \cdots = \frac{a_0 + a_1 x + \cdots + a_M x^M}{1 + b_1 x + \cdots + b_L x^L}$ (9)

In equation (9), if the cross-multiplication multiplication is done, we have

$(c_0 + c_1 x + c_2 x^2 + \cdots)(1 + b_1 x + \cdots + b_L x^L) = a_0 + a_1 x + \cdots + a_M x^M$ (10)

From the coefficient equality of both sides in equation (10), We have

$c_l + \sum_{k=1}^{M} c_{l-k} b_k = a_l \ (l = 0, \cdots, M)$ (11)

$c_l + \sum_{k=1}^{L} c_{l-k} b_k = 0 \ (l = M+1, \cdots, M+L)$ (12)

By solving the linear equation (12), we get $b_k (k = 1, \cdots, L)$. And if we substitute b_k in equation (9), we get $a_k (l = 1, \cdots, M)$ [7,8].

5. Laplace-Padé Series Method (LPSM)

The following steps are done for the Laplace-Padé series method [15].

1. The Laplace transform is applied to the obtained power series.
2. In the resulting equation, s is replaced by $1/x$.
3. We convert it from order $[M / L]$ to Padé series. M and L are arbitrarily chosen, but they should be of smaller value than the order of the power series.
4. $1/s$ is written instead of x.
5. Finally, the inverse laplace transform is taken.

Thus, the exact or numerical solution of the given equation is obtained.

6. Applications

In this section, we have solved the three differential-algebraic equations (DAEs) with the the Laplace-Padé series method (LPSM).

1. We consider the following linear differential-algebraic equation [15]:

$$\begin{aligned} &y_1' + y_1 - xy_3 + y_4 = 0, \\ &y_2' - y_1 + y_2 - x^2 y_3 + xy_4 = 0, \\ &y_3' - x^3 y_1 + x^2 y_2 - y_3 = 0, \\ &xy_1 - y_2 + xy_3 - y_4 = 0, \end{aligned} \quad (13)$$

and initial values

$$y_1(0) = y_3(0) = 1,$$
$$y_2(0) = y_4(0) = 0,$$

The exact solution is

$$y_1(x) = \exp(-x),$$
$$y_2(x) = x\exp(-x),$$
$$y_3(x) = \exp(x),$$
$$y_4(x) = x\exp(x).$$

From initial values, the solutions of (13) can be supposed as

$$\begin{aligned} &y_1(x) = y_{0,1} + a_1 x \Rightarrow y_1(x) = 1 + a_1 x \\ &y_2(x) = y_{0,2} + a_2 x \Rightarrow y_2(x) = a_2 x \\ &y_3(x) = y_{0,3} + a_3 x \Rightarrow y_3(x) = 1 + a_3 x \\ &y_4(x) = y_{0,4} + a_4 x \Rightarrow y_4(x) = a_4 x \end{aligned} \quad (14)$$

Substitute (14) into (13) and neglect higher order terms, we have

$$\begin{aligned} &a_1 + 1 + O(x) = 0 \\ &a_2 - 1 + O(x) = 0 \\ &a_3 - 1 + O(x) = 0 \\ &(2 - a_2 - a_4)x + O(x^2) = 0 \end{aligned} \quad (15)$$

These formulas correspond to (6). The linear equation corresponding to (7) and (8) can be given as:

$\mathcal{M}a = \mathcal{N}$ (16)

Where

$$\mathcal{M} = \begin{pmatrix} 1 & 0 & 0 & 0 \\ 0 & 1 & 0 & 0 \\ 0 & 0 & 1 & 0 \\ 0 & -1 & 0 & -1 \end{pmatrix}, \mathcal{N} = \begin{pmatrix} 1 \\ -1 \\ 1 \\ 0 \end{pmatrix}$$

$$a=\begin{pmatrix} a_1 \\ a_2 \\ a_3 \\ a_4 \end{pmatrix} \tag{17}$$

From equation (16), we have linear equation

$$\begin{pmatrix} 1 & 0 & 0 & 0 \\ 0 & 1 & 0 & 0 \\ 0 & 0 & 1 & 0 \\ 0 & -1 & 0 & -1 \end{pmatrix}\cdot\begin{pmatrix} a_1 \\ a_2 \\ a_3 \\ a_4 \end{pmatrix}=\begin{pmatrix} -1 \\ 1 \\ 1 \\ -2 \end{pmatrix} \tag{18}$$

Solving equation (18), we have

$$a=\begin{pmatrix} -1 \\ 1 \\ 1 \\ 1 \end{pmatrix} \tag{19}$$

and

$$\begin{aligned} y_1(x)&=1-x, \\ y_2(x)&=x, \\ y_3(x)&=1+x, \\ y_4(x)&=x. \end{aligned} \tag{20}$$

From (17) the solutions of (13) can be supposed as

$$\begin{aligned} y_1(x)&=1-x+a_1x^2 \\ y_2(x)&=x+a_2x^2 \\ y_3(x)&=1+x+a_3x^2 \\ y_4(x)&=t+a_4x^2. \end{aligned} \tag{21}$$

In like manner, substitute (18) into (13) and neglect higher order terms, then we have

$$\begin{aligned} (2a_1-1)x+O(x^2)&=0 \\ (2a_2+2)x+O(x^2)&=0 \\ (2a_3-1)x+O(x^2)&=0 \\ (-a_2-a_4)x^2+O(x^3)&=0. \end{aligned} \tag{22}$$

Where

$$\mathcal{M}=\begin{pmatrix} 2 & 0 & 0 & 0 \\ 0 & 1 & 0 & 0 \\ 0 & 0 & 2 & 0 \\ 0 & -1 & 0 & -1 \end{pmatrix},\ \mathcal{N}=\begin{pmatrix} 1 \\ -1 \\ 1 \\ 0 \end{pmatrix},$$

$$a=\begin{pmatrix} a_1 \\ a_2 \\ a_3 \\ a_4 \end{pmatrix}$$

from (19) we have linear equation

$$\begin{pmatrix} 2 & 0 & 0 & 0 \\ 0 & 1 & 0 & 0 \\ 0 & 0 & 2 & 0 \\ 0 & -1 & 0 & -1 \end{pmatrix}\cdot\begin{pmatrix} a_1 \\ a_2 \\ a_3 \\ a_4 \end{pmatrix}=\begin{pmatrix} 1 \\ -1 \\ 1 \\ 0 \end{pmatrix} \tag{23}$$

Solving equation (23), we have

$$a=\begin{pmatrix} 0.5 \\ -1 \\ 0.5 \\ 1 \end{pmatrix}. \tag{24}$$

Therefore

$$\begin{aligned} y_1(x)&=1-x \\ y_2(x)&=x \\ y_3(x)&=1+x+0.5x^2 \\ y_4(x)&=x+x^2 \end{aligned} \tag{25}$$

Repeating above procedure we have

$$\begin{aligned} y_1(x)&=1-x+\frac{x^2}{2}-\frac{x^3}{6}+\frac{x^4}{24}, \\ y_2(x)&=x-x^2+\frac{x^3}{2}-\frac{x^4}{6}, \\ y_3(x)&=1+x+\frac{x^2}{2}+\frac{x^3}{6}+\frac{x^4}{24}, \\ y_4(x)&=x+x^2+\frac{x^3}{2}+\frac{x^4}{6}. \end{aligned} \tag{26}$$

Then, Laplace transformation is applied to (26)

$$y_{L1}(s)=\frac{1}{s}-\frac{1}{s^2}+\frac{1}{s^3}-\frac{1}{s^4}+\frac{1}{s^5},$$
$$y_{L2}(s)=\frac{1}{s^2}-\frac{2}{s^3}+\frac{3}{s^4}-\frac{4}{s^5},$$
$$y_{L3}(s)=\frac{1}{s}+\frac{1}{s^2}+\frac{1}{s^3}+\frac{1}{s^4}+\frac{1}{s^5},$$
$$y_{L4}(s)=\frac{1}{s^2}+\frac{2}{s^3}+\frac{3}{s^4}+\frac{4}{s^5}.$$

and then $\frac{1}{x}$ is written in place of s.

$$y_{L1}\left(\frac{1}{x}\right)=x-x^2+x^3-x^4+x^5,$$
$$y_{L2}\left(\frac{1}{x}\right)=x^2-2x^3+3x^4-4x^5,$$
$$y_{L3}\left(\frac{1}{x}\right)=x+x^2+x^3+x^4+x^5$$
$$y_{L4}\left(\frac{1}{x}\right)=x^2+2x^3+3x^4+4x^5.$$

Afterwards, Padé approximant of order $[2/2]$ is applied

$$y_{1,[2,2]}(x)=\frac{x}{1+x},$$
$$y_{2,[2,2]}(x)=\frac{x^2}{x^2+2x+1},$$
$$y_{3,[2,2]}(x)=\frac{x}{1-x},$$
$$y_{4,[2,2]}(x)=\frac{x^2}{x^2-2x+1},$$

and $\frac{1}{s}$ is written in place of x for each variable

$$y_{1,[2/2]}\left(\frac{1}{s}\right)=\frac{1}{1+s},$$
$$y_{2,[2/2]}\left(\frac{1}{s}\right)=\frac{1}{(s+1)^2},$$
$$y_{3,[2/2]}\left(\frac{1}{s}\right)=\frac{1}{s-1},$$
$$y_{4,[2/2]}\left(\frac{1}{s}\right)=\frac{1}{(s-1)^2}.$$

Finally, by using the inverse Laplace transformation,

$$y_1(x)=\exp(-x),$$
$$y_2(x)=x\cdot\exp(-x),$$
$$y_3(x)=\exp(x),$$
$$y_4(x)=x\cdot\exp(x).$$

We obtain the exact solution for (13).

2. We consider the following linear differential-algebraic equation[15]:

$$\begin{aligned} y_1' &= 2y_1y_2z_1z_2,\\ y_2' &= -y_1y_2z_2^2,\\ z_1' &= (y_1y_2+z_1z_2)u,\\ z_2' &= -y_1y_2^2z_2^2u,\\ y_1y_2^2 &= 1. \end{aligned} \qquad (27)$$

and initial values

$$y_1(0)=y_2(0)=1,$$
$$z_1(0)=z_2(0)=1,$$
$$u(0)=1.$$

where prime denotes derivative with respect to x.
Applying the above method to Equation (27)

$$\begin{aligned} y_1(x) &= 1+2x+2x^2+\frac{4}{3}x^3+\frac{2}{3}x^4,\\ y_2(x) &= 1-x+\frac{1}{2}x^2-\frac{1}{6}x^3+\frac{1}{24}x^4,\\ z_1(x) &= 1+2x+2x^2+\frac{4}{3}x^3+\frac{101}{174}x^4,\\ z_2(x) &= 1-x+\frac{1}{2}x^2-\frac{1}{6}x^3+\frac{59}{696}x^4,\\ u(x) &= 1+x+\frac{1}{2}x^2-\frac{1}{174}x^3-\frac{25}{58}x^4. \end{aligned} \qquad (28)$$

Then, Laplace transformation is applied to (28) and then $\frac{1}{x}$ is written in place of s . Afterwards, Padé approximant of order $[2/2]$ is applied and $\frac{1}{s}$ is written in place of x for each variable. Finally, by using the inverse Laplace transformation, we obtain the exact solution for (27).

$$
\begin{aligned}
&y_1(x)=\exp(2x),\\
&y_2(x)=\exp(-x),\\
&z_1(x)=\exp(2x),\\
&z_2(x)=\exp(-x),\\
&u(x)=\exp(x).
\end{aligned}
\tag{29}
$$

3. Physical Problem

Consider the linear circuit given in Figure 1. The modified nodal analysis leads directly to the system

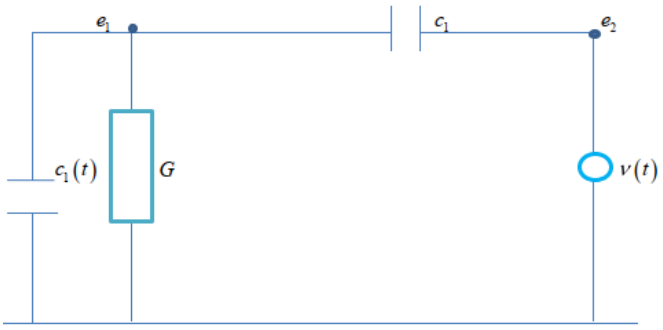

Fig. 1. Linear circuit with a time-dependent capacitance.

$$
\begin{pmatrix}1 & -1\\ 0 & 1\\ 0 & 0\end{pmatrix}\begin{pmatrix}B_1(t)k_1(t)\\ \\ B_2(t)k_1(t)+B_2(t)k_2(t)\end{pmatrix}'+
\begin{pmatrix}H & 0 & 0\\ 0 & 0 & -1\\ 0 & 1 & 0\end{pmatrix}\begin{pmatrix}k_1(t)\\ k_2(t)\\ j(t)\end{pmatrix}=\begin{pmatrix}0\\ 0\\ W(t)\end{pmatrix}
\tag{30}
$$

Choosing

$$B_1(t)=1+0.25(\sin(t)+\cos(t)),\quad B_2=1,\quad H=2 \tag{31}$$

And input voltage

$$W(t)=4\sin(t)+0.25\sin(2t). \tag{32}$$

Substitute equation (31) and (32) into equation (30), we can get the following

$$
\begin{aligned}
&\left[2+0.25\left(\cos(t)-\sin(t)\right)\right]k_1(t)+\left[2+0.25\left(\cos(t)+\sin(t)\right)\right]k_1'(t)-k_2'(t)=0,\\
&-k_1'(t)+k_2'(t)-j(t)=0,\\
&k_2(t)=4\sin(t)+0.25\sin(2t)
\end{aligned}
\tag{33}
$$

Exact solution of equation (33) is

$$
\begin{aligned}
&k_1(t)=\sin(t)+\cos(t),\\
&k_2(t)=4\sin(t)+0.25\sin(2t),\\
&j(t)=3\cos(t)+0.5\cos(2t)+\sin(t)
\end{aligned}
$$

For the consistent initial values

$$k_1(0)=1, k_2(0)=0, j(0)=3.5.$$

Equation (33) is form of equation (1).

Applying the above method to equation (33), we have

$$
\begin{aligned}
&k_1(t)=1+t-0.5t^2-0.1666666667t^3+0.04166666667t^4,\\
&k_2(t)=4.5t-t^3,\\
&j(t)=3.5+t-2.5t^2-0.1666666667t^3+0.4583333333t^4.
\end{aligned}
\tag{34}
$$

Then, Laplace transformation is applied to (34) and then $\frac{1}{t}$ is written in place of s. Afterwards, Padé approximant of order $[2/2]$ is applied and $\frac{1}{s}$ is written in place of t for each variable. Finally, by using the inverse Laplace transformation, we obtain the exact solution for (30).

$$
\begin{aligned}
&k_1(t)=\sin(t)+\cos(t),\\
&k_2(t)=4\sin(t)+0.25\sin(2t),\\
&j(t)=3\cos(t)+0.5\cos(2t)+\sin(t).
\end{aligned}
$$

Conclusion

This work presented Laplace-Padé series method as a combination of the classic series method and method based on the Laplace and Padé series. By solving three problems, we presented the Laplace-Padé series method as a useful tool with high potential to solve linear/non-linear differential-algebraic equations. The Laplace-Padé Series Method(LPMS) is used for rapid convergence of solutions or to find exact solutions. The proposed method possesses a straightforward procedure, suitable for science and engineers. The method presented in our next work will be applied to different problems modeled as linear and non-linear differential-algebraic equations (DAEs).

Acknowledgments

The authors have been supported by the Kyrgyz-Turkish Manas University BAP Coordination Unit with Project number KTMU-BAP-2023.FB.02.

REFERENCES

[1]. K. E. Brenan, S.L. Campbell and L.R. Petzold, Numerical Solution of Initial Value Problems in Differential Algebraic Equations, Elsevier, New York, 1989.

[2]. E. Hairer, S.P. Norsett and G. Wanner, Solving Ordinary Differential Equations II. Stiff and Differential-Algebraic Problems, Springer, New York, 1992.

[3]. L.R. Petzold, Numerical solution of differential-algebraic equations, Adv. Numer. Anal. 4 (1995).

[4]. U.M. Ascher, On symmetric schemes and differential-algebraic equations, SIAM J. Sci. Stat. Comput. 10, 937–949, 1989.

[5]. C.W. Gear and L.R. Petzold, ODE systems for the solution of differential-algebraic systems, SIAM J. Numer. Anal. 21, 716–728, 1984.

[6]. U.M. Ascher and L.R. Petzold, Projected implicit Runge–Kutta methods for differential-algebraic equations, SIAM J. Numer. Anal. 28, 1097–1120, 1991.

[7]. E. Çelik and M. Bayram, On the numerical solution of differential-algebraic equation by Pade´ series, Appl. Math. Comput. 137, 151–160, 2003.

[8]. E. Çelik and M. Bayram, The numerical solution of physical problems modeled as a systems of differential-algebraic equations(DAEs), Journal of Franklin Institute, 342, 1-6, 2005.

[9]. U.M. Ascher and P. Lin, Sequential regularization methods for higher index differential-algebraic equations with constant singularities: the linear index-2 case, SIAM J. Numer. Anal. 33, 1921–1940, 1996.

[10]. U.M. Ascher and P. Lin, Sequential regularization methods for non-linear higher index differential-algebraic equations, SIAM J. Sci. Comput. 18, 160–181, 1997.

[11]. S.L. Campbell, A computational method for general higher index singular systems of differential equations, IMACS Trans. Sci. Comput. 89, 555–560, 1989.

[12]. S.L. Campbell, E. Moore and Y. Zhong, Utilization of automatic differentiation in control algorithms, IEEE Transactions on Automatic Control, 39 (5), 1047 – 1052,1994.

[13]. S. K. Vanani and A. Aminataei, "Numerical solution of differential algebraic equations using a multiquadric approximation scheme," Mathematical and Computer Modelling, 53 (5-6), 659 – 666, 2011.

[14]. Y. Khan and N. Faraz, Application of modified laplace decomposition method for solving boundary layer equation, Journal of King Saud University - Science, 23 (1), 115 – 119, 2011.

[15]. H.Vazquez-Leal, Exact solutions for Differential-Algebraic Equations, Miskolc Mathematical Notes, 15 (1), 227-238, 2014.

[16]. H. Singh and A. Wazwaz, Computational Method for Reaction Diffusion-Model Arising in a Spherical Catalyst, International Journal of Applied and Computational Mathematics, 7 (3), 65, 2021.

[17]. H. Singh, Analysis for fractional dynamics of Ebola virus model, Chaos solitons & fractals, 138, 109992, 2020.

[18]. H. Singh, Analysis of drug treatment of the fractional HIV infection model of CD4+ T-cells, Chaos Solitons & Fractals, 146, 110868, 2021.

[19]. H. Singh, Jacobi collocation method for the fractional advection-dispersion equation arising in porous media, Numerical methods for partial differential equations, 2020.

[20]. H. Singh, H.M. Srivastava and D. Kumar, A reliable numerical algorithm for the fractional vibration equation, Chaos, Solitons and Fractals, vol. 103, 131-138, 2017.

[21]. H. Singh, Chebyshev spectral method for solving a class of local and nonlocal elliptic boundary value problems, International Journal of Nonlinear Sciences and Numerical Simulation, 24(3), 899-915, 2021

MANAS Journal of Engineering
ISSN 1694-7398 | e-ISSN 1694-7398

Volume 12, Issue 1, (2024) Pages 135-144
https://doi.org/10.51354/mjen.1465571

Effect of Packaging Methods and Storage Temperatures on the Quality of Erzurum Cheese Halva

Hayrunnisa ÖZLÜ[1], Meryem AYDEMİR ATASEVER[2,*], Sevda URÇAR GELEN[2], Mustafa ATASEVER[2]

[1] Ataturk University, Graduate School of Natural and Applied Sciences, Erzurum, Türkiye, hayrunnisa@atauni.edu.tr, ORCID: 0000-0002-5007-6121

[2] Ataturk University, Faculty of Veterinary Medicine, Department of Food Hygiene and Technology, Erzurum, Türkiye, meryematasever@atauni.edu.tr, ORCID: 0000-0003-2938-5808, surcar@atauni.edu.tr, ORCID: 0000-0002-1852-3614, atasever@atauni.edu.tr, ORCID: 0000-0002-1627-5565

ABSTRACT

Erzurum cheese halva is a traditional food registered with a geographical indication with its own taste and flavor, which is produced with saltless fresh civil cheese, fresh cream and flour mixture. This study was conducted to investigate the changes in the physical, chemical and microbiological properties of Erzurum cheese halva in different packaging and storage tempareture. The produced cheese halva samples were stored for two months in two different packaging methods (aerobic and vacuum packaged) and at three different storage temperatures (room temperature, +4°C and -18°C). Some microbiological, chemical, physicochemical and sensory analysis of cheese halva samples were investigated during storage period. Furthermore, the dry matter, ash, protein, fat, salt and aw contents of cheese halva samples were determined on the 0th day of storage. The most obvious sign of deterioration were moldiness on aerobic packaged samples both the room temperature and +4°C stored, and they were spoiled on the10th and 15th day of storage, respectively. It was observed that the acidity has increased and consumability has decreased in vacuum packaged samples stored at +4°C. Although neither chemical nor microbiological deterioration occurred in the vacuum packaged cheese halva samples stored on -18°C, negatively affects in the fibrous structure of the product and reduces the overall acceptability of the product. For this reason, future studies must be carried out that is necessary to search for more suitable packaging methods (e.g. modified atmosphere packaging) to protect the product's typical textural structure during the shelf life.

ARTICLE INFO

Research article

Received: 5.04.2024
Accepted:10.06.2024

Keywords:
Erzurum cheese halva, traditional food, vacuum-packaging, shelf life

**Corresponding author*

1. Introduction

Natural and economic conditions, religion, culture and traditions are effective in changing the foods consumed in human nutrition from country to country. [1-2]. The identification of a particular origin is a necessary but not sufficient condition to classify a product as traditional; thus, only some local products can be considered traditional. In this regard, traditional food products are defined as those "frequently consumed or associated with specific celebrations and/or seasons, transmitted from one generation to another, made in a specific way according to gastronomic heritage, naturally processed, and distinguished and known because of its sensory properties and associated with a certain local area, region or country"[3-4].

Throughout Türkiye, each region, steeped in rich cultural and historical heritage, and boasting diverse geographical and ecological landscapes, embraces a plethora of traditional culinary delights. In Türkiye, the recognition of many

traditional foods is limited to the rural regions where they are produced. Consequently, due to urbanization, awareness of these foods is gradually diminishing among younger generations, leading to insufficient utilization of these traditional products, which possess significant potential for added value [5-6].

"Erzurum cheese halva," bearing a protected geographical indication, is a traditional delicacy exclusive to the Erzurum province. It was officially recognized as a geographical indication within the "Bakery and pastry products, pastries, desserts" category on July 16, 2021. This savory halva is prepared in copper boilers, using Erzurum civil cheese, wheat flour or whole wheat flour, milk cream, and salt. Its production is primarily concentrated during the summer months when milk is plentiful. Referred to as "hores" in the region, Erzurum cheese halva distinguishes itself with its fibrous texture, attributed to the usage of fresh and unsalted civil cheese [7-8]. Erzurum cheese halva is mostly produced in villages and consumed by households. Furthermore, a small portion of Erzurum cheese halva production is undertaken by select businesses within the city, catering to the local market demand. Although cheese halva is known in Erzurum province of Türkiye, it is not well known throughout the country. There are many products called cheese halva made with cheese in various regions of Türkiye. Erzurum cheese halva stands apart from other cheese halvas due to its distinct lack of sweetness, as it contains no sugar. This unique characteristic extends to both its ingredients and preparation methods

Erzurum civil cheese, one of the main ingredients of cheese halva, is a local cheese produced from skim milk.. This product obtained a geographical indication certificate under the name "Erzurum civil cheese" in 2009. It is a local product with a salt-free, fat-free/low-fat, produced from cows' milk fed on the high-altitude pastures of Erzurum province [9]. The fibrous structure of Erzurum cheese halva is the most important textural feature of this product. For this reason, the civil cheese to be used in the production of cheese halva is not salted and is asked to be kept in the hanger for a longer time to gain a more fibrous structure and release its water thoroughly. In addition, the temperature at which the cheese is added into the halva is of great importance in order to form the desired fibrous structure in the cheese halva.

It is stated that standard production method cannot be provided in traditional products, new technologies cannot be used, capacities cannot be increased much and high efficiency cannot be achieved [10]. Due to the fact that the production of Erzurum cheese halva does not use standard production methods and does not provide hygienic conditions, there are differences in the colour, taste, smell and aroma of the product, which leads to negative effects on the quality of the product. On the other hand, the packaging used in cheese halva sold in the market negatively affects the consumer's perception that the product does not protect the quality parameters, thus reducing the interest in the product. It is very important to determine an appropriate packaging method that will preserve the quality parameters, extend its shelf life and increase its appeal of traditionally produced Erzurum cheese halva during storage.

The geographical indication registration certificate of Erzurum cheese halva is states that the product should be stored at +4°C for a maximum of 10 days, and if longer storage is required, it should be frozen. However, they are offered for sale in the market under different packaging and storage conditions. For this reason, there is a need to standardize the packaging method and storage temperature that better preserve the microbial and textural properties of cheese halva during storage. In this study, the effects of different packaging methods and storage conditions of Erzurum cheese halva on the quality characteristics of the product were investigated. In addition, some chemical and microbiological properties of cheese halva obtained from the market were determined and compared with experimentally produced cheese halva.

2. Materials and methods

2.1. *Materials*

The cheese and cream used in production were provided by Atatürk University, Food and Livestock Application and Research Center.

In the production of halva, daily fresh cream, wheat flour and unsalted civil cheese, which was kept for about 4 hours after production to gain the desired stringiness (fibrousness) were used.

2.2. *Methods*

Erzurum cheese halva production was made based on the procedure obtained as a result of interviews and preliminary tests with local businesses and village producers (Figure 1).

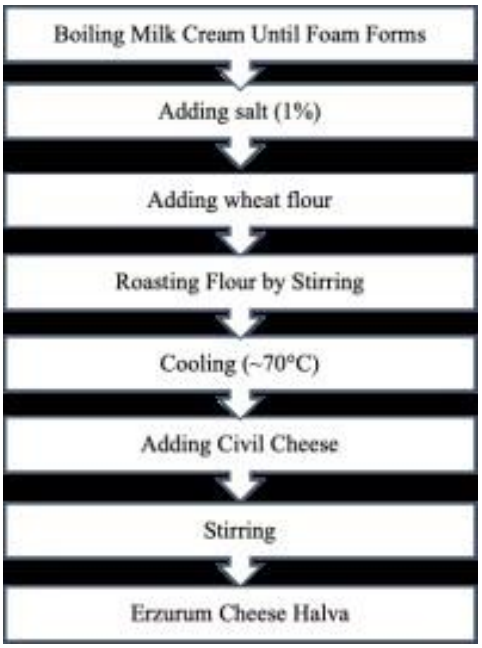

Figure 1. Production flow chart of Erzurum cheese halva

In order to determine the general properties of the produced Erzurum cheese halva, dry matter, ash, aw, protein, fat and salt analyses were performed on 0th day. The produced fresh cheese halva samples was packed under normal atmosphere and vacuum packaged. Packaged cheese halva samples were stored at -18±1ºC, 4±1ºC and room temperature (24±1ºC) for 60 days. Microbiological, chemical, physicochemical and sensory analyzes of the samples were performed on the 0th, 5th, 10th, 15th, 30th, 45th and 60th days of storage.

In addition, cheese halvas sold in local markets in Erzurum were collected and some microbiological, chemical and physicochemical analyzes were performed.

2.3. *Microbiological analyses*

To determine the microbial quality of experimentally produced Erzurum cheese halva samples; total mesophilic aerobic counts (TMAB), total psychrophilic aerobic bacteria count (TAPB), lactic acid bacteria counts(LAB), coliform bacteria counts and total yeast and mold counts were determined on specific days of storage during storege the halvas at room, +4°C and -18°C temperature. TMAB, TPAB, LAB, yeast and mold counts were determined as log cfu/g using Plate Count Agar (PCA, Merck) (48 hours at 37°C), PCA (10 days at 7°C), de Man Rogosa and Sharpe (MRS, Merck) Agar (48 hours at 37°C, anaerobic conditions (5% CO2)), Rose Bengal Chloramphenicol (RBC, Merck) Agar (5 days at 20°C) culture media, respectively. In addition, the coliform group bacterial count of cheese halva samples obtained from local markets was determined using Violet Red Bile Agar (VRBA, Merck) (24 hours at 35-37°C) [11-12].

2.4. *Chemical and physicochemical analyses*

Dry matter and ash (gravimetric method), protein (micro-Kjeldahl method) and titratable acidity (% lactic acid) of Erzurum cheese halva samples were determined using the AOAC (2007) standard method [13]. Fat determination was made using the Van Gulik method [14]. The salt content of cheese halva samples was calculated using the Mohr method [15].

The aw values and the color values of Erzurum cheese halva samples were determined using a water activity device (Aqualab 4TE, USA) and a color measuring device, respectively. (Konica Minolta CR-400, Osaka, Japan). In color measurement, measurements were taken at 3 different points on the cross-sectional surface of the cheese halva; L* (L*=0, black; L*=100, white; brightness/darkness); a* (+a* = red, -a*= green; redness/greenness) and b* (+b*= yellow, -b*= blue; yellowness/blueness) values were made three-dimensional measurements [16-17].

2.5. *Sensory analyses*

Sensory analysis was conducted by 7 panelists (between 25 and 55 age) in the Food Hygiene and Technology Department of Atatürk University, Erzurum, Turkey. The panelists were selected based on their interest, non-smoker and non-food allergic. Samples (15-20 g portions) were served in a plate along with bread and water. Plates were labelled with one-digit random codes. Each sample was evaluated using the hedonic scale (1-9) anchored on the left with ‘dislike extremely’ and on the right with ‘like extremely’. Sensory evaluation was based on color, appearance, structure, taste/odor and general acceptability. The panelists were asked to evaluate the cheese halvas in terms of quality criteria and to indicate in writing the defects that caused the cheese halvas to decrease in score.

2.6. *Statistical analysis*

It was carried out using the IBM SPSS Statistics 20.0 package program according to variance analysis (ANOVA) method. Mean values were considered significant at $p<0.05$ using the Duncan multiple comparison method.

3. Results and Discussion

Some chemical and physicochemical analysis results of Erzurum cheese halva samples after production were given in Table 1. Erzurum cheese halva is an important food for human nutrition because it contains high amounts of protein and fat [18].

Table 1. Some chemical and physicochemical analysis results of Erzurm cheese halva samples

Parameters	Mean±SD	Parameter	Mean±SD
Dry matter (%)	76.41±4.53	Protein (%)	16.25±1.18
Ash (%)	1.81±1.56	Fat (%)	28.85±3.15
aw	0.946±0.016	Salt (%)	1.17±0.12

The TMAB, TPAB, LAB and total mould-yeast counts of Erzurum cheese halva samples varied between 4.37-5.83, 1.71-4.17, 4.35-6.76 and 3.23-4.81 log cfu/g, respectively during of 60 days storage at different temperature (Table 2). There was a significant increase in the TAMB, TAPB, LAB and yeast/mould counts of experimentally produced cheese halva during storage period at +4℃ and room temperature, both air and vacuum packing ($p<0.05$). When the microbial counts of samples differently packaged at the same temperature were examined, it was determined that vacuum packaging extended the shelf life of the product. It had no effect on the storage time of cheese halva stored at -18℃ (Table 2).

The results of the chemical and physicochemical analyses of Erzurum cheese halva during the storage period are given in Table 3. The dry matter content, fat content, pH, titratable acidity, and aw values of the analyzed samples varied between 74.16 -79.98 g/100 g, 22.50-30.50 g/100 g, 3.55-5.55, 0.22-0.42 g/100 g, 0.9329-0.9616, respectivly during of 60 days storage at diffrent temperature.

Table 2. Microbiological properties of Erzurum cheese halva samples during the storage period (log cfu/g)

	Packaging-Storage temperature	Storage time (day)						
		1	5	10	15	30	45	60
TAMB	-18 VP	4.47±0.27	4.52±0.08c	4.54±0.20c	4.15±0.12c	4.58±0.12b	4.54±0.05a	4.39±0.06
	-18 AP	4.52±0.15	4.64±0.14bc	4.59±0.38c	4.28±0.23c	4.65±0.10b	4.60±0.06b	4.46±0.10
	+4 VP	4.37±0.20	4.73±0.29bc	4.85±0.14bc	5.17±0.02b	5.06±0.17a	5.24±0.13a	
	+4 AP	4.45±0.12	4.80±0.01bc	5.16±0.02b	5.83±0.16a			
	RT-VP	4.56±0.16	4.88±0.07b	5.65±0.18a				
	RT-AP	4.73±0.28	5.52±0.20a					
	p		***	***	***	**	***	
TAPB	-18 VP	1.71±0.22	1.88±0.06b	2.45±0.36bc	2.28±0.06d	2.33±0.10b	2.78±0.15b	3.00±0.09
	-18 AP	1.86±0.10	1.86±0.10b	2.95±0.10a	2.58±0.25c	2.45±0.36b	2.80±0.14b	3.05±0.17
	+4 VP	1.79±0.21	2.12±0.38b	3.88±0.12a	3.95±0.19b	3.72±0.45a	3.24±0.10a	
	+4 AP	1.89±0.05	2.75±0.28a	3.11±0.19a	4.17±0.10a			
	RT-VP	1.83±0.14	2.02±0.20b	2.18±0.05b				
	RT-AP	1.88±0.07	2.05±0.26b					
	p		**	***	***	**	*	
LAB	-18 VP	4.85±1.18	4.72±0.29b	4.85±0.14c	4.84±0.31c	4.72±0.37b	4.84±0.24b	5.10±1.48
	-18 AP	4.93±1.56	4.63±0.37b	4.79±0.48c	4.72±0.33c	4.86±0.24b	4.80±0.13b	4.94±0.59
	+4 VP	4.82±1.10	4.78±0.42b	5.84±0.54ab	6.32±0.12a	6.56±0.93a	5.25±0.86a	
	+4 AP	4.35±3.19	4.68±0.25b	5.66±0.10b	5.95±0.44b			
	RT-VP	4.73±2.61	4.92±0.31b	6.18±0.25a				
	RT-AP	4.89±1.18	5.54±0.10a					
	p		**	***	***	**	**	
Total Mould/ Yeast	-18 VP	3.27±0.12	3.23±0.10d	3.32±0.16b	3.69±0.27b	3.32±0.16	4.21±0.11b	4.39±0.06
	-18 AP	3.31±0.13	3.35±0.09d	3.41±0.05b	3.42±0.06b	3.41±0.05	4.25±0.08b	4.46±0.10
	+4 VP	3.30±0.10	3.48±0.07cd	3.59±0.08b	3.60±0.16b	3.59±0.08	4.81±0.42a	

+4 AP	3.36±0.09	3.71±0.18bc	4.35±0.19a	4.20±0.36a		
RT-VP	3.40±0.24	3.89±0.30b	4.41±0.20a			
RT-AP	3.56±0.22	4.35±0.19a				
p		***	**	**		**

-18 VP: vacuum packaging and -18 AP: aerobic packaging Erzurum cheese halva stored at -18°C; +4 VP: vacuum packaging and +4 AP: aerobic packaging Erzurum cheese halva stored at +4°C; RT-VP: vacuum packaging and RT-AP: aerobic packaging Erzurum cheese halva stored at room temperature

: in the same column indicates significant differences (:p<0.05; **:p<0.01; ***:p<0.001) between different packaging methods and storage temperature Erzurum cheese halva for each parameter at fixed storage time.

It was observed that acidity increased and consumability decreased in the vacuum-packed samples stored at +4°C. The LAB counts of the vacuum packaged samples than the aerobically packaged samples showed a greater increase during the storage period, but a decrease occurred in the vacuum packaged sample after the 30th day of storage. There was a decrease in the counts of LAB due to the increase in acidity in the cheese halva samples. Similarly, was reported in the study by Akarca et al., (2015) [19] study comparing different packaging methods for cheese, they reported that the acidity in vacuum-packaged samples increased after a certain day of storage.

Physical, chemical and microbiological hazards in traditional foods; it can also occur during packaging and storage stages besides manufacturing stage [20]. No study was found in the literature reviews to determine the effect of packaging method and storage temperature will affect on the microbiological, chemical and sensory properties of Erzurum cheese halva. However, it has been reported that the packaging method and storage time affect the microbiological, chemical and sensory properties of the Erzurum Civil Cheese, one of the main components of Erzurum cheese halva [21]. Moreover, it is stated that vacuum packaging is one of the effective preservation methods in preserving the microbiological quality and sensory properties of the civil cheese [21-22].

Table 3. The chemical and physicochemical properties of Erzurum cheese halva samples during the storage period

	Packaging-Storage temperature	Storage time (day)						
		1	5	10	15	30	45	60
pH	-18 VP	3.55±0.15b	4.13±0.15c	4.22±0.07d	4.49±0.04b	4.56±0.09c	4.68±0.04c	4.86±0.10b
	-18 AP	3.93±0.14a	4.19±0.08c	4.35±0.10dc	4.68±0.24b	4.80±0.14b	4.93±0.11b	5.10±0.05a
	+4 VP	3.87±0.33ab	4.53±.13b	4.53±0.28c	5.18±0.08a	5.32±0.06a	5.55±0.09a	
	+4 AP	3.90±0.16a	4.56±0.12b	5.14±0.04b	5.44±0.26a			
	RT-VP	3.72±0.12b	4.57±0.16b	5.32±0.07ab				
	RT-AP	3.68±0.18b	4.75±0.05a					
	p	*	**	***	***	***	***	*
Titratable Acidity (% LA)	-18 VP	0.22±0.05	0.23±0.02c	0.24±0.01d	0.25±0.01d	0.28±0.02b	0.31±0.01b	0.31±0.02
	-18 AP	0.27±0.05	0.24±0.03c	0.23±0.02dc	0.24±0.01bc	0.28±0.02b	0.42±0.04a	0.34±0.02
	+4 VP	0.24±0.02	0.26±0.02bc	0.27±0.02bc	0.29±0.03b	0.33±0.03a	0.34±0.06b	
	+4 AP	0.22±0.04	0.28±0.03ab	0.29±0.03b				
	RT-VP	0.27±0.03	0.29±0.03ab	0.33±0.02a	0.36±0.04a			

	RT-AP	0.25±0.04	0.32±0.04 a					
	p		**	***	***	*	**	
aw	-18 VP	0.9511±0.03	0.9329±0.01	0.9477±0.05	0.9614±0.01	0.9549±0.04	0.9417±0.52	0.9488±0.01
	-18 AP	0.9396±0.02	0.9624±0.04	0.9495±0.05	0.9581±0.04	0.9432±0.06	0.9416±0.11	0.9442±0.03
	+4 VP	0.9495±0.03	0.9392±0.03	0.9537±0.02	0.9445±0.18	0.9461±0.03	0.9448±0.01	
	+4 AP	0.9468±0.05	0.9429±0.09	0.9462±0.07	0.9409±0.23			
	RT-VP	0.9584±0.42	0.9616±0.08	0.9445±0.03				
	RT-AP	0.9463±0.07	0.9599±0.01					
Dry Matter (%)	-18 VP	79.51±4.83	78.91±1.79	79.44±1.08a	79.98±2.15	76.13±1.41	77.81±0.82	78.78±1.10
	-18 AP	78.25±2.73	75.76±0.60	74.78±0.31bc	76.77±2.41	74.71±4.63	74.33±2.73	74.32±1.39
	+4 VP	77.31±2.13	79.35±1.33	76.44±1.36b	75.60±4.53	79.16±0.52	76.28±0.85	
	+4 AP	76.23±5.27	74.45±6.27	74.99±0.46c	74.16±4.02			
	RT-VP	78.14±2.30	76.57±1.33	75.54±0.66b				
	RT-AP	76.64±3.87	75.15±9.46					
Fat (%)	-18 VP	27.50±1.71	26.50±0.71	29.50±0.71	30.50±2.12	27.50±2.12	29.50±0.71	28.00±1.41
	-18 AP	26.75±1.06	26.00±2.83	27.00±1.41	29.50±0.71	27.50±0.71	28.50±0.71	29.50 ±1.41
	+4 VP	27.00±1.41	29.00±1.41	29.00±1.41	29.00±2.83	29.00±1.41	30.05±1.48	
	+4 AP	22.50±4.95	30.50±2.12	31.00±5.66	26.50±0.71			
	RT-VP	26.50±3.54	26.50±0.71	27.00±1.41				
	RT-AP	27.00±1041	28.50±2.12					

-18 VP: vacuum packaging and -18 AP: aerobic packaging Erzurum cheese halva stored at -18°C; +4 VP: vacuum packaging and +4 AP: aerobic packaging Erzurum cheese halva stored at +4°C; RT-VP: vacuum packaging and RT-AP: aerobic packaging Erzurum cheese halva stored at room temperature

* in the same column indicates significant differences (*:p<0.05; **:p<0.01; ***:p<0.001) between different packaging methods and storage temperature Erzurum cheese halva samples for each parameter at fixed storage time.

The change in color values of Erzurum cheese halva over the storage period is detailed in Table 4. According to TPE (2021) [7], Erzurum cheese halva should be made available for sale in quantities matching demand and packaged in accordance with established food packaging standards. In the meantime, it has also been stated that it should be stored at +4°C for a maximum of 10 days, and if longer storage is necessary, it should be stored by freezing. In our research, the primary factors contributing to the degradation of aerobically packaged cheese halva samples stored at room temperature and +4°C are mold growth and color deterioration. Mold development not only impacts the appearance but also compromises the aroma of the product.

Table 4. Color parameters of Erzurum cheese halva samples during the storage period

	Packaging-Storage temperature	Storage time (day)						
		1	5	10	15	30	45	60
L*	-18 VP	42.26±0.20	44.90±1.45	45.43±3.14	49.21±1.91	50.96±2.54	51.81±4.66	52.09±2.70
	-18 AP	42.29±0.29	44.78±2.21	46.12±0.72	50.36±4.44	51.11±1.95	52.11±3.95	52.78±3.75
	+4 VP	42.58±0.35	43.45±1.71	45.08±1.18	50.21±1.91	56.01±3.45	58.68±3.88	
	+4 AP	42.19±0.02	45.00±2.86	48.11±0.27	50.85±2.52			
	RT-VP	42.18±1.05	45.33±2.02	49.27±0.31				
	RT-AP	41.99±1.36	47.56±1.47					
a*	-18 VP	6.05±0.09	7.02±0.15	7.65±0.39	7.90±0.34	7.34±0.30	7.01±1.42	6.67±0.30
	-18 AP	6.01±0.17	7.12±0.09	7.62±2.34	7.92±0.26	7.13±0.43	6.89±1.29	6.49±0.33
	+4 VP	6.08±0.70	7.33±0.11	7.62±0.56	7.86±2.16	7.22±0.10	6.79±2.20	
	+4 AP	6.17±0.37	7.37±0.42	7.75±1.09	7.95±0.13			
	RT-VP	6.09±0.27	7.38±0.05	7.70±0.25				
	RT-AP	6.02±0.72	7.49±0.08					
b*	-18 VP	23.21±0.10	24.04±0.32	24.94±0.80	25.35±0.65	24.66±0.39	24.41±0.43	24.13±0.80
	-18 AP	23.32±0.29	24.24±1.21	24.95±0.23	25.29±0.52	24.70±2.37	24.17±1.26	24.04±0.22
	+4 VP	23.30±0.10	24.06±0.18	25.10±0.28	25.13±0.49	24.31±0.86	24.16±0.76	
	+4 AP	23.53±0.64	24.49±1.27	24.74±0.54	25.02±0.90			
	RT-VP	23.46±0.02	24.22±1.59	24.70±0.24				
	RT-AP	23.55±0.13	24.11±0.57					

-18 VP: vacuum packaging and -18 AP: aerobic packaging Erzurum cheese halva stored at -18°C; +4 VP: vacuum packaging and +4 AP: aerobic packaging Erzurum cheese halva stored at +4°C; RT-VP: vacuum packaging and RT-AP: aerobic packaging Erzurum cheese halva stored at room temperature

The results of the sensory analyses of Erzurum cheese halva made in the storage period are given in Figure 2.

Erzurum cheese halva has a fibrous structure due to the fresh and unsalted nature of Erzurum civil cheese. The cheese in the halva displays a uniformly stringy texture and readily disintegrates upon tasting, creating a pleasant mouthfeel. [7]. In sensory tests conducted to determine the effect of storage temperature and packaging on cheese halvas, panelists scored the appearance and structure properties of vacuum-packaged samples lower than aerobic packaged samples. Vacuum packaging negatively affects the fibrous structure of the product and reduces the overall acceptability of the product.

While vacuum packaged Erzurum Cheese Halva was not liked by the panelists, Cambaztepe et al. (2009) [21] reported that vacuum packaged civil cheese samples were preferred by consumers. When civil cheese is vacuum packaged, there is no change in the structure of the cheese. However, during the production of Erzurum cheese halva, civil cheese transforms into a thinner fibrous structure, and the vacuum packaging process negatively affects this distinct fibrous structure. This situation causes negative perception in consumer preference.

Vacuum packaging is a method often used to prevent moldiness in products [23]. In our study, it was not observed moldiness in vacuum-packaged samples. However, the most obvious cause of deterioration in vacuum packaged products stored at room temperature and +4°C was determined to be acidification. However, although no microbial deterioration was observed in vacuum-packed cheese halva samples at -18°C, some changes in their textural properties were observed. Our results showed that vacuum packaging can't guarantee the complete acceptability of the product for the consumer.

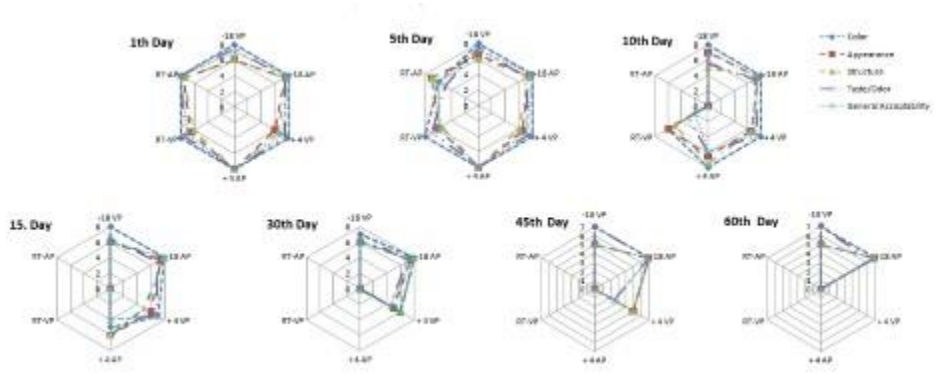

Figure 2. Changesin the sensory parameters of Erzurum cheese halva samples during the storage period

The results of the chemical, physicochemical and microbiological analyses of cheese halvas obtained from the market are given in Table 5 and 6.

When the microbiological analysis results of the experimentally produced cheese halva samples and the cheese halvas sold in the local markets were examined, it was found that both the TAMB and yeast/mould counts were higher in the cheese halva samples sold in the local market (Table 2 and Table 5). These results show that the necessary hygiene conditions are not complied with during the production, storage and marketing of Erzurum cheese halva sold in the Erzurum local markets. This situation is thought to pose some public health risks. Likewise, Urçar Gelen and Ceylan (2020) [24] highlighted in their study that Erzurum civil cheese, a key ingredient in cheese halva, is often not produced under hygienic conditions by local producers.

The increase in halva diversity has been influenced by the use of cheeses produced in different ways in Anatolia [25]. Erzurum cheese halva is an important food for human nutrition because it contains high amounts of protein and fat [20]. It was determined that the dry matter, protein and fat contents of the cheese halva samples were high both produced experimentally and sold from the Erzurum local market (Table 1 and Table 6).

Table 5. Some microbiological analyses results of Erzurum cheese halva samples sold in local markets (log cfu/g)

Product Code1	A	B	C	D	E	p
TAMB	4.47±0.77c	6.99±0.19a	5.64±0.12b	5.24±0.37b	4.00±0.14c	**
TAPB	3.43±0.02a	3.14±0.41a	2.91±0.02c	3.56±0.01b	2.94±0.01c	**
Total Mould/ Yeast	3.69±0.09b	4.84±0.23a	4.77±0.15a	3.00±0.44c	2.74±0.04c	**
Coliform	3.00±0.74a	3.15±1.63a	2.77±0.33a	1.95±0.35b	1.95±0.05b	*

1: Erzurum Cheese Halva which purchased local market is given code.
p: in the same line indicates significant differences (*:p<0.05; **:p<0.01) between different Erzurum cheese halva for each parameter

Table 6. Some chemical and physicochemical analyses results of Erzurum cheese halva samples sold in local markets

Product Code1	A	B	C	D	E	p
Dry Matter (%)	85.21±0.68c	87.56±0.13b	78.92±2.21d	89.86±0.11a	89.61±0.66a	***
Ash (%)	1.52±0.24b	1.55±0.15b	1.45±0.65c	1.92±0.31a	1.85±0.22a	**
aw	0.87±0.001b	0.87±0.01b	0.94±0.001a	0.77±0.001c	0.67±0.02d	***
pH	4.48±0.2bc	4.69±0.1ab	4.30±0.5c	4.73±0.1a	4.59±0.1ab	**
Acidity (% L.A.)	0.077±0.005b	0.072±0.009b	0.12±0.014a	0.066±0.014bc	0.050±0.005c	***
Protein (%)	10.92±1.31b	13.75±0.94a	11.23±0.35a	14.57±1.24b	13.61±0.57a	*
Fat (%)	35.00±2.0b	44.00±1.50a	28.00±1.50c	44.00±2.00a	36.00±3.00b	***
Salt (%)	3.44±0.29d	2.29±0.23e	4.45±0.39c	6.88±2.29a	5.74±0.40b	***
L*	47.74±5.30b	51.44±20.30b	58.49±1.95a	48.74±1.74b	58.18±1.32a	*

Color	a*	6.54±0.72bc	5.92±0.68cd	5.23±0.84d	7.62±0.37ab	8.28±0.23a	**
Parameters	b*	24.49±0.68b	23.28±2.28b	24.49±1.63b	24.95±0.06b	31.17±0.44a	***

1: Erzurum cheese halva which purchased local market is given code.
p: in the same line indicates significant differences (*:p<0.05; **:p<0.01) between different Erzurum cheese halva for each parameter

4. Conclusion

The objective of this study was to determine appropriate packaging method and storage temperature for Erzurum cheese halva sold in the Erzurum local market. While vacuum packaging at -18℃ extends the shelf life of the product, the general appearance of the product deteriorates due to vacuum packaging, which negatively affects consumer perception. It was determined that the fibrous structure, which is the most important feature of this traditional product, was preserved in the product aerobic packaged at +4℃ storaged. However, it was determined that the storage period of the product could be maximum 15 days under these conditions. For this purpose, studies should be carried out on the suitability of packaging methods such as vacuum-packaging, modified atmosphere-packaging (MAP) and reducing atmosphere-packaging (RAP) for the product.

In future studies, it would be beneficial to investigate alternative packaging methods (e.g., modified atmosphere packaging) that could potentially preserve the properties of this traditional product for a longer period during storage.

References

[1]. Guerrero L., Dolors Guàrdia M., Xicola J, Verbeke W., Vanhonacker F., Zakowska-Biemans S., Sajdakowska M., Sulmont-Rossé C., Issanchou S., Contel M., Scalvedi M.L., Signe Granli B., Hersleth M. Consumer-driven definition of traditional food products and innovation in traditional foods. A qualitative cross-cultural study. Appetite, 52 (2), (2009), 345-354.

[2]. Kocatepe D., Tırıl A.. Sağlıklı beslenme ve geleneksel gıdalar. Journal of Tourism and Gastronomy Studies, 3(1), (2015), 55-63.

[3]. Belc N., Smeu I., Macri A., Vallauri D., Flynn K. Reformulating foods to meet current scientific knowledge about salt, sugar and fats. Trends in Food Science & Technology, 84, (2018), 25-28.

[4]. Fernández-Ferrín P., Calvo-Turrientes A., Bande B., Artaraz-Miñón M., Galán-Ladero M. M. The valuation and purchase of food products that combine local, regional and traditional features: The influence of consumer ethnocentrism. food quality and preference. Food Quality and Preference, 64, (2018), 138-147.

[5]. Altuntaş A., Gülçubuk B. Yerel kalkınmada yaygınlaşan bir araç olarak geleneksel gıdalar ve geleneksel gıda mevzuatının yaygınlaştırılabilirliği. Journal of Agricultural Faculty of Gaziosmanpaşa University, 31(3), (2014), 2-80.

[6]. Seçim Y., Uçar G. Evaluation of the desserts; which are hosmerim, cheese halva, kunafah produced in Turkish cuisine -in aspect of tourism. International Journal of Social Sciences and Education Research, 3(5), (2017), 1478-1484.

[7]. Türk Patent Enstitüsü, Erzurum Peynir Helvasının Cİ Tescil Belgesi, Tescil No:806,16.07.2021. Available at:https://www.ci.gov.tr/.

[8]. Çakmakçı S., Salık M. A. Erzurum'un coğrafi işaret tescili almış ürünleri: Güncel bir bakış ve öneriler. ATA-Gıda Dergisi, 1(2), (2022), 1-12.

[9]. Türk Patent Enstitüsü, Erzurum Civil Peynirinin Cİ Tescil Belgesi, Tescil No:116, 2009. Available at:https://www.ci.gov.tr/.

[10]. Kuşat N. Sürdürülebilir işletmeler için kurumsal sürdürülebilirlik ve içsel unsurları. Afyon Kocatepe Universitesi İktisadi ve İdari Bilimler Fakültesi Dergisi, 14(2), (2012), 227-242.

[11]. Halkman A. K. Gıda Mikrobiyolojisi Uygulamaları. Ankara: Başak Matbaacılık ve Tanıtım Hizmetleri, 2005.

[12]. Temiz A. Genel Mikrobiyoloji Uygulama Teknikleri. 5th ed. Ankara: Hatiboğlu Yayınevi; 2010.

[13]. AOAC. Official Methods of Analysis. 18th ed. Gaithersburg: Association of Official Analytical Chemists, 2007.

[14]. ISO 3433:2008 (IDF 222: 2008). Cheese-Determination of Fat Content-Van Gulik Method; International Standard Organization: London, UK, 2008.

[15]. Metin M., Öztürk G. F. Süt ve Mamulleri Analiz Yöntemleri. İzmir: Ege Üniversitesi Basımevi, 2012.

[16]. León K., Mery D., Pedresci D., Leon J. Color measurement in L*a*b* units from RGB digital images. Food Research International, 39(10), (2006), 1084-1091.

[17]. Hunt R. W. G., Pointer M. R. "Colour vision," in Measuring Colour, R. W. G. Hunt and M. R. Pointer, Ed. 4th ed. New Jersey: John Wiley & Sons, Incorporated; 2011, pp.1-17.

[18]. Şengül M., Ertugay M. F. Microbiological and chemical properties of Cheese Helva produced in Turkey. International Journal of Food Properties, 9(2), (2006), 185-193.

[19]. Akarca G., Tomar O., Gök V. Different packaging for sliced Mozzarella Cheese. Journal of Food Processing and Preservation, 39, (2015), 2912-2918.

[20]. Lücke F. K., Zangerl P. Food safety challenges associated with traditional foods in German-speaking regions. Food Control. 43, (2014), 217-230.

[21]. Cambaztepe F., Cakmakci S., Dagdemir E. Effect of some technological parameters on microbiological, chemical and sensory qualities of Civil cheese during ripening. International Journal of Dairy Technology, 62(4), (2009), 541-548.

[22]. Yardimciel Ü., Güven M. Çeçil peynirinin özellikleri üzerine pastörizasyon işleminin ve salamura tuz oranının etkileri. Çukurova Üniversitesi Fen ve Mühendislik Bilimleri Dergisi, 26 (2), (2011), 145-154.

[23]. Sengun I., Yaman D., Gonul S. Mycotoxins and mould contamination in cheese: a review. World Mycotoxin Journal, 1(3), (2008), 291-298

[24]. Urçar Gelen S., Ceylan Z. G. The existence of Enterococcus spp. in Civil Cheese. Turkish Journal of Agriculture - Food Science and Technology, 8(12), (2020), 2574-2576.

[25]. Ulu E. K. Türk mutfak kültüründe peynir tatlıları. Aydın Gastronomy, 3(1), (2019), 37-42.

MANAS Journal of Engineering
ISSN 1694-7398 | e-ISSN 1694-7398

Volume 12, Issue 1, (2024) Pages 145-156
https://doi.org/10.51354/mjen.1477354

Synthesis and characterization of chitosan ethers: Hydroxypropyl chitosan and Hydroxyethyl chitosan

Nuran Çelikçi[1*], Cengiz Ayhan Zıba[2], Mustafa Dolaz[3,4], Mehmet Tümer[5]

[1]Department of Material Science and Engineering, Institute of Science and Technology, Kahramanmaras Sutcu Imam University, Kahramanmaras, Turkey, nurancelikci@gmail.com,
[2]Department of Chemical Technologies, Afsin Vocational School, Kahramanmaras Sutcu Imam University, Kahramanmaras, Turkey
[3]Department of Environmental Engineering, Faculty of Engineering, Kyrgyz-Turkish Manas University, Bishkek, Kyrgyz Republic
[4]Department of Environmental Engineering, Faculty of Engineering and Architecture, Kahramanmaras Sutcu Imam University, Kahramanmaras, Turkey
[5]Chemistry Department, Faculty of Science, Kahramanmaras Sutcu Imam University, Kahramanmaras, Turkey

ABSTRACT

The hydroxypropyl chitosan (HPCH) and hydroxyethyl chitosan (HECH) are multifunctional chitosan derivatives with biocompatible and biodegradable properties. Due to their hydroxypropyl and hydroxethyl groups, they have water solubility, moisture retention, and gelling properties. In this study, the chitosan derivatives HPCH and HECH were obtained in two steps alkalisation and etherification. For alkalisation, chitosan was kept in an alkaline medium at -18 □C for 7 days. For etherification; the reaction was carried out for 48 hours by mixing alkaline chitosan with propylene oxide and ethylene oxide separately in a pressure reactor. The structures of the obtained HPCH and HECH were characterised by FT-IR, 1H(13C)-NMR, XRD, and TG analysis methods. Since the degree of deacetylation (DA) of chitosan is 75-85%, the chitosan units contain N-acetyl (-N-(CO)-CH3)) groups in addition to -NH2 functional groups. When the 1H(13C)-NMR spectrum of chitosan was examined, the peak value of these acetyl groups was observed at δ1.89 ppm. When the XRD spectra were examined, it was observed that the strong peak in chitosan at 2θ=20° was weakened in HPCH and HECH. In addition, the thermal stability of HPCH and HECH was found to be higher than chitosan in TG analysis.

ARTICLE INFO

Research article

Received: 02.05.2024
Accepted: 14.06.2024

Keywords:

Etherification, Hydroxyethyl Chitosan, Hydoxypropyl Chitosan, NMR

**Corresponding author*

1. Introduction

Chitosan is a natural cationic biopolymer composed of unbranched chains containing both D-glucosamine (deacetylated units) and N-acetyl-D-glucosamine (acetylated units) randomly linked by β (1-4) glycosidic linkages [1-2]. It is obtained by the deacetylation of chitin in some or all acetyl groups using an inorganic base at high temperatures and concentrations (Figure 1) [3]. Chitosan is an amphiphilic natural polysaccharide with excellent physical and biological properties, including biocompatibility, biodegradability, and non-toxicity [4].

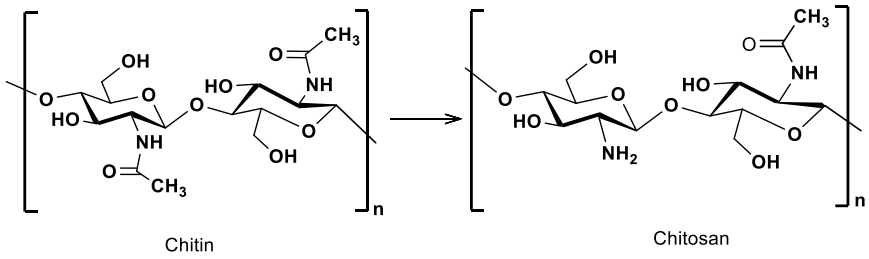

Figure 1. Chemical structure of chitin and chitosan

Chitosan is insoluble in water (pH ~7) due to the presence of amino groups (-NH_2) in its structure, but soluble in nearly all aqueous acidic solutions or mineral acids below pH=6.5 [5]. The presence of these groups makes chitosan a cationic biopolymer [6]. Its applications are limited due to its poor solubility in neutral and basic environments, low porosity, and low mechanical properties [7]. Chitosan derivatives are obtained by incorporating the reactive amino and hydroxyl groups in the structure of chitosan into the structures of molecules, i.e. by chemical modification of chitosan. Hence, the water solubility, biological activities, and mechanical properties of chitosan can be improved [8]. Modification can be achieved by physical or chemical processes such as grafting, cross-linking, composites, incorporation of substituents, etc. [9]. Chitosan and its derivatives are known for their biocompatibility [10], biodegradability [11], antimicrobial and antioxidant properties [12], and anti-tumor activity [13]. They are also hydrophilic, non-toxic, and low-cost, which makes them suitable for various applications in the food industry, biotechnology, biomedical and pharmaceutical industries, cosmetics, and tissue engineering [11, 14-17]. In addition, the extensive use of chitosan in 3D bioprinting applications for tissue regeneration or drug delivery systems is currently being investigated [18-19]. HPCH a kind of water-soluble functional derivative of CH, is obtained by etherification through propylene oxide under alkaline conditions [20-21]. It is used in wound dressings, medical carriers, and tissue engineering due to its biodegradability, non-toxicity, antimicrobial activity, and film-forming properties [22-25]. Compared to chitosan, HPCH exhibits superior properties in terms of hygroscopicity and adsorption [25]. Furthermore, HPCH was found to have higher moisture retention and a better antibacterial effect than chitosan [26]. As another important chitosan derivative, HECH has a multifunctional one that dissolves well in water and has biocompatible and biodegradable properties [27]. It is obtained by reacting chitosan and ethylene oxide under alkaline conditions.

Within the scope of this study, the chitosan derivatives HPCH and HECH were synthesized from chitosan. There are many studies about chitosan in the literature, but studies on HPCH and HECH, which are important derivatives of chitosan, are limited. Therefore, these derivatives were synthesized and their structures were characterized by spectroscopic methods (FT-IR, XRD, NMR), and the surface morphologies and thermal properties were investigated by SEM and DTA-TG analysis, respectively.

2. Materials and methods

Chitosan (degree of deacetylation 75-85%), Propylene oxide (PO, molecular weight 58.07 g/mol), Ethylene oxide (EO, molecular weight 44 g/mol), sodium hydroxide (NaOH) 99%, hydrochloric acid (HCl) 37%, glacial acetic acid (CH_3COOH), isopropyl alcohol (IPA), ethanol, methanol and acetone were obtained from Sigma Aldrich. All chemicals used in this research were of analytical grade.

2.1. Synthesis of the chitosan derivatives HPCH and HECH

The synthesis of HPCH was carried out according to [28] with some modifications. First, for alkalisation, 0.54 g (0.003mol) of chitosan was mixed with 10 mL of 40% NaOH and kept at -18 ^oC for 7 days. The alkalised chitosan was then brought to room temperature, and 20 mL of IPA was added and stirred for 30 minutes. The mixture was placed in a pressure reactor, 0.94 mL (0.013mol) of PO was added and the reaction was carried out at 40^oC for 48 hours. After 48 hours the solution was brought to room temperature, filtered, and neutralised with HCl, and the final solid was washed several times with anhydrous ethanol and dried at room temperature. The HPCH reaction is shown in Figure 1.

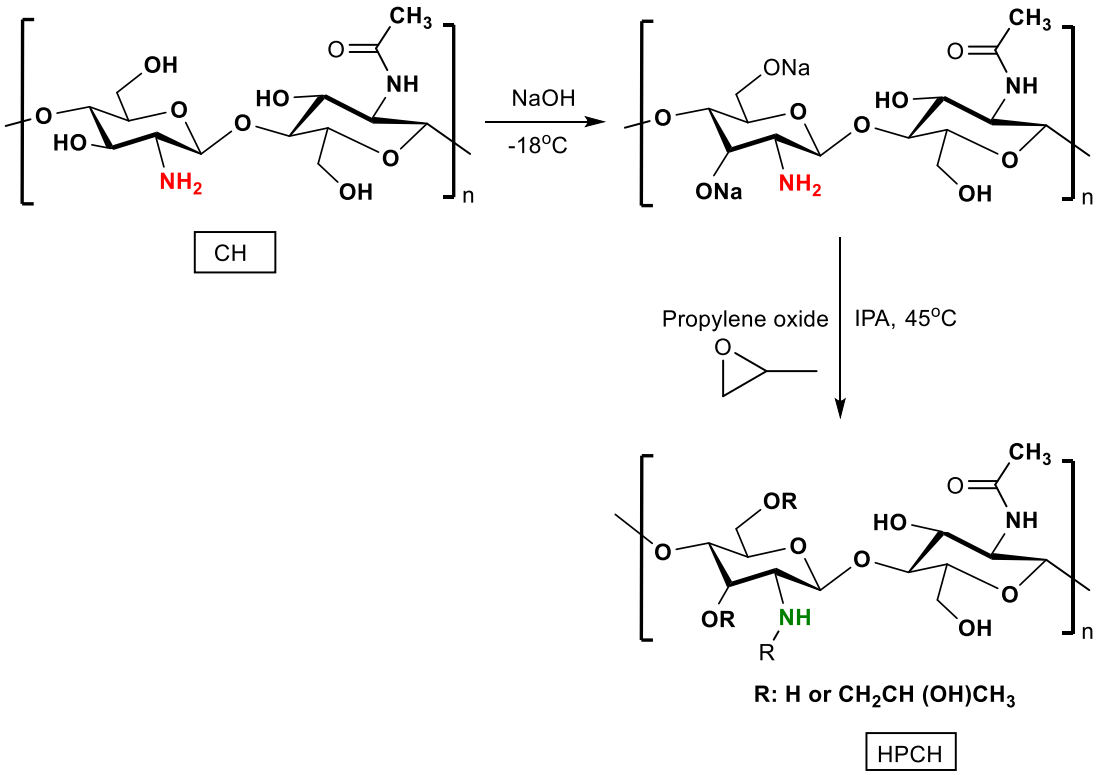

Figure 1. Synthesis reaction of HPCH

The synthesis of HECH was carried out according to [28] with some modifications. First, 0.50 g (0.003mol) of alkalised chitosan and 20 mL of IPA were stirred for 30 minutes. The mixture was placed in a pressure reactor, 0.67 mL (0.013mol) of EO was added and the reaction was carried out at 40°C for 48 hours. The solution was brought to room temperature, filtered, and neutralised with HCl, and the final solid was washed several times with anhydrous ethanol and dried at room temperature. The HPCH reaction is shown in Figure 2.

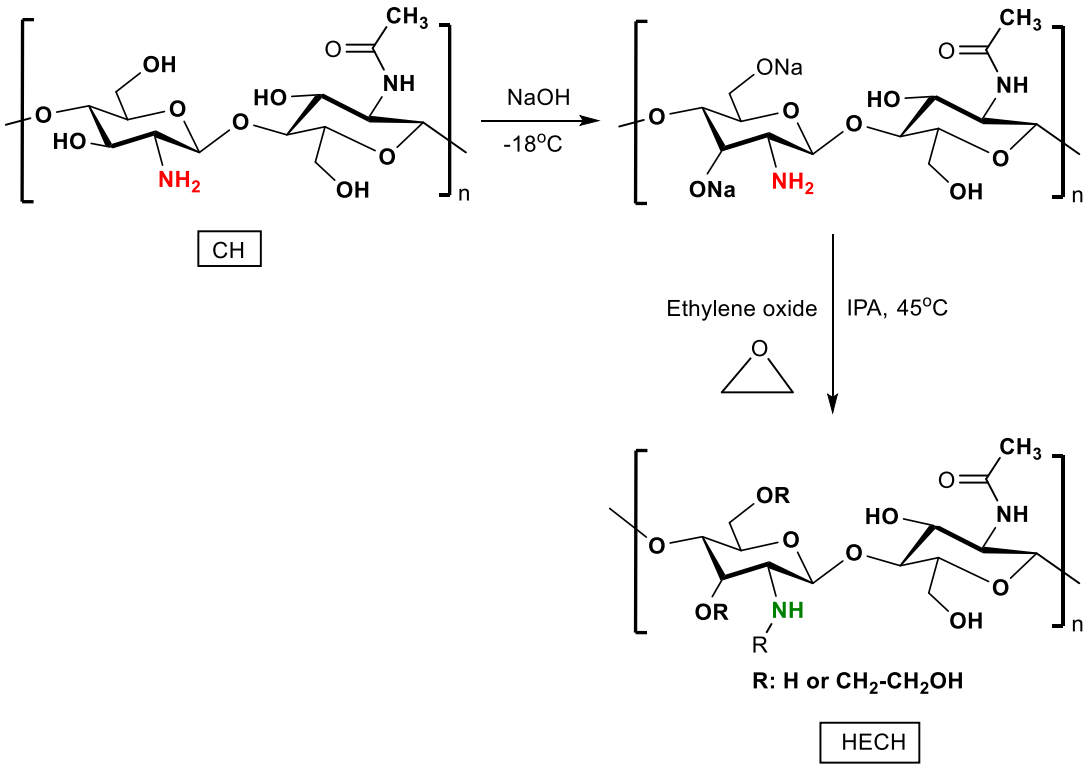

Figure 2. Synthesis reaction of HECH

2.2. Characterization

The morphology of the samples was characterized using a scanning electron microscope (SEM) (JEAL / NEOSCOPE JCM-5000) at EHT = 20 kV. Fourier Transform Infrared (FT-IR) spectra of the samples were recorded from 4000 to 400 cm^{-1} using a Perkin Elmer Spectrum 400 infrared spectrophotometer with ATR apparatus. $^{1}H(^{13}C)$-NMR spectra of the samples were recorded at 30 °C using a Bruker-200 MHz Varian spectrometer (90° pulse and 16 scans). The samples were dissolved in deuterium oxide (D_2O) at a concentration of 25-30 mg/600 µL. Chemical shifts were reported as ppm and the results were calibrated against the residual solvent signal of D_2O (δ 4.8 ppm) as an internal standard. X-ray diffraction (XRD) patterns of the samples were analyzed using an XRD diffractometer (Philips X'Pert PRO) operating with CuKα radiation, the voltage of 40 kV, and current of 30 mA at monochromatic radiation (λ=154060 nm). All samples were scanned from 10 °C to 90 °C at a scan speed of 5° 2θ /min with a step size of 0.02°. The thermal behavior of the samples was measured using a TG-DTA (SEIKO II, Seiko, Japan). The samples (15±5 mg) were placed in a ceramic dish and heated from 30 °C to 600 °C at a heating rate of 20 °C/min under a nitrogen atmosphere (20 mL/min).

3. Result and discussion

3.1. SEM of CH Derivatives

SEM analysis of chitosan involves examination of the surface morphology. SEM micrographs can reveal the structure and distribution of chitosan particles. As shown in Figure 3, the surface of chitosan was smooth and had no fibrous structure. The SEM micrographs of HPCH and HECH showed a rougher and grained surface with an increase in the pore structure of chitosan. This may be due to the hydroxypropyl and hydroxyethyl reactions of chitosan.

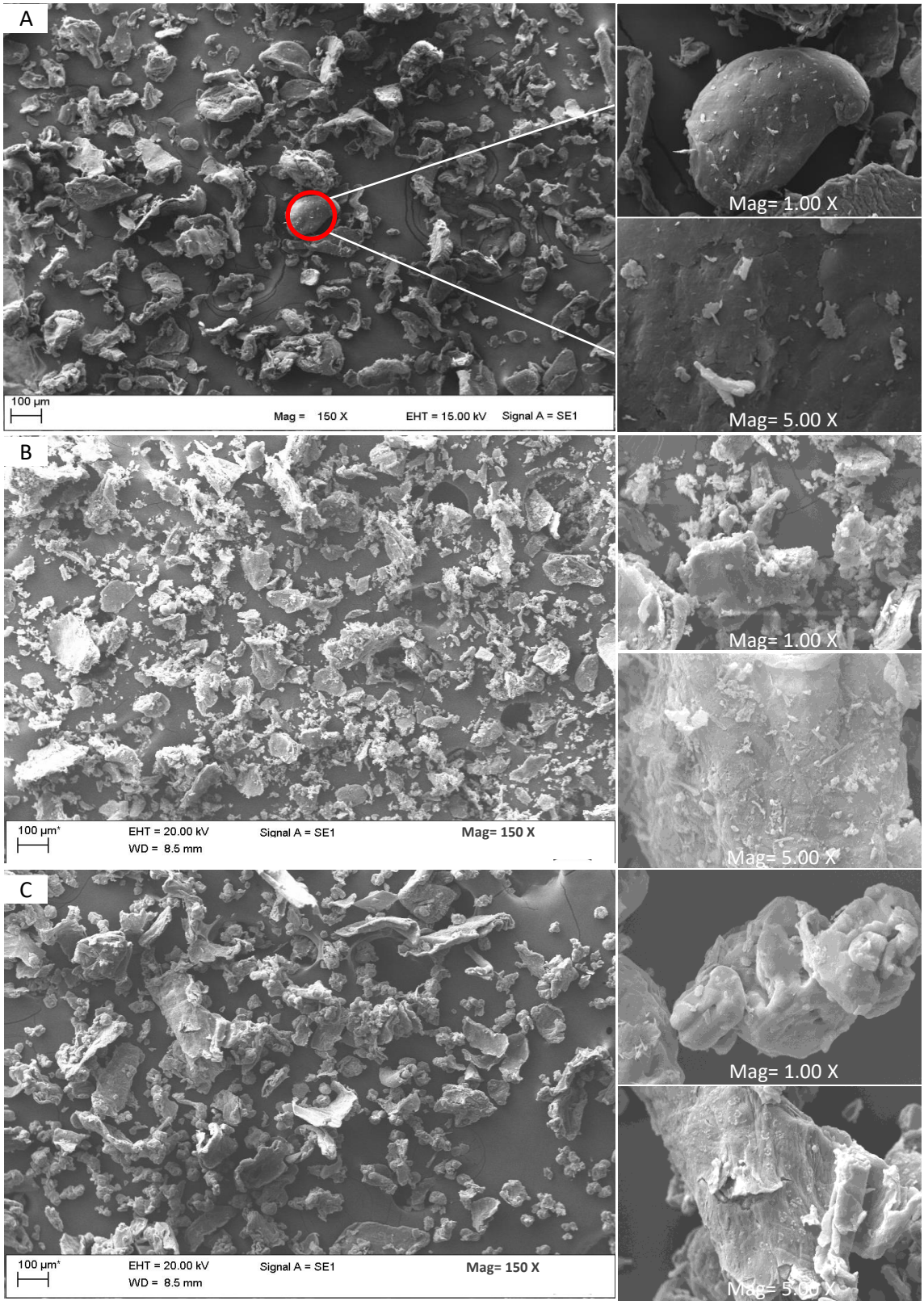

Figure 3. SEM images of CH (A), HPCH (B) and HECH (C) with a magnification of 150X, 1000X and 5000X

3.2. FTIR spectrums of CH Derivatives

FTIR spectra of CH, HPCH and HECH were shown in Figure 4. The broad bands at 3281-3386 cm^{-1} correspond to molecular hydrogen bonding and N-H and O-H vibrations [29]. A bands in the range of 2920-2868 cm^{-1} are due to the symmetric and asymmetric stretching of the amides. The band at 1643 cm^{-1} shows the C-O stretches of amides I and the band at 1325 cm^{-1} shows the C-N stretches of amides III. The peak at 1620 cm^{-1} is caused by the N-H bending of a protonated amine group ($-NH_2$). The peak at 1587 cm^{-1} corresponds to the N-H bending of amide I. The CH_2 bending and the CH_3 symmetric deformations were confirmed by the presence of bands at 1423 and 1371 cm^{-1}, respectively [30-31]. The band at 1149 cm^{-1} corresponds to the asymmetric stretching of the C-O-C bridge, and the bands at 1066 and 1024 cm^{-1} correspond to the stretching of the primary and secondary OH groups [23]. The small signal at 1256 cm^{-1} indicates the bending vibrations of the OH groups present in chitosan [32]. In the FT-IR spectrum of HPCH and HECH, the peak intensities at 2890 cm^{-1}, and 1423 cm^{-1} were increased ascribing to stretching vibration of C-H, indicating the presence of more methylene groups in the structure. The peaks at 1066 cm^{-1}, and 1024 cm^{-1} were notably increased due to the hydroxypropyl and hydroxyethyl groups being replaced by both hydroxyl groups and amino groups of CH [28].

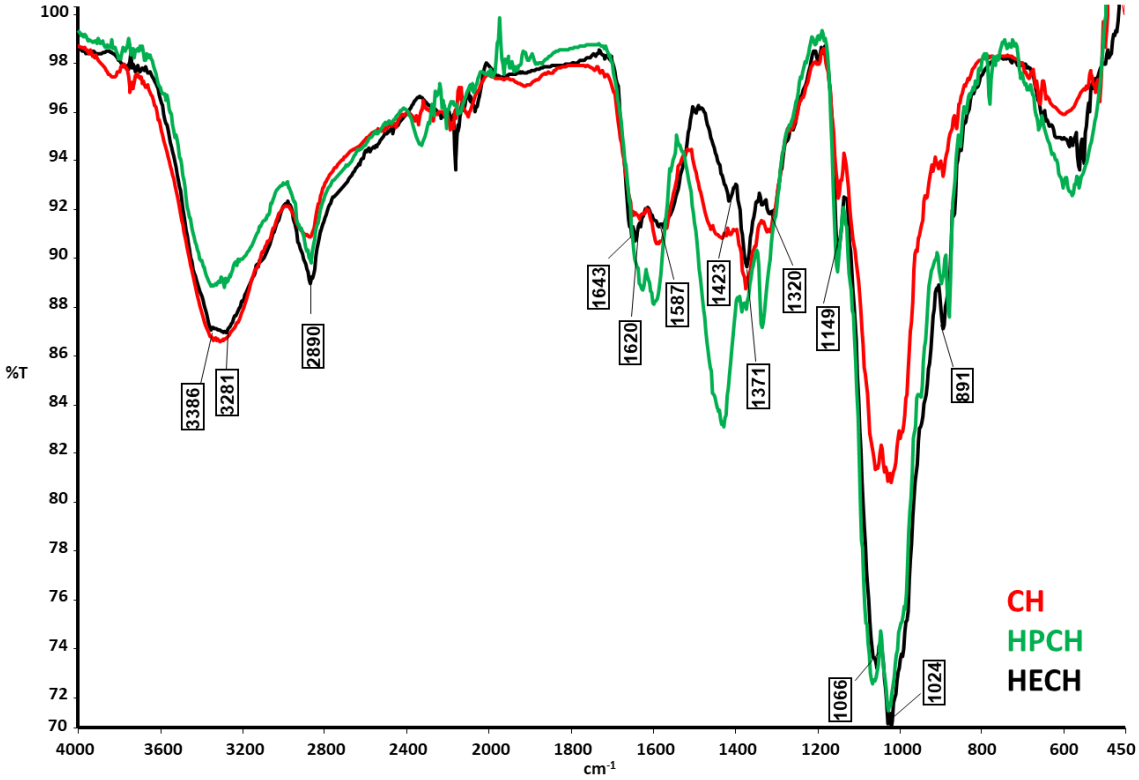

Figure 4. FTIR spectra of CH, HPCH and HECH

3.3. ^{1}H- NMR spectrum of CH Derivatives

The ^{1}H-NMR spectrum of CH was illustrated in Figure 5. The peak at δ 1.89 ppm is due to the H atoms of the acetyl group. As the deacetylation degree of the chitosan used is 75-85%, there are also significant amounts of N-acetyl ($-N-(CO)-CH_3$)) groups in the chitosan units, as well as $-NH_2$ functional groups. As a result of the deacetylation of chitin, it is not possible to obtain chitosan compounds with 100% removal of acetyl groups due to the polymeric structure. The peak at δ3.01 ppm belongs to the hydrogen (C2) of the glucosamine ring and the signals between δ3.56-3.74 ppm belong to the hydrogens at C4, 6, 3, 5 of the main chain in chitosan. The peak at 4.62 is attributed to hydrogen in OH groups [29, 33-36]. The peak at 4.81 ppm is due to hydrogen in the C1 group.

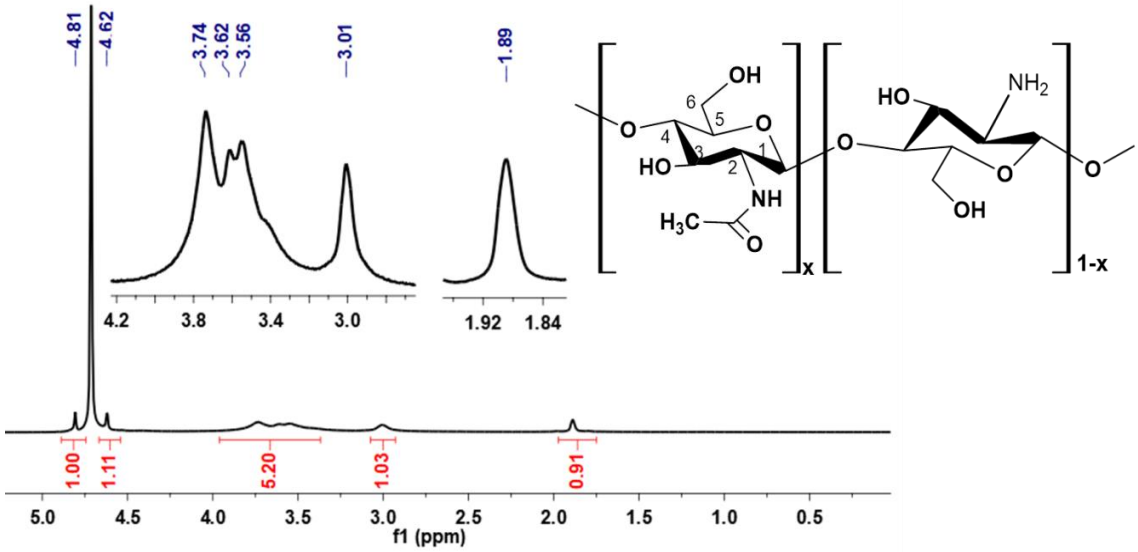

Figure 5. ^{1}H NMR of CH

The ^{1}H NMR spectrum of HPCH is given in Figure 6. The peak at δ1.13 ppm is attributed to the H protons of methyl group (H9). This is evidence that hydroxypropyl is incorporated into the chitosan ring [37-38]. Protons (H3-H8) of HPCH were observed at δ 3.36-3.91 ppm, and the peak at δ 2.03 ppm indicates the methyl hydrogen (H10) of N-acetylglucosamine. The peak at δ 2.68 ppm indicates the hydrogen (H2) of the glucosamine ring.

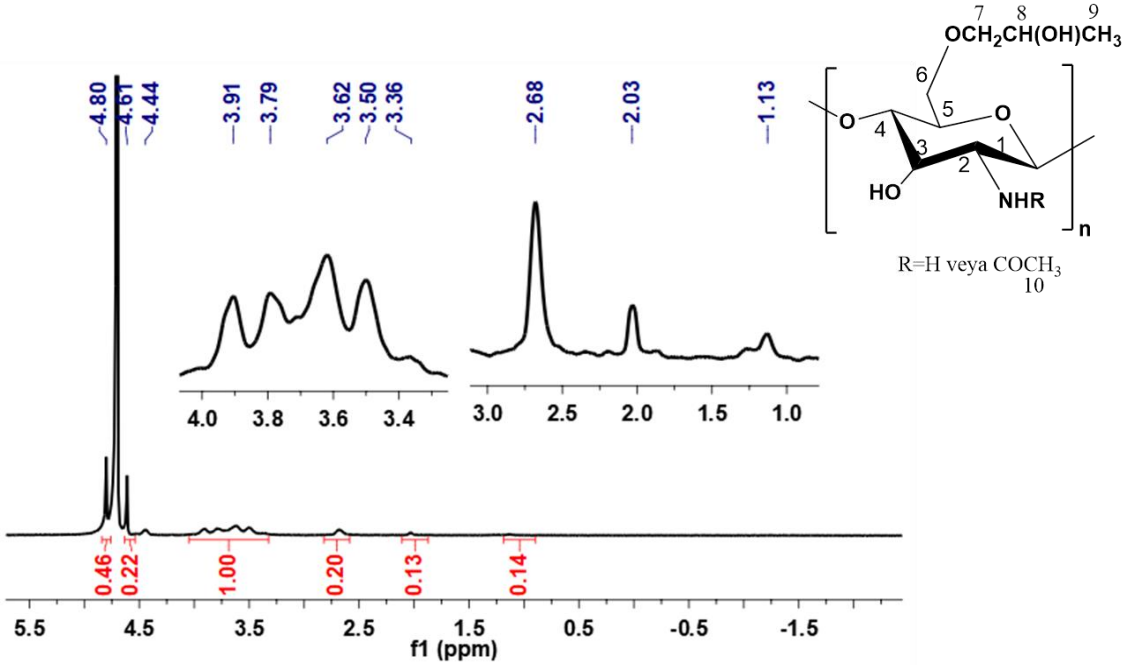

Figure 6. ^{1}H NMR of HPCH

The ^{1}H NMR spectrum of HECH is presented in Figure 7, the ring protons (H4,5,6) were considered to resonate between δ 3.91-3.30 ppm. The peak at δ 2.64 ppm indicates the hydrogen (C2) of the glucosamine ring.

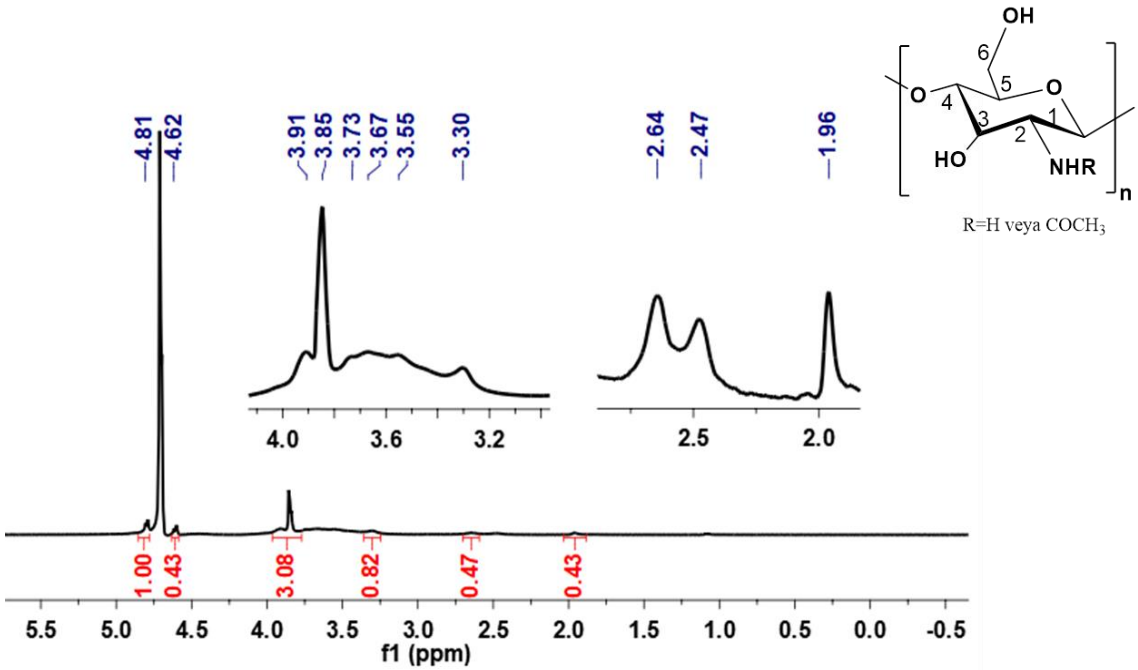

Figure 7. ^{1}H NMR of HECH

3.4. XRD spectrums of CH Derivatives

XRD patterns of CH, HPCH and HECH were shown in Figure 8. The specific peaks of chitosan are observed as 2θ=15° and 20° and these diffractions correspond to crystalline regions in chitosan [39]. This can be explained by the regularity in the polymer chain structure due to the strong intermolecular hydrogen bonds formed between the hydroxyl and amino groups present in chitosan. The strong peak at 2θ=20° in chitosan was weakened in HPCH and HECH. It can be seen that amorphous regions are replaced by a crystalline structure at 2θ=31° in HPCH, 2θ=27°, 31°, 45°, 56° and 66° in HECH. This can be explained by the incorporation of functional groups into the natural structure of chitosan as a result of the hydroxypropyl, and hydroxyethyl reactions.

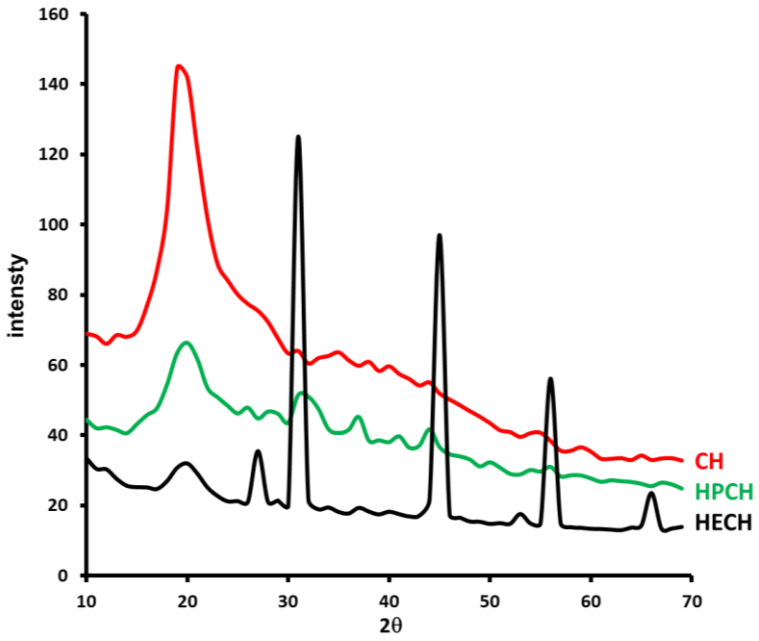

Figure 8. XRD pattern of CH, HPCH and HECH

3.5. TG-DTA spectrums of CH Derivatives

Thermogravimetric analysis (TGA) is used to study the thermal stability or thermal degradation behaviour where the weight loss of the sample is measured continuously. The thermal behaviours of CH, HPCH and HECH were given in Figure 9. CH and its derivatives showed two degradation stages: the first step was occurred around 100 °C and was assigned to the evaporation of the remaining water due to the strong affinity of polysaccharides to water. The initial weight loss at 100 °C was 6.4% in chitosan, 0.1% in HPCH, and 0.2% in HECH. Then, the weight of partially chitosan remained stable about 250 °C followed by a rapid substantial loss of weight [40-41]. The second step occurred around 310 °C in CH and the weight loss was 24.6 %. The second step occurred around 400 °C in HPCH and HECH and the weight loss was 51.0% and 51.1, respectively. The total weight loss at the final temperature (599.9 °C) was 67.9 % in CH. The total weight loss at the final temperature (599.9 °C) was 98.7% and 98.6 % in HPCH and HECH, respectively.

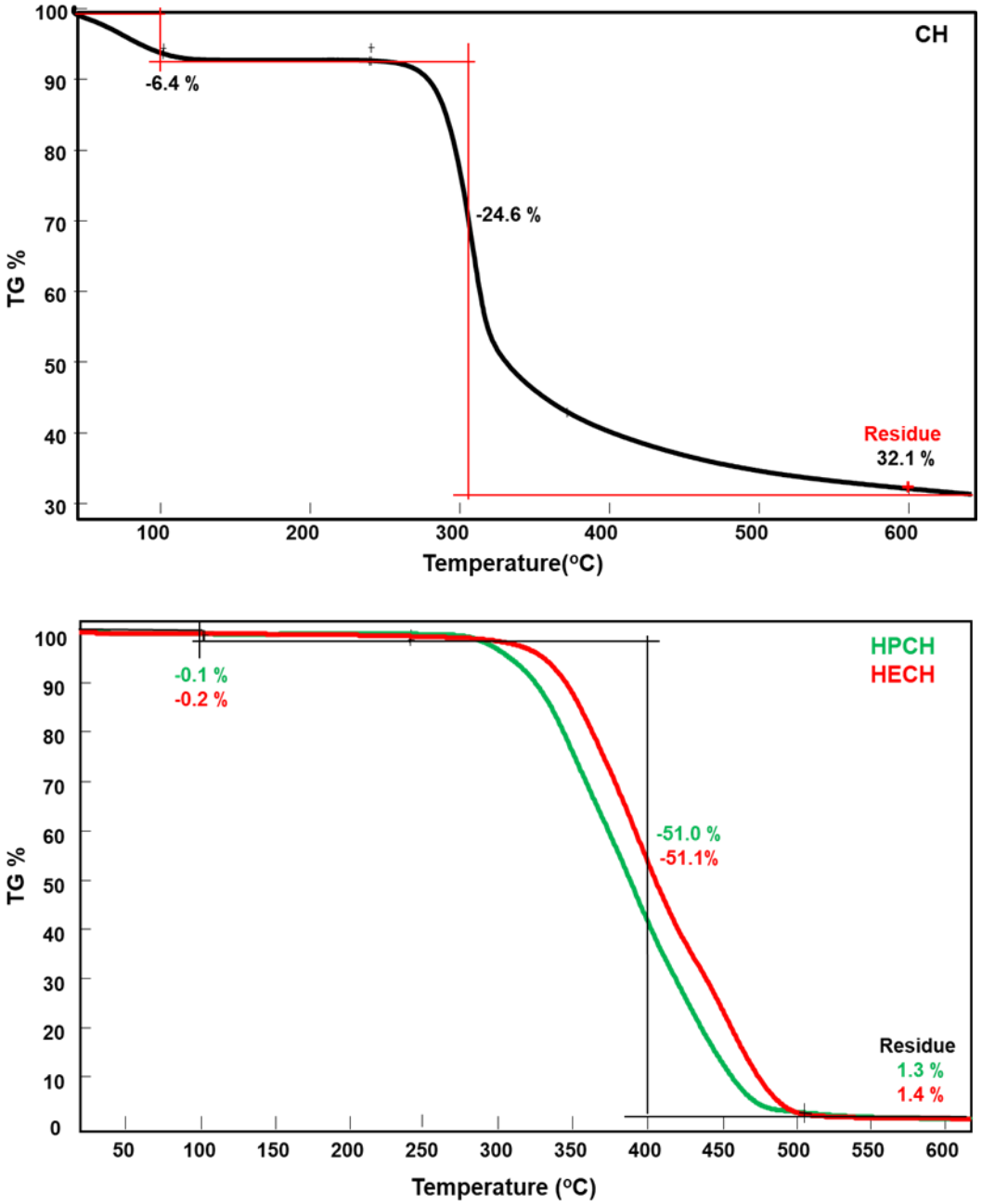

Figure 9. TG of CH, HPCH and HECH

Conclusion

This study successfully synthesized chitosan ethers: HPCH and HECH. Structures of synthesized chitosan derivatives were characterized by FT-IR, XRD, and ^{1}H-NMR spectroscopy, and the surface morphologies and thermal properties were investigated by SEM and DTA-TG analysis, respectively. Chitosan and its derivatives have become promising polymers in multidisciplinary fields due to their distinct properties such as biocompatibility, biodegradability, non-toxicity, and low reactivity. However, there are few studies in the literature on the synthesis of HPCH and HECH, which are important chitosan derivatives. Therefore, this study will contribute to the literature and science.

References

[1]. Antony, R., Arun, T., Manickam, S. T. D. "A review on applications of chitosan-based Schiff bases", International Journal of Biological Macromolecules, 129, (2019), 615-633.

[2]. Weng, J., Durand, A., Desobry, S. "Chitosan-based particulate carriers: structure, production and corresponding controlled release", Pharmaceutics, 15, (2023), 1455.

[3]. Celikci, N., Ziba, C. A., Dolaz, M. "Synthesis and characterization of carboxymethyl shrimp chitosan (CMSCh) from waste shrimp shell", MANAS Journal of Engineering, 8, (2020), 77-83.

[4]. Elhag, M., Abdelwahab, H. E., Mostafa, M. A., Yacout, G. A., Nasr, A. Z., Dambruoso, P., El Sadek, M. M. "One pot synthesis of new cross-linked chitosan-Schiff base: Characterization, and anti-proliferative activities", International Journal of Biological Macromolecules, 184, (2021), 558-565.

[5]. Antunes, J. C., Domingues, J. M., Miranda, C. S., Silva, A. F. G., Homem, N. C., Amorim, M. T. P., Felgueiras, H. P. "Bioactivity of chitosan-based particles loaded with plant-derived extracts for biomedical applications: Emphasis on antimicrobial fiber-based systems", Marine Drugs, 19(2021), 359.

[6]. Kim, I. Y., Seo, S. J., Moon, H. S., Yoo, M. K., Park, I. Y., Kim, B. C., Cho, C. S. "Chitosan and its derivatives for tissue engineering applications", Biotechnology Advances, 26(2008), 1-21.

[7]. Giri, T. K., Thakur, A., Alexander, A., Badwaik, H., Tripathi, D. K. "Modified chitosan hydrogels as drug delivery and tissue engineering systems: present status and applications", Acta Pharmaceutica Sinica B, 2, (2012), 439-449.

[8]. Hashmi, S. A., Chandra, A., Singh, R. K., Chandra, A., Chandra, S. (Eds.). (2015). Electroactive Polymers: Materials and Devices (Vol. 5). Allied Publishers.

[9]. Bakshi, P. S., Selvakumar, D., Kadirvelu, K., Kumar, N. S. "Chitosan as an environment friendly biomaterial–a review on recent modifications and applications", International Journal of Biological Macromolecules, 150, (2020), 1072-1083.

[10]. Al-Azmi, A., Keshipour, S. "Cross-linked chitosan aerogel modified with Pd(II)/ phthalocyanine: synthesis, characterization, and catalytic application", Scientific Reports, 9, (2019), 13849.

[11]. Matica A., Gheorghiţa M., Vasile O. "Biodegradability of Chitosan Based Products", New Frontiers in Chemistry 26, (2017), 75-86.

[12]. Hassan, M. A., Tamer, T. M., Valachová, K., Omer, A. M., El-Shafeey, M., Eldin, M. S. M., Šoltés, L. "Antioxidant and antibacterial polyelectrolyte wound dressing based on chitosan/hyaluronan/phosphatidylcholine dihydroquercetin", International Journal of Biological Macromolecules, 166, (2021), 18-31.

[13]. Kim, S. "Competitive biological activities of chitosan and its derivatives: antimicrobial, antioxidant, anticancer, and anti-inflammatory activities", International Journal of Polymer Science, (2018), Article ID 1708172

[14]. Ahmed, S., Ikram, S. "Chitosan its derivatives: a review in recent innovations", International Journal of Pharmaceutical Sciences and Research, 6, (2015), 14.

[15]. Aranaz, I., Acosta, N., Civera, C., Elorza, B., Mingo, J., Castro, C., Heras Caballero, A. "Cosmetics and cosmeceutical applications of chitin, chitosan and their derivatives", Polymers, 10, (2018), 213.

[16]. Wang, H., Qian, J., Ding, F. "Emerging chitosan-based films for food packaging applications", Journal of Agricultural And Food Chemistry, 66, (2018), 395-413.

[17]. Kazemi A., M., Zandi, M., Shokrollahi, P., Ehsani, M., Baharvand, H. "Chitosan surface modified hydrogel as a therapeutic contact lens", Polymers for Advanced Technologies, 31, (2020), 741-748.

[18]. Elkasabgy, N. A., Mahmoud, A. A., Maged, A. "3D printing: An appealing route for customized drug delivery systems", International Journal of Pharmaceutics, 588, (2020), 119732.

[19]. Decante, G., Costa, J. B., Silva-Correia, J., Collins, M. N., Reis, R. L., Oliveira, J. M. "Engineering bioinks for 3D bioprinting. Biofabrication", 13, (2021), 032001.

[20]. Fan, L., Li, M., Gong, Y., Peng, K., Xie, W. "Preparation and characterization of alginate/Hydroxypropyl chitosan blend fibers", Journal of Applied Polymer Science, 125, (2012), 829-835.

[21]. Wang, Z., Yan, Y., Jiang, Y., Li, W., Hu, X., Fu, B., Qin, C. "Effect of orally administered hydroxypropyl chitosan on the levels of iron, copper, zinc and calcium in mice", International Journal of Biological Macromolecules, 64, (2014), 25-29.

[22]. Zhao, T., Jiang, L. "Contact angle measurement of natural materials", Colloids and Surfaces B: Biointerfaces, 161, (2018) 324-330.

[23]. Queiroz, M. F., Teodosio Melo, K. R., Sabry, D. A., Sassaki, G. L., Rocha, H. A. O. "Does the use of chitosan contribute to oxalate kidney stone formation?", Marine Drugs, 13, (2014), 141-158.

[24]. Yue, L., Wang, M., Khan, I. M., Xu, J., Peng, C., Wang, Z. "Preparation, characterization, and antibiofilm activity of cinnamic acid conjugated hydroxypropyl chitosan derivatives", International Journal of Biological Macromolecules, 189, (2021), 657-667.

[25]. Cao, J., He, G., Ning, X., Wang, C., Fan, L., Yin, Y., Cai, W. "Hydroxypropyl chitosan-based dual self-healing hydrogel for adsorption of chromium ions", International Journal of Biological Macromolecules, 174, (2021), 89-100.

[26]. Zhu, C., Zou, S., Rao, Z., Min, L., Liu, M., Liu, L., Fan, L. "Preparation and characterization of hydroxypropyl chitosan modified with nisin", International International Journal of Biological Macromolecules, 105, (2017) 1017-1024.

[27]. Nie, L., Deng, Y., Li, P., Hou, R., Shavandi, A., Yang, S. "Hydroxyethyl chitosan-reinforced polyvinyl alcohol/biphasic calcium phosphate hydrogels for bone regeneration", Acs Omega, 5, (2020), 10948-10957.

[28]. Guo, W., Cai, Z., Xu, Q., Sun, K., Huang, X., Cao, Z. "Synthesis and properties of dehydroabietyl glycidyl ether grafted hydroxypropyl chitosan", BioResources, 15, (2020), 4110-4123.

[29]. Malekshah, R. E., Shakeri, F., Khaleghian, A., Salehi, M. "Developing a biopolymeric chitosan supported Schiff-base and Cu (II), Ni (II) and Zn (II) complexes and biological evaluation as pro-drug", International Journal of Biological Macromolecules, 152, (2020), 846-861.

[30]. Yasmeen, S., Kabiraz, M. K., Saha, B., Qadir, M. D., Gafur, M. D., Masum, S. "Chromium (VI) ions removal from tannery effluent using chitosan-microcrystalline cellulose composite as adsorbent", Int. Res. J. Pure Appl. Chem., 10, (2016), 1-14.

[31]. EL Knidri H., Belaabed R., El khalfaouy R., Laajeb A., Addaou A., A. Lahsini. "Physicochemical Characterization of Chitin and Chitosan Producted from Parapenaeus Longirostris Shrimp Shell Wastes", Journal of Materials and Environmental Sciences, 8, (2017), 3648-3653.

[32]. Ainali, N. M., Xanthopoulou, E., Michailidou, G., Zamboulis, A., Bikiaris, D. N. "Microencapsulation of fluticasone propionate and salmeterol xinafoate in modified chitosan microparticles for release optimization", Molecules, 25, (2020), 3888.

[33]. Vaezifar, S., Razavi, S., Golozar, M. A., Karbasi, S., Morshed, M., Kamali, M. "Effects of some parameters on particle size distribution of chitosan nanoparticles prepared by ionic gelation method", Journal of Cluster Science, 24, (2013), 891-903.

[34]. Pereira, A. G., Muniz, E. C., Hsieh, Y. L. "^{1}H NMR and ^{1}H–^{13}C HSQC surface characterization of chitosan–chitin sheath-core nanowhiskers", Carbohydrate Polymers, 123, 2015, 46-52.

[35]. Liu, Q., Zhang, J., Li, D., Lang, J., Zai, S., Hao, J., Wang, X. "Inhibition of amphiphilic N-Alkyl-O-carboxymethyl chitosan derivatives on Alternaria macrospora", BioMed Research International, (2018). Article ID 5236324.

[36]. Triana-Guzmán, V. L., Ruiz-Cruz, Y., Romero-Peñaloza, E. L., Zuluaga-Corrales, H. F., Chaur-Valencia, M. N. "New chitosan-imine derivatives: from green chemistry to removal of heavy metals from water", Revista Facultad de Ingeniería Universidad de Antioquia, (89), (2018), 34-43.

[37]. Lin, Z., Cheng, X. "Synthesis and properties of pH sensitive carboxymethylated hydroxypropyl chitosan nanocarriers for delivery of doxorubicin", Journal of Macromolecular Science, Part A, 58, (2021), 600-609.

[38]. Wang, P., Lv, X., Zhang, B., Wang, T., Wang, C., Sun, J., Zhang, Y. "Simultaneous determination of molar degree of substitution and its distribution fraction, degree of acetylation in hydroxypropyl chitosan by ^{1}H NMR spectroscopy", Carbohydrate Polymers, 263, (2021), 117950.

[39]. Abd El-Aziz, M. E., Morsi, S. M. M., Salama, D. M., Abdel-Aziz, M. S., Abd Elwahed, M. S., Shaaban, E. A., Youssef, A. M. "Preparation and characterization of chitosan/polyacrylic acid/copper nanocomposites and their impact on onion production", International Journal of Biological Macromolecules, 123, (2019) 856-865.

[40]. Al Fulaij O., Abdel-Zaher Abdelaziz E., Fakharia A. "Utility of newly modified chitosan in the removal of heavy metal ions from aqueous medium: ion selectivity, XPS and TGA." Bulletin of Materials Science, 42, (2019), 237.

[41]. Claverie, E., Perini, M., Onderwater, R. C., Pianezze, S., Larcher, R., Roosa, S., Yada B.,Wattiez, R. "Multiple Technology Approach Based on Stable Isotope Ratio Analysis, Fourier Transform Infrared Spectrometry and Thermogravimetric Analysis to Ensure the Fungal Origin of the Chitosan", Molecules, 28, (2023), 4324.